# Measurement of the Optical Properties of the Deep Mediterranean – the ANTARES Detector Medium.

Wolfgang H. Schuster
St. Catherine's College, Oxford

Thesis submitted in partial fulfilment of the requirements for the degree of Doctor of Philosophy at the University of Oxford

Trinity Term 2002

**Abstract**

The observation of high energy neutrinos to probe astrophysical sources requires a large detector embedded in an optically transparent medium to record the Cherenkov light from the neutrino-induced muons. Astrophysical models for the observed flux of cosmic rays at the top of the Earth's atmosphere suggest that a few tens of neutrinos of PeV energy might be observed per year in a detector with a square kilometer effective area. A smaller version of such a detector, with an effective area of 0.1 $km^2$, is currently under construction by the ANTARES Collaboration in the deep Mediterranean Sea. The performance of this detector depends upon the optical properties of its surrounding medium. In this thesis, these properties were studied in great detail with in situ measurements at the ANTARES site.

A stand-alone experiment, designed and constructed as part of the ANTARES Collaboration, was immersed during various seasons and the data were analysed using Monte Carlo simulations. The water properties were found to be sufficiently good, with low enough absorption and scattering, not to significantly limit the performance of the ANTARES detector. To within the limitations of the experiment, no seasonal variations could be observed. The best available data yielded an absorption length of $25.9 \pm 0.5(\text{stat.}) \pm^{1.2}_{1.1}$ (syst.) m at 375 nm. In the blue (473 nm) a lower limit to the absorption length of $46.0 \pm 0.4(\text{stat.}) \pm^{2.4}_{2.0}$ (syst.) m was extracted. Both of these values lie within the range observed for deep lake water by the Baikal experiment and that of clear oceans. Scattering was divided into that by small scattering centres and by large scattering centres. A scattering length for small centres (with forward-backward symmetric scattering properties) of $137 \pm 6(\text{stat.}) \pm^{17}_{17}$ (syst.) m (at 375 nm) was found, consistent with the values obtained by other experiments. The large centre scattering length (at 375 nm) was found to be $173 \pm 10(\text{stat.}) \pm^{17}_{17}$ (syst.) m and the average cosine of the large centre scattering angular distribution $0.54 \pm 0.05(\text{stat.}) \pm^{0.08}_{0.08}$ (syst.). The angular distribution at the ANTARES site (excluding a potential contribution from very forward-peaked scattering which could not be resolved) was found to be less forward-peaked than would have been expected on the basis of some of the few "typical" measurements of the scattering angular distribution of previous experiments. Evidence was found that these discrepancies were due to the difference in wavelength used to probe the water as well as the difference in the environmental conditions between the experiments: the ANTARES measurements were performed at a larger depth than the experiments with a more forward-peaked angular distribution and in water that is much more pure.

Currently there are no reliable measurements for the scattering properties in the blue, which is the wavelength range of maximum sensitivity of the ANTARES detector. However these properties are not expected to be less favourable than in the UV, from which the accuracy on the detector efficiency is estimated at $\sim$20% and on the angular resolution at $\sim 0.1^\circ$. Current detector simulation results suggest that the limitations to the neutrino angular resolution due to the optical properties are smaller than due to the reconstruction, yielding an overall angular resolution of $\sim 0.65^\circ$ at 1 TeV and $\sim 0.25^\circ$ at 100 TeV. More measurements at blue wavelengths together with more detailed detector simulations using the measurement results in this thesis are however needed for a more accurate quantification of these effects.

# Acknowledgements

I am very thankful to a large number of people for contributing in some way or other to the completion of this thesis. I am very grateful to my first supervisor, Martin Moorhead, whose enthusiasm for ANTARES was bestowed upon me and whose inventiveness and experience were guiding me in the initial(!) stages of my DPhil. I am very thankful to my second and third supervisors, Serap Tilav and Susan Cooper, for inspiring me throughout the rest of this thesis, for pointing me in the right direction when the deep Mediterranean seemed darker than usual, as well as for their constructive criticism, patience and care in proof-reading this thesis and pointing out when things were being obscure. A very big thank you as well to Susan for the financial support, and for enabling me to travel to various exotic places to meet up with other people from the ANTARES Collaboration. I am gratefully indebted to David Bailey for his always willingness to help with any computer problems and thankful for many interesting discussions.

A debt of gratitude is owed to the entire ANTARES Collaboration. In Oxford, I am very thankful to Barney Brooks, who designed and built various components for the experiment, and to Johan Fopma, who contributed in many ways to the successful working of the data acquisition system. From the Saclay group, I should thank various people, amongst others especially Nico de Botton, Nathalie Palanque-Delabrouille, Jean-Pierre Schuller, François Gournay, Jean Poinsignon and Richard Azoulay, who all contributed to the success of the experiments. In Sheffield, I gratefully acknowledge a number of useful and interesting conversations with John MacMillan.

I am also very grateful to various people at the Rutherford Appleton Laboratory, and especially to Andrew Sansum, for the reliable computing support. In Oxford, thank you to all the computing support staff of the Nuclear and Astrophysics Laboratory for all their help, and to all the technical and secretarial staff for putting up with me during all this time, especially to Beverly Roger for her patience(!) in dealing with my late travel plans, etc. On the industrial side, many thanks go to Electron Tubes Ltd. for their industrial case award and the valuable experience I gained by working in their laboratories. My thanks go especially to my supervisor Andy Cormack and the technical director Ron McAlpine.

Last but not least, I would like to thank my parents, brothers and all my friends for their constant support in one way or other, and for their everlasting friendship, understanding and patience.

The list of people to whom I am thankful is too long to mention everyone here, but whoever has not been mentioned and should be thanked can be assured of my sincere gratitude.

Wolfgang Schuster

# Contents

# List of Figures

# List of Tables

# Glossary

**AGN** **A**ctive **G**alactic **N**uclei: galaxies with a very compact nucleus with long jets of radio-emitting material, mainly electron synchrotron radiation from high energy electrons accelerated in galactic and extra-galactic magnetic fields.

**ANTARES** **A**stronomy with a **N**eutrino **T**elescope and **A**bysss **E**nvironmental **RE-S**earch: a neutrino telescope in its construction phase in the deep Mediterranean Sea.

**ASIC** **A**pplication **S**pecific **I**ntegrated **C**ircuits: electronic circuits designed for specific applications, usually built on small silicon wafers and containing many layers of transistors and wiring.

**ATW** **A**ctive **T**ime **W**indow of the TDC: the time interval during which the TDC can register a hit.

**Blue** Wavelength of the light source of Test 3′ with a central value of 472.6 nm and a FWHM of 14.5 nm.

**CPU** **C**entral **P**rocessing **U**nit: the central unit ("brain") of the computer containing the logic circuitry that performs the instructions of a computer's programs.

**CTSA** **C**alibration **T**ime **S**pectrum in **A**ir: histogram of photons from the pulsed light source of Test 3′ taken in the laboratory (in air).

**DAC** **D**igital to **A**nalog **C**onverter: A device that converts a digital input signal (binary numbers) to an analog output signal (voltage) carrying equivalent information.

**DC** **D**irect **C**urrent: unidirectional flow of electric charge.

**Direct photons** Photons that have not scattered in the medium between their point of emission and their point of detection.

**EPROM** **E**rasable **P**rogrammable **R**ead **O**nly **M**emory: a programmable ROM that can be erased and re-used. Erasure is achieved by shining intense ultraviolet radiation through a window designed into the memory chip.

$f$ The **f**raction of pulses of the light source which have a photon registered by the TDC.

**FIFO** **F**irst **I**n **F**irst **O**ut: an approach to handling program work requests from queues or stacks so that the oldest request is handled next.

**FPGA** **F**ield **P**rogrammable **G**ate **A**rray: an integrated circuit (see ASIC definition) which can be programmed by the user after manufacture.

**FWHM** **F**ull **W**idth **H**alf **M**aximum: the width of a distribution at which the value is half of its maximum value.

**GD** **G**enerated **D**ata: histogram produced using HTD as input and applying the appropriate jitter using Poisson statistics to simulate lower statistics data distributions.

**GRB** **G**amma **R**ay **B**urst: objects producing short "bursts" of very high energy gamma rays with afterglows lasting several months.

**HTD** **H**igh statistics **T**ime **D**istribution: same as TD but with much higher statistics (400M or 800M events as described in text).

**HV** **H**igh **V**oltage

**IC** **I**nteraction **C**entre: any entity in the medium that causes a photon either to be scattered or to be absorbed.

**LC** **L**arge **C**entre: scattering centre of size larger than about one twentieth of the wavelength of the incident radiation (the approximate limit for SC scattering). In the literature this is often referred to as Mie or particle scattering centre.

**LED** **L**ight-**E**mitting **D**iode: a semiconductor device that emits incoherent optical radiation when an electric current passes through it. A set of six such units was used to create an isotropic pulsed light source with a very fast rising pulse for the measurements of the optical properties at the ANTARES site.

**MBX** Microprocessor OS-9: the central processing unit used to run the data acquisition of Test 3′.

**MC** **M**onte **C**arlo: a statistical simulation method using a technique of random sampling to generate a sample population of a system to determine its physical properties.

**MTD** **M**onte Carlo **T**ime **D**istribution: TD obtained by simulating the path of many photons in the water using the Monte Carlo technique.

$\boldsymbol{\mu}$ The mean number of photons arriving at the detector during the data acquisition with Test 3′.

**OM** **O**ptical **M**odule: the basic unit of the ANTARES detector. A pressure resistant glass sphere housing a PMT and its electronics, set into a transparent gel which is optically matched with the glass. It also contains a calibration LED (not for Test 3′).

**PC** **P**hoto**C**athode: layer on the inside of the PMT glass from which electrons are ejected via the photoelectric effect and accelerated towards the anode via a large potential difference.

**PMT** **P**hoto**M**ultiplier **T**ube: a device for detecting single photons using the photoelectric effect and amplifying the signal produced by use of a large potential difference to accelerate the photoelectron onto a series of metal dynodes.

**PRGS** **P**ressure-**R**esistant **G**lass **S**phere: transparent spherical unit housing the various components of the experiment to be immersed into the water.

**RAM** **R**andom-**A**ccess **M**emory: place in a computer where the operating system, application programs and data in current use are kept to allow fast access by the computer's processor.

**ROM** **R**ead-**O**nly **M**emory: "built-in" computer memory containing data that can only be read and not written to.

**RS-232** **R**ecommended **S**tandard-**232**: standard interface for connecting serial devices transmitting one data bit at a time.

**SC** **S**mall **C**entre: scattering centre of size so small that the field created by an incident electromagnetic wave is uniform over its extent, characterized by forward-backward symmetric scattering properties. The literature typically refers to these as Rayleigh or Einstein-Smulochowski scatterers.

**SNR** **S**uper**n**ova **R**emnant: gaseous remainders of a supernova explosion forming a rapidly expanding and slowly fading cloud mixing with interstellar matter.

$\boldsymbol{S_{TDC}}$ **S**pectrum of **TDC**: the histogram of arrival times at the detector of photons from a pulsed LED source using as the timing device the TDC of Test 3′, taking into account the TDC's single-hit nature (Eq. 5.18, p. 73).

**TD** **T**ime **D**istribution: a histogram of the arrival time of photons emitted from a light source and registered at various times (determined by the optical properties of the medium) after propagating through the medium.

**TDC** **T**ime-to-**D**igital **C**onverter: the timing device of Test 3′. It transforms the number of cycles of a 40 MHz clock into a digitised signal. Each cycle is divided into 32 channels by means of delay lines, yielding a resolution of 781.25 ps.

**Test 3′** The name given by the ANTARES collaboration to the experiment used for the in situ measurement of the optical properties at the ANTARES site.

**TTL** **T**ransit-**T**ime **L**ogical signal: a simple 8-bit value that is physically represented as the sequence of high and low voltage states in pins 2 through 9 of a parallel port at a given point in time.

**UV** **U**ltra**V**iolet: wavelength of the light source of Test 3′ with a central value of 374.5 nm and a FWHM of 5.2 nm.

**VDS** **V**irtual **D**etector **S**phere: the detector configuration used in the simulations of the ANTARES Test 3′ experiment.

# Introduction

*The most beautiful experience we can have is the mysterious. It is the fundamental emotion which stands at the cradle of true art and true science...*

*A. Einstein (1879-1955)*

ANTARES is a neutrino telescope in the construction phase in the deep Mediterranean Sea (at 2400 m depth, 50 km off the coast of Toulon) with the primary aim to observe neutrinos from distant and energetic astrophysical objects to open a new window on the high energy universe. In practice this is achieved by means of a large array of photomultiplier tubes which record the arrival time of Cherenkov light emitted by muons (as they travel through the deep ocean), the result of neutrino-nucleon interactions in the Earth below the detector. For the performance of this detector, the understanding of the optical properties of the surrounding medium -the deep ocean- is important. In this thesis these properties will be analysed using measurements taken in situ at the ANTARES site.

In Chapter 1, the reasons for using neutrinos to study distant and energetic astrophysical sources are briefly put into context. The reasons for the need of an accurate understanding of the optical properties of the medium surrounding the ANTARES detector are given, followed by a brief description of the experiment proposed by the ANTARES collaboration to study these neutrinos. In Chapter 2, the theoretical background for the study of the optical properties of the deep sea is described and the technique developed by M. Moorhead[1] and the author from the Oxford group of the ANTARES collaboration explained.

Chapter 3 gives a description of the experimental equipment used for measuring the optical properties at the ANTARES site with details of the different configurations used. The various measurements taken with this experiment are then summarized. Detailed measurements were made by the author with this experiment in the laboratory and the results from these were analysed to gain an accurate understanding of the experimental equipment. Using the results from this detailed analysis, the method for the treatment and calibration of the experimental data of Test 3′ is established (Chapter 4).

In Chapter 5, the Monte Carlo tools necessary for the analysis of the acquired data, developed by the author, are described and the sensitivity of the experiment to the different optical parameters is analysed by means of Monte Carlo simulations. The analysis

[1] First D-Phil supervisor

method of the data, based upon the comparison of the shapes of the arrival time distributions of the data (Chapter 4) and the Monte Carlo simulations (Chapter 5), is then established (Chapter 6). The results, together with a detailed study of the systematic errors, are then presented. In the last Chapter, a comparison is made between the results obtained by the experiment described in this thesis and other experiments, followed by a brief discussion of the ANTARES detector performance. Ideas for future measurements are then given.

A better understanding of the optical properties of the ANTARES detector medium, through the studies described in this thesis, will aid ANTARES to gain a better knowledge about the systematic uncertainties in the ANTARES detector efficiency and neutrino angular resolution. The Monte Carlo code and the analysis method developed in this thesis will be important tools for the continuous monitoring of the in situ water optical properties with future measurements.

# Chapter 1

# Neutrino Astronomy

This chapter puts the choice of neutrinos as a source of information about the nature of astrophysical objects into context. The principle of neutrino detection is briefly described and the reasons for the need of an accurate understanding of the optical properties of the medium surrounding the detector are given. An overview of the detector designed by the ANTARES Collaboration to identify sources of neutrinos is then given.

*I have done a terrible thing: I have postulated a particle that cannot be detected...*

*W. Pauli (1900-1958)*

## 1.1 Motivation

The observations of very high energy cosmic rays from all directions at the top of the Earth's atmosphere with energies exceeding $10^{19}$ eV [1, 2] remains a mystery to date, leaving questions about the nature of their source and its acceleration mechanisms. Figure 1.1 shows the cosmic ray flux obtained by various experiments [3].

Amongst the potential sources of acceleration for particles in the universe are Active Galactic Nuclei (AGNs), Gamma Ray Bursts (GRBs) and Supernova Remnants (SNRs). AGNs have been observed to accelerate particles to very high energies and to produce a high intensity of TeV gamma rays [4, 5]. GRBs are the most energetic events in the universe and it is speculated that they have the potential to accelerate particles and hence to produce high energy neutrinos [6]. In a very recent publication [7] good evidence is given that in SNRs, in addition to electrons, protons are also accelerated. In the case where protons are accelerated, inevitably associated with their acceleration is the production of neutrinos via the interaction of hadrons in the surrounding medium to produce charged pions which then decay to muons and muon neutrinos:

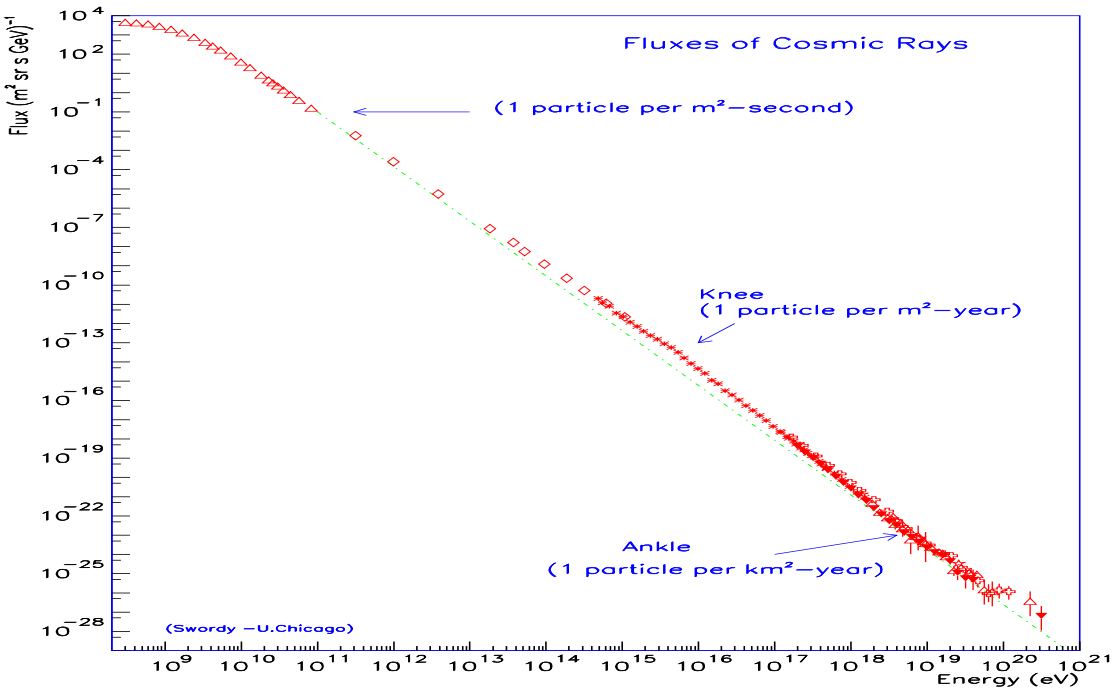


**Figure 1.1:** *Measured cosmic ray spectrum with data from LEAP, Proton, Akeno, AGASA, Fly's Eye, Haverah Park and Yakutsk* [3].

$$\begin{array}{ccccccc} p+(p,\gamma) & \rightarrow & \pi^0 & + & \pi^{\pm} & + & X. \\ & & \downarrow & & \downarrow & & \\ & & \gamma\gamma & & \mu\nu_\mu & & \\ & & & & \downarrow & & \\ & & & & \nu_\mu\nu_e e & & \end{array} \tag{1.1}$$

The muons then decay into electrons and electron and muon neutrinos. These neutrinos would then escape and provide a valuable source of information about the nature of these astrophysical objects. The fact that both photons and cosmic rays (which are much easier to detect) could be used as sources of information about these objects still leaves the question: why neutrino astronomy?

Cosmic rays carry limited information about their origin because they are subject to deflection by complex cosmic magnetic fields except at very high energies ($\gtrsim 10^{19}$ eV). However in the rest frame of protons with energies above $\sim 10^{19}$ eV the cosmic microwave background photons appear as gamma ray photons, sufficiently energetic to produce pions via the excitation of the $\Delta$-resonance (GZK effect, [9, 10]) and therefore causing the protons to be strongly absorbed (Figure 1.2).

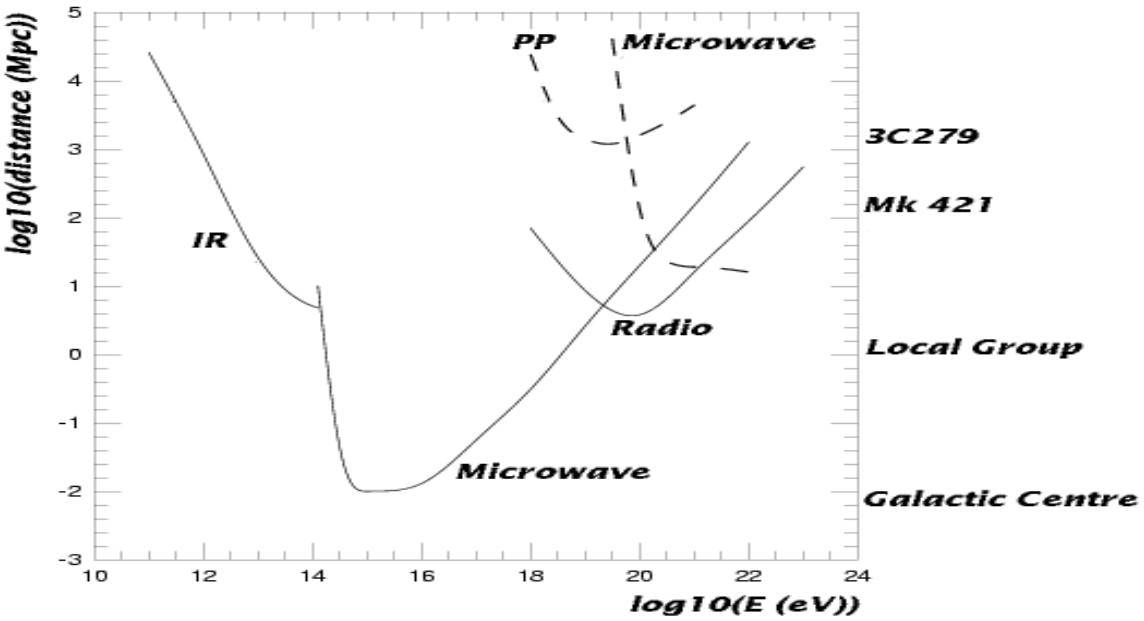


**Figure 1.2:** *Absorption length of photons (solid lines) and protons (dashed lines): photons interact with the infra-red, microwave and radio cosmological backgrounds. Protons interact with the cosmic microwave background and are lost via direct pair production (Figure taken from [8]).*

Up to date, most of the current knowledge about the high energy universe was derived from the observation of photons: energies up to 1 TeV [11] have been used in the past as the primary source of information about the high energy universe. Whilst photons are electrically neutral and stable, and whilst they are copiously produced, the central regions of hot and dense high energy astrophysical sources are mostly opaque to photons. Additionally, high energy photons interact with cosmic microwave background and photons of the infrared radiation background producing electron-positron pairs (an effect described in [12]), which suppresses the possibility of surveying the sky for distances greater than 100 Mpc using gamma rays with energies above a few TeV (Figure 1.2). Photons are therefore of limited use in the understanding of the high energy universe at large distances. The exact source of the high energy cosmic rays is thus unknown. Between TeV gamma rays and these very high energy cosmic rays, a territory spanning some seven orders of magnitude in wavelength is therefore still unexplored.

Neutrinos, being weakly interacting and electrically neutral, can escape without interacting in the material surrounding the sources and travel to the Earth without being absorbed and without deflection by inter-galactic magnetic fields (Figure 1.3). Neutrinos therefore provide an elegant and powerful tool to provide the only[1] direct information on the nature of the most energetic astrophysical phenomena, with the possibility of

[1]Other candidate particles such as neutrons, muons, etc. were not considered in the above discussions because they are unstable and can therefore not be used to carry information over astrophysical distances.

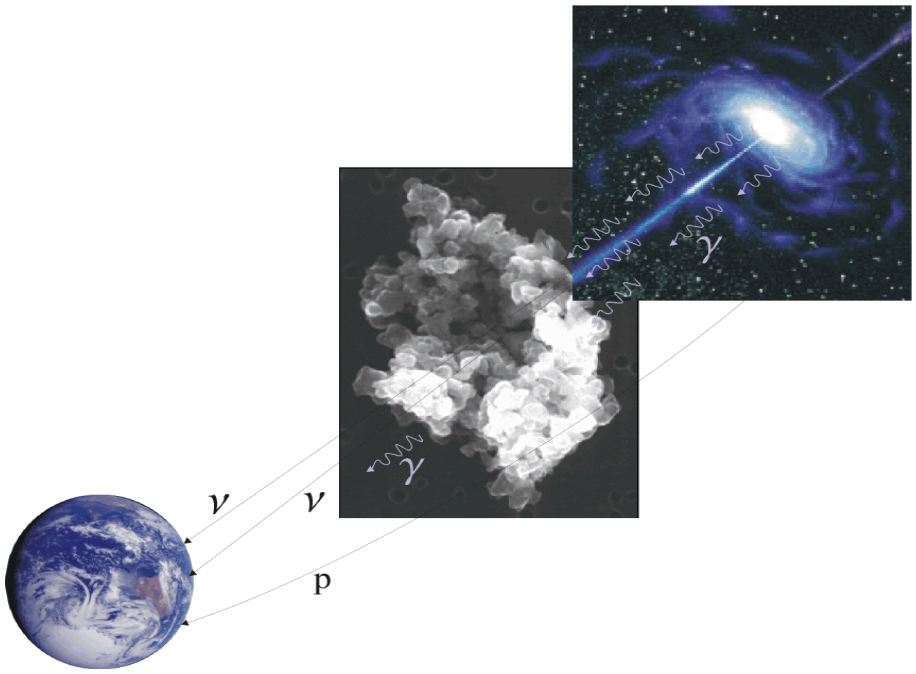


**Figure 1.3:** *Carriers of information about distant astrophysical objects: photons, cosmic rays and neutrinos. A large fraction of photons is absorbed in the source, by cosmic dust and by cosmic background radiation. Charged cosmic rays are deflected by intergalactic magnetic fields except at the very highest energies, where they are however absorbed on the cosmic microwave background. Neutrinos are the only known reliable carriers of information which preserve their direction of emission, being undeflected by magnetic fields and not absorbed.*

observing hitherto unknown objects.

## 1.2 Principle of Neutrino Detection

In the previous section the interest and reasons for choosing neutrinos as a source of information about astrophysical sources of high energy cosmic rays were described. This section gives a brief overview of the detection principles of the neutrinos from astrophysical sources and will be followed in the next section by a description of the detector configuration proposed by the ANTARES Collaboration.

High-energy neutrinos from astrophysical sources travel through the Earth and a small fraction (varying with the energy-dependent interaction cross-section) of these produce upward going high-energy muons in the medium surrounding the detector (Figure 1.4) through weak charged-current interactions:

$$\nu_\mu + N \longrightarrow \mu^- + X, \tag{1.2}$$

where $N$ is a proton or neutron and $X$ are hadrons yielding a shower at the interaction vertex.

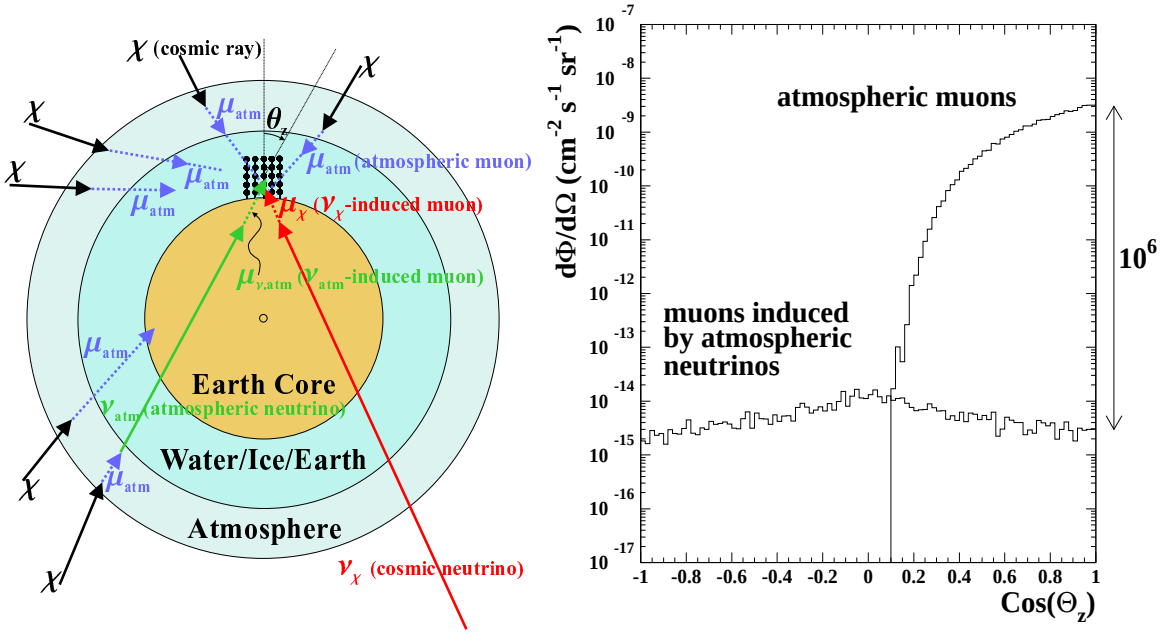


**Figure 1.4:** *Left: the Earth shields the detector against all upward going particles except neutrinos and the water above the detector largely reduces the flux of downward going muons from cosmic rays. Right (taken from [13]): Muon and neutrino fluxes above 1 TeV at the depth of 2.3 km of the ANTARES site below the surface of the ocean.*

These muons are very penetrating and, when travelling in a transparent medium like water or ice, are detected by their Cherenkov light emissions if their path intersects the instrumented volume of the detector. The arrival time of these Cherenkov photons is recorded with photomultiplier tubes (PMTs) at various locations, allowing the energy and direction of the muon and, given the approximate collinearity between the muon and neutrino direction at high energies, hence of the parent neutrino to be reconstructed. Muon paths are typically several hundred meters long for muon energies of the order of 100 GeV rising to maximum path lengths of the order of 40 km at $10^9$ GeV.

Various factors affect the choice of the site, the size and the configuration of a detector capable of recording this Cherenkov light:

**Site:** The detector must be able to distinguish between the muons induced by $\nu_\mu$-nucleon interactions below the detector and the much larger flux of downward going atmospheric muons (see right-hand plot of Figure 1.4), induced when high energy cosmic rays interact with nuclei in the upper atmosphere to produce pions which subsequently decay to muons. This presents a technological challenge. Using a natural shield such as a thick layer of water or ice can make the distinction between signal and background easier[2]: the detection of upward-going muons is used as a signature of $\nu_\mu$-nucleon interactions in the matter

[2]In addition to the water or ice shield above the detector, the Earth also shields the detector from below against all particles except neutrinos.

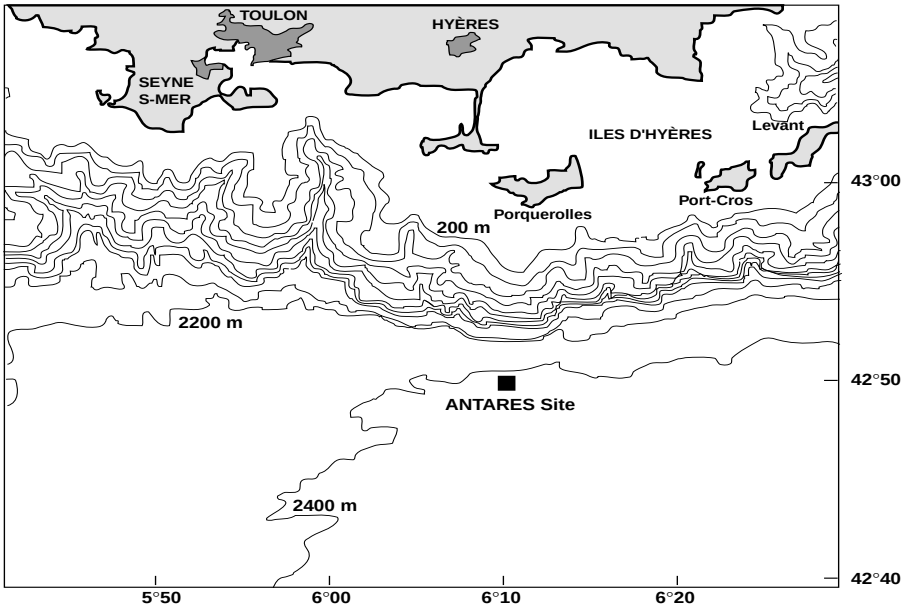


**Figure 1.5:** *Map showing the ANTARES site near Toulon (about 50 km from the southern coast of France). The contour lines show the depth of the ocean floor.*

below the detector, providing discrimination against the downward going atmospheric muons. The ANTARES Collaboration has chosen the first option: the deep Mediterranean Sea, 50 km off the French coast of Toulon at 2400 m depth (Figure 1.5). The main background signal for the upward-going muons is due to muons induced from atmospheric neutrinos (which can penetrate the Earth), produced when some of the atmospheric muons decay in flight. These are shown as a relatively flat (compared to the distribution of atmospheric muons) background in Figure 1.4 (right).

**Size:** Whilst the low interaction cross sections of neutrinos enables them to travel over astronomical distances without being strongly attenuated, it also requires very large detectors to observe a statistical significant rate of neutrinos. The flux $\phi_\mu$ of upward-going muons from neutrinos of astrophysical origin observed by the detector is the convolution of various factors:

$$\phi_\mu \sim A \otimes \phi_{\nu_\mu} \otimes \sigma_{\nu_\mu} \otimes R_\mu N_A, \tag{1.3}$$

where $A$ is the area of the detector, $\phi_{\nu_\mu}$ the neutrino flux, $\sigma_{\nu_\mu}$ the interaction cross section per nucleon of neutrinos as they travel through the Earth, $R_\mu$ the (energy dependent) range of the resulting muons such that they arrive at the detector above the minimum energy threshold for Cherenkov light production and $N_A$ Avogadro's number. The last two terms combined represent the probability that a neutrino with a trajectory intersecting the detector yields a muon above threshold at the detector. Based upon fits to the high energy cosmic ray spectrum above $10^{19}$ eV and the assumption that the fraction of the proton energy carried by a neutrino produced through a photo-meson interaction,

$E_{\nu_\mu} \approx 0.05 E_p$, is independent of energy, Waxman and Bahcall [14] derive the upper bound on the differential neutrino flux as

$$\phi_{\nu_\mu} \approx 10^{-4} \quad E_{\nu_\mu}^{-2} \quad \mathrm{GeV}^{-1}\mathrm{m}^{-2}\mathrm{s}^{-1}\mathrm{sr}^{-1}. \tag{1.4}$$

Using the above flux together with the results for the probability that a neutrino will yield a signal at the detector, given in [15] as $P_{\nu\to\mu} \approx 1.3 \times 10^{-6} \times E^{0.8}$ (where $E$ is in units of TeV) for $E = 1 - 10^3$ TeV, the event rate is estimated at $10^{-5} - 10^{-4}$ events per year per m$^2$. To observe a measurable flux of neutrinos, detectors with an effective area of the order of 1 km$^2$ are thus required.

**Configuration:** The configuration for such a detector will be determined by the physics studies it is designed for and the optical properties of the medium surrounding the detector.

### Effect of the Water Properties upon the Detector Performance

Elaborating on the last point of the previous paragraph, the total number of detected Cherenkov photons and the time taken by these photons to travel from their point of emission along the muon track to the detector elements will be influenced by the transparency of the water through which they travel. The more scattering there is, the larger the number of indirect photons (i.e. those that have scattered) arriving at the PMTs. In the presence of a high density of absorption centres in the water, a large fraction of photons will be lost before reaching the PMTs.

Early simulations (described in [16]) based upon a much less detailed model (from the one established in this thesis) of the optical properties at the ANTARES site, for which the scattering due to "pure water" was taken from Morel [17] and the scattering angular distribution of impurities[3] in the water was assumed to correspond to the average measured by Petzold [18], showed that the optical properties of the water have a significant impact upon the performance of the ANTARES detector. As an example, the event rate was reduced by 5-10% when changing the scattering length from 50 m to 40 m and a change in the $\langle \cos\theta \rangle$ by $\sim$0.1 changed the event rate by 5-20% (over the muon energy range $10^2 - 10^8$ GeV). These effects are shown in Figure 1.6. The angular resolution was found to be most strongly correlated to the overall scattering length (see Figure 1.7), the effect being most significant at high energies ($\sim$100 TeV) where the quality of the reconstruction dominates the angular resolution, whilst at lower energies the angular resolution of the neutrino direction is dominated by the uncertainty in the neutrino-muon angle at the interaction vertex. It can also be seen from the right-hand plots of Figures 1.6 and 1.7 that the knowledge of the effective scattering length (defined in Section 5.4) is not sufficient to determine the detector efficiency and the detector angular resolution since variations up to 30% and uncertainties up to 0.2° can be observed for a given effective scattering length.

[3] See Chapter 2 for a complete description of the meaning of these terms.

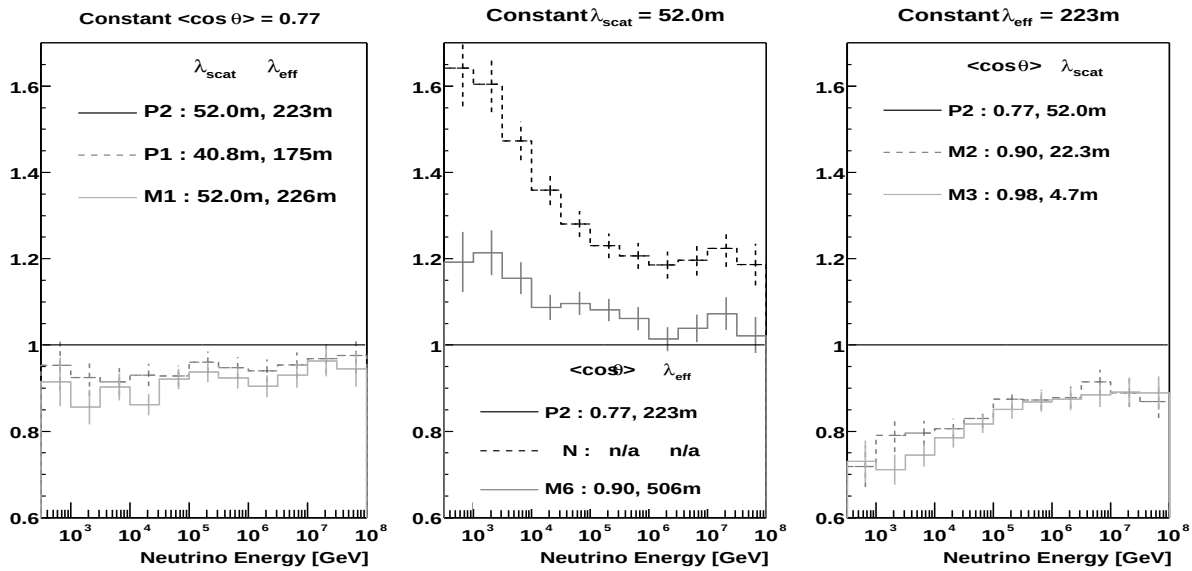


**Figure 1.6:** *Relative event rates for various water models keeping one parameter constant in each case (Figure taken from [16]).*

The above effects can be explained with the hypothesis that it is the number of Cherenkov photons detected with each PMT at (corresponding to unscattered photons) or very close to (corresponding to photons which have scattered through very forward-peaked angles) zero time delay which is important in the muon track reconstruction. For the detector efficiency, photons scattered at large angles are lost and the more scattering there is, the less photons are detected, causing the detector efficiency to decrease with decreasing scattering length and decreasing $\langle \cos\theta \rangle$. For the angular resolution, increased scattering will reduce the number of useful photons in the reconstruction, hence degrading the detector performance for smaller scattering lengths. The impact of the $\langle \cos\theta \rangle$ is more complicated: for small scattering lengths, a more forward-peaked angular distribution improves the angular resolution by reducing the spread in the arrival time of the near-direct photons, whilst for larger scattering lengths ($\gtrsim$40 m), the angular resolution is relatively unaffected.

The experimental accuracy required for the measurements of the scattering parameters can be estimated from Figures 1.6 and 1.7. As an example, for an accuracy of 20% on the efficiency, the scattering length must be known to within $\sim$15 m and the $\langle \cos\theta \rangle$ to within $\sim$0.1. In order to know the angular resolution to within 0.1°, the scattering length should be known to within $\sim$30 m and the $\langle \cos\theta \rangle$ to within $\sim$0.15, for scattering lengths $\gtrsim$20 m. It should be noted, however, that these results are based upon linear interpolations between water models with relatively forward-peaked angular distributions and relatively short scattering lengths, and that extrapolations to much larger $\lambda_{scat}$ should not be linear, since they must asymptotically converge towards a water model with no scattering. The above estimates are therefore only very approximate (although conservative) and the required accuracies could be largely overestimated.

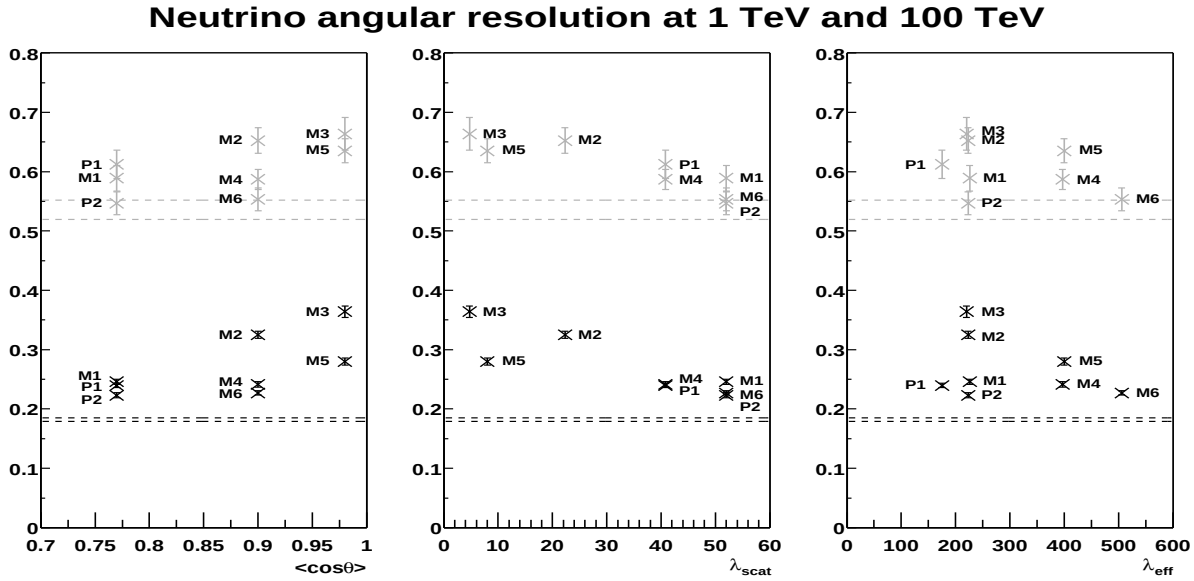


**Figure 1.7:** *Neutrino angular resolution for 1 TeV (top) and 100 TeV (bottom) neutrinos as a function of* $\langle \cos\theta \rangle$, $\lambda_{scat}$ *and* $\lambda_{eff}$ *(defined by Eq. 5.25, p. 79). The horizontal lines correspond to the angular resolution (within the statistical errors) when photon scattering is neglected (Figure taken from [16]).*

Absorption will influence the range over which Cherenkov photons can be detected. For typical distances between detector elements of ∼60 m, variations in the absorption length of the order of 10% (i.e. 2.5 m for an absorption length of 25 m at a photon wavelength of ∼375 nm and 5 m for an absorption length of 50 m at a photon wavelength of ∼473 nm) cause the number of photons detected to fluctuate by approximately 10-25%. Intuitively, increased absorption will reduce the range over which muons can be detected, hence making the effective size of the detector smaller (and therefore reducing its efficiency). At lower energies, a change in the absorption length is also expected to cause a change in the detector energy threshold. The impact of the absorption length upon the angular resolution is less evident due to the different impacts it has upon the direct and scattered Cherenkov photons: whilst increased absorption reduces the number of direct photons, it increases the ratio of direct to indirect photons. As a general trend however, it is expected that the larger the muon energies, the less significant the effect of a varying absorption length upon the detector performance because of the larger number of photons produced with increasing energies. Quantitative results of the impact of these fluctuations upon the detector performance are pending further investigation with detailed simulations.

The relevance of an accurate knowledge of the angular resolution is lying in the fact that it will determine the signal to background ratio for the detector. At small angles for example, the background rate will scale as $\delta\theta^2$ which, with typical ranges of the optical properties considered in Figure 1.7, would lead to uncertainties in the background rate of up to ∼200%! These, in turn, alter the statistical significance of any observed

events from potential astrophysical sources. It is thus very important to have an accurate understanding of the angular resolution.

From the above discussions, it is clear that the optical properties of the medium will have an important impact upon the ultimate detector performance, and will also influence the design of the potential future 1 km$^2$ ANTARES detector. Given the sensitivity of the ANTARES detector to each of the various optical parameters, it is important to understand each of these parameters separately. This motivated the detailed study of the optical properties of the ANTARES detector medium, a study in which both the "pure water" scattering length and the $\langle \cos\theta \rangle$ were left as free variables in order to obtain the real range of possible water models, and will be the topic in the rest of this thesis: ***Measurement of the Optical Properties of the Deep Mediterranean – the ANTARES Detector Medium.***

## 1.3 Design of the ANTARES Detector

The ANTARES experiment is a neutrino telescope currently in the construction phase. The telescope will eventually consist of an array of detector elements -PMTs- capable of recording the precise arrival time and number of Cherenkov photons emitted by muons as they travel through the water. The individual elements of the detector are assembled in various laboratories before being deployed into the deep sea.

The first generation of the ANTARES detector will consist of an array of 10 to 14 flexible strings[4] anchored on the sea bed by means of a heavy weight at a depth of 2400 m, such that the active length starts 100 m above the sea bed (Figure 1.8). Each line consists of 30 storeys, each separated by 12 m, maintained vertical by a buoy at the top of the line. Each storey consists of a cluster of 3 Optical Modules (OMs [20]), oriented at 45 degrees to the line towards the sea bed and painted in black on the back half. This configuration simultaneously minimises the rate of biofouling and sediment adhering [21] to the surface of the OM and yields high detection efficiencies for the Cherenkov light emitted by muons whose trajectories are lying between the up-going vertical and the horizontal. It also ensures lower detection efficiencies for downward-going muons. Each OM consists of a pressure-resistant glass sphere with an outer diameter of 17″ containing a 14-stage 10″ Hamamatsu PMT R7081-20 [22] inside a mu-metal grid, to shield the PMT against the Earth's magnetic field. The three OMs of each floor are grouped symmetrically around a local control module which holds the electronics for each storey. The electronics controlling the individual elements as well as the power distribution to the PMTs are located at the bottom of each line and derive their power from the main "Junction Box", to which the whole detector is connected. Power is transfered from the shore via a 50 km long electro-optical cable (connected to the Junction Box), which also supports the data transmission to and from the shore via optical fibres.

Acoustic positioning systems, tiltmeters and compasses are attached at various loca-

[4] For a complete description, the reader is referred to the ANTARES proposal [13] and the ANTARES Technical Design Report [19].

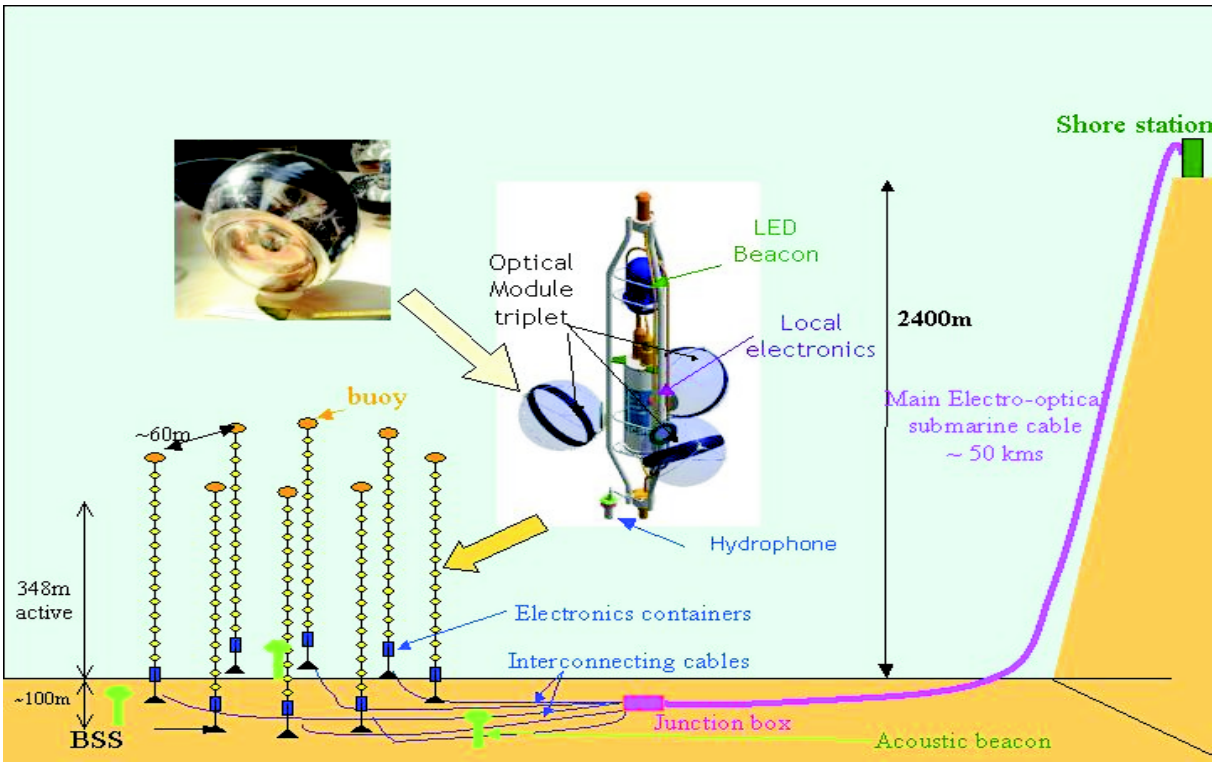


**Figure 1.8:** *Artist's view of the 0.1 km$^2$ ANTARES detector (reproduced from the ANTARES TDR [19]).*

tions along the line to determine the relative positioning and orientations of the detector elements, giving the relative positions of the OMs accurately to within 10 cm (corresponding to a time resolution of ∼0.5 ns in water) and their relative orientations to within 1°. An acoustic system coupled to a global positioning system is used for absolute geographic positioning of the detector. Optical beacons at the bottom of each string together with an instrumentation line will be used to monitor the water optical properties continuously.

## 1.4 Summary

In this chapter, the concept of neutrino astronomy was briefly introduced and its advantages with respect to more conventional methods like "cosmic ray" or "photon" astronomy in the observation of distant astrophysical objects were discussed (Section 1.1). The principles of detecting neutrinos and the factors limiting their observation were then described (Section 1.2). Reasons for the need of an accurate knowledge of the optical properties were presented. A description of the detector proposed by the ANTARES Collaboration was then given (Section 1.3).

# Chapter 2

# Optical Properties in the Deep Oceans

This chapter gives a brief history of the development of our understanding of the interaction of light with matter. It then gives the necessary theoretical background to distinguish between various interactions of photons with the medium, leading to the definition of the optical parameters used in the rest of this thesis. Previous experiments by various oceanography institutes and several other neutrino-experiment collaborations are described and their results discussed. The model for the optical properties at the ANTARES site is then established.

*The real voyage of discovery consists not in seeking new landscapes, but in having new eyes.*

*M. Proust (1871-1922)*

## 2.1 Introduction

In Chapter 1, the importance of a detailed knowledge of the optical properties at the ANTARES site in the accurate understanding of the performance of the ANTARES experiment was described. In this chapter, the theoretical and experimental background, as well as a technique for measuring the optical properties in situ at the ANTARES site, will be given.

The wavelength range of interest to the ANTARES experiment is $350 \lesssim \lambda \lesssim 550$ nm. This interval is determined by the Cherenkov light spectrum

$$\frac{d^2N}{dxd\lambda} = \frac{2\pi\alpha}{\lambda^2} \times \left(1 - \frac{1}{\beta^2 n^2}\right) \tag{2.1}$$

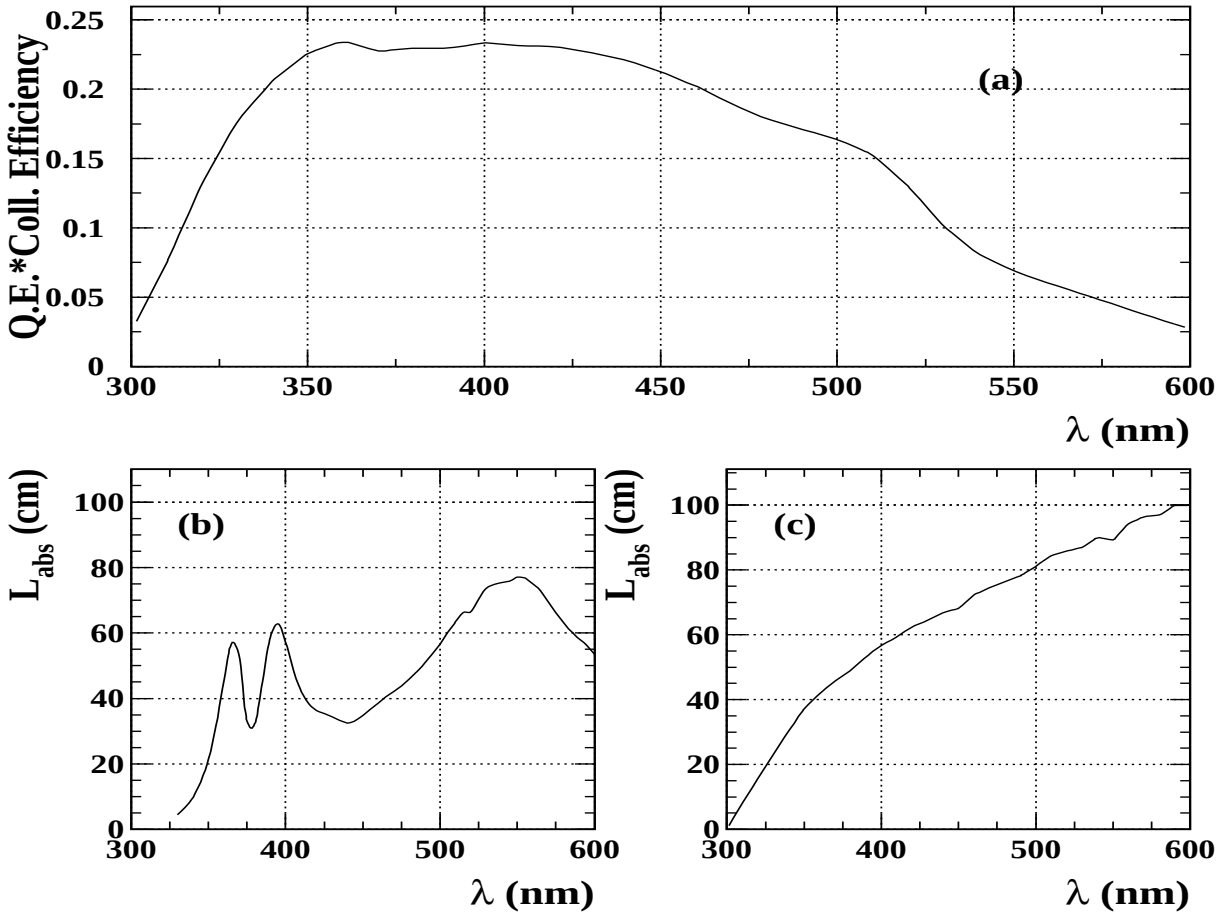


**Figure 2.1:** *ANTARES OMs: (a) Quantum efficiency times collection efficiency of Hamamatsu R7081-20 PMTs, (b) measured absorption length of the glass sphere*[1] *and (c) of the silicone gel as a function of the incident-light's wavelength* [*20*].

(where $x$ is the distance traveled by the charged particle), the optical properties of several of the elements of the ANTARES detector, as well as the optical properties of the water surrounding the detector. The lower bound is given by the cut-off in the transmission of light through the glass of the OM and the upper bound by the quantum efficiency of the PMTs (Figure 2.1).

## 2.2 Light and Matter: History of Enlightenment

The interaction of light with matter was described more than nine centuries ago in the attempt to explain the origins of colour, which was one of the first impetus for the development of a theory for light scattering. As early as the eleventh century, the Arab physicist Alhazen of Basra noticed that "*the brightness of the daytime sky is due to re-*

[1] The peculiar shape is typical for the borosilicate glass used and can be attributed to its iron content [23]. Given the thickness of 8 mm of the glass sphere, the effect upon the transmission probability (>96% above 350 nm) is however very small.

*flection of sunlight by particles contained in the air*". This was followed by Leonardo da Vinci's observation "*... that the blueness we see in the atmosphere is not intrinsic color, but is caused by warm vapor evaporated in minute and insensible atoms on which the solar rays fall, rendering them luminous against the infinite darkness of the fiery sphere which lies beyond and includes it...*".

Following the observation by Leonardo da Vinci, the interaction of light with matter started to receive a considerable amount of attention in the $19^{\text{th}}$ century, and a thorough scientific study of light scattering commenced with the experiments on aerosols by Tyndall in 1869, and culminated in 1871 with the development of the "Theory of Scattering" on small dielectric spheres by Lord Rayleigh, which considered scattering by very small spherical particles modeled as electric dipoles (which were only much later identified with molecules). This was followed by the work on small absorbing spheres by Lorenz in 1880, on perfectly reflecting spheres by Thomson in 1893 and finally the development of the "Mie Scattering Theory" in 1908 by Gustav Mie, who provided a generalization to the Rayleigh theory for scattering centres of arbitrary size.

The development of each of these theories however has to be attributed in part to the work of Maxwell, summarized in the publication of his famous set of equations in 1865, which formalized the results of the accumulated research on electromagnetism. Following the Mie theory, Smoluchowski (1908) and Einstein (1910) developed a theory related to the scattering of light by small-scale statistical density fluctuations in liquids, which lead to the same general result as the molecular theory developed by Rayleigh. An important discovery was soon to follow, that by Chandrasekhara Raman (1928), with the observation of inelastic scattering of light from liquids.

The preceding list of authors who contributed to the development of our understanding of the propagation of light in matter is clearly non-exhaustive, and only some of the main authors (most relevant to this thesis) have been cited. During the twentieth century, a lot of detailed work was carried out to understand the processes of absorption and scattering in matter, both in small-scale (e.g. quantum theory) and large-scale media (e.g. interstellar and interplanetary dust, atmospheric optical phenomena, radiation transfer in oceans, etc.). Yet the complexity of natural systems is such that our understanding of the optical properties of such systems is still fairly limited.

## 2.3 Photon-Matter Interactions

Scattering and absorption, over the optical range of wavelengths considered in this thesis, can be treated using the results from the theory of classical electromagnetism (summarized in great detail in e.g. [24]). To obtain the solution to a scattering or absorption problem, it is merely a matter of applying these results, together with the appropriate boundary conditions, to yield the resultant photon field. For this, essentially two factors must be known: the geometry of the interaction centre and its electronic structure relative to that of the surrounding medium.

Naturally, a distinction between two different classes of scattering centres can be made

on grounds of size: those centres small enough such that the field is uniform over the entire extent of the scattering centre (causing the angular distribution of scattered photons to exhibit forward-backward symmetry) and those which are larger (causing the angular distribution to be much more complex and strongly angle dependent). These will be discussed in Sections 2.3.1 and 2.3.2 respectively. Apart from the distinction on grounds of the homogeneity of the photon field (which is mainly dependent upon the size of the scattering centre), the electronic structure will determine factors like the probability of absorption or inelastic scattering (e.g. Raman scattering and fluorescence) which will be briefly discussed in Section 2.3.3.

### 2.3.1 Scattering by Small Centres: "Einstein-Smoluchowski" or "Rayleigh" Scattering

The homogeneity of the photon field over the whole scattering centre is determined by its size relative to the wavelength of the incident radiation. For the approximations in the derivation of the theory relating to small scattering centres to be valid, the radius of the scattering centre is required to be smaller than $\sim \lambda/20$ [25], i.e. smaller than ~20 nm at the wavelengths of ~400 nm used in the experiments described in this thesis.

Small centres causing scattering in natural waters can be divided into local fluctuations in the density of the water and (if the water is not perfectly pure) very small impurities (e.g. viruses). Smoluchowski [26] and Einstein [27] developed a theory based upon the statistical analysis of the random motion of the water molecules in a small volume of water, which causes local fluctuations in the density and hence in the refractive index. Prior to their theory, Rayleigh had developed a separate theory [28, 29] for scattering from small spherical particles. The derived angular distribution of the scattered radiation as well as the wavelength dependence is the same for both theories.

In the Einstein-Smoluchowski theory, the scattered number of photons as a function of the angle relative to the incident direction and the distance $r$ is given by [27]

$$N(\theta) = \left(\frac{N_o}{2r^2}\,\frac{\pi^2}{\lambda_o^4}\right) \times \left[kT_o\kappa\rho^2\left(\frac{\partial\epsilon}{\partial\rho}\right)^2\right] \times \left(1+\cos^2\theta\right) \tag{2.2}$$

with the variables:

| | | |
|---|---|---|
| $N_o$ | = | number of incident photons |
| $\lambda_o$ | = | central wavelength of incident radiation |
| $k$ | = | Boltzmann constant |
| $T_o$ | = | temperature |
| $\kappa$ | = | isothermal compressibility |
| $\rho$ | = | density |
| $\epsilon$ | = | dielectric constant. |

The above expression is reminiscent of the form given by the Rayleigh theory, yielding

$$N(\theta) = \left(\frac{N_o}{2r^2}\,\frac{\pi^2}{\lambda_o^4}\right) \times \left[(4\pi)^2 a^6 \left|\frac{m^2-1}{m^2+2}\right|^2\right] \times \left(1+\cos^2\theta\right), \tag{2.3}$$

where $a$ is the radius of the scattering centre and $m$ is the complex relative refractive index between the medium and the scattering centre. Eqs. 2.2 and 2.3 both yield the well-known result that the intensity of light scattered by a scattering centre small compared to the wavelength of the incident light is proportional to $1/\lambda^4$, under the assumption that the term in square-brackets in both equations is independent of wavelength. In the case of scattering in water, the wavelength dependence of this term is however not negligible.

In the case of density fluctuations, various empirical models were proposed to relate the dielectric constant to the density of the liquid. Amongst these are for example that of Lorentz-Lorenz:

$$\frac{\epsilon-1}{\epsilon+2} = C\rho, \tag{2.4}$$

where $C$ is a constant. Using this expression in the calculation of the second term in Eq. 2.2 in terms of the dielectric constant or the refractive index $n^2 = \epsilon$ yields

$$N(\theta) = \left(\frac{N_o}{2r^2}\,\frac{\pi^2}{\lambda_o^4}\right) \times \left[kT_o\kappa\,\frac{(n^2-1)^2\,(n^2+2)^2}{9}\right] \times \left(1+\cos^2\theta\right). \tag{2.5}$$

Using the wavelength dependence for the refractive index given in Section 2.7.3 (Eqs. 2.22 and 2.23) and expressing the result in terms of a power law, the best exponent is calculated as $-4.34 \pm 0.31$. Very similar results are obtained when using various other proposed empirical models for the relation between the dielectric constant and the density. The average of these yields an exponent $-4.32 \pm 0.31$, the same central value as that found in [17], where experimental results of scattering in pure water at various wavelengths were used to obtain the best fit. Similarly the best exponent in the Rayleigh theory for small particles (Eq. 2.3) yielded $-4.22 \pm 0.30$, compatible with the previous result. In the rest of this thesis an exponent of $-4.32$ will therefore be assumed and any systematic errors arising from this choice will be quantified in Section 6.3.4. The probability of scattering from small ICs (which will be expressed in terms of the small centre scattering length $\lambda_{SC}$ in Section 2.4), as a function of the wavelength of the radiation, can therefore be written as

$$\frac{1}{\lambda_{SC}(\lambda)} \propto \left(\frac{1}{\lambda}\right)^{4.32}. \tag{2.6}$$

From Eqs 2.2 and 2.3, the angular distribution of the scattered light is $\propto (1+\cos^2\theta)$. This result was derived for small spherical inhomogeneities. Water molecules however are asymmetric and this anisotropy was experimentally found to cause the angular distribution of the scattered light to be proportional to $1+(1-\delta)/(1+\delta) \times \cos^2\theta$ [30], where $\delta$ is the ratio of the intensity of the parallel to perpendicular polarization states at an angle

of 90° (i.e. the depolarization ratio), found by experiment. Using the average $\delta = 0.09$ between various experiments, Morel [17] derives the angular dependence of the number of scattered photons from small scattering centres as

$$N(\theta) \propto \left[1 + \left(\frac{1-\delta}{1+\delta}\right)\cos^2\theta\right] \approx (1 + 0.835\cos^2\theta). \tag{2.7}$$

The above results are however only valid for very small scattering centres. If the scattering centres are larger than $\sim\lambda/20$ and the phase difference between the individual dipoles cannot be neglected, the approximations made in the derivation of the wavelength dependence of the scattering length and of the angular distribution above are not valid and a different treatment applies (as discussed in the next section).

### 2.3.2 Scattering by Large Centres: "Mie" Scattering

ICs larger than $\sim \lambda/20$ (of the incident radiation), cannot be treated as small spheres subject to a uniform electromagnetic field. Instead, to determine the scattering properties of these centres, the full solution to Maxwell's equations, with the appropriate boundary conditions, must be obtained. The work by Gustav Mie [31] provides these solutions for ICs of arbitrary geometry and electronic composition[2]. The solutions to the scattering angular distribution of these large ICs are very complex and vary significantly between centres with different sizes. To calculate an overall angular distribution function for all large centres, the knowledge of the size and density distributions (both of which can vary considerably between different media) is therefore required. The measurement of these distributions in deep oceans is however beyond the reach of any current technology.

In the absence of this knowledge, the scattering angular distribution for large centres can therefore only either be measured experimentally or approximated by some analytical expression. The measurement of the scattering angular distributions in the deep ocean is a technological challenge (for reasons described in Section 2.5.2) and no measurements at the ANTARES site were therefore available. It was therefore only possible to approximate the scattering angular distribution with an analytical expression, under some general assumptions about the shape of the scattering function.

Mie theory predicts that the larger the IC, the more forward-peaked the scattering angular distribution. For large scattering angles, it predicts a series of maxima and minima in the angular distribution which are however expected to disappear when a mixture of IC sizes is present. To model this complex behaviour, an approximation by a simple analytical expression, which can reproduce the general shape of the Mie scattering angular distribution, is used. Various expressions have been proposed of which the most typical function used [32, 33] is the (normalised) Henyey-Greenstein scattering angular distribution function, given by

[2] It is a generalization of the Rayleigh theory leading to the same result in the limit where the particle sizes are small.

$$\widetilde{\beta}_{HG}(g,\theta) \stackrel{\text{def.}}{=} \frac{\beta_{HG}(g,\theta)}{b(\lambda)} = \frac{1}{4\pi} \frac{1-g^2}{(1+g^2-2g\cos\theta)^{3/2}}, \tag{2.8}$$

where $\beta_{HG}(g,\theta)$ and $b(\lambda)$ are defined by Eqs. 2.15 and 2.16 respectively, and the relative amount of forward and backward scattering, determined by the distribution of particle size densities in the medium, can be controlled with the parameter $g$. According to [33], this approximation provides a good representation of the true scattering function once the value of $g$ is known. One of the advantages of this particular analytical function over various others in [32] is that the adjustable parameter $g$ has a direct physical significance in that it is simply the average cosine of the scattering angular distribution:

$$g = -2\pi \int_{-1}^{1} \widetilde{\beta}_{HG}(g,\theta) \cos\theta \; d\cos\theta. \tag{2.9}$$

Additionally, the Henyey-Greenstein function also has the advantage that it is easily invertible, an important consideration for the purpose of sampling from this distribution in Monte-Carlo (MC) simulations, yielding

$$\cos\theta = 2r \times \frac{(1+g)^2(1-g+gr)}{(1-g+2gr)^2} - 1, \tag{2.10}$$

where $r$ is the random number between 0 and 1. Given the advantages of the Henyey-Greenstein function over various other analytical expressions, it was therefore chosen in this thesis as a model to approximate the angular distribution of large ICs.

### 2.3.3 Absorption and Inelastic Scattering

In the discussion of the two types of ICs in the previous two sections, absorption and inelastic scattering were not considered. Both of these are important in that they can considerably alter the final photon distribution. Absorption is mainly determined by the electronic structure of the interaction centre: in the UV for example, the absorption due to pure water can be attributed to electronic transitions within the water molecule; at wavelengths larger than 450 nm the energy of the photons is transferred to one or more of the vibrational modes of the O-H bond in the water molecule [34]. A number of shoulders and peaks in the absorption spectra over this wavelength range have been observed, with the closest shoulders to the wavelengths used in the analysis of the optical properties at the ANTARES site (375 nm and 473 nm) being predicted at 376 nm and 474 nm [35].

In addition to the absorption by pure water, various amounts of impurities (such as organic pollutants and dissolved gases, which increase absorption in the UV [36]) can significantly alter the absorption spectrum. In the case of *true* absorption of a photon, the energy is then dissipated as non-radiative energy, such as thermal energy.

Inelastic scattering in water can be divided into Raman scattering and fluorescence. In the former, a photon is immediately re-emitted with an energy different from that of the incident photon. In the latter, a photon is re-emitted with a different energy after a

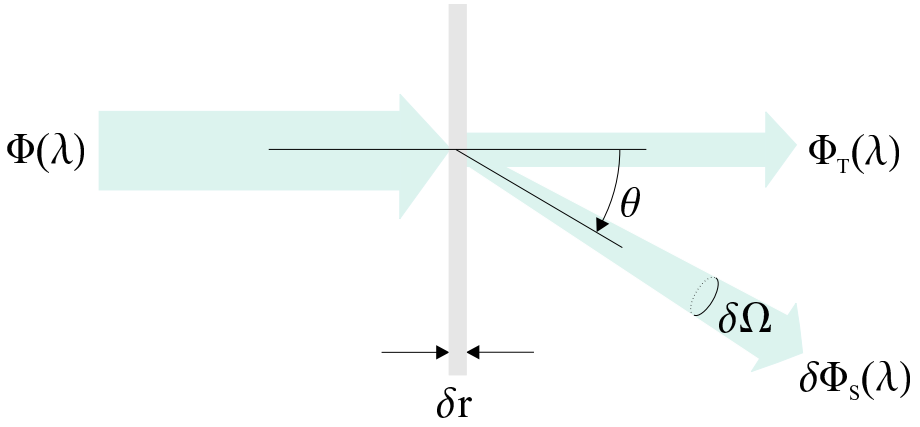


**Figure 2.2:** *A fraction of the number of photons from the incident flux $\Phi(\lambda)$ is absorbed within the slab of thickness $\delta r$. Another fraction $\delta\Phi_S(\lambda)$ is scattered into a solid angle $d\Omega$ and the remainder $\Phi_T(\lambda)$ is transmitted unperturbed.*

time delay of the order of $10\mu$s. For reasons described in Section 2.5.4, inelastic scattering can be neglected in the analysis of the optical properties at the ANTARES site with the experiment described in Chapter 3 and will therefore be left out of subsequent discussions of the optical properties.

## 2.4 Definitions of Optical Parameters

In Section 2.3, considerations of the size and the electronic structure of interaction centres lead to the distinction between two types of scattering centres and absorption centres. In this section, the macroscopic variables used to describe these processes will be defined.

Consider a slab of material like the one shown in Figure 2.2. In the absence of inelastic scattering, the flux of photons after traversing a slab of thickness $dr$ is given by

$$\Phi(r+dr) = \Phi(r)(1-\alpha\ dr) \ \longrightarrow\ \frac{d\Phi(r)}{\Phi(r)} = -\alpha\ dr, \tag{2.11}$$

where $\Phi(r)$ is the flux at point $r$ and $\alpha$ is the probability per unit distance of interacting inside the slab (i.e. of being absorbed or scattered). The probability of being absorbed $P_A$ and that of being scattered $P_S$ are thus usually written in terms of an absorption coefficient $a(\lambda)$ (or absorption length $\lambda_A(\lambda)$) and a scattering coefficient $b(\lambda)$ (or scattering length $\lambda_S(\lambda)$), defined by

$$P_A = \frac{\delta\Phi_A}{\Phi} = -a(\lambda)\delta r = -\frac{\delta r}{\lambda_A(\lambda)} \quad \text{and} \quad P_S = \frac{\delta\Phi_S}{\Phi} = -b(\lambda)\delta r = -\frac{\delta r}{\lambda_S(\lambda)}, \tag{2.12}$$

where the $\lambda$ without a subscript refers to the wavelength of the radiation. From Eq. 2.11, the flux of photons surviving up to distance $r$ without interacting is given by

$$\Phi(r) = \Phi(0)e^{-\alpha r} \quad \text{yielding} \quad P_{\sigma,\alpha}(r) = e^{-\alpha r}, \tag{2.13}$$

where $P_{\sigma,\alpha}(r)$ is the probability of survival (without interacting) up to distance $r$ and $\alpha$ is either the absorption or the scattering coefficient. The attenuation coefficient $c(\lambda)$ is defined as the sum of the absorption and scattering coefficients:

$$c(\lambda) = a(\lambda) + b(\lambda) \quad \longrightarrow \quad \frac{1}{\lambda_{att}} = \frac{1}{\lambda_A} + \frac{1}{\lambda_S}, \tag{2.14}$$

where $\lambda_{att}$ is the attenuation length. The relations of Eq. 2.14 are valid as long as the source is collimated and only one scattering centre is encountered during the trajectory of any photon because if more than one scattering occurs, some of the photons which scattered out of the beam will be scattered back to the detector.

The angular distribution of the scattered flux (per unit incident flux and per unit distance traveled) into a solid angle $\delta\Omega$ centred on $\theta$, as shown in Figure 2.2, is described by

$$\lim_{\delta r \to 0} \lim_{\delta\Omega \to 0} \frac{\delta\Phi_S(\theta,\lambda)}{\Phi(\lambda)\delta r \delta\Omega} \stackrel{def.}{\equiv} \beta(\theta,\lambda), \tag{2.15}$$

called the "volume scattering function" in the oceanography community. It represents the absolute scattered intensity per unit incident irradiance and per unit volume of water, i.e. the differential scattering cross section per unit volume.

Integrating over all solid angles, for each type of IC, the scattering coefficient for unpolarized sources and randomly oriented scatterers can simply be written as

$$b(\lambda) = \int \beta(\theta,\lambda) d\Omega. \tag{2.16}$$

The angular distribution of SC scatterers (Eq. 2.7) can be written in terms of the volume scattering function [17]

$$\beta(\theta,\lambda) = \beta(90,\lambda) \times \left(1 + \frac{1-\delta}{1+\delta} \times \cos^2\theta\right), \tag{2.17}$$

where $\beta(90,\lambda)$ is the differential scattering cross section per unit volume at an angle of 90°, given by the first two terms of Eq. 2.2 multiplied by $r^2/N_o$ and a factor $(6+6\delta)/(6-7\delta)$ (where the $\delta$ is the same as in Eq. 2.7) to take into account the increased scattering due to the anisotropy of the water molecules [37]. Using Eq. 2.16, the total SC scattering coefficient can be derived as

$$b_{SC}(\lambda) = \frac{8\pi}{3} \times \beta(90,\lambda) \times \left(\frac{2+\delta}{1+\delta}\right). \tag{2.18}$$

This expression is used in the computation of the SC scattering coefficient by oceanographers, using the results of their measurement of $\beta(90, \lambda)$, as discussed in the next section (and was therefore included here).

Each type of interaction centre in the medium can be defined by the above variables, independently of each other. To obtain the overall parameter it is then only necessary to sum over the various contributions from the individual types of centres.

## 2.5 Experimental Background

Having discussed the theoretical background for the distinction between absorption centres and two main types of scattering centres, and having defined these in terms of macroscopic variables, the various interaction centres will be discussed in the context of the natural medium of the ANTARES detector: the deep sea.

Natural waters contain optically significant dissolved and particulate matter which are both highly variable in type and concentration. The optical properties of such waters therefore show large spatial and temporal variations and rarely resemble those of pure water. A continuous size distribution, ranging from water molecules of size 0.1 nm to large particles of size ∼1000 nm, is present in the water. This includes organic molecules of size ∼10 nm, viruses of size ∼100 nm, colloids and bacteria of sizes 200-1000 nm, phytoplankton, organic detritus, etc. Figure 2.3 shows a typical particle size distribution as obtained by Stramski [38], although spatial and temporal variations can of course considerably alter the shape of such a distribution.

The diversity in kind and concentration of impurities is such that no single experiment can measure the optical properties of each kind separately. Traditionally, oceanographers have divided the constituents of natural waters into "dissolved" and "particulate" matter [32]: everything that passes through a filter of pore size ∼400 nm is referred to as dissolved matter and everything that is retained on the filter is called a particle. As discussed in Sections 2.3.1 and 2.3.2, from the physics of the interaction of light with matter, this is not the most satisfactory way of distinguishing between the various components that determine the optical properties of a medium. Instead, a distinction based upon the size of the interaction centre, which determines the IC's angular scattering properties, was made. Whilst the numerical results of some of the previous measurements of oceanographers are therefore difficult to interpret in terms of the physics definitions of the optical parameters used in this thesis, valuable information can be obtained about the absorption and scattering processes in natural media based upon the qualitative understanding gained from these measurements. These will be described in the following sections.

### 2.5.1 Measurements of the Optical Properties of the Deep Sea and Ice

A vast amount of literature can be found on the measurement of the optical properties of water by the oceanography community, summarized in great detail by Mobley [32] and Kirk [39]. Extensive experimental studies were also performed by various collaborations

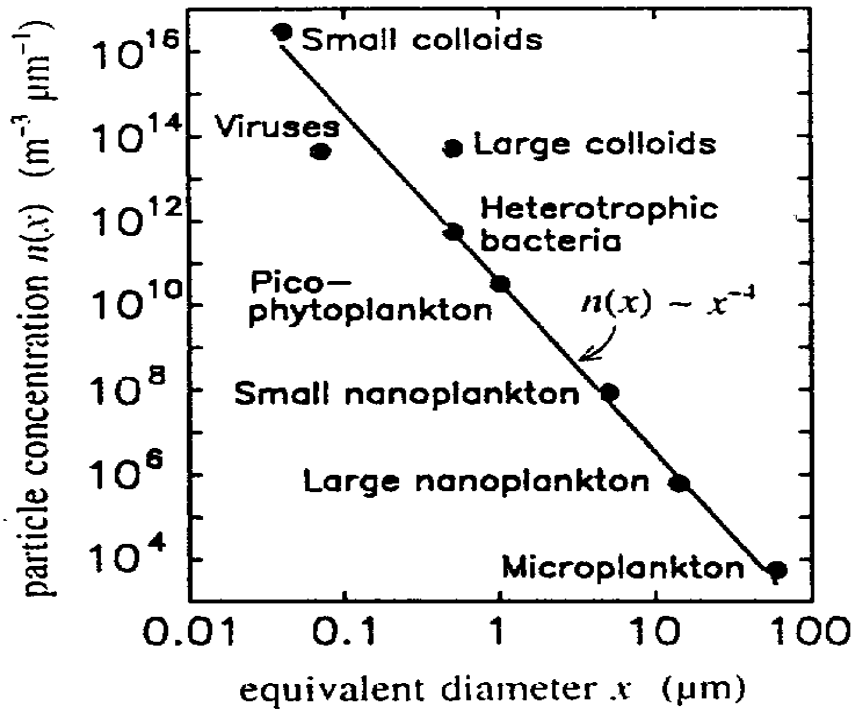


**Figure 2.3:** *Particle size densities typical of biological particles in the open ocean [38]. Measurements of these densities are performed using for example electrical resistance methods such as Coulter counters [32].*

of neutrino experiments, like AMANDA and Baikal, to measure the optical properties of ice [33, 40, 41] and deep lake water [42, 43, 44] respectively.

The optical properties of a medium were described (Section 2.3) in terms of two processes: absorption and scattering. These two processes are random in nature and can therefore only be quantified in terms of statistical averages: ideally one would track a large number of photons through the medium, noting the exact distances between points where each scattered and the total distance after which each photon was absorbed. The average of these distances would then yield a measure of the optical properties and could be used to predict how an "average" photon will propagate inside the medium. In principle, absorption and scattering are thus easily distinguishable processes. In practice, tracking each photon is however an impossible task with current technology and only the final result of tracking many photons through the medium can be measured. The drawback is of course that, in general, neither absorption nor scattering is then measured independently of the other and, to date, very few measurements have therefore been able to distinguish between these two.

Essentially, the in situ determination of the optical properties in natural waters relies upon one of two techniques: the measurement of the distribution of the natural light field within a water column (with for example an instrument described in [45]) to calculate the absorption and backscattering, or the direct measurement of the absorption and scattering

of photons emitted from an artificial light source in the water sample with an instrument capable of recording the number of these photons as a function of angle (for example with an instrument described in [18]), distance or time (e.g. with the experiment described in this thesis) from their point of emission. The first of the two methods is obviously only applicable down to depths to which natural light can penetrate. Measurements in the deep ocean are therefore restricted to the second method and various factors such as low absorption and low scattering coefficients in the visible region (400-700 nm), as well as the difficulty in separating the two[3], contribute to the difficulty of such measurements.

In the next section, a selected sample of measurement techniques and their results will be briefly described. These were either chosen because they were widely cited or because they appeared to be the most accurate measurements available to date. An alternative experiment developed in this thesis as part of the ANTARES Collaboration will then be described and the relative merits between the various experiments discussed.

### 2.5.2 Measurements by Oceanographers

Whilst the diversity of experiments done by the oceanography community is large, few have claimed to be able to measure absorption and scattering in deep ocean directly and independently of the other, leaving relatively large uncertainties in the absolute values of the measurement results for each of the optical parameters. Amongst the measurements of the absorption in water are the widely cited results by Smith & Baker (SB) [46] and the measurements by Pope et al. (RP) [35, 47] who have developed an instrument that attempts to separate scattering from absorption. Amongst the measurements of scattering are the carefully made and widely cited measurements by Petzold [18] of the angular distribution of scattering in various natural waters and the combination of theoretical and experimental work summarized in great detail by Morel [17] to obtain a measure of scattering in pure water.

#### Absorption

SB measured the irradiance from natural sun light at various depths below the surface of several natural waters[4] as a function of wavelength using a spectroradiometer (described in e.g. [45]). The results from various depths were used to yield an attenuation coefficient. Under the assumption that on average this attenuation is due to light that is absorbed and backscattered, the attenuation coefficient $c$ can be related to the absorption coefficient by

$$a \leq c - \frac{1}{2} b_w, \tag{2.19}$$

[3] This is because light that is for example backscattered can be equivalent to light that is absorbed for any detector located in the forward direction.

[4] The experiments were performed in remote open ocean areas where absorption and scattering of dissolved and suspended particulate matter is low.

where $b_w$ is the scattering coefficient of pure water[5]. Using the values for the scattering coefficients from Morel [17], SB therefore calculate an upper estimate for the absorption coefficient in what they quote as the "clearest natural waters". By choosing the average of a consistent set of data from measurements by various experiments of the diffuse attenuation coefficient over a large wavelength range, they provide the absorption coefficient over a wavelength range of 200 - 800 nm. The measurements were deemed to be precise to within 5%. Variations in the distribution of the solar energy however cause the accuracy to be poorer and only ∼25%. In particular, SB note that the attenuation could have been up to 30% higher in the wavelength region of 300-480 nm. A critical review of Eq. 2.19 in [48] argues that the inequality should be even stronger and given by $a \leq c - b_w$. This typically decreases the upper bound by ∼20%. Given however that the values of SB are on the low side and could be larger by up to 30%, the two effects would mostly cancel and the overall uncertainty is such that the values given in [46] are still a useful approximation. At the wavelengths used in the measurements at the ANTARES site (Section 3.2.2), SB find an absorption length of ∼38 m (∼62 m) at 375 nm (473 nm).

RP developed an experiment that tries to circumvent the problem of scattering (which affected the indirect measurement of the absorption coefficient by SB) and claims to be independent of scattering effects at levels that might be observed in ocean waters. Using a highly reflecting cavity containing the sample of water to be analysed, they create an isotropic light field inside the water sample and deduce the optical energy lost within the sample (which is proportional to the absorption coefficient of the sample) by measuring the power input and output from the cavity by means of optical fibres. The isotropy of the light field means that scattering does not cause any further change in the light distribution and, assuming that all scattering is elastic, the total energy lost within the cavity can be attributed to absorption only. The high reflectivity means that an effective path length of the order of 10 m is achieved with a cavity of 10 cm diameter. They find an absorption coefficient of highly purified water (triply distilled) at ∼420 nm wavelength more than a factor of 3 lower (with an accuracy of better than 14%) than the results by SB. As a comparison to the SB results, RP obtain ∼75 m (∼92 m) at 375 nm (473 nm)[6] for their water. The discrepancies between the measurements by SB and those of RP were attributed to various factors such as the purity of the water (the "clearest natural waters" will inevitably contain impurities that will absorb light) and the absence of the effect of scattering upon the absorption in the RP measurements. The results of both measurements are shown in Figure 7.1 on p. 112.

### Scattering

The engineering of instruments capable of accurate in situ measurements of scattering as a function of the scattering angle is even more difficult than that of instruments to measure the absorption. Measurements of the scattered intensity as a function of scattering angle

[5] This expression neglects the particle backscattering coefficient which SB however showed to have a small impact (∼6%) upon the absorption coefficient.

[6] The value at 375 nm was linearly extrapolated using the values at 380 and 385 nm because measurements only existed down to 380 nm.

are very difficult to make because the magnitude of the scattered intensity can increase by five to six orders of magnitude between $\theta = 90°$ and $\theta = 0.1°$ in any natural water sample. Additionally, the scattered intensity between water samples can vary by two orders of magnitude for a specific angle [32]. Such instruments must therefore be very sensitive and at the same time have a large dynamic range. Corrections must also be made for absorption within the sample volume and for attenuation along the incident and scattered beam paths. The very rapid change of the scattered intensity at small angles requires very precise alignment of the optical elements, which is technically difficult for in situ measurements. The result of all these factors is that only very few instruments have been built for the in situ measurements of the scattering angular distributions (over the whole angular range, including scattering at very small angles) and the scattering coefficients.

The most carefully made and widely cited scattering measurements were made by Petzold [18] (in various ocean waters at depths at around 1570 m), who developed two[7] instruments for the measurement of the volume scattering function, one for small scattering angles ($\theta = 0.085°, 0.17°$ and $0.34°$) and one for large scattering angles ($10° < \theta < 170°$). The instruments had a spectral response centred at $\lambda = 514$ nm with a FWHM of 75 nm. To measure the angular distribution at small scattering angles, Petzold used a small point source of light which he collimated to produce a parallel beam of light. This beam then passed through 0.5 m of the water after which it was collected by another lens. Light that was not scattered (and not absorbed) in the water forms an image of the point source at the focal point of the second lens. Scattered light arrives at the image plane displaced by a distance proportional to the scattering angle. Using field stops to delimit the angular interval over which the scattered light was accepted, a PMT was used to measure the intensity for each angular interval at a time. This yielded a relative intensity between the direct beam (attenuated with a filter with a given transmission probability) and the scattered beam at fixed angles (taking due care of the difference in solid angle between the various angles).

For larger scattering angles, Petzold devised a similar instrument, consisting of a projector unit and a receiver unit. The intersection between the collimated beam from the projector and the width of the receiver field of view defined the sample volume and the projector unit could be rotated about this sample volume (see Figure 3 of [18]). By varying the angle between the projector and the receiver, the intensity of the scattered light as a function of the scattering angle could be measured with a photometer spanning almost six orders of magnitude. In addition to the scattering angular distribution, these measurements also provided an absolute value for the scattering coefficient. Individual scattering angular distributions for three different types of oceans yielded average cosines between 0.88 and 0.95. The average of these angular distributions is shown in Figure 7.4 (p. 116).

In general, the inability to do accurate measurements especially at near forward angles, which are crucial in the determination of the total scattering coefficient for very forward-

[7] More than one instrument was needed because of the large difference in intensity (typically up to 6 orders of magnitude) between scattering at very small angles and larger angles.

peaked scattering angular distributions (for which approximately 50% of all scattering can take place at angles of less than a few degrees), makes it very difficult to determine the scattering coefficient directly. As a result, the most commonly used alternative is to determine the scattering coefficient indirectly by using a beam transmissometer [49, 50]. This measures the loss of intensity from a narrow parallel beam passing through a known path length of the medium, yielding an attenuation coefficient which can be used, together with measurements of the absorption coefficient from another experiment, to determine the total amount of scattering[8].

An instrument similar to the one used by Petzold can also be used to measure scattering in purified water to extract the most fundamental scattering properties of water. The results of such measurements together with those of Petzold can then be used to obtain the scattering coefficient and angular distribution of impurities in the water. From Eq. 2.18 (p. 22) it is sufficient to measure the volume scattering function at 90 degrees to the incident beam direction in pure water to obtain the pure water scattering coefficient. Morel [17] compared a number of such measurement results with theoretical predictions from the Einstein-Smoluchowski theory [26, 27] and found good agreement between the two. These results are discussed in Section 7.3.

### 2.5.3 Other Neutrino Experiments

In addition to the measurements done by the oceanography community, various collaborations of neutrino experiments have performed their own set of experiments to deduce the optical properties of their medium, e.g. the AMANDA and Baikal experiments.

The AMANDA Collaboration very extensively measured the optical properties of the ice at the South Pole in the wavelength range of ~337-610 nm [33, 40, 41]. Using time-of-flight measurements from a large combination of source-detector distances, they find (averaged over the depths of the "deep" AMANDA detector) absorption lengths between 90 and 100 m for wavelengths below 460 nm and an effective scattering length (defined in Section 5.4) between 24 and 30 m. The average cosine of the scattering angle is taken as ~0.8 at those depths. The attenuation lengths were measured using DC sources, yielding values of ~27 m with variations of the order of 30% over their depth range. These results are very different from those of natural waters for which the values of the absorption lengths and the scattering lengths are reversed, typically yielding a shorter absorption length and a longer scattering length in water compared to ice.

The Baikal Collaboration performed a similar experiment to AMANDA using a pulsed laser with an emission maximum at 475 nm [44]. They used the combination of the mean amplitudes of a large number of PMTs from their detector array at various distances from the source to deduce the absorption length approximately independently of scattering. The scattering properties were determined from the average arrival time of photons as a function of their distance of emission from the source. In the analysis of Baikal, scattering

[8] Note that some oceanographers use the measured attenuation to derive the absorption under the assumption of a theoretical scattering model [46] whilst others [32] use the attenuation to "measure" scattering under the assumption of a known absorption!

by pure water is considered to be negligible and only very forward-peaked scattering is considered. The absorption length is ∼22 m at 475 nm and the scattering length is quoted as an effective scattering length of ∼480 m, yielding a geometrical scattering length between 24 m and 48 m depending upon the assumed $\langle \cos\theta \rangle$ (between 0.90 and 0.95) of the angular distribution.

### 2.5.4 Comparison of Experiments and Discussion of Results

In the previous sections various experiments by the oceanography community and by several neutrino-experiment collaborations were described. In this section, the advantages as well as the limitations of these experiments will be discussed and their results used in the prediction of the optical properties at the ANTARES site.

#### Advantages and Limitations of Experiments

The measurements by SB have the advantage of using large volumes of water to measure the diffuse attenuation coefficient and, whilst they suffer from the drawback that the absorption length is only obtained indirectly using the measurements of scattering from another experiment, provide a valuable estimate of "typical" average absorption lengths in natural waters.

The experiments by RP have the advantage of disentangling scattering from absorption and are therefore very valuable in the determination of the absorption in pure water, providing a lower limit to the expected absorption coefficient. They are however less valuable in the measurement of the in situ (total) absorption coefficient because they rely upon the sampling of small volumes of water. This has the drawback that the presence of optically significant large aggregates may not be detected if such particles are too few in number to be reliably captured in the sample volume. Such aggregates could however affect the optical properties of large volumes of water such as the ANTARES detector.

The measurements by Petzold [18] are very accurate measurements of the total[9] scattering angular distribution in natural waters. The computation by Mobley et al. [51] of the "particle" angular distribution function from these measurements by subtracting the "pure water" contribution is however uncertain for several reasons: firstly, the huge spectral range of the light source used by Petzold (FWHM = 75 nm!), which causes the average scattering coefficient of "pure water" to be higher than the coefficient at the central wavelength assumed in the calculations by Mobley by about 7%[10]. Secondly, for reasons described in Section 2.3, subtracting simply the "pure water" scattering coefficient (obtained under different environmental conditions, such as different amounts of impurities with sizes smaller than $\lambda/20$, different temperatures and different pressures) to obtain the "particle" scattering coefficient is incorrect. This is because some dissolved impurities exhibit "pure water" scattering properties and the concentration of these is not necessar-

[9] i.e. not making any distinction between contributions from different types of scattering centres in natural waters (as described in Section 2.3).

[10] This is because the scattering coefficient of pure water has a strong dependence upon wavelength ($\lambda^{-4.32}$).

ily the same for different natural waters. One would also expect density fluctuations to depend upon temperature and pressure. Therefore, the deduced "particle" angular distribution function from the in situ measurement of the total angular distribution function presents unknown errors.

### Discussion of Results

From the differences in the measurement of the absorption between the purest water [35] and the "clearest natural waters" [46] it is obvious that (in natural waters), in addition to absorption by pure water, light absorption must be attributed to several other components of the aquatic ecosystem, e.g. inanimate particulate matter, etc. (see [39] for a description of an extensive list of potential absorption centres in natural waters). The total absorption coefficient will therefore vary between different natural waters depending upon the amount of "impurities" contained within them. In contrast, the salt in water appears to have no significant effect (to within 10%) on the absorption in the visible range [46, 52].

Previous measurements of the absorption can only give an approximate estimate of the range of values to be expected for the absorption coefficient in natural waters[11] and from the measurements of purest water and those of clear natural waters and lake (Baikal) water, the absorption length in the UV (resp. blue) could therefore be expected to be confined between 5 m and 75 m (resp. between 20 m and 95 m). Several other measurements of pure and natural waters summarized in [34] give results that all lie within those ranges. Whilst this range is large, the actual result for the ANTARES site is of course expected to be much closer to typical natural waters than to triply distilled water, with values somewhere between 5 m and 38 m (at 375 nm) and 20 m and 62 m (at 475 nm).

The interpretation of the results from measurements of scattering is more delicate. With the theoretical distinction between the two types of scattering centres in Sections 2.3.1 and 2.3.2, it is possible to identify each constituent in the water with one of the two types. Clearly scattering in pure (sea) water determines the most fundamental scattering properties in natural waters and therefore provides an upper limit to the expected overall scattering length. In pure water, scattering was identified with the random molecular motions of water molecules [26, 27] causing small-scale ($\ll \lambda$) density fluctuations as well as large scale ($\gg \lambda$) turbulence-induced fluctuations in the real index of refraction. Therefore, pure (sea) water exhibits both SC scattering (from the small-scale density fluctuations) and LC scattering (from the large scale turbulence-induced fluctuations in the real index of refraction).

In addition to pure water scattering, impurities contribute to both $\lambda_{SC}$ and $\lambda_{LC}$: biological particles, such as viruses and small colloids that are smaller than $\sim \lambda/20$, contribute to SC scattering whilst larger impurities contribute to $\lambda_{LC}$. The SC scattering length is thus expected to vary between different natural waters as different concentrations of small "particles" contaminate the water. The results for the "Rayleigh" scattering

[11] A lake for example would be expected to have a larger absorption coefficient than clear deep ocean waters because of the larger density of impurities.

measurements by oceanographers would include these "particles" and therefore provide a good estimate of the expected SC scattering length. At 375 nm (473 nm) the SC scattering length was therefore expected to be roughly ∼125 m (∼341 m) using the average of the results obtained from various natural waters [17]. This average does not yet include the effect of salt, which was shown to decrease $\lambda_{SC}$ by ∼25% (with typical salinities of 35‰ – 38‰) and various other systematic effects due to the different temperature and pressure conditions under which these experiments were performed.

The total scattering angular distributions measured by Petzold show variations in the concentration of LC scatterers between different waters by approximately two orders of magnitude. This was to be expected as natural waters contain various amounts of particulate constituents larger than $\sim \lambda/20$, such as large organic and inorganic particles (typically $> \lambda$), large colloids, bacteria, etc. and varying amounts of large scale turbulence-induced fluctuations in the refractive index. The LC scattering length is therefore fairly unpredictable. Similarly, the angular distribution of LC scatterers is also fairly unpredictable since it depends upon the relative concentration of particles of different sizes as well as the wavelength of light used to probe them. Although the general shapes of the total scattering angular distributions of different waters are fairly similar for a given wavelength (yielding variations in the average cosine of the distributions between 0.88 and 0.95 at 514 nm), the difference in wavelength cannot be neglected: results of measurements over a range of angles between 30° and 150° by Morel [53] (see Figure 7.5, p. 118) confirm that the shape of scattering angular distributions can significantly vary with wavelength, yielding less forward-peaked distributions for smaller wavelengths. After subtracting the SC contribution from the total distribution, non-negligible differences between the shapes of the LC angular distributions remain, showing that the LC angular distributions are wavelength dependent. The wavelengths used in the measurements at the ANTARES site (375 nm and 473 nm) are very different from the wavelength used by Petzold (514 nm) and it is therefore not possible to use his measurements of the angular distribution function in the analysis at those wavelengths.

On a further note of scattering, the probability of Raman scattering is expected to be more than one order of magnitude smaller than the probability of elastic scattering by water [54, 55]. Therefore, the process of Raman scattering will be neglected in the model of the optical properties of the water established in Section 2.7. Fluorescence, even though its absence cannot be verified, produces photons that are emitted on the scale of micro-seconds after the incident photon has been absorbed. In the experiment described in Chapter 3, the propagation time of photons is measured over a time interval of 0.86 $\mu s$. Therefore, photons emitted by fluorescence are not detected in the experiment and can safely be neglected. Overall, inelastic scattering therefore does not affect the measurements of Test 3′ and can therefore be neglected in the ANTARES model of the optical properties.

Using the information gained from previous experiments, an experiment (described in Chapter 3) that tried to overcome some of the above mentioned limitations in the measurement of the individual optical parameters of the deep ocean was designed and built. The technique of this experiment as well as its advantages and limitations are

described in the next section.

## 2.6 ANTARES Technique

For the purpose of the ANTARES neutrino experiment, it was essential to design and develop an "instrument" that would be able to perform in situ measurements (to obtain the optical properties exactly as they are for the ANTARES detector), be able to distinguish between the absorption coefficient and the coefficient and angular distribution of scattering (since all three parameters have different impacts upon the performance of the ANTARES detector), not limited by small samples of water (to include all optically relevant impurities) and that would be independent of any other measurement results (to ensure that the accuracy of these results and the correlations between them are well understood, and to exclude any uncertainties due to differences in the optical properties between different sites).

The ANTARES technique (discussed in detail in Chapter 3), developed in Oxford as part of the ANTARES Collaboration, uses a stand-alone experiment consisting of a detector (PMT) which measures (in situ) the distribution of arrival times of photons emitted at various distances ($\sim$15 m, $\sim$24 m and $\sim$44 m)[12] by a pulsed isotropic light source. Different optical properties yield different distributions of the path lengths and thus different distributions of the detection times of the photons. The arrival time distribution thus gives information about the average path followed by photons in the medium which, together with the relative number of counts between two distances, can be related to the optical properties via appropriate MC simulations (as described in Chapter 5).

Below, some advantages and limitations of the ANTARES technique compared to other experiments are given:

1. The ANTARES light propagation experiment (called *Test 3'* in the ANTARES Collaboration) uses the information of very large volumes of water around the detector and is not limited by small volume samples. This presents the advantage that no optically significant constituent of the medium is excluded from the analysis of the data (therefore yielding a global result for the optical properties at the ANTARES site). Additionally, the relatively large distances used in the experiment ensure that even for long absorption or scattering lengths, the experiment can still discriminate between the various optical properties.

2. Only two measurements (for reasons explained in Section 6.1), taken in situ within a time interval of a few hours with the same equipment, are required to determine the absorption and scattering properties independently of each other. This is possible since both absorption and scattering have different impacts upon the arrival time distribution of the photons. Moreover the experimental and analysis methods developed and described in this thesis have the advantage of being sensitive to different types of scattering centres and no physical or chemical separation between

[12] These distances were chosen on the basis of the expected absorption and scattering lengths at the ANTARES site.

individual components of the water is required to determine the individual scattering contributions (as described in Section 2.3) exactly as found in situ. Because the optical properties were deduced from measurements in situ under the conditions (and at the depth) of the ANTARES site, there was no uncertainty on the optical properties due to influencing factors like temperature, pressure and salinity [56].

3. The main disadvantage is that the experiment relies upon an analytic approximation to the scattering angular distribution of large scattering centres because the angular distribution was not measured at the ANTARES site. Whilst this angular distribution is able (as will be shown in later chapters) to describe the scattering contribution from large scattering centres with the measurements of Test 3′, results from simulations in Figures 1.6 and 1.7 (p. 10, 11) have shown that for the reconstruction of muon tracks in the water, two angular distributions with different shapes but with the same average cosine of the scattering angular distribution, can change the detector efficiency by ∼10% whilst the ANTARES detector angular resolution is relatively unaffected (for more details see [16]).

4. Another limitation is the need for very large computing resources for the analysis of the data. The MC simulations need very large statistics (much larger than one might intuitively think!) to be able to do an accurate analysis of the data (see Appendix D). The need for these large statistics, together with the (initially) large range of possible values for each of the parameters, causes the computing times to be extremely large. Typically, the analysis of one set of data with the statistics used in the current analysis uses approximately 200 weeks (≈4 years!) of continuous CPU time with a 800 MHz processor! Huge computing resources are thus needed.

## 2.7 Model of the ANTARES Site Optical Properties

In Sections 2.5 and 2.6, a number of measurement techniques of the optical properties of various waters and ice and the ANTARES technique as well as its advantages and limitations were described. In this section, a model will be described, making use of the qualitative information gained from previous measurements and taking into account the limitations of the ANTARES technique.

### 2.7.1 Absorption

Clearly the nature of the Test 3′ experiment precludes the ability to distinguish between different kinds of absorption centres since the experiment has no means of telling how a photon was absorbed. Therefore, the absorption will be modeled by an absorption length $\lambda_A$ which includes both the pure sea water component and any absorption due to impurities.

### 2.7.2 Scattering

From the discussion in Sections 2.3 and 2.5, it can be concluded that it is preferable to make the distinction between different types of scattering centres of natural waters not on grounds of chemical differences (i.e. dissolved or particulate matter) but on grounds of size. Naturally this leads to the distinction between "Rayleigh-like" scattering centres with sizes smaller than $\sim \lambda/20$ and "Mie-like" scattering centres with sizes larger than this dimension. From now on, to emphasize the distinction on grounds of size, these will be referred to as small scattering centres (or SCs) and large scattering centres (or LCs) respectively. Each will be modeled in terms of their own scattering length, $\lambda_{SC}$ and $\lambda_{LC}$ (defined by Eq. 2.12, p. 21).

From the experimental results of measurements discussed in [17], the angular distributions for SCs can be approximated by Eq. 2.7 (p. 19). In the absence of a measured LC scattering angular distribution at the ANTARES site, only a theoretical distribution could be assumed. The exact theoretical calculation of the Mie scattering angular distribution function is however very complex and would require the exact knowledge about the size, shape and density distribution of LCs – clearly far beyond the reach of any current experiment. A simpler strategy based upon the Henyey-Greenstein approximation (Eq. 2.8, p. 20) was therefore chosen, leaving the average cosine of the distribution $g$, from now on referred to as $\langle \cos\theta \rangle_{LC}$, as a variable to account for the size distributions of LC scatterers in the medium.

### 2.7.3 Speed of Propagation and Refractive Index

The method for extracting the water optical properties at the ANTARES site from the light propagation experiment relies upon the time-of-flight measurement of photons between a pulsed light source and a detector. To be able to relate the path length distributions (from the MC simulations in Chapter 5) to the time distributions of these measurements, an accurate knowledge of the speed of propagation of the photons is required.

Historically, ANTARES (and other similar experiments) have used the phase velocity as the speed of propagation of photons in water. As was pointed out in a recent note by Kuzmichev [57], this is incorrect and the group velocity should be used instead. The group velocity for light pulses traveling in a medium with angular frequency $\omega$ and wavevector $k = 2\pi/\lambda$ is given by

$$v_{gr} = \frac{d\omega}{dk}. \tag{2.20}$$

Using the result that $w/k = c/n_{ph}$ (where $n_{ph}$ is the phase velocity refractive index), the equation above can be written as

$$v_{gr} = \frac{c}{n_{ph}} - \frac{ck}{n_{ph}^2}\frac{dn_{ph}}{dk} = \frac{c}{n_{ph}}\left(1 + \frac{\lambda}{n_{ph}}\frac{dn_{ph}}{d\lambda}\right). \tag{2.21}$$

In analogy with the phase velocity refractive index, the group velocity refractive index $n_{gr}$ can be defined as

$$n_{gr}(\lambda) = \frac{n_{ph}(\lambda)}{1 + \frac{\lambda}{n_{ph}(\lambda)} \frac{dn_{ph}(\lambda)}{d\lambda}}, \tag{2.22}$$

with $v_{gr} = c/n_{gr}$. The electromagnetic properties of the water are dependent upon the salinity, the temperature and the pressure; the group velocity refractive index is therefore expected to vary with each of these. This dependence was omitted in Eq. 2.22 for the sake of clarity.

Millard & Seaver [58] (hereafter referred to as MS) have developed a 27-term algorithm that gives the phase index of refraction to part-per-million accuracy valid over a large fraction of the oceanographic parameter ranges ($\lambda = 500 - 700$ nm, salinity $S = 0 - 40‰$, temperature $T = 0 - 30°$C and pressure $P = 0 - 1100$ bar), using four experimental sets of data acquired under various conditions and accuracies. Measurements taken at the ANTARES site yield values for the salinity and temperature of $38.44 \pm 0.02‰$ and $13.1 \pm 0.1°$C respectively [59]. The stability of these results was confirmed by comparison with a set of independent measurements performed in the *Gulf of Lyon* in 1969 [60]. As described in Section 2.1, the wavelength region of interest for the ANTARES detector is however limited to the 350-550 nm interval, with only a small overlap with the range of validity of the MS equation.

Quan & Fry [61] (hereafter referred to as QF) provide another empirical equation for $n_{ph}(S, T, \lambda)$ based on experimental data selected by Austin and Halikas [62], valid for a wavelength range of 400 - 700 nm (coinciding partly with the wavelength region of interest for water-based Cherenkov detectors), a temperature range of 0-30° and a salinity range of $0 - 35‰$, but neglecting any *pressure dependence*. To include the pressure dependence in the QF equation, a first-order polynomial was added in the expression and fitted to the MS equation over the 500-700 nm interval. The fit was done at a pressure of 220 bar (the pressure at the average depth of the ANTARES detector). The QF equation corrected for pressure then becomes

$$\begin{aligned} n_{ph}(S, T, P, \lambda) = n_0 \;\; &+ \;\; n_1 \; P + (n_2 - n_3 \; T + n_4 \; T^2) \; S \\ &- \;\; n_5 \; T^2 + \frac{n_6 + n_7 \; S - n_8 \; T}{\lambda} - \frac{n_9}{\lambda^2} + \frac{n_{10}}{\lambda^3}, \end{aligned} \tag{2.23}$$

where $P$ is the pressure in bar, $T$ the temperature in [°C] and $S$ the salinity in parts per thousand [‰], $\lambda$ the wavelength of light in [nm] and the coefficients are given in Table 2.7.3. The agreement between the fitted QF and the MS curves of the group velocity refractive index is extremely good, with deviations smaller than 0.017% in the wavelength range 500-700 nm and less than 0.066% in the range 350-500 nm (see top left of Figure 2.4). The very good agreement between the MS and QF curves of the phase and group velocity refractive indices (of distilled water at atmospheric pressure and standard

| *Coefficient* | *Value* |
|---|---|
| $n_0$ | 1.31405 |
| $n_1$ | $1.45 \times 10^{-5}$ |
| $n_2$ | $1.779 \times 10^{-4}$ |
| $n_3$ | $1.05 \times 10^{-6}$ |
| $n_4$ | $1.6 \times 10^{-8}$ |
| $n_5$ | $2.02 \times 10^{-6}$ |
| $n_6$ | 15.868 |
| $n_7$ | 0.01155 |
| $n_8$ | 0.00423 |
| $n_9$ | 4382 |
| $n_{10}$ | $1.1455 \times 10^{6}$ |

**Table 2.1:** *Coefficients of Eq. 2.23 for the calculation of the refractive index of sea water. The dimensions were omitted for the sake of clarity.*

temperature as well as of salt water at the nominal values at the ANTARES site) and the good agreement of both equations with another independent set of data from Kuzmichev (KL [63]) suggests a good knowledge about the refractive index of the water as long as the salinity, temperature and pressure are known (see bottom left of Figure 2.4). Although the QF equation only claims to be valid down to 400 nm, the good agreement with the MS equation and the KL data in the wavelength interval below 400 nm suggests the reliability of the QF equation also for wavelengths below 400 nm. The QF equation was therefore used in the MC simulations to determine the speed of the photons.

The top right of Figure 2.4 shows the variation of the refractive index of the QF curve with salinity, temperature and pressure. The maximum observed fluctuation in salinity of 0.02‰ [59] produces an associated error in the group velocity refractive index of at most $2.5 \times 10^{-6}$ in the wavelength region of interest. Similar considerations for maximum temperature fluctuations, estimated to be at most 0.2°C [59], yield variations in the group velocity refractive index of at most $1.45 \times 10^{-5}$. Finally, an examination of the pressure variations over vertical distances of the order of 50 m yield a maximum error of 0.00014. The worst case scenario therefore yields a maximum total error in the group velocity refractive index over the wavelength region of interest for ANTARES of $\sim$0.00015. This figure translates into an error on the arrival time of photons at a distance of 50 m of less than 0.05 ns. The bottom right of Figure 2.4 shows the phase and group velocities as determined from the respective refractive indices. The values for the group velocity refractive index at the wavelengths used in the measurements with Test 3′ are: 0.213292 m/ns (375 nm) and 0.217644 m/ns (473 nm).

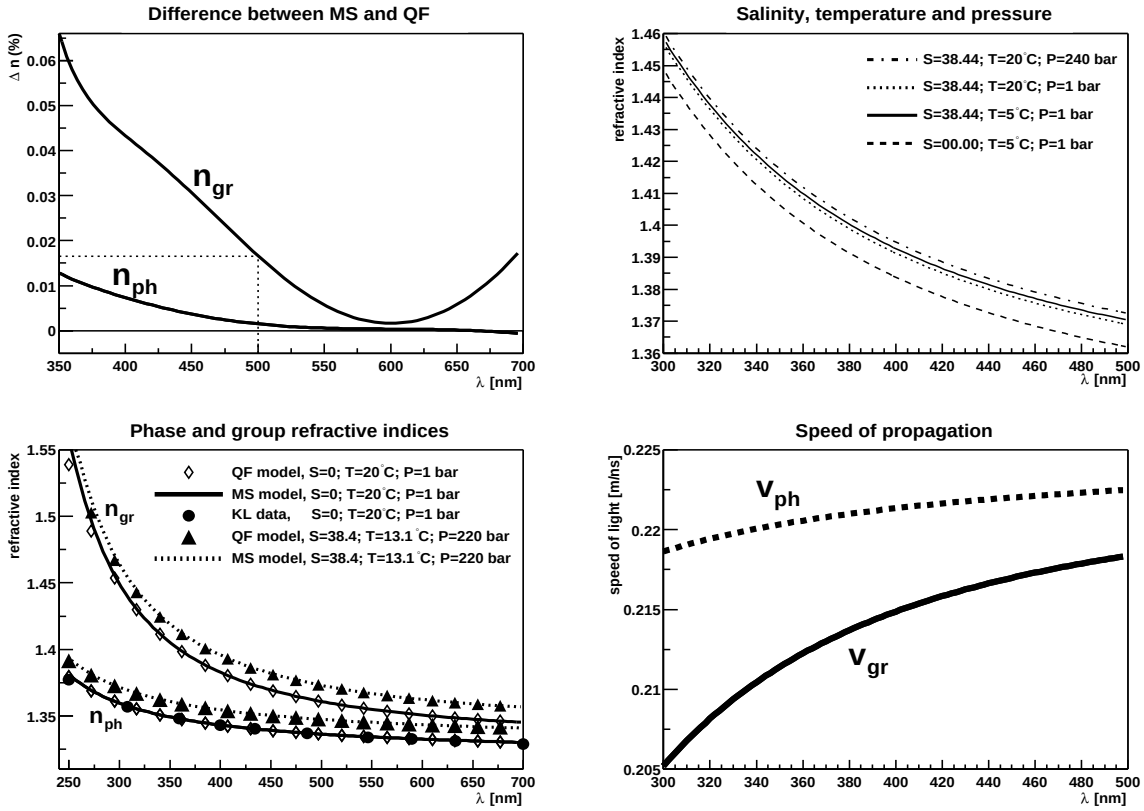


**Figure 2.4:** *Difference in refractive indices between the MS and QF curves (top left). Variation of $n_{gr}$ with salinity, temperature and pressure (top right). Refractive indices $n_{ph}$ and $n_{gr}$ for the MS and QF models and $n_{ph}$ from the KL data (bottom left). Phase and group velocities at the nominal values for pressure, salinity and temperature at the ANTARES site (see text) as a function of wavelength (bottom right).*

## 2.8 Summary

In this chapter, a brief overview was given about the history of the development of our understanding of the interaction of light with matter (Section 2.2). The distinction between two types of scattering centres was made on the basis of their size relative to the wavelength of the incident radiation, leading to a total of three types of interaction centres (Section 2.3): absorption centres, SCs (with forward-backward symmetric scattering properties) and LCs (with more forward-peaked scattering properties than SCs). The various macroscopic parameters used to describe the optical properties of a medium were then defined (Section 2.4). A description of a selected sample of experiments by the oceanography community and other neutrino collaborations was given and their results compared and discussed (Section 2.5). The ANTARES technique, as well as its advantages and disadvantages, was described (Section 2.6) and a model defining the optical properties of the ANTARES detector medium was constructed (Section 2.7), based upon the qualitative results of previous measurements from other experiments and theoretical results from classical electromagnetism and statistical thermodynamics.

# Chapter 3

# The Light Propagation Experiment: Test 3′

This chapter describes the experimental equipment used to measure the optical properties in situ at the ANTARES site. The experimental procedure to acquire the data is presented and a table of the measurements is given. The calibration of the experiment is then discussed.

*...since the measuring device has been constructed by the observer... we have to remember that what we observe is not nature itself but nature exposed to our method of questioning.*

*W. Heisenberg (1901-1976)*

## 3.1 Introduction

To measure the optical properties in situ at the large depths of the ANTARES site, a new experiment (called Test 3′) was designed and constructed[1]. Using the data from various immersions of this experiment together with MC simulations (described in Chapter 5), the absorption length and the various scattering parameters (described in Section 2.7) were measured independently.

Four sets of measurements were performed at the ANTARES site (Figure 1.5) – in July 1999, September 1999, June 2000 and September 2000 – at a depth of ∼2400 m. Measurements were done at ultraviolet (∼375 nm) and blue (∼473 nm) wavelengths. Immersions were done from the ship "Prof. Georges Petit" (very similar to the other ship used by the ANTARES Collaboration, shown in Figure 3.1).

[1] The software for the data acquisition [64] was written in C programming language by the author but lacking relevance to the discussions in this thesis will not be mentioned further.

**Figure 3.1:** *The Thetys, one of two ships used by the ANTARES Collaboration for the deployment of various experiments (including Test 3′).*

## 3.2 Experimental Details

The light propagation experiment was designed to measure absorption and scattering independently. Scattering affects the path length which a photon will travel between its source and its point of detection and absorption determines the number of photons which will reach the detector as a function of the path length they traveled. A system was therefore devised that uses the time-of-flight of photons from a pulsed light source to the detector to determine the distribution of path lengths of photons in the ocean. In addition to photons from the light source, the detector also registered photons from various background light sources present in the deep ocean (see Section 6.2.2).

### 3.2.1 Global Structure

The difficulty of immersing rigid structures under even moderate sea conditions lead to the design of a flexible structure (Figure 3.2) principally consisting of two triangular frames connected only via cables, allowing it to be immersed with a swell up to 1.5 m. A rigid structure is attached to each frame, one holding a pressure-resistant glass sphere (from now on simply referred to as glass sphere) containing an isotropic light source, and the other holding two different glass spheres, one containing the detector (a PMT of 30 mm diameter) and one the electronics.

The line is maintained vertical in the water by means of a heavy anchor at the bottom and buoys at the top, exerting a tension of ∼1883 N. Control of the experiment and data transmission to the ship during the experimental runs is achieved via a microprocessor (MBX-OS9) in the electronics glass sphere and acoustic modems.

Each glass sphere consists of two halves that are held together by creating a partial vacuum inside the sphere. Before assembly, each sphere is individually tested for leakage at the high pressure testing facility in Brest (France). The line is then assembled on the shore as shown in Figure 3.3.

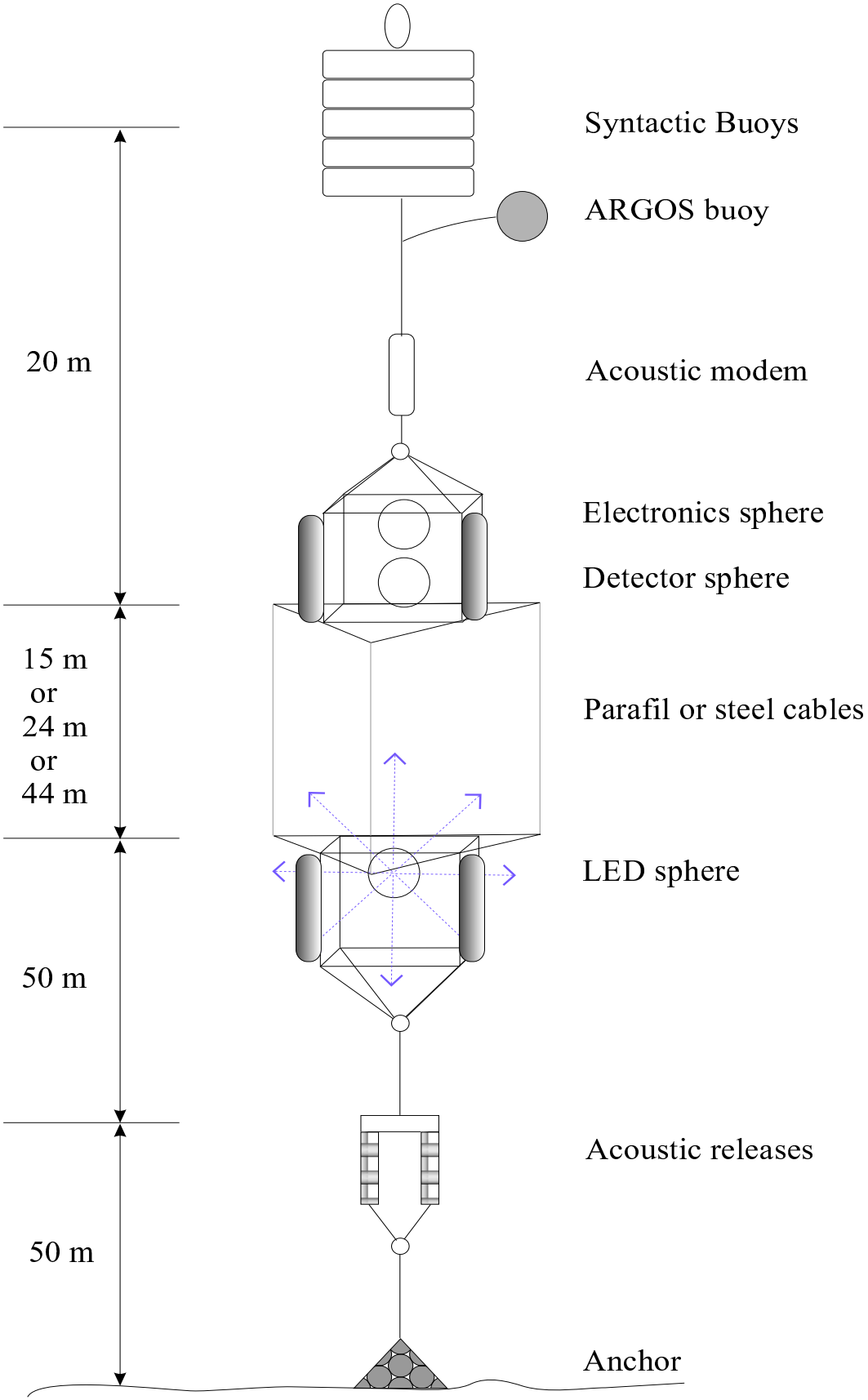


**Figure 3.2:** *Sketch of the line used for the measurements of the water optical properties at the ANTARES site. Note the distortion of the vertical axis.*

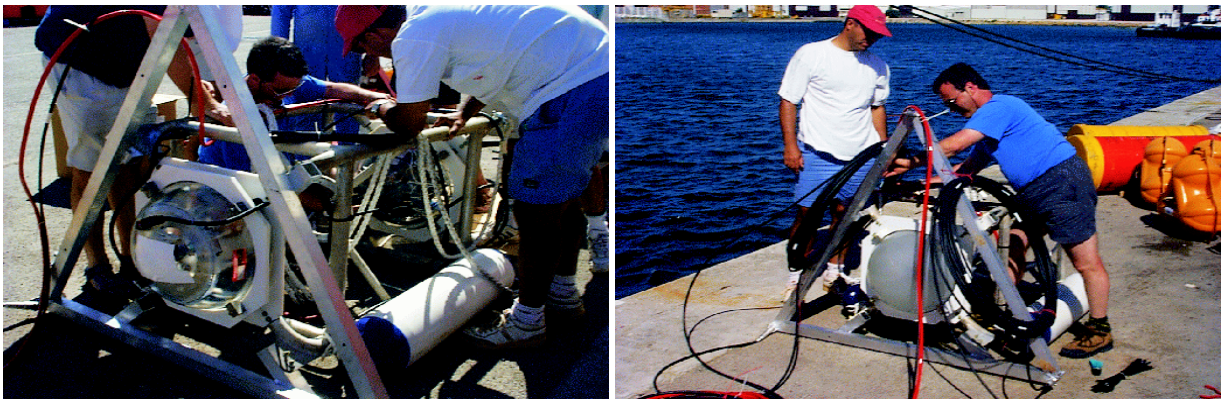

**Figure 3.3:** *Assembly of the line used for the light propagation experiments at the ANTARES site. The detector and electronics glass spheres are shown in the left photo and the glass sphere housing the light source in the right photo.*

### 3.2.2 Light Source

The light source was made from six identical light-emitting-diodes (LEDs) mounted on the faces of a cube of side-length 10 cm. Two wavelengths, one representing the wavelength of Cherenkov light yielding the maximum detection efficiency for the ANTARES PMTs (∼473 nm) and one extreme of the useful wavelength range over which Cherenkov light can be detected (∼375 nm) were chosen. For the experiments performed in July 1999 and September 1999, only one UV LED was mounted on each face of the cube. A switch allowing the selection of one of two LEDs on each face was developed for the immersions in June 2000 and September 2000, to be able to do measurements with the blue and UV LEDs consecutively during the same immersion.

To make the source isotropic, the cap of the blue LEDs was cut off. The bare LEDs were measured and found to give a roughly $\cos^2\theta$ angular dependence. Placing six of such LEDs on the faces of a cube produced a fairly isotropic light source by itself, since $\cos^2\theta + \sin^2\theta = 1$! Due to the technical construction of the UV LEDs, the cap could not be chopped off. Instead, a spherical cap of glue mixed with glass micro-beads was formed around the LEDs, making the intensity distribution around each of them fairly isotropic. The isotropy was improved by adjusting the intensity emitted by the individual LEDs with a variable capacitor-resistor combination in the LED-driver circuit (Figure 3.4). The LED cube was then placed at the centre of a sand-blasted glass sphere to ensure an even better isotropy[2].

To charge the capacitors on the LED cards, a DC signal was sent via a twisted pair cable to a DC/DC converter on the LED card inside the cube. To pulse the LEDs synchronously, a low voltage differential signal was sent via another twisted pair cable to the LED driver card to discharge the capacitors on the individual LED cards simultaneously. This yielded a very fast rising pulse, with rise times of 3 ns and 2 ns for the blue and UV LEDs respectively. The long exponential decay of the LED capacitors was avoided by discharging the capacitors via another switch (shown as IC6-C/IC6-D in Figure 3.4) after

[2]More details on the measurements of the isotropy are given in Section 3.5.2.

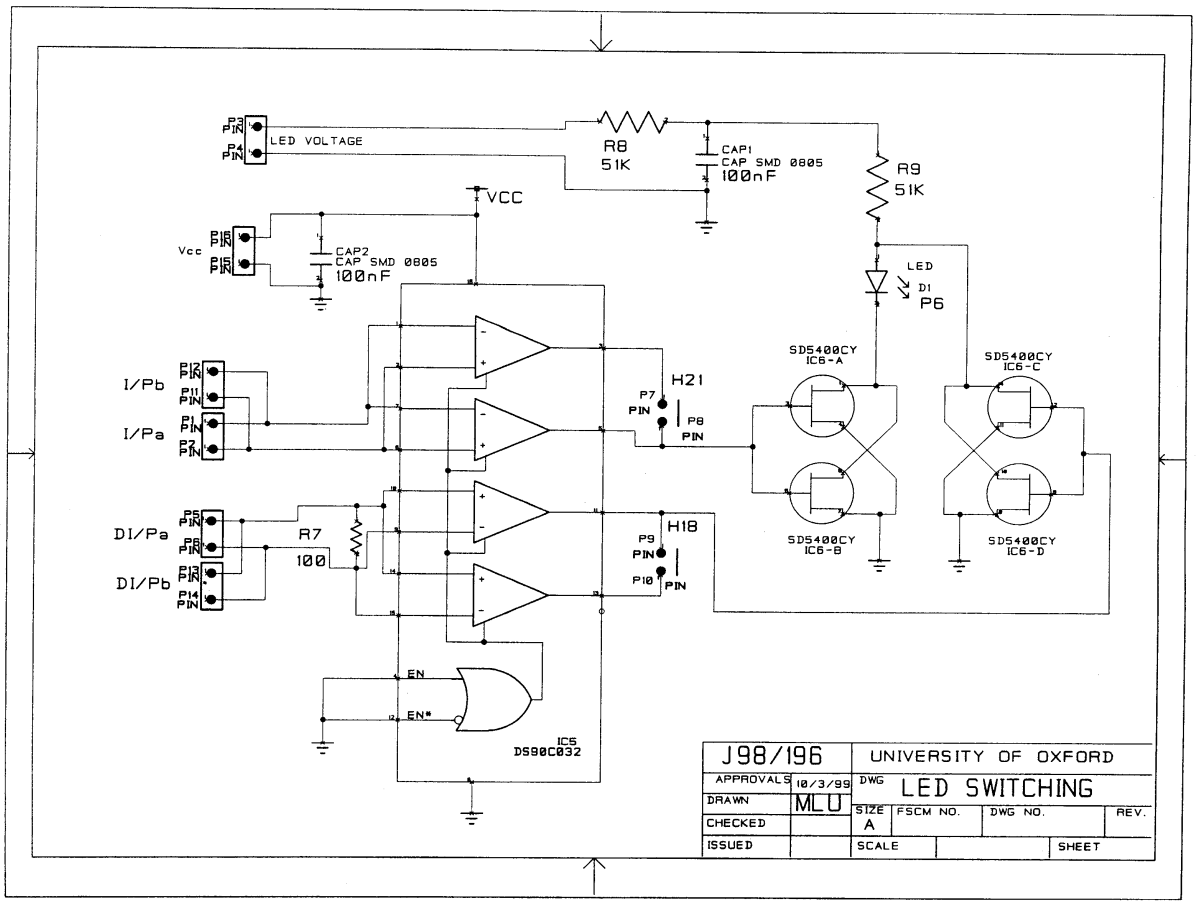


**Figure 3.4:** *Circuit diagram of the LED driver (designed by B. Brooks, Oxford University) used for the measurements with Test 3′. The capacitor labeled as CAP1 is a variable capacitor which allows the LED intensities for each of the six LEDs on the cube to be matched.*

a delay of 2 ns, yielding a FWHM (with a LED-driver voltage of 5.80 V) of the whole setup of ∼6 ns (∼9 ns) in the UV (blue). This width is slightly dependent upon the voltage applied to the LEDs, yielding an increases of ∼1 ns when the voltage is increased from 4.75 V to 5.80 V for the UV LEDs. The LEDs were pulsed at a frequency of ∼6 kHz, the maximum frequency for which the time interval between pulses was long enough to allow the capacitors to be recharged (and to allow the MBX to read the TDC).

### LED Sources: 374.5 nm (UV) and 472.6 nm (blue)

The Saclay group of the ANTARES Collaboration measured the spectral response of the blue and UV LEDs in the pulsed mode as used during the data acquisitions. Two different voltages were applied, revealing no significant difference between the shapes of the spectra, with both the central values and the widths consistent with each other (Figure 3.5).

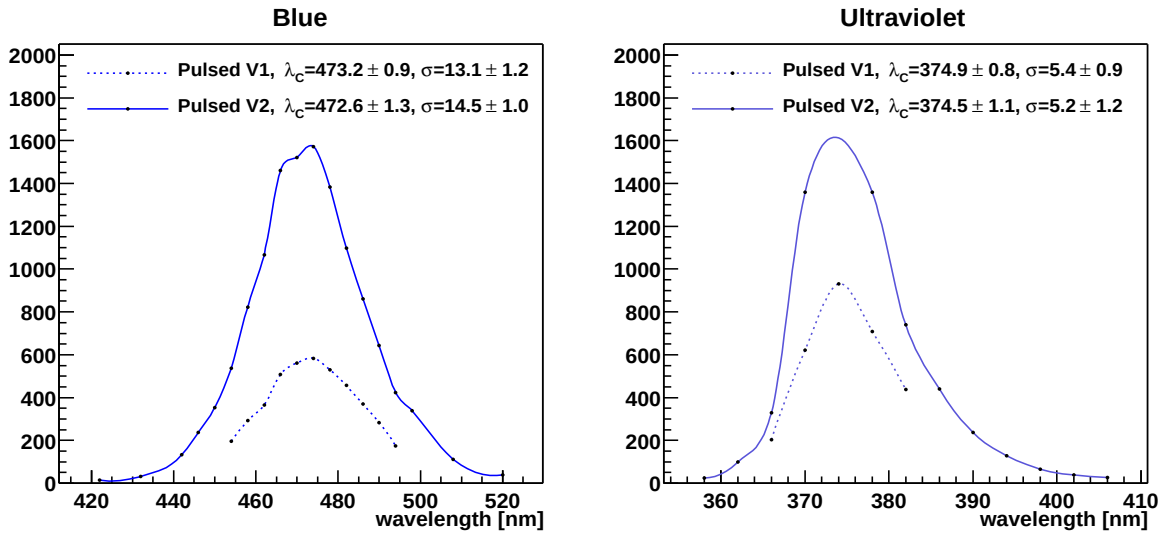


**Figure 3.5:** *Spectral response of the blue and UV LEDs. The pulsed measurements were carried out at two different voltages (V1 and V2).*

### 3.2.3 Detector Sphere

The detector consists of a 30 mm C637-ETL PMT of type 9125SA, housed inside a 17″ diameter glass sphere to which it is glued with optically matching gel to reduce reflections. The high voltage is supplied from the electronics glass sphere via a 3 m long cable consisting of twisted pairs and a common ground. The discriminator shown in Figure 3.6 has an adjustable threshold and is fixed onto the base of the PMT. The discriminator threshold was set via a DAC on the MBX to trigger on the analogue signal of the PMT at a threshold of 40 mV, corresponding to approximately 0.3 of the average amplitude of the single-photoelectron pulse height. This was sufficient to eliminate electrical noise and to ensure that, apart from photons from the light source, only photons from various background light sources (described in Section 6.2.2) would be recorded. The discriminator output a TTL signal via a twisted pair cable to stop the time-to-digital converter (TDC) in the adjacent electronics sphere.

### 3.2.4 Data-Acquisition Electronics

Figure 3.7 shows a sketch of the electronics of Test 3′. The MBX microprocessor running the VxWorks real-time operating system is used to control the data-acquisition. It is composed of a main board housing a OS9-MBX CPU, 2 EPROM chips (512 kB) and the RAM (2 MB) for storing the acquired data. The MBX is connected via a simple bus to an extension card which is used as an interface to the TDC. The MBX is also directly connected to an acoustic modem, allowing the electronics to be controlled from a computer on the ship during the immersions.

The TDC is a digital ASIC originally designed for the MINOS experiment [65] and is mounted on an extension card of the MBX. It has a resolution of ∼0.78 ns, which is

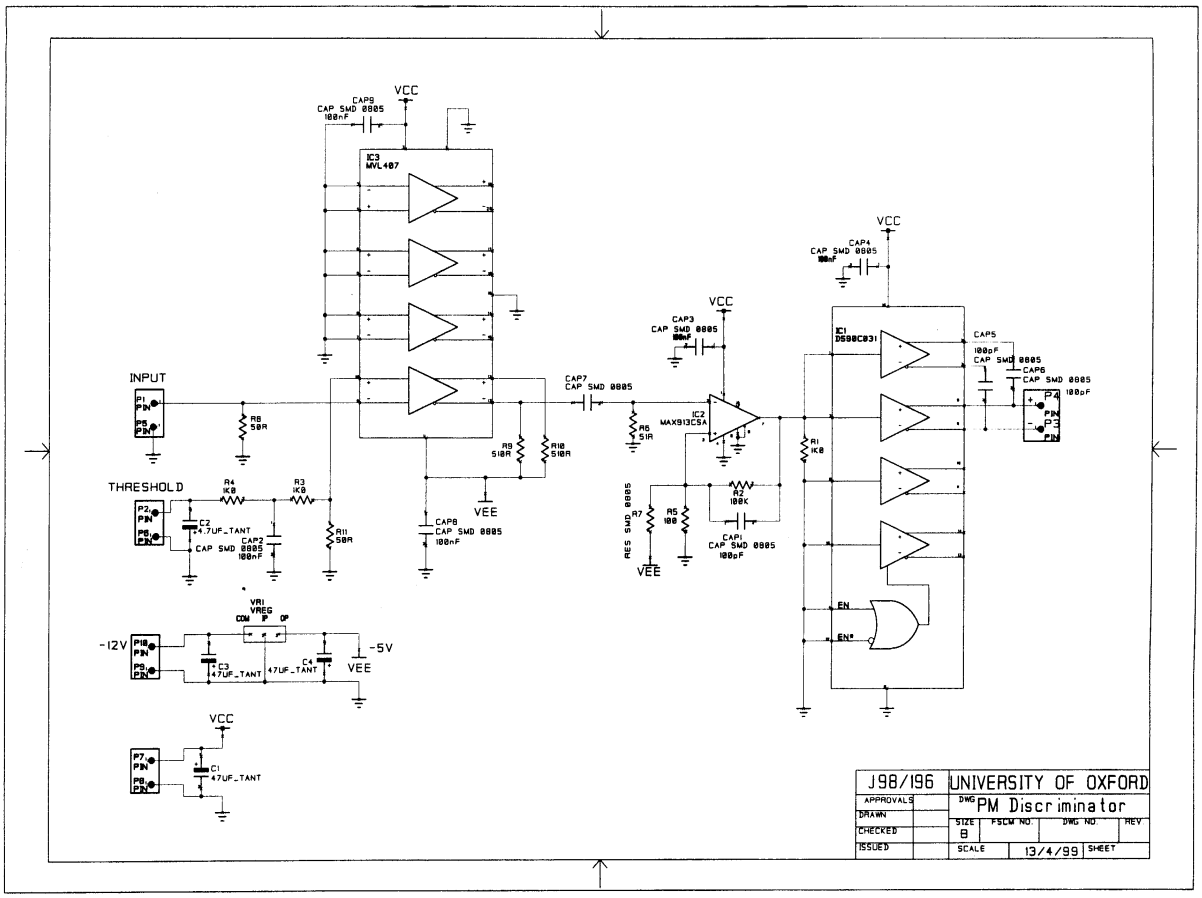


**Figure 3.6:** *Circuit diagram of the PMT-signal discriminator (designed by B. Brooks, Oxford University) of Test 3′.*

achieved by means of a coarse and a fine time stamp. A 40 MHz quartz clock determines the coarse time stamp of the TDC and measures the number of 25 ns cycles since the TDC chip was enabled. Each of these cycles is divided into 32 approximately equal channels by means of a delay locked loop module (with a series of delay lines) yielding the fine stamp with the average resolution of 781.25 ps. Further details of the TDC are given in Section 3.5.1 and Appendix A.

A Xilinx FPGA is used as the interface between the TDC and the MBX. Upon receiving an MBX command, it generates a TTL signal (after a certain delay) that enables the TDC and starts its active time window (ATW). After a further time delay of a few clock cycles, the FPGA then sends a signal to a splitter, which sends one (TTL) signal to one of the inputs of the TDC and another (low voltage differential) signal to the driver in the LED sphere via a 50 m long electrical cable to pulse the LEDs. The time over which the TDC can register a hit can be adjusted by defining its ATW and was set to 0.86 $\mu$s for most acquisitions.

Also contained in the electronics sphere are the power supply, consisting of a set of batteries, to supply the high voltage for the PMT, and the remainder of the electronics, the voltage distribution card and a compass.

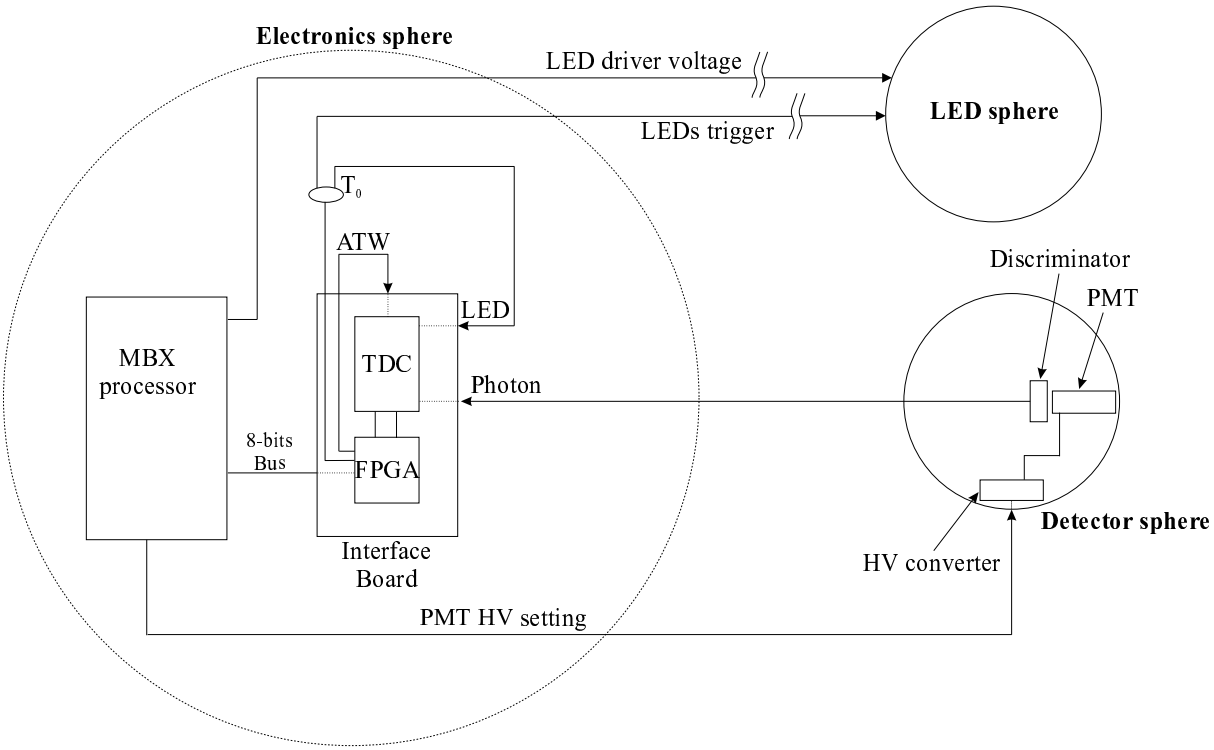


**Figure 3.7:** *Sketch of the electronics used for the data acquisition of the light transmission experiments. Note that the electronics sphere, the detector sphere and the LED sphere in the experiment all have the same diameter of 17″. For a detailed description of the acquisition sequence see Appendix A.*

### 3.2.5 Parafil versus Steel Cables

Two types of cables were used to link the triangular frames of the mooring line (Figure 3.2) at a predefined source-detector separation. In the first series of experiments, three different lengths of parafil cables [66] were used: 15.14 ± 0.02 m, 23.94 ± 0.02 m and 44.41 ± 0.02 m, from now on referred to as the 15 m, 24 m and 44 m data. These were measured independently by several people on the shore before and after the immersions.

After a first set of measurements, it was realized that there was a slight uncertainty in the arrival times of direct (i.e. unscattered) photons at two different distances[3] (see Section 6.3.4 for more details). It was found that the observed discrepancy could be attributed to an insufficient knowledge about the tensile strain of the parafil ropes [66] under the tension of the buoyancy force during the immersion in the sea. Therefore, for the immersions in September 2000, the parafil cables were replaced by steel cables which have a much smaller tensile strain than the parafil cables. However, due to equipment failure, data are only available at one distance with this setup, which precludes their analysis since the method developed in this thesis requires measurements at two different distances (see Section 6.1).

[3]This difference was deduced from the measured distances on the shore and the speed of the photons in the water.

**Figure 3.8:** *Deployment of the Test 3′ line for the water optical properties measurements at the ANTARES site. The elements are immersed in the order of top to bottom for the line shown in Figure 3.2.*

## 3.3 Experimental Procedure

### 3.3.1 Deployment

The line (shown in Figure 3.2) is deployed from the back of the ship (Figure 3.8), putting the buoyancy elements of the line into the water first, followed by the frame holding the detector and electronics spheres. The cables are put into water whilst moving slowly forward with the boat to ensure that they are laid out without tangling. This is followed by the release of the LED frame. Buoys are attached to two of the sides of each frame to ensure that the line will not twist during the immersion and recovery processes. Finally, the heavy anchor is released from the ship. Due to the weight of the anchor, the line descends vertically in the water with a speed varying between 0.84 and 1.14 m/s, taking typically 30 to 40 minutes to reach the bottom.

A Global Positioning Satellite system records the exact coordinates where the anchor was released. Once the line reached the bottom, between 30 and 60 minutes were given for the line to stabilize and to allow any particles disturbed by the anchor hitting the sea bed to settle.

### 3.3.2 Data-Acquisition Procedure

The data-acquisition software is started either interactively from the computer on the ship or automatically once the line has settled at the bottom of the sea. The PMT is switched on by the MBX. The light intensity of the LEDs is set via a DAC on the MBX which controls the LED driver voltage to yield a detection of roughly one photon per hundred triggers. This ensures that the PMT is mainly detecting single photons. Several data sets of typically between $2 \times 10^6$ and $5 \times 10^6$ triggers are acquired during one immersion.

The TDC records the arrival time of the first photon during the time it is active. It then does not register any more photons until the next pulse of the LEDs[4]. After each

[4]i.e. it is used as a single-hit TDC for reasons described in Appendix A.

| *Setup* | *LEDs* | height above sea bed |
|---|---|---|
| A | UV | 100 m |
| B | UV/blue switchable | 100 m |
| C | UV/blue switchable | 400 m |

**Table 3.1:** *Summary of various setups used for the immersions in the Years 1999 and 2000.*

pulse, the time is passed on to the MBX where it is stored in a histogram on the RAM of the MBX. In addition to being locally stored, these histograms are also transmitted (between acquisitions) to the computer on the ship via a set of acoustic modems. The local (ATM-851) modem is attached to the ship and connected to the computer on the ship via an RS-232 serial interface, and the remote (ATM-845) modem is housed in an aluminium pressure-resistant case containing its own power supply and connected to the electronics sphere also via an RS-232 serial interface. The two modems receive commands over the frequency range 13-15 kHz and transmit over 15-20 kHz, with a typical transmission rate of 600 Baud from the remote unit to the ship and 16 Baud in the other direction.

### 3.3.3 Recovery of Line

After acquiring a set of histograms, the acoustic release linking the bottom of the line to the anchor is activated and the line ascends vertically under the buoyancy force of the buoys attached to the top of the line, leaving the anchor at the bottom of the ocean (i.e. a new anchor is required for each immersion). After ascending, the line is floating horizontally on the water and each element is retrieved by means of a crane on the ship in the reverse order from the immersion. The whole process of immersion, data acquisition and recovery typically takes about 4 hours. To perform measurements with a different source-detector distance, a different set of mechanical cables is then attached to link the source and detector frames and it is immersed again. The same electrical cable is used for both distances.

## 3.4 Available Data

The data were acquired in situ at the ANTARES site (at 2400 m depth), on four days over a period of two years, using the procedure described in Section 3.3. The measurements were taken during various seasons to measure potential seasonal variations of the optical properties of the water. Three different setups were used for the data described here and are summarized in Table 3.1. Setup A was described in Section 3.2 and was used for the July 1999 and September 1999 immersions with UV LEDs. Setup B was the same as setup A except that the LED source was equipped with both a blue and a UV LED on each face of the cube. Consecutive measurements at two different wavelengths were therefore possible during a single immersion. Setup C differed from setup B only in that measurements were taken at 400 m above the sea bed (compared to the usual 100 m) to

| *Date* | *Time of runs* | *Source-detector distance [m] (Setup)* | *LED driver voltage [V]* | *Number of LED pulses ($\times 10^6$)* | *Probability of detecting a photon from the LEDs: f* |
|---|---|---|---|---|---|
| 03rd July 1999 | $09^{25} - 09^{30}$ | 15.14 (A) | 5.15 | 2 | 3.94 % (4.11 %) |
| | $09^{31} - 09^{37}$ | | | 2 | 3.95 % (4.09 %) |
| | $09^{38} - 09^{43}$ | | | 2 | 4.00 % (4.25 %) |
| | $09^{44} - 09^{50}$ | | | 2 | 3.96 % (4.10 %) |
| | $13^{44} - 13^{57}$ | 23.94 (A) | 5.15 | 5 | 1.06 % (1.43 %) |
| | $14^{14} - 14^{27}$ | | | 5 | 1.05 % (1.90 %) |
| | $14^{31} - 14^{44}$ | | | 5 | 1.06 % (1.92 %) |
| | $15^{03} - 15^{17}$ | | | 5 | 1.05 % (1.42 %) |
| 08thSept. 1999 | $07^{53} - 08^{00}$ | 23.94 (A) | 5.80 | 2.5 | 3.60 % (4.42 %) |
| | $08^{16} - 08^{29}$ | | | 5 | 3.57 % (4.83 %) |
| | $08^{30} - 08^{43}$ | | | 5 | 3.61 % (3.96 %) |
| | $12^{02} - 12^{15}$ | 44.41 (A) | 5.80 | 5 | 0.41 % (0.87 %) |
| | $12^{56} - 13^{09}$ | | | 5 | 0.41 % (0.80 %) |
| | $13^{10} - 13^{24}$ | | | 5 | 0.42 % (0.64 %) |
| | $13^{25} - 13^{38}$ | | | 5 | 0.41 % (0.98 %) |
| 11thJune 2000 | $11^{53} - 12^{06}$ | 44.41 (B) | 9.50 | 5 | 0.61 % (1.16 %) |
| | $12^{07} - 12^{20}$ | | | 5 | 0.60 % (0.95 %) |
| 14thJune 2000 | $11^{21} - 11^{29}$ | 23.94 (B) | 9.50 | 3 | 4.58 % (5.00 %) |
| | $11^{29} - 11^{38}$ | | | 3 | 4.59 % (5.08 %) |
| | $13^{48} - 13^{56}$ | $23.94^{(*)}$ (C) | | 3 | 4.53 % (6.06 %) |
| | $13^{56} - 14^{05}$ | | | 3 | 4.59 % (5.66 %) |

**Table 3.2:** *UV data ($\lambda_C$ = 374.5 nm) taken at the ANTARES site to determine the light transmission properties. The difference in LED driver voltages between the 1999 and 2000 data are attributable to a difference in the LED drivers used. The fraction f of LED pulses with a detected photon corrected for the background noise, as described in Section 4.1, is given in the last column (the original probabilities of detecting any photon are shown in parentheses).* $^{(*)}$ *The data on 14 June 2000 were taken at 400 m above the sea bed.*

measure any potential variations of the water optical properties over the range of depths of interest to the ANTARES experiment. Setups A, B and C all used parafil cables. A summary of the available data for the analysis of the optical properties at the ANTARES site is shown in Tables 3.2 and 3.3.

## 3.5 Calibration

This section describes the measurements made to calibrate the TDC and to determine the intrinsic time width of the LED source. These measurements were made in a darkened laboratory with the same electronic setup as for the in situ measurements.

| *Date* | *Time of runs* | *Source-detector distance [m] (Setup)* | *LED driver voltage [V]* | *Number of LED pulses ($\times 10^6$)* | *Probability of detecting a photon from the LEDs: f* |
|---|---|---|---|---|---|
| 11$^{\text{th}}$June 2000 | $11^{28} - 11^{41}$ | 44.41 | 6.30 | 5 | 1.11 % (1.41 %) |
| | $12^{22} - 12^{35}$ | (B) | | 5 | 1.10 % (1.56 %) |
| 14$^{\text{th}}$June 2000 | $11^{01} - 11^{09}$ | 23.94 | | 3 | 5.75 % (6.54 %) |
| | $11^{10} - 11^{18}$ | (B) | 6.30 | 3 | 5.81 % (6.40 %) |
| | $14^{07} - 14^{15}$ | $23.94^{(*)}$ | | 3 | 5.81 % (6.46 %) |
| | $14^{16} - 14^{24}$ | (C) | | 3 | 5.78 % (6.81 %) |

**Table 3.3:** *Blue data ($\lambda_C = 472.6$ nm) taken at the ANTARES site to determine the light transmission properties. The fraction f of LED pulses with a detected photon corrected for the background noise, as described in Section 4.1, is given in the last column (the original probabilities of detecting any photon are shown in parentheses).* $^{(*)}$ *The data on 14 June 2000 were taken at 400 m above the sea bed.*

### 3.5.1 TDC Bin Size

The performance of the TDC was studied by recording photons from diffuse ambient background light with the LEDs switched off (from now on referred to as a white-noise spectrum). The light level was made low enough that a photon arrived at the PMT for typically less than 1% of the triggers. The low detection rate ensured that the probability of more than one photon hitting the PMT within a single active time window was small. This was important because the TDC used in Test 3′ only operates in the single-photon mode (i.e. it can only register one photon during each active time window). Under these conditions, if the TDC had equal bin widths, the white-noise spectrum would be flat (given high enough statistics). If the rate of photons is however increased, the fraction of registered photons decreases.

Actual data is shown in Figure A.1 on p. 125. Figure 3.9 shows a portion of region D of that figure, including statistical error bars. This is the region of the spectrum relevant for the data acquired during the immersions. Large fluctuations can be observed. Figure 3.10 shows the spread in number of events per bin over region D of Figure A.1. If the variation in number of hits between the various bins was purely statistical, a Gaussian distribution with a sigma $= \sqrt{N}$ would be observed, where $N$ is the average number of hits per bin. For Figure 3.10 this predicts a spread of $\approx 34$. The width of the distribution is however more than double this value. Non-equal lengths of the delay lines within the TDC could cause unequal bin widths across the spectrum. These could be responsible for the non-statistical distribution of white-noise hits. To confirm this, a series of test pulses from a LeCroy pulse generator with a well-known time delay were used to trigger the TDC. By increasing the time delay of the test pulses, it was confirmed that the 32 delay lines subdividing each 40 MHz clock cycle presented variations in length of the order of 0.03 ns from the nominal value of 0.78 ns.

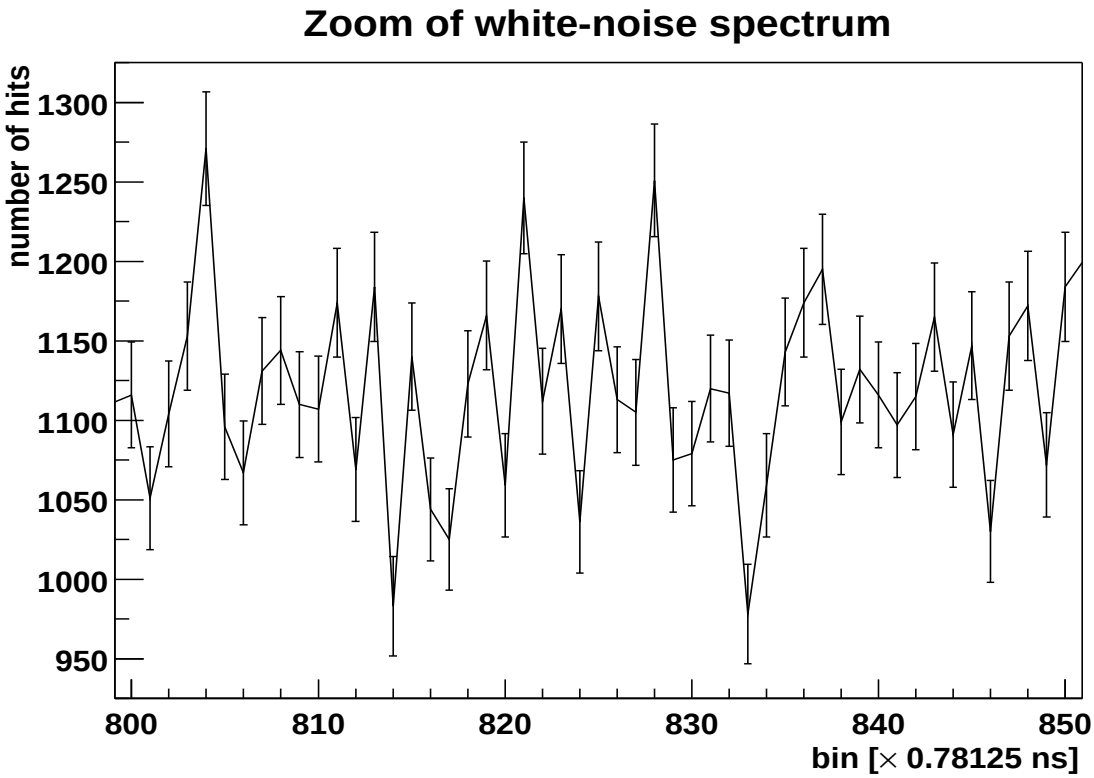


**Figure 3.9:** *Section of region D (the relevant section for the analysis of the data) of the white-noise spectrum of Figure A.1 (p. 125).*

When one such white-noise spectrum was divided by another, taken under identical conditions but several months apart, the deviation of the divided spectrum from a flat spectrum was shown to be statistical only: a fit of a straight line to the divided spectrum gives a satisfactory $\chi^2/df = 425/399$ as shown in Figure 3.11. This result shows the reproducibility of the TDC features and therefore strongly supports the idea that the non-statistical behaviour between the number of hits recorded across the spectrum can be attributed to the intrinsic features of the TDC. At the same time, the reproducibility of such spectra shows their stability under different layouts of the electrical cables, etc. One can therefore be confident that dividing a data spectrum bin-by-bin by a white-noise spectrum will eliminate the variation in the bin widths to within the statistics of the white-noise spectrum. The statistical error due to this division is taken into account in the bin-by-bin statistical error calculations of the corrected data (see Chapter 4).

Whilst individual bins across the TDC present different widths, the overall average bin width is determined by the 40 MHz clock, whose frequency is known to an accuracy of 6 ppm, yielding an average bin width of 781.25 ps with an error smaller than $\sim$0.005 ps.

The impact of a temperature variation upon the width of the individual bins was investigated by acquiring several white-noise spectra with the TDC at different temperatures. This was achieved by spraying the TDC during the acquisitions with Aztec Chemicals

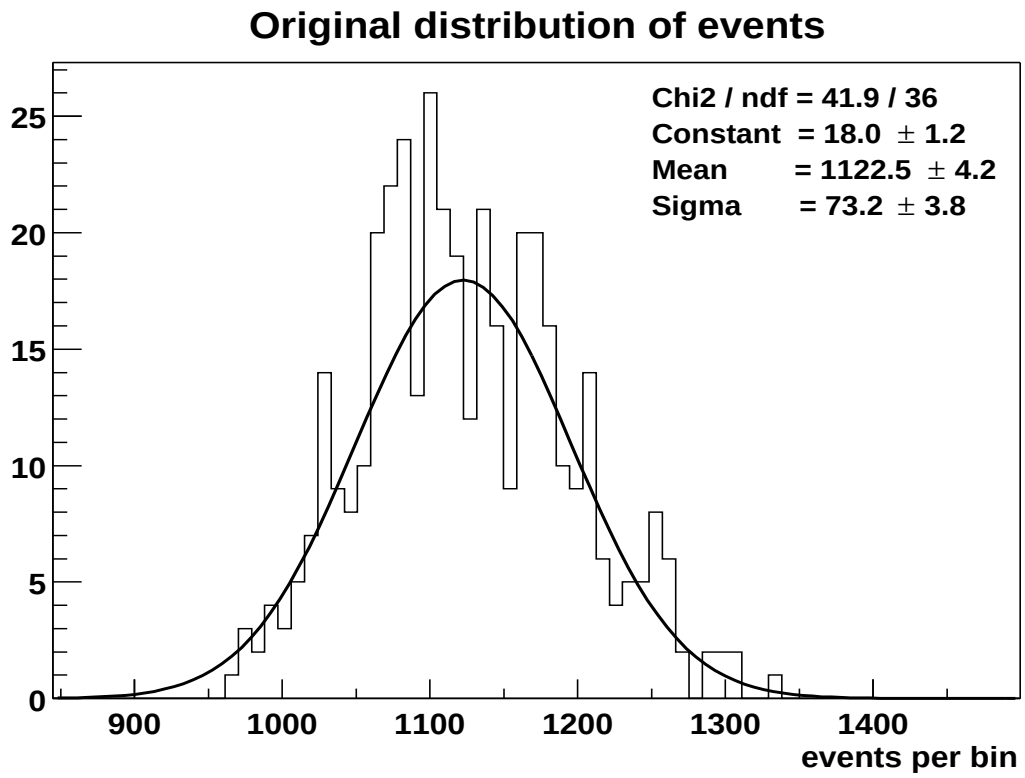


**Figure 3.10:** *Histogram of the number of hits recorded per bin in the white-noise spectrum of Figure A.1 (p. 125) over the region relevant to the analysis of the data. The solid curve shows a Gaussian fit to the data.*

coolant sprays, causing the temperatures to drop to less than 0°C[5]. No significant variation was observed between measurements taken at freezing and room temperatures.

### 3.5.2 Time Width of Light Pulse: Air Spectrum

Two factors are responsible for the spread in the arrival times of the photons: the finite width of the light source and the optical properties of the medium. When trying to measure the latter, it is important to account for the former. To disentangle these two effects, the same setup as the one used in the immersions was studied in air in the laboratory in a dark room. Several factors made this a challenge: the source-detector distance had to be roughly the same as the distances at which the data were acquired during the immersions. This was to ensure that, with the LED intensities used during the immersions, the probability of multiple photons arriving at the detector simultaneously was negligible (to minimize the impact of the single-hit nature of the TDC upon the spectra). At the same time, the amount of scattered light must be minimal as only direct photons must be recorded in order to observe the time width purely due to the experimental setup.

[5]This could be seen by the condensation of frost on the surface of the TDC.

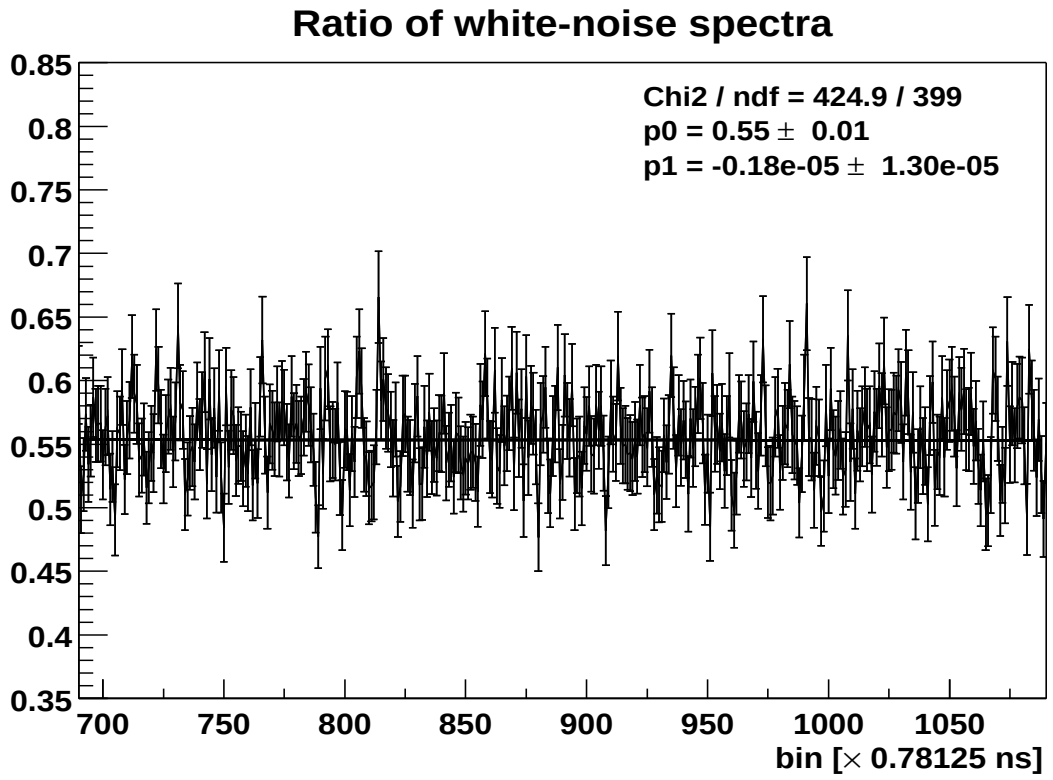


**Figure 3.11:** *The ratio of two white-noise spectra taken under similar TDC conditions, but different external environments. The thick solid line shows the best straight-line fit to the data.*

Because the shape of the spectra could be affected by scattering in the source sphere, it was important to use the complete LED sphere at approximately the same distance as during the immersions. The LED and PMT spheres were therefore situated approximately 23 m apart at each end of a corridor, the maximum length that could be darkened in the laboratory, yielding a detection probability of more than one photon arriving at the PMT simultaneously of $\sim$1%.

To eliminate any stray light, absorbent material was placed in such a way as to reduce to a minimum possible the detection of any indirect photons (Figure 3.12). In addition to the material shown, the ceiling and floor were also covered with absorbent materials and a wooden panel with a hole of the same diameter as the OMs was placed in front of both spheres. The surface of the panel was roughened and covered in black absorbent paint. To check that no scattered light reached the PMT, a measurement was performed with only the surface area on the OM in front of the PMT covered up. With the remainder of the OM uncovered, only photons that had scattered were able to reach the PMT. No photon was detected, showing that the configuration used in the measurements of the air spectra only measured direct photons.

The dark-current noise rate of the 30 mm PMT of type 9125SA used in the measurements with Test 3′ is typically $\sim$100 Hz. This contribution was mostly removed by the

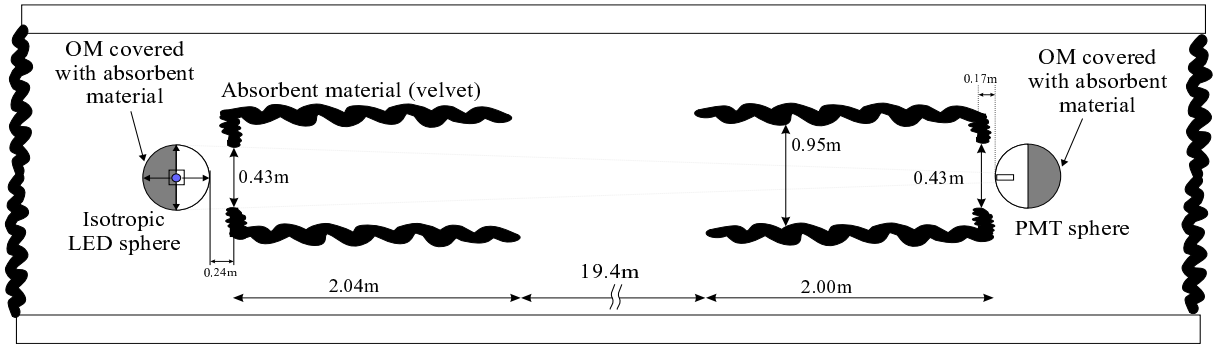


**Figure 3.12:** *Top view of the experiment for the measurement of the air calibration spectra. A 23 m long corridor was used to accommodate the LED sphere at one end and the detector sphere at the other. Very absorbent black velvet was arranged around both spheres to ensure that all scattered photons were absorbed and only direct photons were detected by the PMT.*

coincidence requirement with the ATW of the TDC.

Measurements were performed at all voltages applied to the LED drivers during the immersions because the shape of the time distribution of the LEDs depends upon the voltages applied to the LED drivers. Each set of data acquired during the immersions is analysed with a calibration spectrum taken in air at the same voltage. Typical air spectra are shown in Figure 3.13 for LED driver voltages of 4.75 V, 5.15 V and 5.80 V. Both an increase in the time width and a difference in the arrival time of the first photon on the rising edge can be observed.

The stability and reproducibility of the air spectra is excellent. Figure 3.14 shows the compatibility of the ratio of two air spectra, taken both at 4.75 V more than a week apart after dismantling and setting up the experiment several times[6], with a horizontal straight-line fit. Because the stability is excellent, these air spectra are reliable as calibration spectra for disentangling the LED time width and the optical properties in the data spectra.

Comparisons of the time distributions of air spectra with different orientations of the LED sphere yielded very similar results to Figure 3.14, so that even a different orientation of the LED sphere with respect to the detector sphere[7] during the immersions would not alter the shape of the calibration spectrum.

### Isotropy of source

The isotropy of the LED source was checked by recording the integral number of hits of spectra taken in air with different orientations of the LED sphere. After final adjustments of the variable capacitors on the LEDs, isotropy with less than 15% maximum variations

[6]The corridor in the laboratory was needed during the day to give access to other laboratories and the experiment therefore had to be dismantled after each night of measurements.

[7]In practice, the orientation of the LED sphere is fixed relative to that of the PMT during the immersions and is thus well-known.

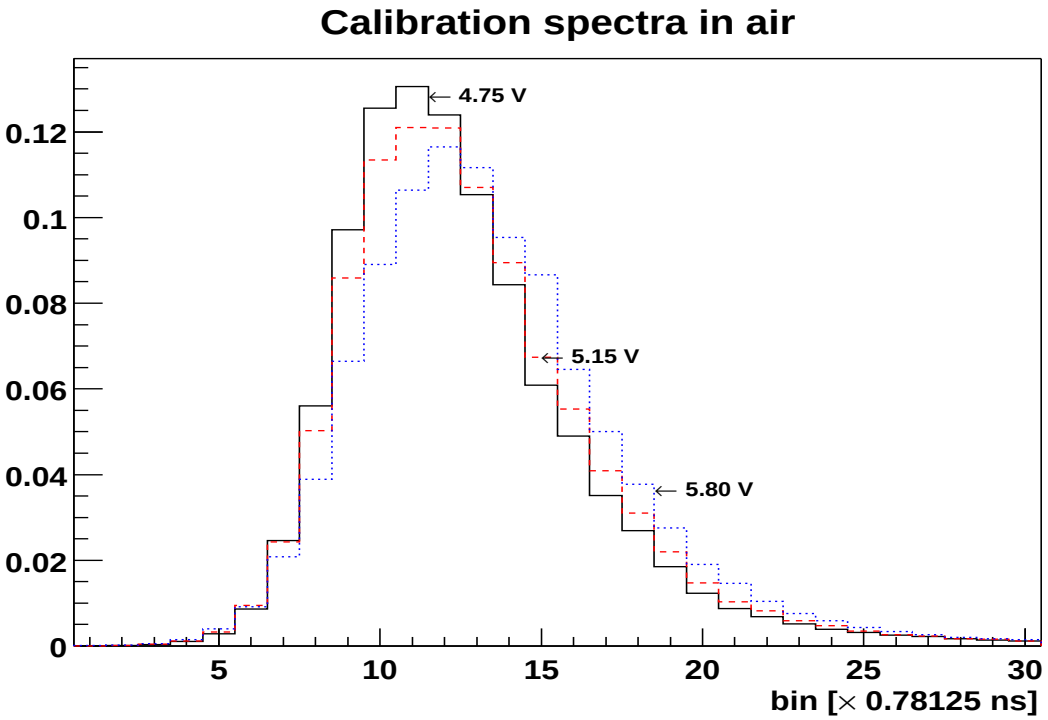


**Figure 3.13:** *Time distributions of air calibration spectra measured with different voltages applied to the LED drivers.*

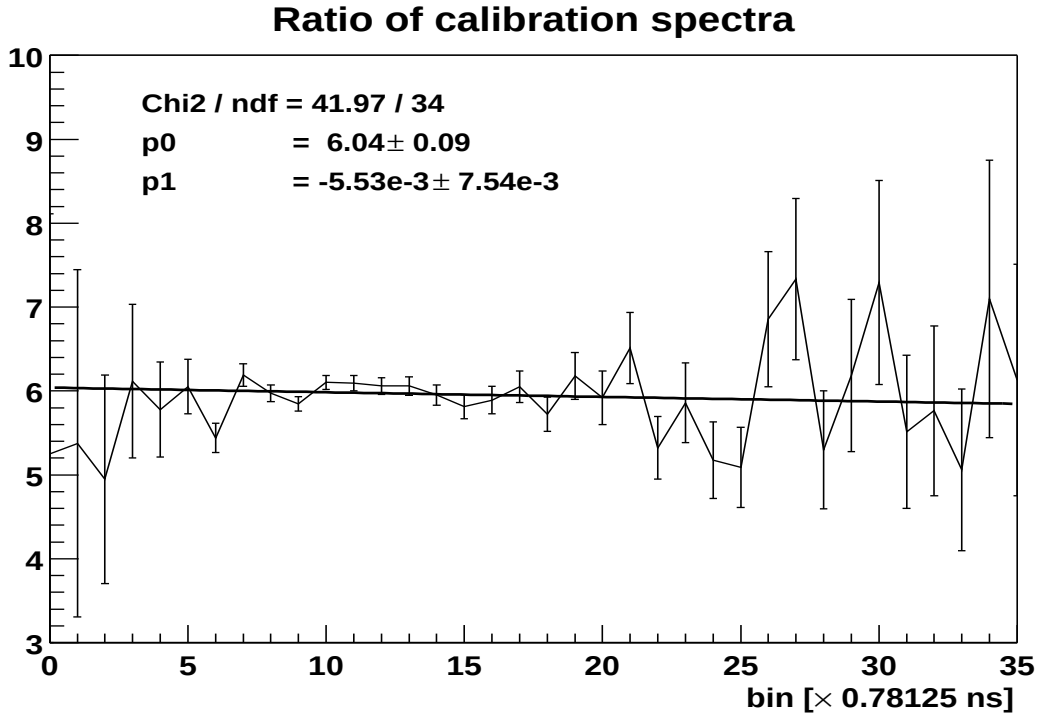


**Figure 3.14:** *The spectrum with error bars shows the bin-by-bin ratio of two air spectra taken at the same LED driver voltage (4.75 V). The solid line is a straight-line fit to this data.*

was achieved. These variations will contribute to the systematic errors as discussed in Section 6.3.4.

## 3.6 Summary

In this chapter, an experiment to measure the optical properties of deep waters in situ was described (Section 3.2). The procedures for immersing this experiment into the sea for the measurements at the ANTARES site were given (Section 3.3). The available data from the various immersions were presented and the differences between various configurations of the experiment were discussed (Section 3.4). The calibration of the experiment was then explained (Section 3.5).

# Chapter 4

# Treatment of Experimental Data

This chapter describes the method developed in this thesis to correct the data for various effects of the electronics of the Test 3′ experiment as well as for the background noise, yielding the "clean" data spectra which are used in the analysis described in Chapter 6.

*A mathematician may say anything he pleases, but a physicist must be at least partially sane.*

*J.W. Gibbs (1839-1903)*

## 4.1 Introduction

The data were acquired with the setup described in Section 3.2. Each data acquisition produces a file containing a histogram of the number of photon hits (from now on also sometimes referred to as events), from a pulsed set of LEDs at a known distance from the detector, as a function of the arrival time. Several histograms were acquired under identical conditions for each immersion (i.e. on the same date). For future reference, a *set of data files* is defined as all the data files which were taken under identical conditions (i.e. on the same date, at the same distance and with the same LED intensity).

The photons recorded in each histogram can have two origins: the LED source or some background source in the water (see Section 6.2.2). The detected number and arrival time of photons from the LED source is determined by the optical properties of the water, which determine the path length and velocity of the photon (Chapter 2). Bioluminescence, potassium-40 decays and other random background-noise sources additionally contribute to the number of photons recorded in each bin. Figure 4.1 shows several typical raw data spectra as obtained directly from in situ measurements.

Each histogram, from now on referred to as a spectrum, presents some specific features that are not related to the optical properties of the water. To be able to compare the

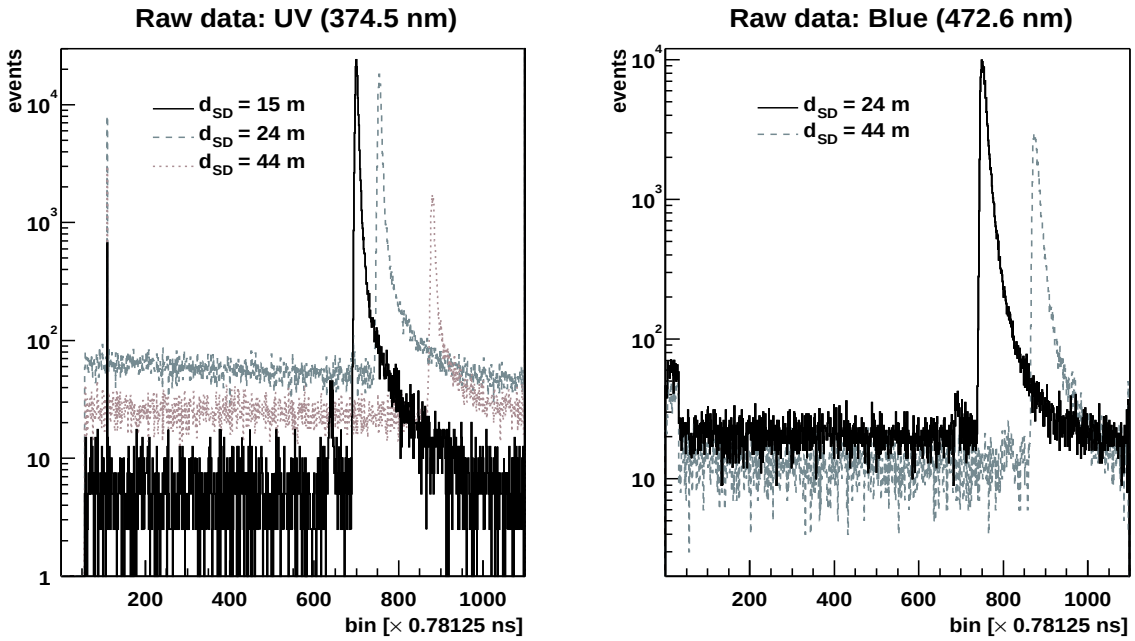


**Figure 4.1:** *Histograms of events recorded as a function of time during the immersions with light sources of central wavelengths 374.5 nm (UV) and 472.6 nm (blue) at various source-detector distances $d_{SD}$. More details about various features of these spectra are given in Appendix A.*

data with the MC spectra described in Chapter 5, the data had to be corrected for these features. The correction of the data was done essentially in two steps: correcting for the varying bin width and subtracting the background noise for each spectrum. Each data file was first corrected independently of the others to ensure that any potential variations in the water optical properties over time would be preserved. If the analysis results of each file from a given set were consistent with each other, the raw data files were added and then corrected as a single spectrum.

## 4.2 Correcting for Unequal Bin Widths

Varying bin widths across the range of the TDC alter the spectrum as described in Section 3.5.1. They were corrected for by dividing the data spectrum by a high-statistics white-noise spectrum. If $N_o(i)$ and $N_w(i)$ are the number of hits in bin $i$ of the original data histogram and the white-noise spectrum respectively, the histogram corrected for unequal bin widths is given by

$$N_c(i) = N_o(i) \times \frac{F(i)}{N_w(i)} \tag{4.1}$$

where $F(i)$ takes care of the effect of the single-hit nature of the TDC on the white-noise spectrum as described below.

Any spectrum is biased by the single-hit nature of the TDC because, even with very low event rates, there is a finite probability of two (or more) photons arriving at the detector within the same ATW. The probability that the TDC will record a photon after a time $t$ in a time interval $\delta t$ for a constant random event rate $R$ is given by the probability that it has not detected any photon up to time $t$ (since it can only record one photon per LED trigger) times the probability that it will detect a photon in the time interval $\delta t$:

$$P(t)\,\delta t = e^{-Rt} \times R\delta t. \tag{4.2}$$

The single-hit nature of the TDC has thus the effect of suppressing later hits, creating an exponentially decreasing probability of registering a photon even with a uniform rate. For the probabilities of detecting a LED photon in the measurements with Test 3′, $e^{-Rt} \sim 1$. Whilst the decrease in probability is small, the effect is not negligible and must be taken into account in the division by the white-noise spectrum and in the computation of the background-noise spectrum. For the acquired histograms, $t$ corresponds to $i \times \delta t$ where $\delta t$ is the average bin width across the spectrum.

The fit function $F(i)$ to the white-noise spectrum was constructed from Eq. 4.2[1], constraining the integral to the total number of events in the white-noise spectrum over the same range:

$$F(i) = \left(\sum_{j_{min}}^{j_{max}} N_w(j)\right) \times \left(\frac{R\delta t \;\; e^{-iR\delta t}}{e^{-j_{min}R\delta t} - e^{-j_{max}R\delta t}}\right), \tag{4.3}$$

where $j_{min}$ and $j_{max}$ are delimiting the range of the fit[2]. The fit was done using ROOT (with MINUIT [67] as the minimizer) and yielded the best value of $\nu = R\delta t$ together with its error $\sigma_\nu$. The best estimate of the corrected data is then given by Eq. 4.1. To account for the error on $\nu$, the minimum and maximum spectra were constructed[3]:

$$N_c(i) = \frac{N_o(i)}{N_w(i)} \times \frac{\left[\sum_{j_{min}}^{j_{max}} N_w(j)\right] \nu \; e^{-i\nu}}{e^{-j_{min}\nu} - e^{-j_{max}\nu}} \tag{4.4}$$

$$N_c^{min}(i) = \frac{N_o(i)}{N_w(i)} \times \frac{\left[\sum_{j_{min}}^{j_{max}} N_w(j)\right] (\nu - \sigma_\nu) e^{-i(\nu-\sigma_\nu)}}{e^{-j_{min}(\nu-\sigma_\nu)} - e^{-j_{max}(\nu-\sigma_\nu)}} \tag{4.5}$$

$$N_c^{max}(i) = \frac{N_o(i)}{N_w(i)} \times \frac{\left[\sum_{j_{min}}^{j_{max}} N_w(j)\right] (\nu + \sigma_\nu) e^{-i(\nu+\sigma_\nu)}}{e^{-j_{min}(\nu+\sigma_\nu)} - e^{-j_{max}(\nu+\sigma_\nu)}}. \tag{4.6}$$

[1] For the fit, the white-noise spectrum was grouped in units of 32, corresponding to the number of delay lines dividing one cycle of the clock driving the TDC as described in Section 3.2.4. This grouping eliminates any potential bias to the fit introduced by the unequal bin widths.

[2] The range was chosen such that the fit was done on the part of the spectrum unaffected by the peculiarities (see Figure A.1, p. 125).

[3] The error on $\nu$ could not be used in the calculation of the $\chi^2$ in the comparison of the data and the MC simulations because the $\chi^2$ assumes that the errors for each bin are independent of each other.

The difference between Eqs. 4.4, 4.5 and 4.6 was however so small (because of the large statistics in the white-noise spectrum) that it could not be detected in the analysis. Only the central value of the fit to the white-noise spectrum (Eq. 4.4) was therefore used to correct for the unequal bin widths.

## 4.3 Background Noise

Each spectrum is naturally divided into the region before the main LED photon peak and the signal region. Any photons that are registered in the region before the peak come from various background-noise sources in the water. The signal region consists of a mixture of photons from the LED and background-noise photons. To obtain the spectrum of LED photons only, the background noise must be subtracted over the entire spectrum. It could however only be measured over the range before the peak and therefore had to be extrapolated into the signal region.

In analogy to the fit to the white-noise spectrum, the background noise was calculated by performing a fit of Eq. 4.2 similar to Eq. 4.3 in the region before the peak on the corrected data[4], giving the background noise $B(i)$ over the pre-signal region as

$$B(i) = \left( \sum_{i_{min}}^{i_{max}} N_c(i) \right) \times \left( \frac{R'\delta t \;\; e^{-iR'\delta t}}{e^{-i_{min}R'\delta t} - e^{-i_{max}R'\delta t}} \right). \tag{4.7}$$

This background noise was then used in the computation of the background noise in the signal region. To account for the systematic errors on the final data introduced by the errors on $\nu' = R'\delta t$ obtained from the fit, the minimum and maximum spectra were constructed (in analogy to the fit to the white-noise spectrum):

$$B^{min}(i) = \left( \sum_{i_{min}}^{i_{max}} N_c(i) \right) \times \left( \frac{(\nu' - \sigma_{\nu'}) \;\; e^{-i(\nu' - \sigma_{\nu'})}}{e^{-i_{min}(\nu' - \sigma_{\nu'})} - e^{-i_{max}(\nu' - \sigma_{\nu'})}} \right) \tag{4.8}$$

$$B^{max}(i) = \left( \sum_{i_{min}}^{i_{max}} N_c(i) \right) \times \left( \frac{(\nu' + \sigma_{\nu'}) \;\; e^{-i(\nu' + \sigma_{\nu'})}}{e^{-i_{min}(\nu' + \sigma_{\nu'})} - e^{-i_{max}(\nu' + \sigma_{\nu'})}} \right). \tag{4.9}$$

Naively one would extrapolate each of these functions directly into the signal region to determine the background contribution there. However the single-hit nature of the TDC has a larger effect in the signal region because of the higher rate. The exponential in Eq. 4.7 already takes care of the effect of the previous background hits, but it is necessary

[4]The fit region was delimited by bin 110 (for reasons described in Appendix A) and a spurious pre-signal peak (approximately 50 bins before the peak, as shown in Figure 4.1), which was identified with a fraction of pulses being picked up by the discriminator at a constant time difference with respect to the start of the signal region due to the pulse shape.

to add on the effect of the LED hits in the signal region. The number of background-noise hits $B_{SR}(i)$ in the signal region is therefore given by

$$B_{SR}(i) = B(i) \times [1 - P_{LED}(i)]\,, \tag{4.10}$$

where $P_{LED}(i)$ is the probability of having registered any LED photon up to bin $i$ given by $N^i_{LED}/N_{tot}$, where $N^i_{LED}$ is the total number of LED photons registered up to bin $i$ and $N_{tot}$ is the total number of triggers that did not register any background photon and could have registered a LED photon. $N^i_{LED}$ is given by

$$N^i_{LED} = \sum_{j=0}^{i} \{\ N_c(j) - B(j) \times [1 - P_{LED}(j-1)]\ \} \tag{4.11}$$

and $N_{tot}$ is simply related to the total number of triggers $N_T$ by

$$N_{tot} = N_T - \sum_{j=0}^{max} \{\ B(j) \times [1 - P_{LED}(j-1)]\ \}\,. \tag{4.12}$$

Using Eqs. 4.11 and 4.12, the probability of detecting a LED photon can be written as

$$P_{LED}(i) = \frac{\sum_{j=0}^{i} N_c(j) - B(j) \times [1 - P_{LED}(j-1)]}{N_T - \sum_{j=0}^{max} B(j) \times [1 - P_{LED}(j-1)]}, \tag{4.13}$$

where the sum in the denominator is over all bins in the histogram. In the denominator, the total number of background-noise hits was subtracted from the total number of triggers, to yield the best estimate of the total number of triggers that could have given a LED hit.

The background noise in the signal region, obtained from Eqs. 4.10 and 4.13, is subtracted bin-by-bin from the corrected data to yield three histograms of LED data (using the appropriate $B(i)$ from Eqs. 4.7 - 4.9)

$$N_{LED}(i) = N_c(i) - B_{SR}(i) \tag{4.14}$$
$$N^{min}_{LED}(i) = N_c(i) - B^{min}_{SR}(i) \tag{4.15}$$
$$N^{max}_{LED}(i) = N_c(i) - B^{max}_{SR}(i) \tag{4.16}$$

for each raw data spectrum, and each is analysed separately as described in Chapter 6. The central value is used to determine the best fit and the two extremes are used to determine the systematic error on the optical parameters due to the error on the fit to the background noise. Figure 4.2 shows a typical data spectrum corrected for the unequal bin widths together with the final cleaned LED spectrum.

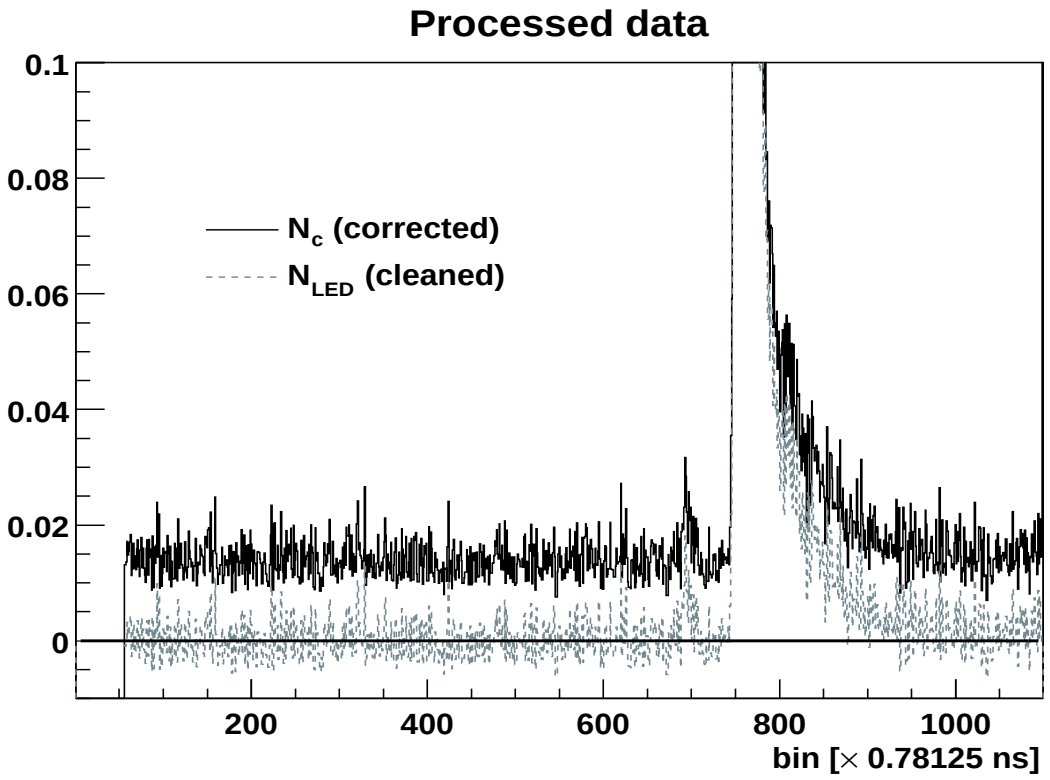


**Figure 4.2:** *Typical data spectrum "corrected" for the unequal bin widths of the TDC, and "cleaned" spectrum for which the background-noise photons were subtracted.*

## 4.4 Statistical Errors

The errors on the number of events recorded as a function of bin number were assumed to be Gaussian distributed. For this approximation to be valid a minimum of ten[5] events was required for each bin [68]. Any bin that did not satisfy this requirement was grouped with adjacent bins until the minimum statistics was attained, thus creating a variable bin width histogram.

As described previously, the errors on the fits to the white-noise spectrum were negligible and the errors on the fits to the background noise were taken into account by creating three different cleaned spectra and analysing each separately. The statistical errors $\sigma_c$ on the data divided by the white-noise spectrum are simply given by

$$\sigma_c^2(i) = N_c^2(i)\left(\frac{\sigma_o^2(i)}{N_o^2(i)} + \frac{\sigma_w^2(i)}{N_w^2(i)}\right), \tag{4.17}$$

where the $\sigma$'s correspond to the Gaussian errors ($\sigma_o = \sqrt{N_o}$, etc.) and the subscripts have the same meaning as before. The statistical error on the noise subtraction must be added

[5]The difference between the variance of a Poisson distribution and a Gaussian distribution with a mean of 10 events is $\lesssim 0.03\%$.

to the errors on the corrected data to obtain the total statistical error for each bin after the final treatment of the data. The statistical errors on the noise computation in the signal region only consist of the errors associated with the number of LED hits recorded. The errors associated with $B_{SR}$ in Eqs. 4.14 to 4.16 are computed using Eq. 4.13 yielding

$$\sigma^2_{P_{LED}}(i) \approx \frac{\sum_{j=0}^{i} B^2(j) \times \sigma^2_{P_{LED}}(j-1)}{\left\{ N_T - \sum_{j=0}^{max} B(j) \times [1 - P_{LED}(j-1)] \right\}^2} \tag{4.18}$$

where the error on the denominator of Eq. 4.13 was shown to be negligible. The statistical error of the background-noise subtraction is therefore given by

$$\sigma^2_{B_{SR}}(i) = B(i)^2 \times \sigma^2_{P_{LED}}(i) \tag{4.19}$$

and the total statistical error on the cleaned LED data $N_{LED}$ is calculated from

$$\sigma^2_{N_{LED}}(i) = \sigma^2_c(i) + \sigma^2_{B_{SR}}(i). \tag{4.20}$$

It is this final error together with the error on each bin of the MC simulations that is used in the calculation of the $\chi^2$ when comparing the MC simulations to the data (as described in Chapter 6).

## 4.5 Summary

In this chapter, the treatment applied to each data histogram was described. The unequal bin widths of the TDC were corrected for and the single-hit effect of the TDC was taken into account in this correction (Section 4.2). The background noise was then subtracted, taking into account the decrease in the background-noise rate in the signal region caused by the single-hit nature of the TDC (Section 4.3). If the individual data from a set were consistent with each other, the raw data were added and treated as a single file, using the same method as for the individual data. The statistical errors on the final data (corrected for the variation in bin widths and the background noise) were then calculated (Section 4.4).

# Chapter 5

# Light Propagation Monte Carlo: LITEPROP

This chapter gives a description of the MC simulation of Test 3′. The simulations are based upon the qualitative understanding of the optical properties at the ANTARES site, gained from previous measurements in natural waters (described in Chapter 2), and take into account the calibration of the experiment. By comparing the shapes of the arrival time distributions of different water models, the capability of distinguishing the various optical parameters with the Test 3′ experiment is demonstrated.

*An approximate answer to the right question is worth a good deal more than the exact answer to an approximate problem...*

*J. Tukey (1915-2000)*

## 5.1 Introduction

A Monte Carlo (MC) code was designed and written to simulate the arrival time distributions of photons from a pulsed light source at a detector. It constitutes a stand-alone package for tracking photons through a medium with four adjustable optical parameters: an absorption length $\lambda_A$, a scattering length for small centres (SC) $\lambda_{SC}$, a scattering length for large centres (LC) $\lambda_{LC}$ and the average cosine of its angular distribution $\langle cos\theta \rangle_{LC}$ (the angular distribution of the SCs is fixed and given by Eq. 2.7, p. 19). Additionally, it requires as input the time distribution and the wavelength distribution of the light source used in the experiments, the angular efficiency of the detector glass sphere, as well as a time offset which takes into account the various delays in the electronics of the experimental equipment. Figure 5.1 shows a flow chart of the MC simulation[1].

[1] An analytical model, valid in the limit where multiple scattering between the source and the detector can be neglected, is described in Appendix E.

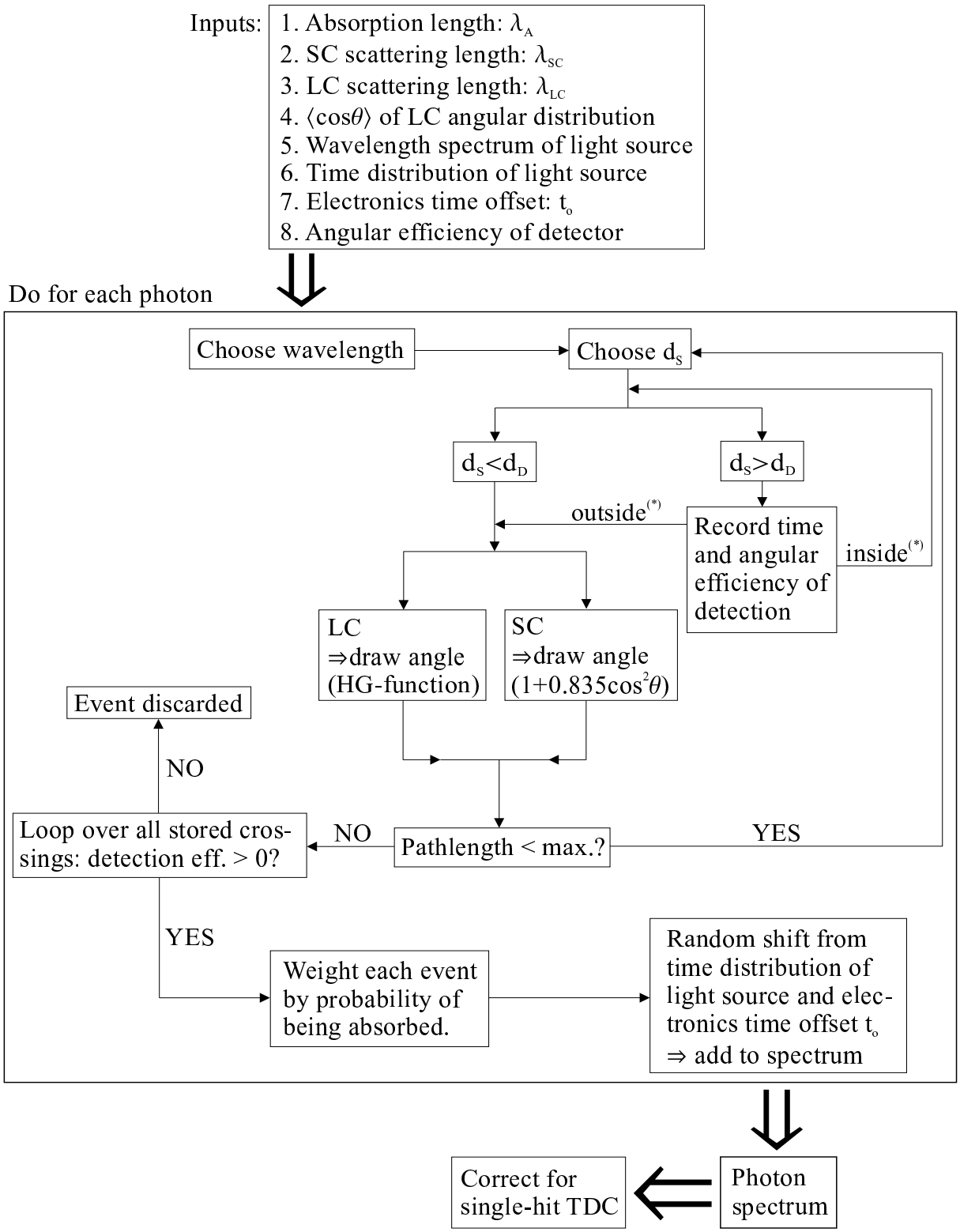


**Figure 5.1:** *The flow-chart of the MC simulation: $d_S$ and $d_D$ are the distance to the next scattering centre (corrected for the distance already traveled) and the distance to the virtual detector sphere in the direction of photon propagation respectively. The MC photon spectrum is corrected for the effect of the single-hit TDC. (*) refer to being inside or outside of the virtual detector sphere (see text for an explanation).*

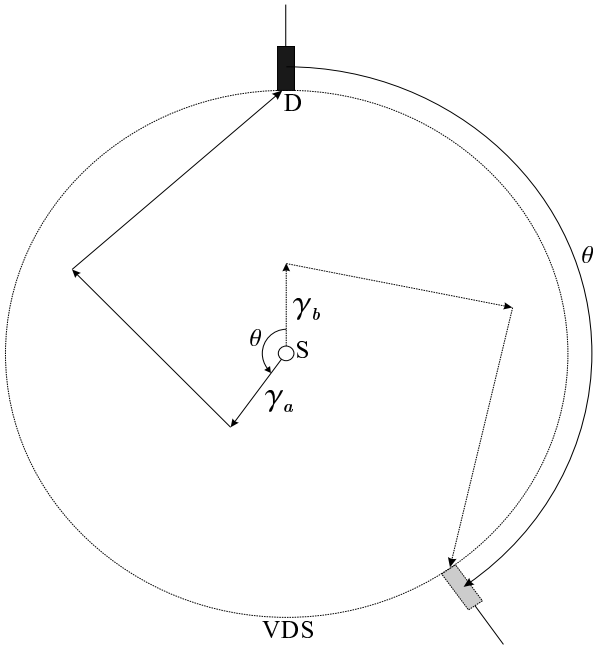


**Figure 5.2:** *For each photon $\gamma_a$, emitted from the source S at an angle $\theta$ to the direction to the detector D, there is an equivalent photon $\gamma_b$, emitted towards D and reaching the virtual detector sphere VDS at an angle -$\theta$.*

## 5.2 Simulation of Test 3′

### 5.2.1 Geometry

The solid angle subtended by the detector at the light source is very small ($\Omega \sim 10^{-7}$) in the experimental setup (described in Section 3.2) and only a very small fraction of photons emitted by the light source are registered by the detector. A direct simulation of the experimental setup is therefore very inefficient and the large statistics required (for each point in the parameter space[2]) for the analysis of the data precluded the direct simulation of the geometry of the experiment. As a result, an alternative approach was required. A model was developed which maximizes the detection efficiency in the simulation. A virtual detector sphere (VDS) covering the total solid angle was defined.

The spherical symmetry of the light source is such that for each photon $\gamma_a$, emitted from the light source at an angle $\theta$ with respect to the direction to the detector, which eventually scatters into the detector, there is an equivalent photon $\gamma_b$, emitted towards the detector, which crosses at angle $-\theta$ the virtual detector sphere centred on the light source and passing through the detector (Figure 5.2). Therefore, there is a one-to-one correspondence between the setup using an isotropic light source and a point detector and a simulation using a unidirectional light source and a detector sphere centred on the light source. The former is by far the cheaper experiment, the latter the more efficient

[2]For each set of data of the experiment, a data base of approximately $10^5 - 10^6$ water models with different parameter combinations needs to be generated.

simulation. This increases the statistics of the simulations by a factor $4\pi/\Omega$, yielding typically between $\sim 4 \times 10^6$ and $\sim 4 \times 10^7$ (depending upon the source-detector distance) more statistics than the direct simulation.

### 5.2.2 Tracking

Each of a large number of photons was propagated individually according to the algorithm described below (and summarized in Figure 5.1).

#### Choosing Photon's Wavelength

The speed of propagation of the photons (and hence the arrival time measured with Test 3′) depends upon their wavelength. The finite spectral width of the source therefore causes photons to travel at different group velocities through the water and creates a spread in the arrival times of the photons. For every photon, the wavelength is therefore randomly chosen from the measured wavelength distribution of the source (Figure 3.5, p. 43) and the group velocity of that photon is determined from Eq. 2.21 (p. 34) using Eq. 2.23 (p. 35) to calculate the required refractive index. Figure 5.3 shows the effect of the spectral spread on the arrival time distribution of direct photons (i.e. that have not scattered). The spread is relatively large (FWHM $\approx$ 1 ns), with the earliest photons arriving more than 2 ns before the photons at the central wavelength of the source (shown as the vertical line in Figure 5.3).

#### Direction of Emission

Given the geometrical considerations discussed in Section 5.2.1, all photons are emitted from the source into a unique predefined direction.

#### Optical Parameters for Each Photon

Because the optical properties of the water are determined at a single wavelength, the input parameters for the optical properties are always chosen to correspond to the central wavelength $\lambda_C$ of the LED source. For photons from the spectral distribution with a wavelength other than $\lambda_C$, these values can be different.

The variation with wavelength of the absorption length and of the scattering length of LCs is not well known, but is assumed to be negligible over the wavelength spread of the source ($\sigma \approx 5$ nm in the UV and $\sigma \approx 15$ nm in the blue, see Figure 3.5, p. 43). For SC, the theoretical relation for the dependence of $\lambda_{SC}$ upon the wavelength (see discussions in Section 2.3.1) is used to calculate $\lambda_{SC}$ for the chosen wavelength of the photon:

$$\lambda_{SC} = \lambda_{SC}^{C} \left( \frac{\lambda}{\lambda_C} \right)^{4.32}, \tag{5.1}$$

where $\lambda_{SC}^{C}$ is the SC scattering length at the central wavelength of the source. For the UV source, the spread of $\lambda_{SC}$ due to the convolution between the wavelength spectrum and the $\lambda^{4.32}$ dependence is shown in Figure 5.4. The mean $\lambda_{SC}$ of this distribution is larger

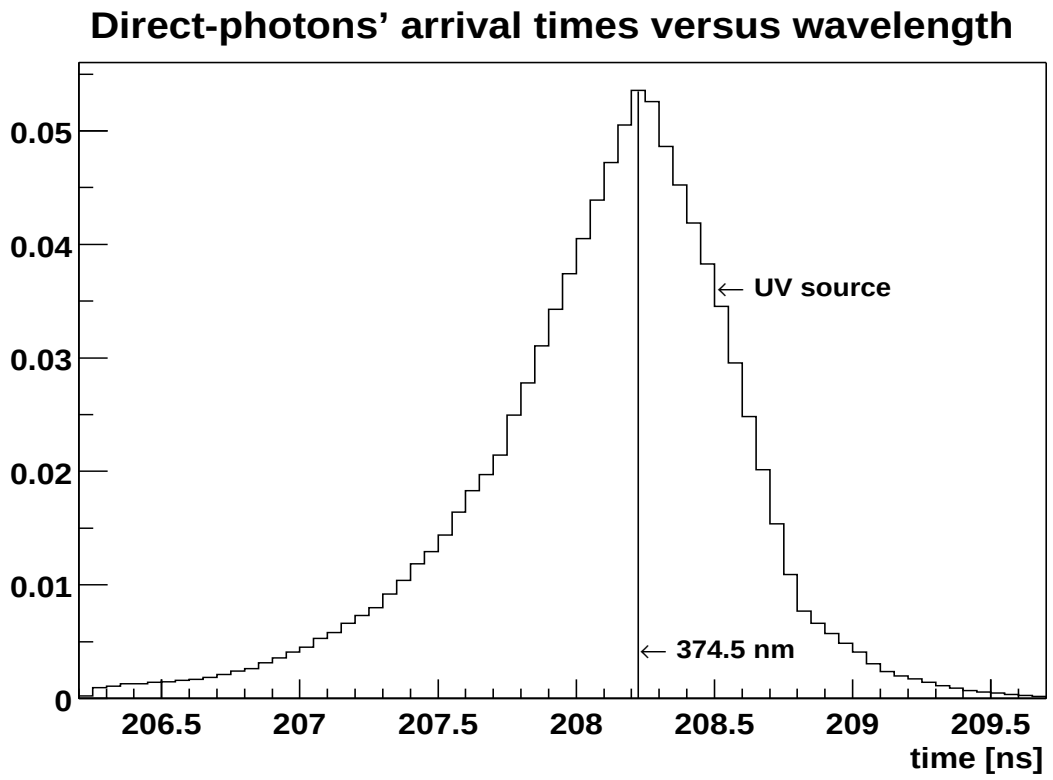


**Figure 5.3:** *Arrival times of direct photons (i.e. those which have not scattered) at a single wavelength (374.5 nm) and with the finite-width UV source used in the measurements with Test 3′ (wavelength "distribution"), with a source-detector separation of 44.41 m.*

than the value of $\lambda_{SC}$ at the central wavelength of the source by 4.5 m, showing that it is important to take the wavelength spread into account in the computation of $\lambda_{SC}$.

### Distance to the Next Scattering Centre

As discussed in Section 2.3, the photon's path can be influenced by the presence of scattering centres in the medium. The probability that a photon will survive without scattering up to distance $r$ was derived as $P_{\sigma,S} = e^{-r/\lambda_S}$ (Eq. 2.13, p. 22), where $\lambda_S$ is the average distance traveled between scattering centres. From the discussion in Section 2.7, $P_{\sigma,S}$ has two contributions: $P_{LC}$ from LCs and $P_{SC}$ from SCs. The total probability of surviving a distance $r$ without any scattering is given by the probability of neither a LC nor a SC affecting the photon's path, given by

$$P_S(r) = P_{LC}(r) \times P_{SC}(r) \quad \longrightarrow \quad e^{-r/\lambda_S} = e^{-r/\lambda_{LC}} \times e^{-r/\lambda_{SC}}. \tag{5.2}$$

Using the value of $\lambda_{SC}$ calculated in the previous section, $\lambda_S$ is calculated from the requirement

$$\frac{1}{\lambda_S} = \frac{1}{\lambda_{LC}} + \frac{1}{\lambda_{SC}}, \tag{5.3}$$

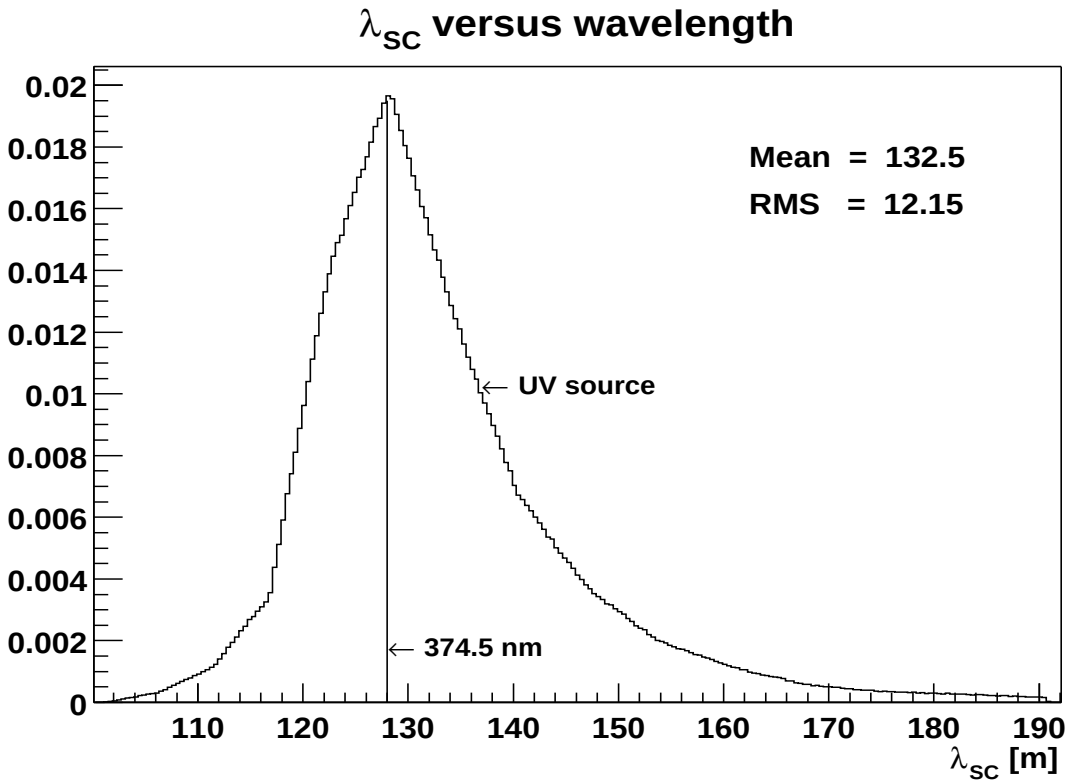


**Figure 5.4:** *Distribution of the SC scattering lengths due to the wavelength distribution of the Test 3' UV LED source, given a $\lambda_{SC}^{C}$ of 128 m at the source's central wavelength (374.5 nm).*

which directly follows from Eq. 5.2. For identical scattering cross sections, Eq. 5.3 is equivalent to stating that the total density of scatterers in the medium is the sum of the densities of the individual scatterers. The distance to the next scattering centre $d_S$ is therefore randomly chosen from the exponential distribution using $\lambda_S$[3], yielding

$$d_S = -\lambda_S \times ln(\rho), \tag{5.4}$$

where $\rho$ is a random number between 0 and 1.

### "Fate" of the Photon

The distance $d_S$ to the scattering centre is compared to the distance to the virtual detector sphere.

[3]It should be noted that this approach of sampling from the average scattering length and then determining the type of scattering centre is different from an approach where one would sample from the individual LC and SC scattering length distributions (which is wrong). If $b_A$ and $b_B$ are the scattering coefficients of the two types of scatterers, in the case of sampling from the sum of the scattering coefficients, the total probability of not scattering is $\propto e^{-(b_A+b_B)d}$ whilst in the other case it is incorrectly calculated as $\propto (e^{-b_A d} + e^{-b_B d})$.

1. If the detector sphere is crossed first, the time and weight from the detection angular efficiency are recorded in an array. Because the photon could be detected after having been outside of the detector sphere (i.e. scatter back into the sphere), the photon is allowed to propagate further until it hits the scattering centre. If the scattering centre is initially closer, the photon is scattered.

2. When the scattering centre is encountered, its type is determined by drawing a random number between 0 and 1 and comparing it to the probability that a scattering centre is a LC or a SC, given by

$$p_{LC} = \frac{b_{LC}}{b_{LC} + b_{SC}} = \frac{\lambda_S}{\lambda_{LC}} \quad \text{and} \quad p_{SC} = 1 - p_{LC} = \frac{\lambda_S}{\lambda_{SC}}. \tag{5.5}$$

The photon then changes direction by an angle $\theta$ chosen from the appropriate angular distribution function (Eq. 2.7, p. 19 and Eq. 2.8, p. 20). This is done by choosing a random number $r$ between 0 and 1 to yield the $\cos\theta$ at which the cumulative distribution function (normalised to unit area) corresponds to this random number, i.e. $\cos\theta$ is extracted from

$$r = \frac{\int_{-1}^{\cos\theta} f(\cos\theta')\ d\cos\theta'}{\int_{-1}^{1} f(\cos\theta')\ d\cos\theta'}. \tag{5.6}$$

### Determining the Photon Direction

Using the chosen $\cos\theta$, the new direction of propagation of the photon is determined as follows [69]:

1. A vector $\underline{v}$ with a randomly chosen angle $\phi$ (implicitly assuming azimuthal isotropy) and angle $\alpha$ with respect to the direction of the incident photon is constructed (as shown in Figure 5.5). In spherical coordinates such a vector can be written as

$$\underline{v} = \begin{pmatrix} \sin\alpha\cos\phi \\ \sin\alpha\sin\phi \\ \cos\alpha \end{pmatrix}. \tag{5.7}$$

2. Construct a vector $\underline{p}$ perpendicular to the plane containing the vectors $\underline{d}_o$ and $\underline{v}$, given by

$$\underline{p} = \begin{pmatrix} d_y\cos\alpha - d_z\sin\alpha\sin\phi \\ -d_x\cos\alpha + d_z\sin\alpha\cos\phi \\ d_x\sin\alpha\sin\phi - d_y\sin\alpha\cos\phi \end{pmatrix}. \tag{5.8}$$

3. The new direction is then given by

$$\underline{d}_n = \cos\theta\frac{\underline{d}_o}{|\underline{d}_o|} + \sin\theta\frac{\underline{p}}{|\underline{p}|}. \tag{5.9}$$

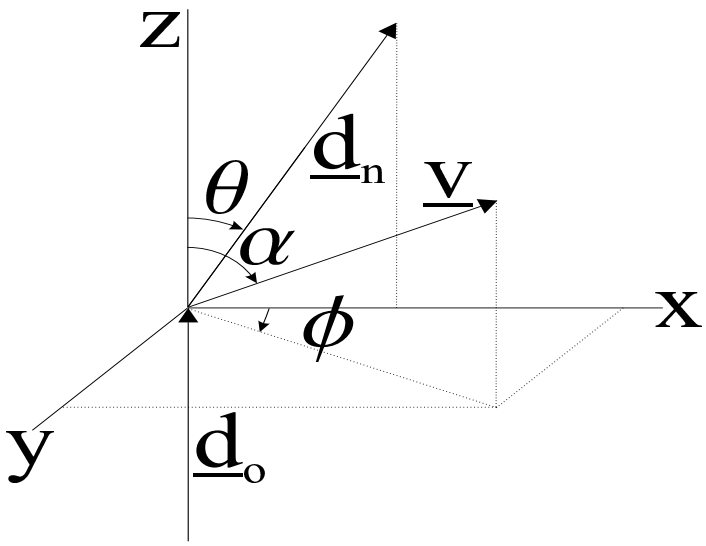


**Figure 5.5:** *Geometry describing how to change the photon direction at the scattering centre: the incident photon with vector $\underline{d}_o$ is scattered at an angle $\theta$ and angle $\phi$ to yield the new direction vector $\underline{d}_n$.*

### Tracking Photon up to the Maximum Path Length

A distance to the next scattering centre is chosen and compared again to the distance to the VDS (provided that the photon actually propagates in a direction that would enable it to cross the sphere again, else it is scattered). If the photon crosses the VDS again, its time and weight determined by the detector angular efficiency are recorded in its array and once again, because the photon is then inside the VDS, the distance to the VDS and to the scattering point are compared. This process is repeated until the track length of the photon exceeds the maximum length, determined by the maximum time recorded with Test 3′.

### Absorption

In a direct simulation of the experiment, for each photon, a distance $d_A$ to the absorption point would be sampled from the exponential distribution of the absorption length and the photon would be stopped there. This method however proved to yield too little statistics and it was therefore necessary to use a different approach: each photon was tracked until it had traveled too far to be recorded in the spectrum and each of the detected photons was afterwards weighted by the probability of surviving the distance it traveled (to the point of detection) without being absorbed. With typical values for the absorption length of 20 to 30 m (at UV wavelengths), the latter method produces typically 5 to 10 times more statistics at a source-detector distance of 44 m. The approach of weighting the photons after tracking them to the detector also allowed to weight the photons with different absorption lengths without the need each time to regenerate the tracks through the water.

#### Weighting

In the absence of any absorption, the probability of the photon hitting the real detector sphere on any particular crossing is $\epsilon$, which is given by $d\Omega/4\pi$, where $d\Omega$ is the solid angle subtended by the detector sphere at the light source. If $\epsilon$ is small, the total probability for a photon which crosses the VDS $n$ times is $n\epsilon$. This is however only valid in the limit where $\epsilon$ is small enough such that the effect of shadowing is negligible[4]. The maximum value of $\epsilon$ for which the above assumption is valid was determined to be 0.001[5]. In Test 3', $\epsilon_{max} \sim 10^{-5}$, approximately two orders of magnitude smaller than this limit. The weight assigned to each photon on any crossing $j$ is given by

$$W_j = e^{-\frac{d_j}{\lambda_A}}, \tag{5.10}$$

where $d_j$ is the distance traveled by the photon from the source until its $j^{th}$ crossing of the VDS and $e^{-d_j/\lambda_A}$ is the probability that it has not been absorbed before the $j^{th}$ crossing.

### 5.2.3 Calibration

#### Width of Photon Pulse and Electronics Time Offset

To simulate the finite time width of the LED source, for each photon, a time is randomly chosen from the appropriate calibration air spectrum (Section 3.5.2) to determine the time of emission of the photon from the LED source (see Appendix C for more details on how to sample accurately from a binned distribution). This time is added to the time of each recorded crossing (from now on referred to as an event). Additionally, in order to take into account the various delays in the electronics of the experimental setup, a variable time offset is also added.

#### Angular Efficiency of the Detector Sphere

No experimental data were available for the relative angular efficiency of the detector glass sphere, given the difficulty of performing such measurements in water. Instead, the angular response of the detector sphere (Figure B.1 on p. 128) was MC simulated, as described in Appendix B, for photons with an angle of incidence smaller than $\pi/2$ with respect to the normal to the PMT face. Because the detector sphere angular efficiency is dependent upon the wavelength of the photons, a high-statistics simulation was produced once in the UV and once in the blue to obtain an average angular efficiency for each as a function of the angle of incidence. Using this tabulated angular efficiency, the efficiency

[4]It is because of the shadowing effect, as well as various other factors determining the detector efficiency described in Appendix B, that the size of the detector sphere is used rather than the size of the PMT.

[5]This number is the result of comparing the number of photons detected for each of a large number of spherical shells in 1 m steps from the origin, using once a simulation that samples a distance to the absorption point for each of a large number of photons and increments the number of photons in each spherical shell until either the photon is absorbed or it hits the detector (the probability for hitting the detector is given by $\epsilon$), and once a simulation which weights each photon at the end of its path based upon the total distance traveled.

for each photon was calculated and used to weight those photons that arrived within an angle $\pi/2$ with respect to the normal of the detector. All other photons were attributed a weight of zero.

### The Single-Hit Nature of the TDC

As described in Appendix A, the TDC is limited to recording only one hit per ATW. Therefore, the MC simulations were corrected for the probability that more than one photon arrived at the detector from the same LED pulse. In the limit where the number of photons tends to infinity and the probability of detecting any particular photon tends to zero, the probability of $n$ photons reaching the detector from any trigger of the LED is given by a Poisson distribution [68]

$$P_n(\mu) = \frac{\mu^n}{n!} e^{-\mu}, \tag{5.11}$$

where the mean $\mu$ is given by $\mu = \sum n \times P_n(\mu)$ and $0 \leq n \leq \infty$. The number of photons registered by the TDC is at most one per LED trigger, irrespective of the number of photons that actually reach the detector. The fraction $f$ of LED triggers that had a photon registered by the TDC after the subtraction of the background noise (described in Section 4.3) is given by

$$f = \sum_{n=1}^{\infty} P_n(\mu) = 1 - P_0(\mu) = 1 - e^{-\mu}. \tag{5.12}$$

This fraction is given for the experimental data in Tables 3.2 and 3.3 on pp. 48-49. In the worst case it is 5.81%, yielding a ratio between the probabilities of detecting three photons and one photon $P_3/P_1 < 10^{-3}$. It is therefore sufficient to take into account just the single- and double-photon events in the simulations. Each MC histogram is corrected for the fraction $f$ measured from each set of data as follows. The true spectrum $\boldsymbol{S}_{true}$ (of photons arriving at the PMT) with $N_{trig}$ triggers is given by

$$\mathbf{S}_{true} = N_{trig} \times \sum_{n=1}^{\infty} n \; \mathbf{S}_n^{true} \; P_n, \tag{5.13}$$

with each $\boldsymbol{S}_n^{true}$ satisfying $\int \boldsymbol{S}_n^{true} dt = 1$. From the definition of the true spectrum, $\boldsymbol{S}_1^{true} = \boldsymbol{S}_2^{true} = ... = \boldsymbol{S}_n^{true}$. Therefore, Eq. 5.13 yields

$$\begin{aligned} \mathbf{S}_{true} &= N_{trig} \times \mathbf{S}_1^{true} \times \sum_{n=1}^{\infty} n \; P_n \\ &= N_{trig} \times \mathbf{S}_1^{true} \times \mu \end{aligned} \tag{5.14}$$

$$\therefore \mathbf{S}_1^{true} = \frac{\mathbf{S}_{true}}{N_{trig} \; \mu}. \tag{5.15}$$

The TDC spectrum is then approximated by the sum of single- and double-photon events:

$$\mathbf{S}_{TDC} = N_{trig} \times \mu \; e^{-\mu} \left( \mathbf{S}_1^{TDC} + \frac{\mu}{2} \times \mathbf{S}_2^{TDC} \right). \tag{5.16}$$

For the LED triggers where only one photon arrived at the detector, the spectrum $\boldsymbol{S}_1^{TDC}$ registered by the TDC is the same as the true single-photon spectrum $\boldsymbol{S}_1^{true}$, as the TDC does not affect the shape or normalisation of single-photon events. To simulate the TDC spectrum for LED triggers with two photons, two arrival times were drawn randomly from $\boldsymbol{S}_{true}$ and only the smallest of the two times was kept. The process was repeated to generate the shape for a spectrum $\boldsymbol{S}'_{true}$ with the same statistical significance as the original true spectrum. $\boldsymbol{S}_2^{TDC}$, normalised to unit area and with a different shape from $\boldsymbol{S}_1^{TDC}$, is then given by

$$\mathbf{S}_2^{TDC} = \frac{\mathbf{S}'_{true}}{N_{trig} \; \mu}. \tag{5.17}$$

The final TDC spectrum which is reproduced by the MC simulations is therefore given by:

$$\mathbf{S}_{TDC} = e^{-\mu} \times \left( \mathbf{S}_{true} + \frac{\mu}{2} \times \mathbf{S}'_{true} \right). \tag{5.18}$$

## 5.3 Scanning the Parameter Space

The range of values of the optical parameters, relevant to the ANTARES medium, and of the time offset, compatible with the various delays in the electronics of the experimental equipment, was determined by producing a MC simulation in rough steps for a large range of values and comparing the MC spectra to the data. A restricted parameter space which gave reasonable agreement with the data was then chosen.

A MC spectrum was run for all combinations of $\lambda_{SC}$, $\lambda_{LC}$ and $\langle cos\theta \rangle_{LC}$ in the defined range with a predefined step size (10 m, 5 m and 0.03/0.04 respectively). Each of these spectra was then weighted and shifted in time to produce all the spectra for the various $\lambda_A$ and $t_o$ combinations (with step sizes 1 m and 0.078 ns respectively), producing a data base of different water models, each with 5 parameters. The photon arrival time distribution from each water model from this data base was then compared to the data to find the best model (using the $\chi^2$ test, as described in Chapter 6).

Typically $2 \times 10^7$ photons are propagated to yield a spectrum. This number of events was chosen as a compromise between CPU time and statistical accuracy (see Appendix D for more details on the statistical limitations of the MC simulations).

## 5.4 Spectral Shapes versus Parameters

Four different parameters describe the intrinsic optical properties of the medium: an absorption length $\lambda_A$, a SC scattering length $\lambda_{SC}$ (with its fixed angular distribution) and a LC scattering length $\lambda_{LC}$ with its angular distribution, determined by $\langle cos\theta \rangle_{LC}$. Varying each of these parameters individually (i.e. keeping the remaining parameters constant) has a very specific impact upon the normalisation and shape of the spectra and will be analysed in this section. Figures 5.6 and 5.7 show these impacts for source-detector distances of 15 m and 44 m respectively.

Each spectrum can be divided into two main regions: the "peak" and the "tail". The peak corresponds to the region where photons have either not scattered, or they have scattered through small angles, such that they arrive close in time to the direct photons. The photons in the tail have traveled longer distances and have therefore usually scattered through larger angles before reaching the detector.

**Absorption** reduces the number of hits recorded in any time interval of the spectrum, although the impact in the tail is larger than in the peak due to the increased distance photons have traveled before being detected: it yields effectively an exponential drop off in the number of photons as a function of time (i.e. distance traveled).

**SC scattering**, with a symmetrical angular distribution, on average causes the photon to scatter at large angles, causing relatively large time delays before they are detected. It therefore reduces the number of photons in the peak and increases the number of photons in the tail of the distribution.

**LC scattering** has a more forward-peaked angular distribution which causes the photons on average to travel a smaller distance than photons which scattered on a SC (although a longer path than direct photons) before being detected. This smaller increase in the path length of the photons means that LC scatterers will affect the shape of the rising edge of the peak as well as the location of the actual peak (in addition to causing some photons to arrive in the tail of the distribution).

The $\langle \cos\theta \rangle$ of the LC angular distribution has a very similar impact to the LC scattering length for very forward-peaked angular distributions, i.e. when $\langle \cos\theta \rangle_{LC} \stackrel{lim.}{\longrightarrow} 1$, whilst for larger $\langle \cos\theta \rangle_{LC}$ (and with only a small number of scatterings between the point of emission and the point of detection) this similarity in behaviour disappears (compare top-right and bottom-right plots of Figures 5.6 and 5.7).

The impact of the various parameters upon different parts of the spectrum becomes more apparent when the ratio of two spectra (differing only by one parameter) is plotted, as shown in Figure 5.8. Curves (1), (2), (4) and (5) show the different impacts of varying $\lambda_A$, $\lambda_{LC}$, $\langle \cos\theta \rangle_{LC}$ and $\lambda_{SC}$ one at a time respectively. No distinction can be made between curves (2) and (3) which are both ratios of two distributions with very forward-peaked $\langle \cos\theta \rangle_{LC}$ and which have the same ratio of the effective scattering length $\lambda^E_{LC}$. The reasons for this similarity will be discussed in the next section.

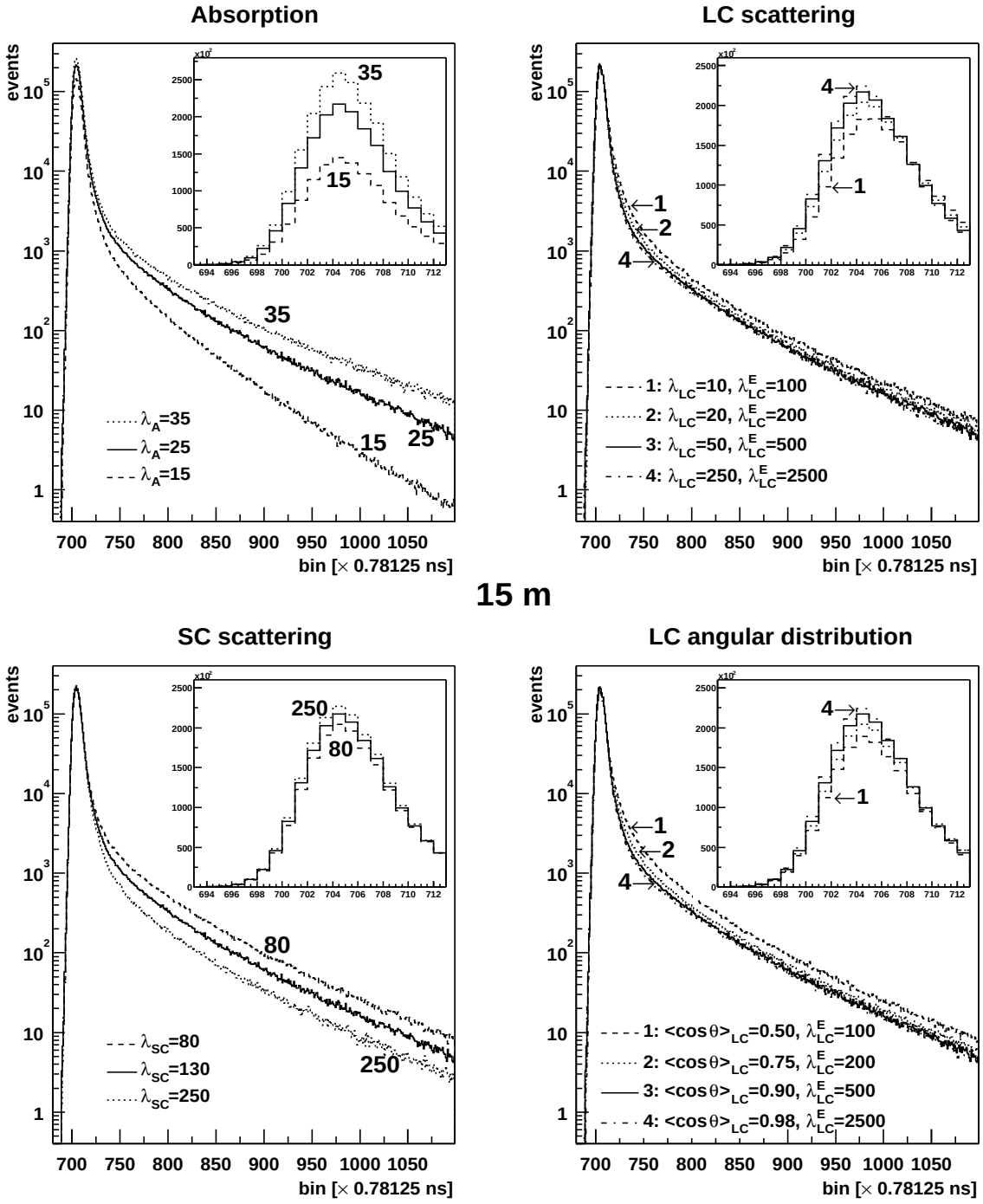


**Figure 5.6:** *MC simulations with a source-detector distance of 15.14 m. The solid line in each of the four plots corresponds to the nominal values $\lambda_A$=25 m, $\lambda_{LC}$=50 m, $\lambda_{SC}$=130 m, g=0.90 and $t_o$ =597.5. Each plot shows the variation in the shape of the spectrum when varying one parameter, keeping all other parameters constant.*

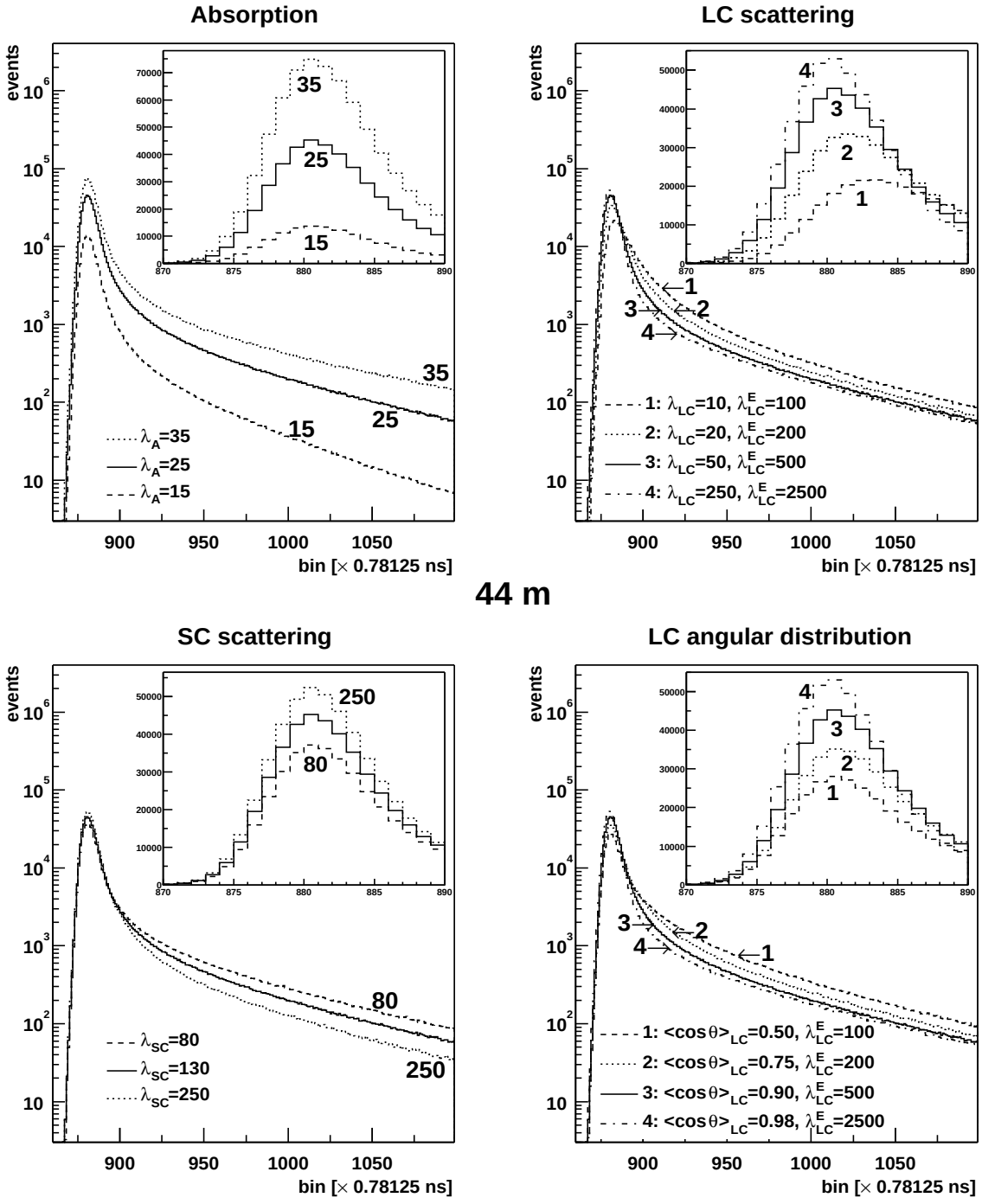


**Figure 5.7:** *MC simulations with a source-detector distance of 44.41 m. The solid line in each of the four plots corresponds to the nominal values as defined in Figure 5.6. Each plot shows the variation in the shape of the spectrum when varying one parameter, keeping all other parameters constant.*

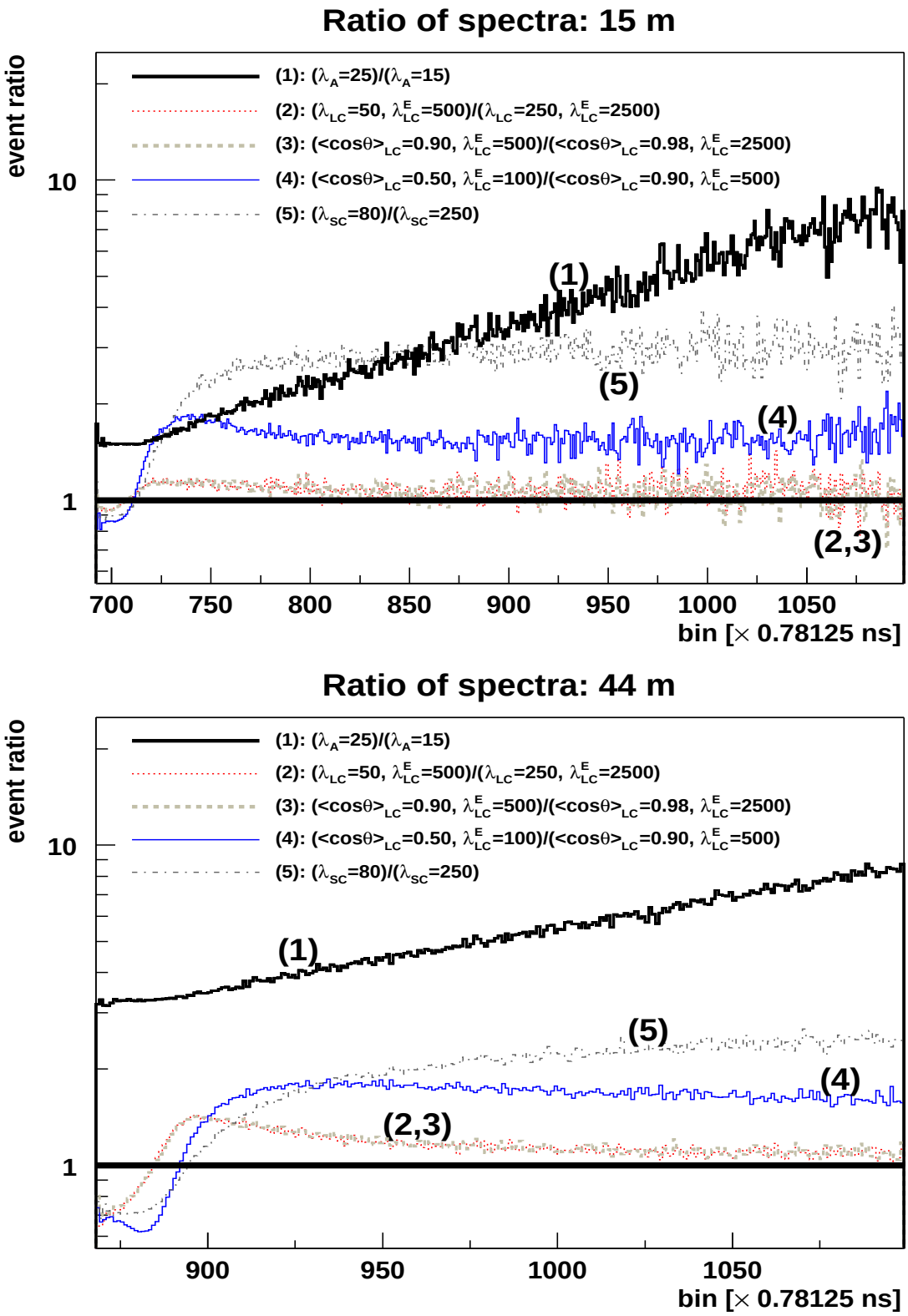


**Figure 5.8:** *Ratio of different MC simulations, varying one parameter at a time and keeping the others constant at the nominal values of Figure 5.6.*

### Effective scattering length

From Figures 5.6, 5.7 and 5.8, it is apparent that there is a certain degeneracy between some combinations of the LC scattering length and the average cosine of the LC angular distribution. The reason for this degeneracy is that the average path length traveled by many photons can be the same for different combinations of $\lambda_{LC}$ and $\langle\cos\theta\rangle_{LC}$.

This can be understood as follows: to reach a given point $\boldsymbol{R}$ at distance $|\boldsymbol{R}|$ from the point of emission, the photons can use many different paths with random vectors $\boldsymbol{r}_i$ $(i = 1, 2, 3, ..., n)$ between scattering events. For photons that have scattered $n$ times:

$$\mathbf{R}_n = \mathbf{r}_1 + \mathbf{r}_2 + \mathbf{r}_3 + ... + \mathbf{r}_n \quad \text{and} \tag{5.19}$$

$$\sqrt{\langle\mathbf{R}^2\rangle}_n = \left\langle \left( \sum_{i=1}^{n} \mathbf{r}_i \right)^2 \right\rangle^{1/2} = \left( \sum_{\alpha=1}^{n} \sum_{\beta=1}^{n} \langle \mathbf{r}_\alpha \cdot \mathbf{r}_\beta \rangle \right)^{1/2} . \tag{5.20}$$

The average distance traveled between two scattering centres is simply $\langle r_i\rangle = \lambda_S$, and $\langle r_i^2\rangle = 2\lambda_S^2$. For $\alpha \neq \beta$ the $\langle \mathbf{r}_\alpha \cdot \mathbf{r}_\beta \rangle$ factor is determined using the fact that, for photons that undergo multiple scattering on particles which exhibit isotropic scattering properties in the azimuthal plane perpendicular to the direction of the incident photon, the average cosine $\langle cos\theta\rangle_i$ of the light field from a thin narrow parallel beam after $i$ scattering events is given by [33, 70]

$$\langle cos\theta\rangle_i = \langle cos\theta\rangle^i \quad \text{yielding} \quad \langle \mathbf{r}_\alpha \cdot \mathbf{r}_{\alpha+i} \rangle = \lambda_S^2 \times (\delta_{0,i} + \langle\cos\theta\rangle^i), \tag{5.21}$$

where $\delta_{0,i}$ is a Kronecker delta function. Using Eq. 5.21, Eq. 5.20 can be written in terms of $\lambda_S$ and $\langle\cos\theta\rangle$ [33]

$$\sqrt{\langle\mathbf{R}^2\rangle}_n \approx \lambda_S \times \left( 2 \sum_{k=0}^{n-1} (n-k) \langle\cos\theta\rangle^k \right)^{1/2} \tag{5.22}$$

$$= \lambda_S \times \left( 2n \times \frac{(1 - \langle\cos\theta\rangle) + (\langle\cos\theta\rangle^{n+1} - \langle\cos\theta\rangle)/n}{(1 - \langle\cos\theta\rangle)^2} \right)^{1/2} , \tag{5.23}$$

with the implicit assumption in deriving Eq. 5.22 from Eq. 5.20 that the average distance $\langle \boldsymbol{r}_n \rangle$ between the last scattering centre and the detector can be approximated by $\lambda_S$. In general, this assumption will be valid if the average path length $d(R) = \langle n(R)\rangle \times \lambda_S$ traveled by the photons between their point of emission (the origin of $\boldsymbol{R}$) and their point of detection (the end point of $\boldsymbol{R}$) is much larger than $\lambda_S$.

In the limit where the number of scatterings is very large, Eq. 5.23 can be written as

$$\sqrt{\langle \mathbf{R}^2 \rangle}_n \approx \left( \frac{2\ n\ \lambda_S^2}{1 - \langle \cos\theta \rangle} \right)^{1/2} \approx \left( \frac{2\ d(R)\ \lambda_S}{1 - \langle \cos\theta \rangle} \right)^{1/2}, \tag{5.24}$$

with a degeneracy in $\lambda_S/(1 - \langle cos\theta \rangle)$, which for LCs leads to the definition of the effective LC scattering length

$$\lambda_{LC}^E \equiv \frac{\lambda_{LC}}{1 - \langle \cos\theta \rangle_{LC}}. \tag{5.25}$$

This degeneracy makes the distinction between LC scattering lengths and $\langle \cos\theta \rangle_{LC}$ impossible. As an example, for the above approximation to be valid at the 1% level, the average number of scatterings must be larger than ~100 for $\langle \cos\theta \rangle \lesssim 0.5$.

An independent approach described in [44] derives, from Eq. 5.22[6], the average time taken by a photon to reach a detector at distance $R = |\mathbf{R}|$ from the source for the limit $\langle cos\theta \rangle \to 1$:

$$t(R) = \frac{d(R)}{v_g} \approx \frac{R}{v_g} \left( 1 + \frac{R}{3\lambda_S} (1 - \langle cos\theta \rangle) \right)^{1/2}, \tag{5.26}$$

where $v_g$ is the group velocity, yielding again the degeneracy in the effective scattering length.

However, when the number of scatterings is relatively small and $\langle cos\theta \rangle$ is much smaller than 1, the assumptions in the derivation of Eq. 5.24 and Eq. 5.26 break down and this degeneracy should disappear. Confirmation of this theory is shown in Figure 5.9, which shows the ratio of two spectra with identical $\lambda_{LC}^E$, once comparing two very forward-peaked angular distributions and once comparing a forward-peaked distribution with one having a much smaller $\langle \cos\theta \rangle_{LC}$ (and a small $n$): a complete degeneracy between identical effective LC scattering lengths occurs at very forward-peaked scattering angular distributions of LC, whilst for less forward-peaked distributions and a small number of scatterings this degeneracy is non-existent.

For the reconstruction of muons, where the number of photons arriving within a small time interval of the arrival time of direct photons is most important, it will become self-evident (from the results obtained in Chapter 6) that the effective scattering length is not a good parameter to describe the scattering properties of the ANTARES detector medium.

## 5.5 Summary

In this chapter, the MC algorithm developed to simulate the Test 3′ experiment was described. It was shown that the direct simulation was too time consuming and an alternative was therefore developed to yield much larger MC statistics per CPU time

[6] Notice the factor of "2" missing for the first "$n$" in their Eq. 7.

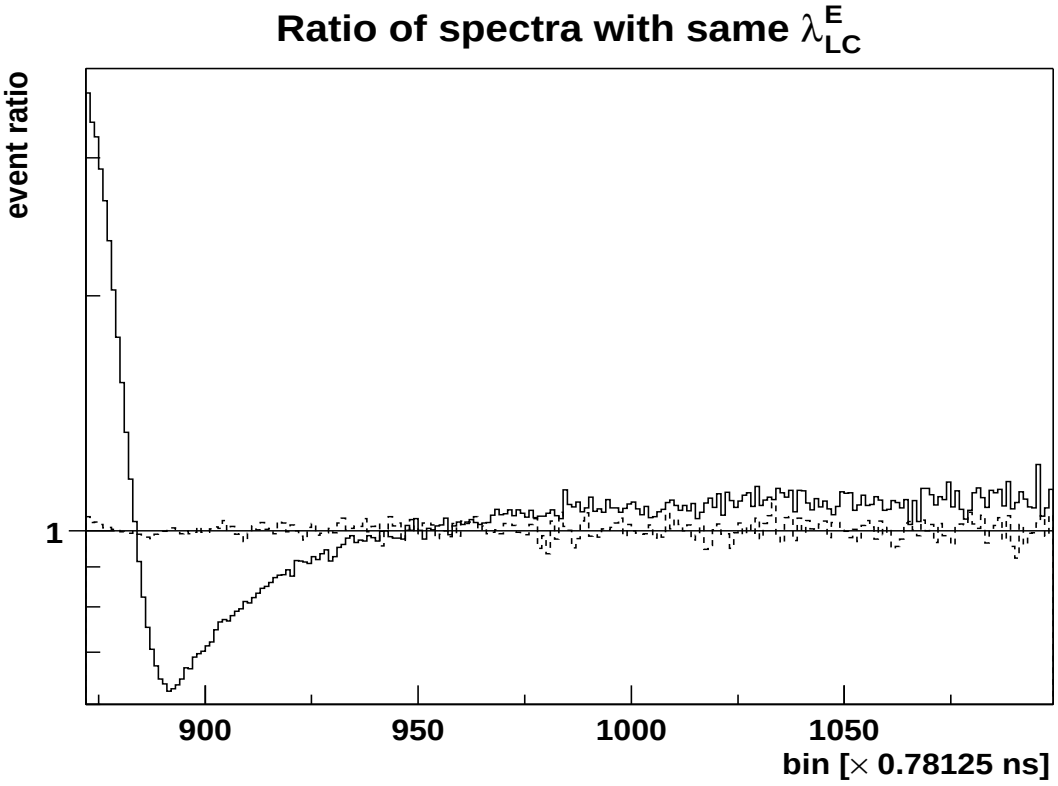


**Figure 5.9:** *Solid histogram: ratio of two MC spectra with identical effective LC scattering lengths, one with* $\langle\cos\theta\rangle_{LC} = 0.9$ *and the other with* $\langle\cos\theta\rangle_{LC} = 0.5$ *(and a small number of scatterings). Dotted histogram: ratio between two spectra with identical effective LC scattering lengths, one with* $\langle\cos\theta\rangle_{LC} = 0.98$ *and one with* $\langle\cos\theta\rangle_{LC} = 0.90$.

(Sections 5.2.1 and 5.2.2). The corrections applied to the MC simulations were then given (Section 5.2.3). A wide range of water models were scanned and a selected set was used to produce a data base of MC simulations (Section 5.3). A comparison of the spectral shapes of water models as a function of each of the optical parameters was then made, showing the sensitivity of Test 3′ to the different optical parameters (Section 5.4). The effective scattering length was defined and the reason for the degeneracy between some $\lambda_{LC}$ and $\langle\cos\theta\rangle_{LC}$ was explained.

# Chapter 6

# Analysis and Results

This chapter details the method used in the analysis of the Test 3′ data. The results of this analysis are presented for data of two different seasons and various systematic errors are identified and quantified via appropriate MC simulations. The correlations between the optical parameters are analysed. Data at two different depths are then compared.

*There is inherent in nature a hidden harmony that reflects itself in our minds under the image of simple mathematical laws. That then is the reason why events in nature are predictable by a combination of observation and mathematical analysis. Again and again in the history of physics this conviction, or should I say this dream, of harmony in nature has found fulfillments beyond our expectations.*

*H. Weyl (1885-1955)*

## 6.1 The Method

The analysis method of the optical properties at the ANTARES site is based upon the comparison of the shapes of the photon arrival time distributions of the Test 3′ data (TD) and of MC simulations (MTD$^{\omega}$)[1] with different input parameter combinations $\omega = (\lambda_A, \lambda_{LC}, \lambda_{SC}, \langle cos\theta \rangle_{LC}, t_o)$, referred to as (water) models. Many MC simulations are generated to explore the parameter space within the range of models relevant for the ANTARES Test 3′ data, yielding a data base of water models. The range and step size of the various parameters (including the electronics time offset) were chosen after several iterations, such that the best fit values were not on either extreme of the range.

[1] For each MTD 20M photons were generated.

Each MTD spectrum is corrected for the single-hit nature of the TDC, yielding a spectrum given by $S_{TDC}$ (Eq. 5.18, p. 73). The data are first corrected for the unequal bin widths of the TDC (Section 4.2), the background noise is then subtracted (Section 4.3) and the statistical errors from these processes are calculated (Section 4.4). The $\chi^2$ test, defined by

$$\chi^2_{d_1}(\omega) = \sum_i \left( \frac{\left[ TD_{d_1}(i) - \eta_{d_1}(\omega) \times MTD^{\omega}_{d_1}(i) \right]^2}{\sigma^2_{TD_{d_1}}(i) + \eta^2_{d_1}(\omega) \times \sigma^2_{MTD^{\omega}_{d_1}}(i)} \right), \tag{6.1}$$

was used to compare each MTD from the data base to the data $TD_{d_1}$, where $d_1$ is the source-detector distance for the data to be analysed and the sum is over all bins $i$ of the data, with a normalisation factor $\eta_{d_1}(\omega)$ for the MTDs (described in the next section). The errors $\sigma_{TD_{d_1}}(i)$ on the number of entries in each bin of the data and $\sigma_{MTD^{\omega}_{d_1}}(i)$ of the MTDs are assumed to be Gaussian distributed. For this to be valid, the minimum number of events per bin was required to be larger than ten. Failing that, the bin was grouped with adjacent bins until this minimum was reached. The propagation of errors when re-binning the MTD according to the binning of the data was taken into account. The $\chi^2$ was defined with errors for both the data and the MTDs because these latter have limited statistics, making it necessary to include these errors in the calculations of the $\chi^2$ [68].

Amongst all the water models, the MTD which gives the minimum $\chi^2$ to within the MC statistics yields the best water model.

### Normalisation of the Monte Carlo Simulations

The absolute number of photons emitted by the light source is not known. However, it is the same (within 2% [71]) for the measurements taken at two different distances. The ratio of the number of photons at the two distances yields an effective absorption length (as described in Section 6.2), assuming that it remains constant over the period of about 4 hours[2] between the two measurements[3]. Exploiting the fact that the effective absorption length (i.e. the ratio of the number of photons at two distances) of the MC simulations must be the same as that of the data, a normalisation factor for the MCs could be obtained.

The MC is given the same probability $f$ of detecting a photon as the data at the fitted distance, yielding the spectrum given by Eq. 5.18 (p. 73). This is needed to be able to fit the shape as well as the normalisation. To normalise the MC to the data at the reference distance $d_2$, the number of photons arriving at the PMT determined only by the

[2]For the Year 2000 data, the measurements at two distances were taken 3 days apart due to bad weather conditions.

[3]This is a reasonable assumption given that the effective absorption length only depends upon the total number of counts at each distance. These were found to be consistent between several measurements at the same distance to within the systematic errors of the background-noise subtraction. There was therefore no reason to assume that it would vary significantly within the four hours between the immersions at two different distances.

optical properties of the water (i.e. not influenced by the single-hit effect of the TDC) is compared in both cases. For the MC this is simply the sum over all bins of $S^{\omega}_{true}(d_2)$ (Eq. 5.13, p. 72), the original MTD at distance $d_2$, not corrected for the single-hit effect of the TDC. For the data it is $\mu^D_{d_2} \times N_{trig}$, where the mean number of photons $\mu^D_{d_2}$ arriving at the PMT at distance $d_2$ is calculated using Eq. 5.12 (p. 72) together with the values of $f$ for $d_2$, given in the last column of Table 3.2 (p. 48) and Table 3.3 (p. 49).

Each $\mathrm{MTD}^{\omega}_{\mathrm{d_1}}$ used in the analysis of the data at distance $d_1$ is then normalised with the factor $\eta_{d_1}(\omega)$ of Eq. 6.1 given by

$$\eta_{d_1}(\omega) = \frac{\mu^D_{d_2} \times N_{trig}}{\sum S^{\omega}_{true}(d_2)} \times \frac{d_2^2}{d_1^2}, \tag{6.2}$$

where the factor $d_2^2/d_1^2$ takes into account the fact that the solid angle in the experiment varies between the two distances, whilst in the MC simulations it does not because the detector covers the total solid angle at both distances (see Section 5.2.1). The systematic errors resulting from this normalisation factor are discussed in Section 6.3.4.

## 6.2 Water Model Independent Parameters

Independent of the model used for the propagation of the photons in the water, the Test 3′ data can be used to extract an effective absorption length and an average background-noise rate for each file.

### 6.2.1 Effective Absorption

For Test 3′, which uses an isotropic light source, the ratio of the number of hits at two different distances gives an effective absorption length $\lambda^E_A$. This $\lambda^E_A$ is specific to the experimental setup of Test 3′, where on average for each photon scattered away from the direction to the detector another will scatter into the direction of the detector. The increased path length due to the scattering however increases the probability of absorption, hence the name "effective" absorption length which, for an isotropic source, can be defined as

$$N(d) = \frac{N_o}{4\pi d^2} \times e^{-d/\lambda^E_A}, \tag{6.3}$$

where $N_o$ is the number of emitted photons. Using the ratio of the number of counts at two different distances (corrected for the single-hit nature of the TDC), the effective absorption length can be calculated as

$$\lambda^E_A = \frac{d_2 - d_1}{ln\left(\frac{N_1 d_1^2}{N_2 d_2^2}\right)} \qquad \text{with} \qquad \frac{N_1}{N_2} = \frac{\mu_1}{\mu_2} = \frac{ln(1-f_1)}{ln(1-f_2)}, \tag{6.4}$$

| *Immersion* | $\lambda_A^E$ [m] |
|---|---|
| July 1999 (UV) | $20.9 \pm 0.2$ (stat.) $\pm^{1.1}_{1.0}$ (syst.) |
| Sept. 1999 (UV) | $21.8 \pm 0.1$ (stat.) $\pm^{0.7}_{0.5}$ (syst.) |
| June 2000 (UV) | $25.2 \pm 0.1$ (stat.) $\pm^{0.8}_{0.6}$ (syst.) |
| June 2000 (blue) | $46.0 \pm 0.4$ (stat.) $\pm^{2.4}_{2.0}$ (syst.) |

**Table 6.1:** *The effective absorption length calculated from the Test 3′ data. The first error corresponds to the statistical error. The systematic error (shown as the second error) was calculated by assuming a 2%[71] variation in the LED intensity between the runs at two distances as well as a 2.15% error on the source-detector distance (see Section 6.3.4), in addition to the error on the normalisation from the background-noise subtraction.*

where $\mu$ is the same as in Section 5.2.3 and the $f$s are given in Table 3.2 (p. 48) and Table 3.3 (p.49).

The results for the various immersions are given in Table 6.1. The effective absorption length in the UV is much shorter than the one in the blue. This was to be expected given that the intrinsic absorption by water in the UV is much larger than in the blue. Whilst the results between the July and September immersions in the Year 1999 are in agreement with each other to within the errors, the data from the Year 2000 immersions show an increase in the effective absorption length (being larger than the September 1999 data at the $4\sigma$-level). This could be due to a decrease in the concentration of particulate absorbers in the water or due to a decreased amount of scattering centres, causing the photons to travel on average smaller distances before reaching the detector and decreasing therefore their probability of being absorbed.

Current measurements at different seasons suggest that variations can occur at least on the time scale of the order of one month. The impacts of such variations upon the muon reconstruction were discussed qualitatively in Section 1.2. Additional measurements on a much smaller time scale, together with a detailed evaluation (with MC simulations) of the impacts of the variation of the absorption length upon the performance of the ANTARES detector, are however needed to be able to make any predictions about the required frequency of the measurements for the calibration of the detector.

### 6.2.2 Background Noise: $^{40}K$ and the Excitement of Flashing Creatures

Two main sources of photons contribute to the optical background in the water. The first contribution is from photons resulting from the radio-active decay of potassium-40 ($^{40}K$):

$$^{40}K \rightarrow {}^{40}Ca + e^- + \overline{\nu}_e \qquad (\beta \text{ decay}) \tag{6.5}$$

$$^{40}K \rightarrow {}^{40}Ar^* \ (+e^+ + \nu_e) \rightarrow {}^{40}Ar + \gamma \qquad \text{(electron capture)}. \tag{6.6}$$

In both of these modes, electrons are produced with sufficient energy to yield Cherenkov

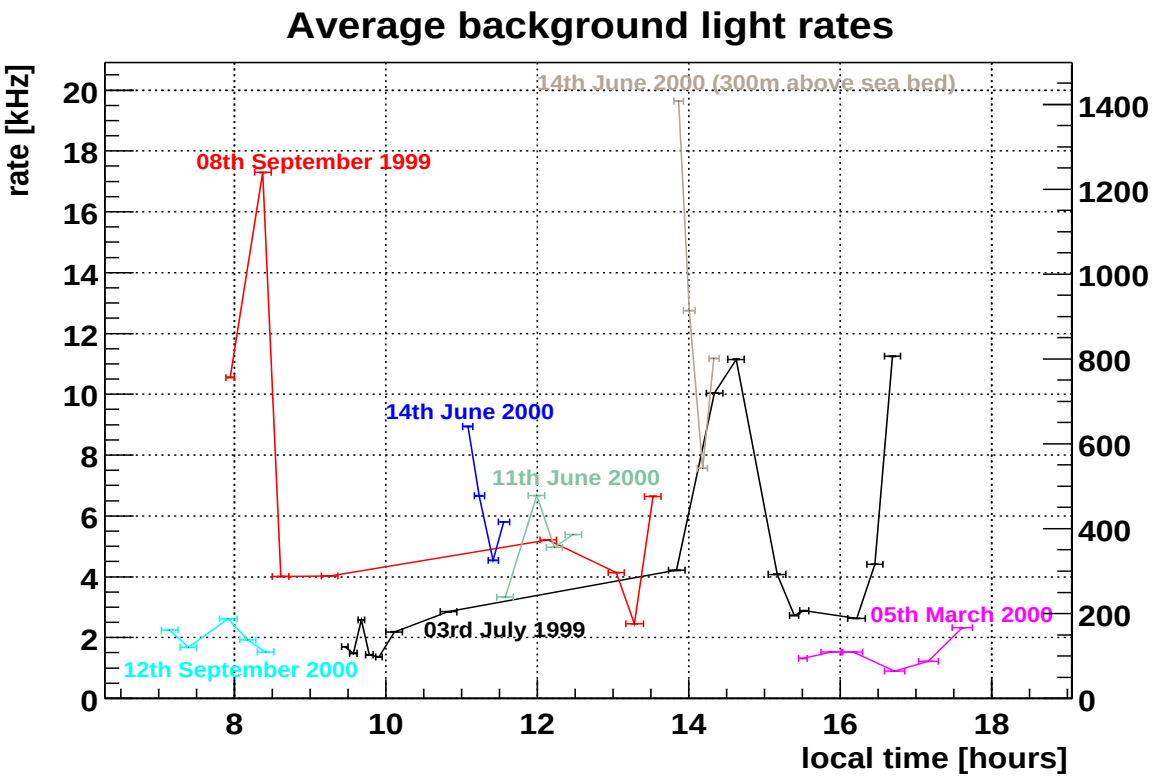


**Figure 6.1:** *Measured background-noise rates at the ANTARES site, averaged over several minutes. The left and right y-axis scales correspond to the rates using a 30 mm ETL PMT and a 10″ PMT of the type used for the ANTARES detector respectively.*

photons in the water, creating a continuous optical background. The second contribution is from bioluminescent organisms. In addition to producing large variations in the number of background photons, they contribute to the continuous optical background. ANTARES has devised special experiments which are devoted to measuring the background noise [72, 73, 74] and monitoring the variations continuously.

From the data of Test 3′ described in this thesis, the background-noise rate averaged over the duration of each experimental run (typically between 5 and 17 minutes) can be determined from the average number of hits recorded per unit time in the region prior to the LED signal, using the results from the fit to the background noise (Eq. 4.7, p. 59) after correcting for the single-hit nature of the TDC. For a total number of triggers $N_T$, the average rate is simply given by:

$$R = \frac{R'}{N_T}. \tag{6.7}$$

Figure 6.1 shows the variation of the average background-noise rate for the various immersions with Test 3′ at the ANTARES site. The background rates are strongly variable. This is because, in addition to the flat background-noise rate from $^{40}K$ decays, background photons are also emitted when bacteria or other micro-organisms are “excited” by

various unknown environmental factors (though a strong correlation was found between the bioluminescence rate and the speed of the currents in the waters in [74], Figure 4) and emit more photons than usual. Results of other measurements at the ANTARES site yield a baseline background rate of ∼60 kHz for a 10″ PMT, in approximate agreement with the lowest observed background rate at the ANTARES site with the measurements of Test 3′ (with a 30 mm PMT).

Whilst large variations in the average background-noise rate can be observed, no direct correlation with either the time of the day or the season can be distinguished from these data. The correction for this background noise was done for each spectrum, as described in Section 4.3. The systematic errors resulting from this background-noise subtraction are investigated in Section 6.3.3.

## 6.3 Data Analysis: UV (374.5 nm) September 1999 Immersions

The data acquired during the immersions in September 1999 are the best available data in the UV, because the longer two (24 m and 44 m) of three distances between the source and the detector were used for the immersions (compared to 15 m and 24 m for the July 1999 data) and because of the larger statistics. The data were first shown to be incompatible with a model of very clear waters without any LCs (Section 6.3.1). The individual files of a set acquired during one immersion were then compared and found to be consistent with each other (Section 6.3.2). The various data at one distance were then added and each distance was analysed separately (Section 6.3.3). The results from both distances were found to be compatible and the data at the two distances were then analysed together to increase the sensitivity of the experiment.

### 6.3.1 Analysis Hypothesis: Purest Water?

As discussed in Chapter 2, various interaction centres contribute to the scattering and absorption of light. Under the assumption that the water is very clear and that the effect of the very forward-peaked scattering due to the turbulence-induced fluctuations in the real index of refraction is negligible (i.e. the density of LC scatterers is approximately zero), the water properties are determined by absorption and SC scattering processes only. Figure 6.2 shows the best fit curves using such a model.

The difference in shape between the two spectra is evident and is strongly reflected in the $\chi^2$ value (see Figure 6.2), larger than the best model found in the subsequent analysis by ∼200 and incompatible with a valid model ($\chi^2/df \sim 1$) at more than 99% confidence level. Therefore, a model in which only SC scatterers and absorbers are present in the water cannot describe the optical properties of the water at the ANTARES site. To account for the difference in the shape of the peak region, another component, which causes on average a smaller increase in the path length of the photons than SC scattering, must be present. Scattering centres with a more forward-peaked scattering angular distribution

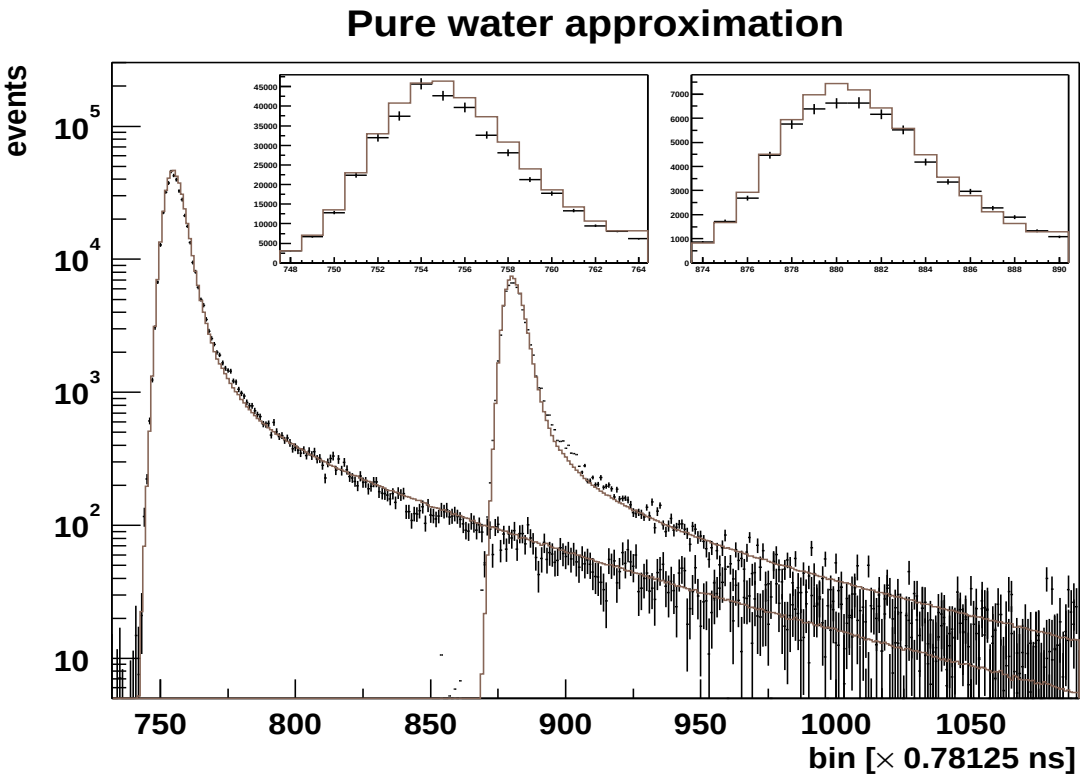


**Figure 6.2:** *Two sets of data taken with a source-detector separation of 24 m (left curve) and 44 m (right curve). The best fits describing the medium with only SC scatterers and an absorption probability are shown as light curves. The insets show the finer details in the peak region of the spectra for the 24 m (left inset) and the 44 m (right inset) data respectively. The best fit to the data at 24 m yields a $\chi^2/df$ ∼582/344 and at 44 m a $\chi^2/df$ ∼500/219.*

would have the desired effect. From the discussions in Section 2.3.2, such centres must be larger in size than SCs and thus belong to the domain of LC scattering.

### 6.3.2 Variations Between Individual Acquisitions?

Initially, all files were treated (as described in Chapter 4) and analysed individually to look for possible variations in the optical properties between measurements. The results did not show any variations (to within the statistical errors) between these measurements (taken typically at 20 minutes time intervals). To increase the statistics, the individual raw data of a set were therefore added and the final analysis was performed on the combined data files for each distance.

### 6.3.3 Analysis of Combined Data

Figure 6.3 shows a typical set of figures of the minimum $\chi^2$, as a function of each of the four physical parameters, for the combined data files at 24 m and at 44 m of the September 1999 immersions, analysed with MC simulations each generated with 20M photons (from

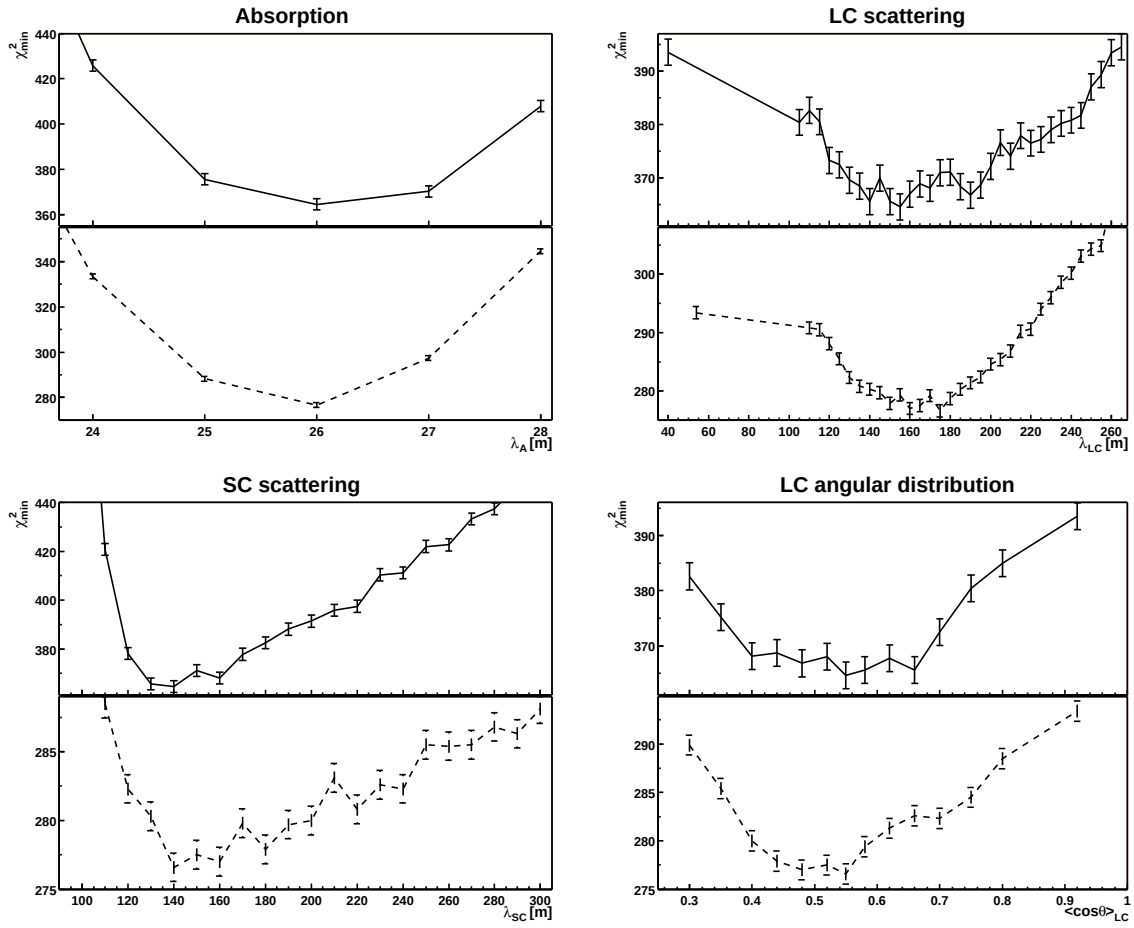


**Figure 6.3:** *Minimum $\chi^2$ as a function of each of the four optical parameters describing the ANTARES medium. Each point corresponds to the minimum $\chi^2$ for the selected value of the parameter when varying all other parameters. The solid lines correspond to the 24 m data and the dashed lines to the 44 m data.*

now on also referred to as "low-statistics" MCs). The $\chi^2$ was calculated using the method described in Section 6.1. Each point on these plots corresponds to the minimum $\chi^2$ for the selected value of the parameter when varying all the other parameters. The error bars reflect the spread in $\chi^2$ values due to the limited MC statistics. This will be described in further detail later in this section.

Around the minimum, the $\chi^2$ is fairly symmetric for all parameters except for $\lambda_{SC}$, for which the experiment is much better at setting a lower limit than an upper limit. The absorption length is very well determined: this was to be expected since it is mainly determined by the effective absorption length (given in Section 6.2). Perhaps counter-intuitively, the $\chi^2$ does not continue to rise indefinitely towards smaller values of $\lambda_{LC}$. This is due to the degeneracy between water models with the same effective LC scattering lengths (as described in Section 5.4), which causes the $\chi^2$ to flatten. This degeneracy depends (amongst others) upon the distance traveled by the photon and causes this degeneracy to be more complete the longer this distance. This can be seen as a flatter $\chi^2$

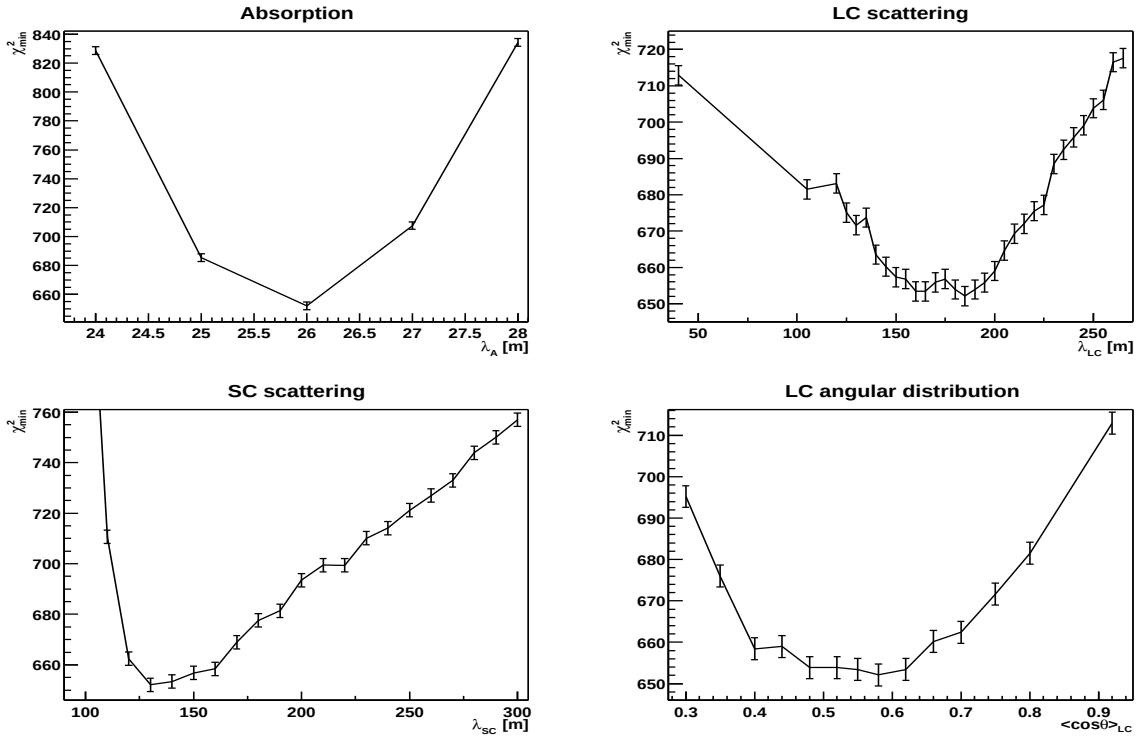


**Figure 6.4:** *Variation of $\chi^2_{min}$ (obtained as described in the caption of Figure 6.3) calculated with the low-statistics MC models with respect to $\lambda_A$, $\lambda_{SC}$, $\lambda_{LC}$ and $\langle\cos\theta\rangle_{LC}$ for the average between the data at the two distances taken in September 1999.*

towards small $\lambda_{LC}$ at 44 m compared to 24 m. The same effect is expected for values of $\langle\cos\theta\rangle_{LC}$ close to 1.

The data from both distances give consistent results for all parameters. Therefore, to obtain an overall average result for the immersions of one season, the curves of the two distances were fitted together simply by adding the $\chi^2$ of each water model between the two distances. These results are shown in Figure 6.4. As expected, combining the information about the optical properties from two different distances yields even better constrained minima.

The main limitation in the usefulness of these $\chi^2$ curves is evidently the jitter, which is the direct result of the limited statistics of the MC simulations (as described in Appendix D), yielding a spread of $\sim$2.5 and $\sim$1 in the $\chi^2$ (with the low-statistics MCs at 24 m and 44 m respectively) for a same water model but different seeds for the random number generator. This spread disappears in the limit of infinite MC statistics, when the MC distribution behaves like a function. Huge computing times however precluded the simulation of much larger statistics for the originally selected range of models. In order to obtain an absolute best model without simply having chosen a model whose $\chi^2$ has fluctuated downwards the most amongst the fluctuations, the statistics of the MCs must nonetheless be much larger yet! However, it is only necessary to run those models that

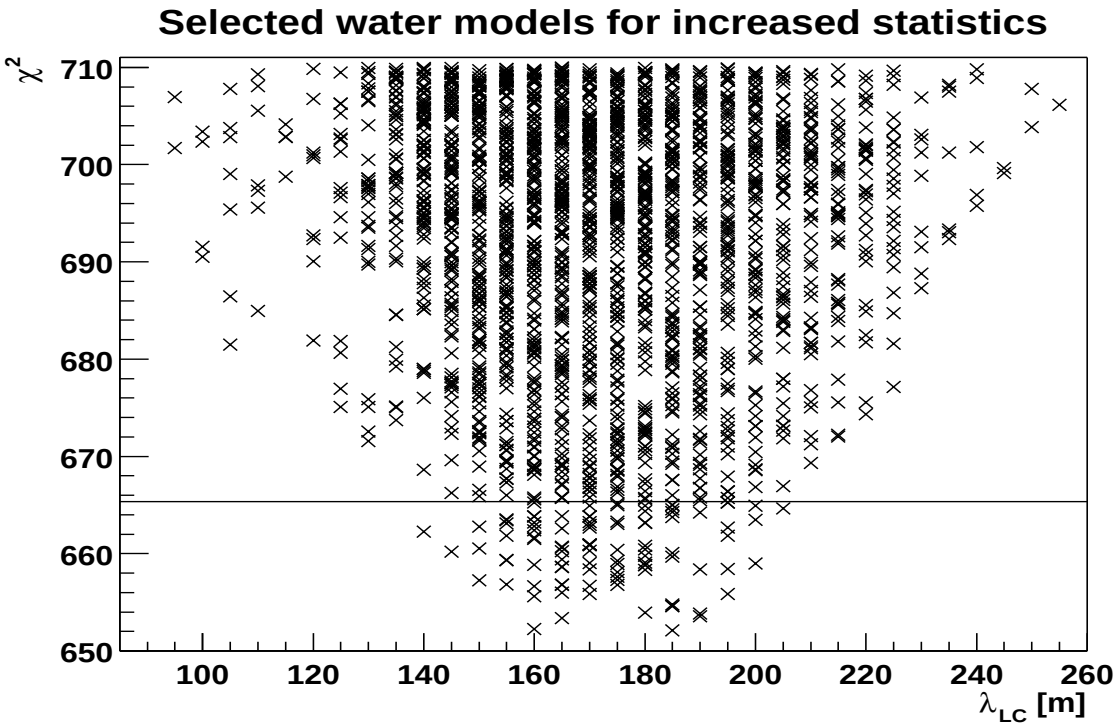


**Figure 6.5:** *Scatter plot of the water models as a function of $\lambda_{LC}$. The water models below the horizontal line are within 5 times the $\chi^2$ spread of the minimum and were used to generate much higher statistics (800M and 400M for the 24 m and 44 m data respectively) MCs to reduce the $\chi^2$ spread below 0.5.*

are close to the actual minimum (obtained with the low-statistics MCs) with much larger statistics, since all other water models can be excluded. The choice of "good" models which require larger statistics is (of course) determined by the spread of the $\chi^2$ around the minimum.

To determine the spread due to the limited MC statistics at the best water model, a set of 200 MC simulations were run with the same water model but different seeds for the random number generator. The $\chi^2$ for each of these simulations was calculated, yielding a histogram of $\chi^2$ similar to the one shown in Figure D.1 (p. 136). The spread was taken as the root mean square deviation of the fit of a Gaussian function to the histogram. This spread was found to be very similar for a random selection of models close to the minimum and was therefore only calculated for the minimum and taken to be the same for all other models in Figures 6.3 and 6.4.

The models contained within 5 times the spread of the minimum $\chi^2$ were simulated with much larger statistics. A typical scatter plot is shown in Figure 6.5, where all models below the horizontal line satisfy this criterium. It should be noted that each of the points in Figure 6.5 corresponds to a given water model and the choice of parameter on the x-axis is irrelevant, $\lambda_{LC}$ having been chosen only as an example. For each of these models 800M (resp. 400M) photons were propagated for the 24 m (resp. 44 m) data, reducing

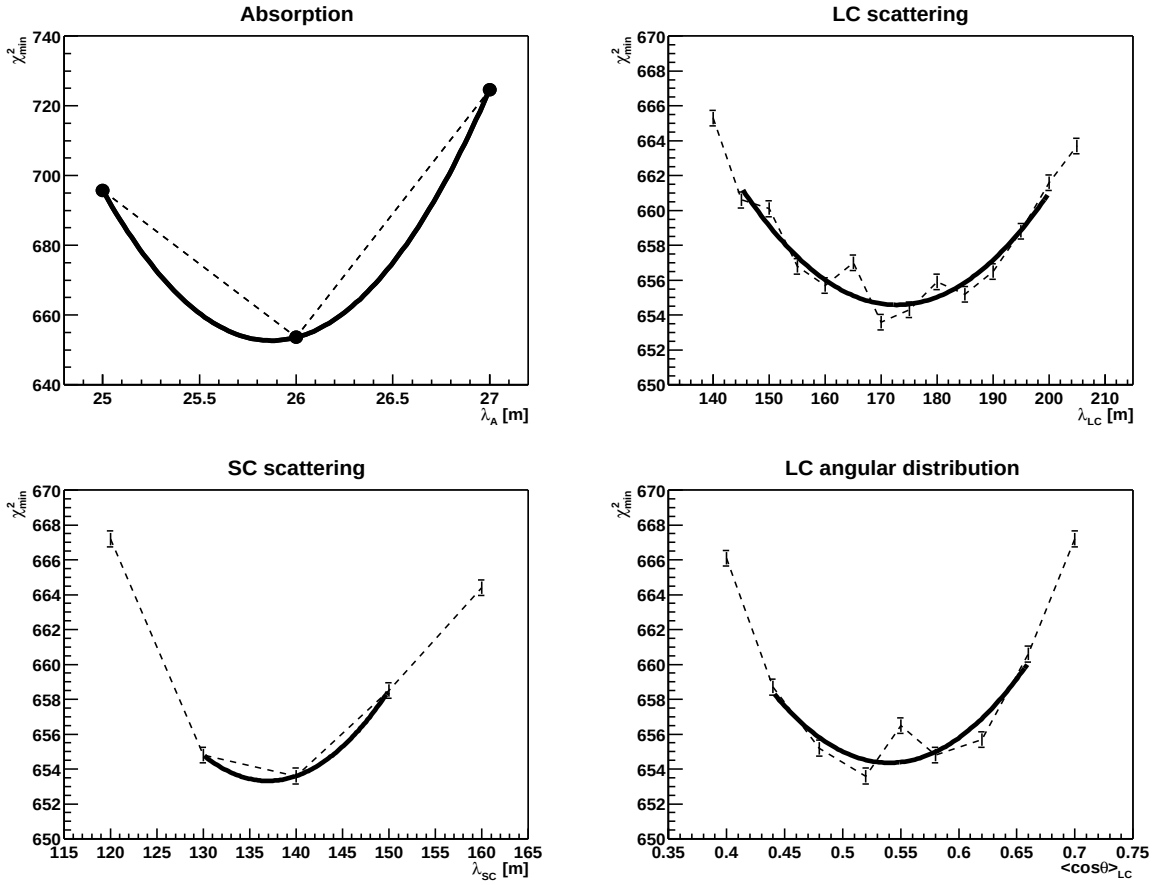


**Figure 6.6:** *Variation of $\chi^2_{min}$ (obtained as described in the caption of Figure 6.3) calculated with the high-statistics MC models for the average data between the two distances taken in September 1999. On the top left plot, the $\chi^2$ spread is smaller than the size of the dots. The solid line is a second order polynomial fit to the data at the minimum.*

the spread on the $\chi^2$ around the minimum to $\sim$0.4 (resp. $\sim$0.2). Figure 6.6 shows the $\chi^2$ curves for the combined data for this improved statistics. The jitter is now much smaller, although even with the much larger statistics it is still not small enough to justify the choice of the model yielding the minimum $\chi^2$ as the best model. However, at the minimum the $\chi^2$ function can be approximated by a second order polynomial. The best fits of such a polynomial are shown as solid curves in Figure 6.6.

The fit to the absorption length is clearly limited by the step size in the parameter and $\lambda_A$ can therefore only be determined to within half a step size. The same applies for $\lambda_{SC}$. The fits to $\lambda_{LC}$ and $\langle\cos\theta\rangle_{LC}$ are evidently good approximations to the real shape of the minimum $\chi^2$. The minimum of all these fits were used to yield the best value for each parameter. This value is slightly dependent upon the range used in the fits and introduces a systematic error into the results. The fits were therefore performed over various ranges around the minimum and the average value of the two extremes was chosen as the best value. The systematic error due to the choice of fit range was then

| | 24 m | 44 m | "24 m + 44 m combined" |
|---|---|---|---|
| $\lambda_A$ | $26.1(\pm 0.0)\pm 0.5\pm^{0.5}_{0.5}$ | $25.9(\pm 0.0)\pm 0.5\pm^{0.5}_{0.5}$ | $25.9(\pm 0.0)\pm 0.5\pm^{0.5}_{0.5}$ |
| $\lambda_{SC}$ | $137(\pm 2)\pm 8\pm^{6}_{5}$ | $148(\pm 1)\pm 15\pm^{18}_{14}$ | $137(\pm 1)\pm 6\pm^{6}_{5}$ |
| $\lambda_{LC}$ | $160(\pm 2)\pm 15\pm^{6}_{3}$ | $165(\pm 0)\pm 16\pm^{7}_{7}$ | $173(\pm 1)\pm 10\pm^{3}_{3}$ |
| $\langle cos\theta \rangle_{LC}$ | $0.56(\pm 0.02)\pm 0.07\pm^{0.05}_{0.03}$ | $0.51(\pm 0.02)\pm 0.06\pm^{0.06}_{0.02}$ | $0.54(\pm 0.02)\pm 0.05\pm^{0.02}_{0.02}$ |

**Table 6.2:** *Analysis results of the ANTARES medium optical properties in the UV (374.5 nm), September 1999 immersions; $\chi^2_{min}/df$ ∼365/344 (24 m), ∼277/219 (44 m) and ∼654/569 (for the combined data). The values in parentheses correspond to the systematic errors from the choice of the fit range of a second order polynomial to the minimum (see text). The first of the remaining two values are the statistical errors at 68% confidence level and the second ones correspond to the systematic errors due to the background-noise subtraction.*

taken as the difference between this central value and the extreme values and is shown in parenthesis in Table 6.2. The statistical errors were calculated by incrementing the minimum $\chi^2$ by 1 and calculating the resulting change in each parameter value. If this change was larger than half of the step size between the water models, it was used as the statistical error. Failing that, the statistical error was conservatively taken as half a step size.

The above analysis was done for the best fit to the background-noise subtraction (as described in Section 4.3). To quantify the systematic errors from the background-noise subtraction, the analysis was repeated for the data of Eqs. 4.15 and 4.16 (p. 60). Again various ranges for the fit to the minimum $\chi^2$ were used and the maximum difference with the best fit parameter values obtained previously (with the best fit to the background noise, Eq. 4.14) was used as a conservative estimate of the systematic errors due to the background-noise subtraction.

The results from this analysis are given in Table 6.2 and the plots of the MC simulations of the best water model are shown in Figure 6.7. The optical parameters extracted for each of the two distances are all in very good agreement with each other. The error due to the choice of fit range is much smaller than the statistical error in all cases and the actual minimum is thus known very accurately. Contrary to the expectation that a longer distance would reveal finer details about the optical properties, the 24 m data yield slightly better constrained parameters. This can be attributed to the fact that the 24 m spectrum contains 5 times more events than the 44 m spectrum. The shapes of the MTDs of the best water model are evidently very good approximations to the data (and much better than those shown in Figure 6.2 (p. 87), where LC scattering was neglected),

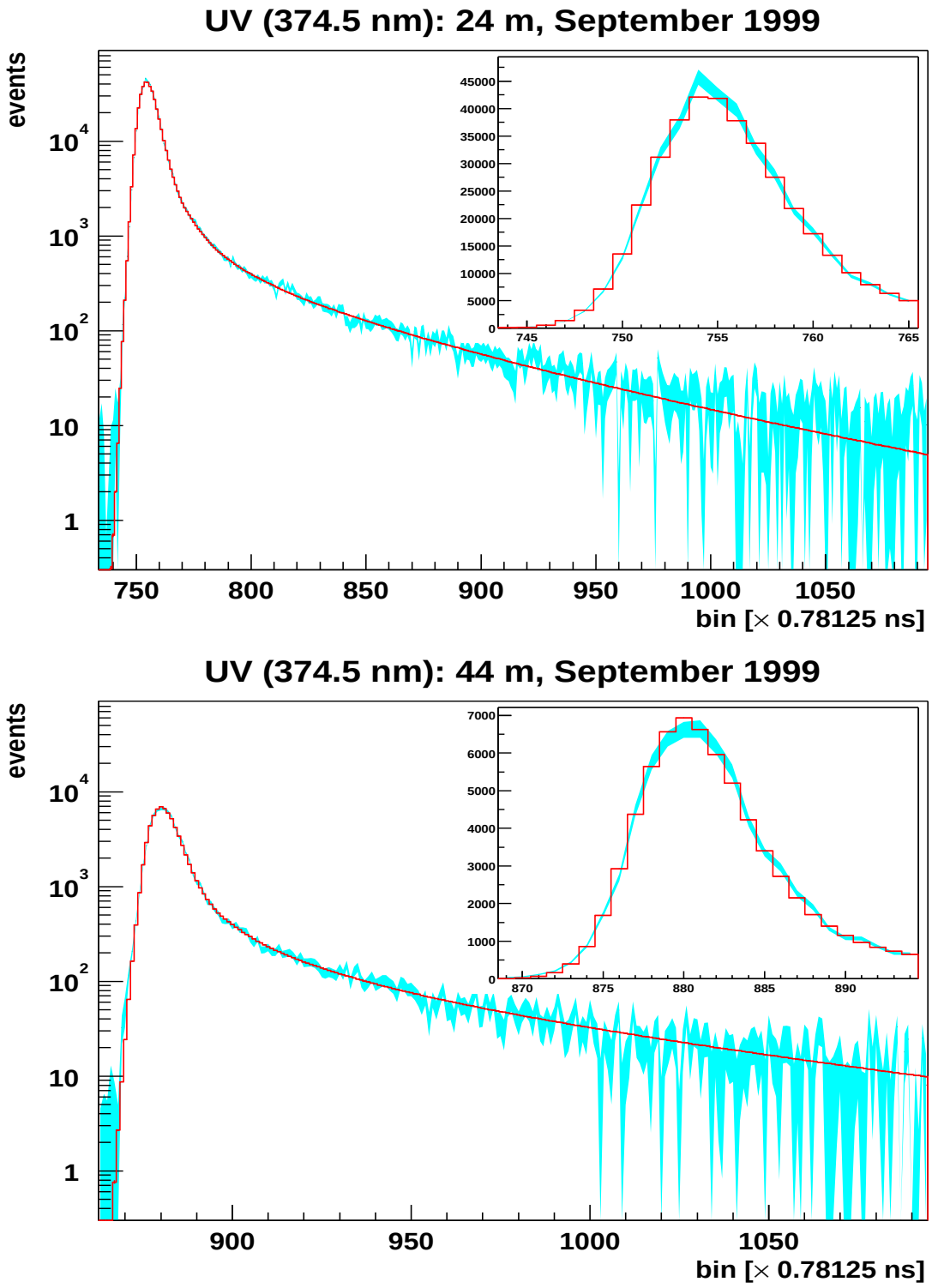


**Figure 6.7:** *September 1999 immersions (with a LED-driver voltage of 5.80 V): shown are the data (grey band) and the best fit MC simulation (histogram) normalised as described in Section 6.1. The statistical errors of the data are shown by the width of the bands. The statistical errors of the MC simulations are too small to be visible.*

which shows that the model chosen in Section 2.7 describes the water optical properties at the ANTARES site extremely well.

### 6.3.4 Systematic Uncertainties

In addition to the errors given in Table 6.2, it is necessary to understand any potential sources of systematic errors arising from the analysis method and various unknown factors about the experiment. These are investigated and quantified in detail in this section.

#### A. Analysis Method

In order to check the analysis method, a number of experiment-equivalent MC data (with similar statistics) were generated (from now on referred to as generated data or GD) for the best water model and analysed with the same MC simulations as the experimental data. To create the GD, a high-statistics ($8 \times 10^8$ events) MC was first generated for each of the two distances. The simulation at the distance to be analysed was then normalised to the total number of events in the experimental data and the simulation at the reference distance was rescaled by the same factor. To simulate the appropriate statistical fluctuations of the data, the number of hits in each bin of the GD was obtained by drawing a random number from a Poisson distribution using the mean value of each bin[4].

Eq. 6.1 (p. 82) was used to calculate the $\chi^2$ for each MTD, replacing the $\mathrm{TD}_{\mathrm{d}_1}$ by $\mathrm{GD}^{\omega}_{\mathrm{d}_1}$ with known optical parameters and using Eq. 6.2 (p. 83) to normalise the MTD, excluding the $d_2^2/d_1^2$ factor which was already taken care of in the generation of the GDs. Figure 6.8 shows a typical plot for the minimum $\chi^2$ values obtained as a function of each parameter. The input parameters are well reconstructed, showing that there are no systematic errors from the analysis method other than the background-noise subtraction and the choice of fit range described in Section 6.3.3.

#### B. Experimental Uncertainties

In the preceding analysis, the systematic uncertainties related to the analysis method of the data were discussed. In addition to these uncertainties, various experimental uncertainties were identified, in particular

1. the source-detector distance during the immersions,
2. the shape of the calibration time distribution of the LED source in air,
3. the absolute stability of the intensity of the light source,
4. the anisotropy of the light source,
5. the angular detection efficiency of the detector sphere and

[4]The direct simulation of the same number of events as in the experimental data was not possible due to the weighting of the hits by $e^{-d/\lambda_A}$ as described in Section 5.2.2, which would largely underestimate the statistical fluctuations in the tail of the GD.

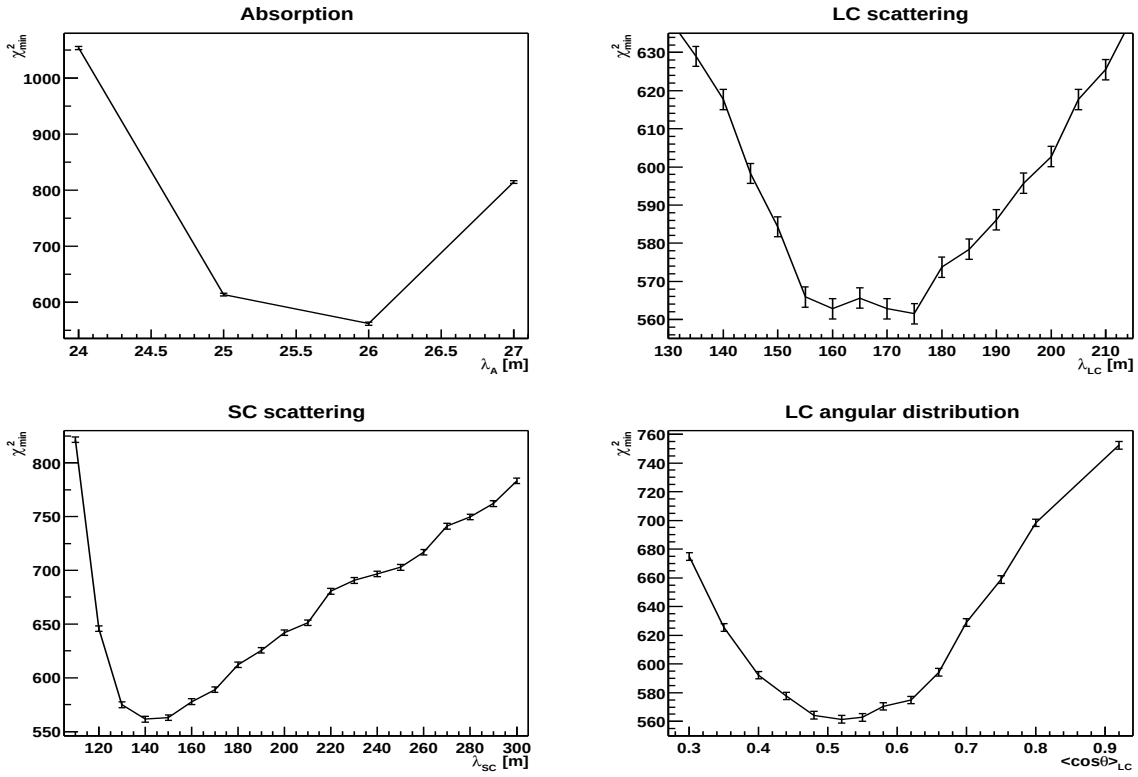


**Figure 6.8:** *Minimum $\chi^2$ (obtained as described in the caption of Figure 6.3) as a function of the optical parameters for a typical reconstructed GD with input values: $\lambda_A = 25.9$, $\lambda_{LC} = 173$, $\lambda_{SC} = 137$ and $\langle \cos\theta \rangle_{LC} = 0.54$.*

6. the wavelength dependence of the SC scattering length.

With the exception of the last factor, a best estimate of the impact of each uncertainty upon the reconstructed optical parameters was obtained by generating a GD (with ∼100 times the data statistics), simulating the uncertainty at the best parameter values of the September 1999 data, and analysing the GD with all the original MTDs of water models from the data base. The systematic error due to each effect was taken as the difference between the input parameter and the reconstructed parameter, proceeding exactly as for the background-noise subtraction (described in Section 6.3.3). Because all systematic errors were deduced for generated data equivalent to the real data of Test 3′ (but with larger statistics), these errors provide a best estimate of the systematic errors on the parameters extracted from the actual data.

### 1. Error on the Source-Detector Distance

Although the source-detector distance was measured with great accuracy on the shore before and after the immersions, there are uncertainties in the exact cable lengths during the immersions. This is due to the large tension acting on the cables during the immersion which causes the cables to stretch. The best estimate of this stretch was obtained by comparing the reconstructed time offsets (as described in Section 5.2.3) $t_o^1$ and $t_o^2$ for each

| | 24 m | 44 m | "24 m + 44 m combined" |
|---|---|---|---|
| $\lambda_A$ | +0.5 | +0.5 | +0.5 |
| $\lambda_{SC}$ | +7 | +8 | +9 |
| $\lambda_{LC}$ | +7 | +5 | +3 |
| $\langle cos\theta \rangle_{LC}$ | -0.04 | -0.03 | -0.03 |

**Table 6.3:** *Best estimate of the systematic errors from the uncertainty in the source-detector distance during the immersions.*

of the two distances $d_1$ and $d_2$. The tensile strain $\sigma$, defined as the ratio between the extension $\delta l$ and the distance, is given by

$$\sigma \approx \frac{(t_o^1 - t_o^2) \times \langle v_g \rangle}{d_1 - d_2}, \tag{6.8}$$

where $\langle v_g \rangle$ is the group velocity at the central wavelength of the source and the tensile strain was assumed to be independent of the length of the cable. With this assumption, the tensile strain was calculated to be $\sim$2.15%. GDs were generated taking into account these tensile strains by increasing the source-detector separation accordingly. Table 6.3 summarizes the best estimate of the systematic errors of the optical parameters due to an increase in the source-detector distance.

From Eq. 6.4 (p. 83), the absorption length was expected to increase. This is because the increased path length must be compensated by an increased absorption length in order to detect the same number of photons at the increased distance compared to the original distance. A similar effect is also seen for the SC scattering length because the normalisation also affects the number of photons in the tail of the distribution, and this number is strongly dependent upon the SC scattering length. Small variations in the shapes due to the increased distances also create uncertainties in the other two parameters.

### 2. Time Distribution of Light Source

The shapes of the calibration time spectra of the source depend upon the voltage applied to the LED drivers. These shapes were shown (in Section 3.5.2) to be very reproducible. However, irrespective of the voltage applied to the LED drivers, the shape of the air calibration time spectra also depend upon the source-detector distance because of the discrete binning of the spectra. The potential[5] difference in shape because of this difference in distance could be critical in the determination of the optical parameters.

The largest difference in shape occurs when the difference in distance at which the data and the air spectrum were taken is such that it shifts the spectrum by exactly half a bin. To simulate this effect, a large sample of events was drawn from the appropriate air spectrum and a shift of half a bin was added before binning the event. Figure 6.9 shows the original (solid line) and the shifted (dotted line) calibration time spectrum in air. The

[5]There is a finite probability that the spectrum is shifted by an integral number of bins.

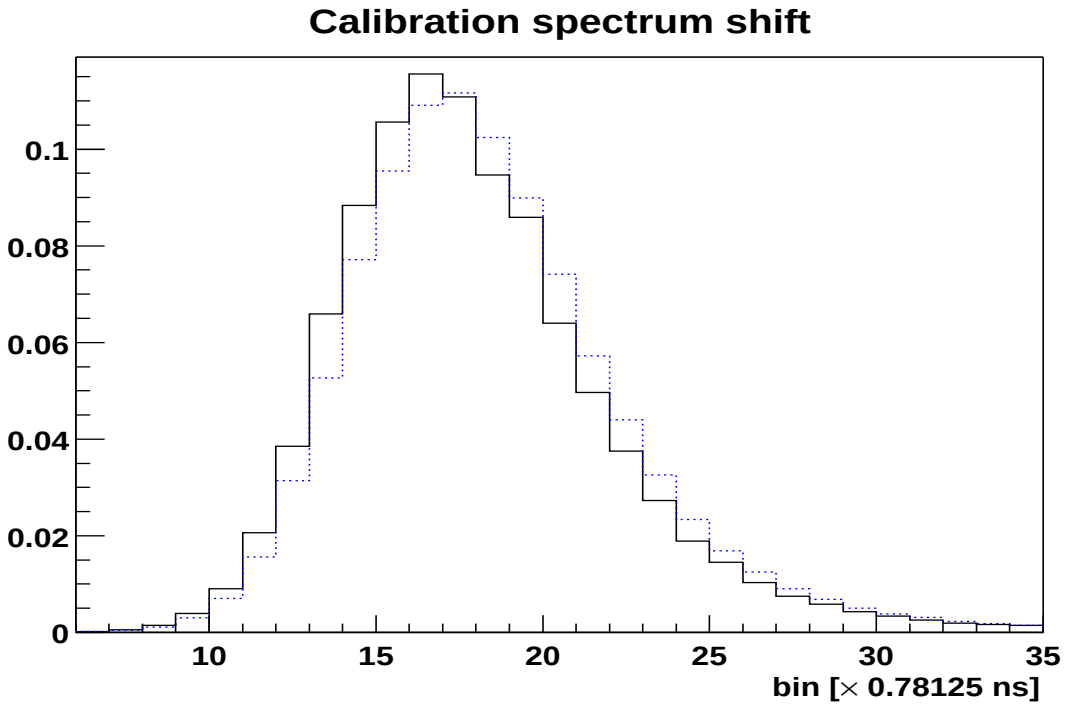


**Figure 6.9:** *Time response of the light source in air at a specific source-detector distance (solid line). The same time response in air at a different source-detector distance such that the spectrum is shifted by half a bin (dotted line).*

difference in shape is clearly evident. The impact of this binning effect upon the optical parameters (i.e. when the shifted air spectrum is used as an input to the MC simulations instead of the original air spectrum) is then analysed by comparing a GD generated with the air spectrum shown as a dotted line in Figure 6.9 with the original MTDs. The results are shown in Table 6.4.

As expected, the largest impact is upon $\lambda_{LC}$ and $\langle \cos\theta \rangle_{LC}$ which both depend crucially upon the shape of the peak (see Figure 5.8, p. 77). The impact is larger at 24 m than at 44 m because of the increased scattering at the longer distance, which causes the shape of the peak region to resemble less the shape of the original air spectrum and hence makes this latter less crucial (compared to the shorter distance) in the accurate determination of the parameters. The effects upon $\lambda_A$ and $\lambda_{SC}$ were very small, but failing to be larger than half a step size were conservatively taken as such.

| | 24 m | 44 m | "24 m + 44 m combined" |
|---|---|---|---|
| $\lambda_A$ | $\pm 0.5$ | $\pm 0.5$ | $\pm 0.5$ |
| $\lambda_{SC}$ | $\pm 5$ | $\pm 5$ | $\pm 5$ |
| $\lambda_{LC}$ | $\pm 18$ | $\pm 8$ | $\pm 14$ |
| $\langle cos\theta \rangle_{LC}$ | $\pm 0.09$ | $\pm 0.04$ | $\pm 0.05$ |

**Table 6.4:** *Best estimate of the systematic errors from the uncertainty in the shape of the calibration air spectrum due to the discrete binning of the spectra.*

| | 24 m | 44 m | "24 m + 44 m combined" |
|---|---|---|---|
| $\lambda_A$ | $\pm^{0.5}_{0.5}$ | $\pm^{0.6}_{0.5}$ | $\pm^{0.5}_{0.5}$ |
| $\lambda_{SC}$ | $\pm^{5}_{5}$ | $\pm^{10}_{5}$ | $\pm^{6}_{8}$ |
| $\lambda_{LC}$ | $\pm^{5}_{10}$ | $\pm^{5}_{4}$ | $\pm^{4}_{4}$ |
| $\langle cos\theta \rangle_{LC}$ | $\pm^{0.05}_{0.04}$ | $\pm^{0.02}_{0.04}$ | $\pm^{0.04}_{0.03}$ |

**Table 6.5:** *Best estimate of the systematic errors from potential LED intensity fluctuations.*

### 3. LED Intensity Fluctuations

Because the analysis uses two different distances to extract the relative normalisation, it implicitly assumes that there are no fluctuations in the LED intensity between the measurements at two different distances.

The stability of individual LEDs was measured by the Sheffield group of the ANTARES Collaboration and results showed that the maximum variation in the average intensity between runs was 2% [71]. The maximum impact upon the parameter reconstruction occurs when the fluctuation is in the opposite direction for the two distances. A GD was therefore produced from the original MC simulations for each of the two distances and the analysis was performed by once increasing and once decreasing the relative normalisation $\eta_{d_1}$ (Eq. 6.2, p. 83) between the analysed and the reference data by 2%. Table 6.5 shows a summary of these results.

LED fluctuations are expected to affect mainly the absorption length and the SC scattering length. A change in the ratio of the emitted number of photons at the two distances reflects a change in the absorption length. Because of the relatively small differences between the number of hits in the tail of the arrival time distributions with different SC scattering lengths, a certain impact upon the SC scattering length can be observed as well. As in the case of the source-detector distance, a change in the normalisation will also affect the other two parameters.

### 4. Anisotropy of Source

Because the light source was made of six individual LEDs, each with their own driver, even after careful adjustment of the LED intensities by means of variable capacitors (as described in Section 3.2.2), variations up to 15% were measured. The exact variation of the LED intensity as a function of the angle relative to the direction to the detector was however unknown. Three extreme scenarios were therefore considered, where

i. the LED facing the detector (the front LED) and the one pointing away from the detector (the back LED) are 100% efficient and the side LEDs are 85% efficient,

ii. the front LED is 85% efficient and all the other LEDs are 100% efficient and

iii. the front LED is 100% efficient and all the other LEDs are 85% efficient.

| | 24 m | 44 m | "24 m + 44 m combined" |
|---|---|---|---|
| $\lambda_A$ | $\pm^{0.5}_{0.5}$ | $\pm^{0.5}_{0.5}$ | $\pm^{0.5}_{0.5}$ |
| $\lambda_{SC}$ | $\pm^{5}_{5}$ | $\pm^{6}_{5}$ | $\pm^{5}_{5}$ |
| $\lambda_{LC}$ | $\pm^{4}_{6}$ | $\pm^{3}_{3}$ | $\pm^{3}_{3}$ |
| $\langle cos\theta \rangle_{LC}$ | $\pm^{0.02}_{0.02}$ | $\pm^{0.02}_{0.02}$ | $\pm^{0.02}_{0.02}$ |

**Table 6.6:** *Best estimate of the systematic errors from the potential anisotropy of the LED source.*

Configuration iii. is very similar to configuration i. except that the back LED is 85% efficient instead of 100% efficient and provides therefore a measure of the importance of the back LED. The total intensity output as a function of the angle relative to the direction to the detector was computed from the intensity angular distribution of each LED given approximately by $\cos^2\theta$. The photon arriving at the detector was then attributed a weight according to its angle of emission with respect to the detector. A GD was simulated for each configuration. The average systematic errors from all three configurations are given in Table 6.6.

In general, the effect of the anisotropy is relatively small. Most of the photons registered by the detector originate from the front LED which therefore determines the absorption length. The absorption length is thus expected to be relatively stable and was indeed well reconstructed to within 0.2 m. Because of step size limitations, the error was however attributed a value of half a step size (0.5 m). The impacts upon the other three parameters are more complex but, because of the dominant effect of the front LED, are relatively small.

### 5. Detector Angular Efficiency

The angular detection efficiency of the glass sphere housing the PMT was simulated (as described in Appendix B) under the assumption of the exact knowledge of various factors, such as the thickness of the gel layer and the angular efficiency of the PMT. Neither of these is known with perfect accuracy: the values for the angular efficiency of the PMT were based upon a parametrisation of the real and imaginary parts of the complex refractive index for the bialkali photocathode (PC) measurements by Moorhead and Tanner (MT) [75], shown as Model $\alpha$ in Figure 6.10. However, measurements of the complex refractive index were only taken over the wavelength range between 390 nm and 800 nm and hence needed to be extrapolated to 374.5 nm (for the measurements in the UV). The large range of acceptable values for the complex refractive index (especially the real part) for the measurements at 390 nm suggests that similar errors can be expected at 374.5 nm. In addition to these errors, large variations in the PC thickness were also observed.

Using the MC for the detector angular efficiency described in Appendix B, it was found that the largest uncertainties could be attributed to the PC thickness and the real part of the complex refractive index of the PC. To quantify these errors, it was assumed that the spread of values for both the real and imaginary refractive index at 390 nm was

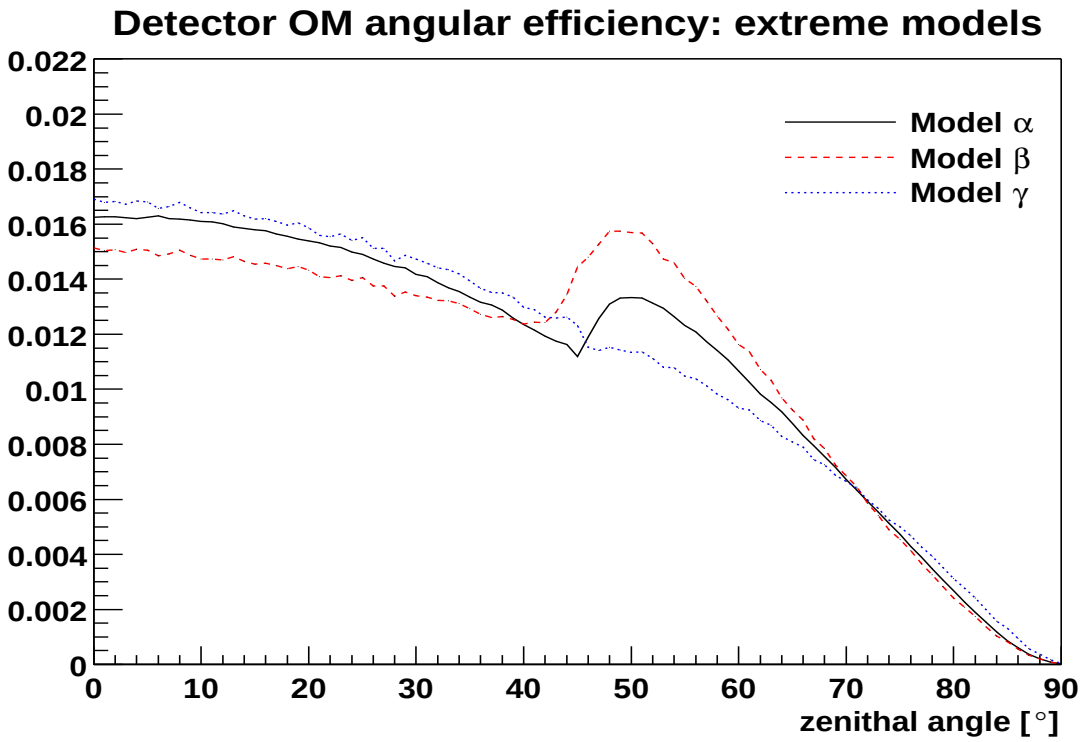


**Figure 6.10:** *Simulations of extreme models for the detector sphere angular efficiency (relative to the normal of the PMT and normalised to unit area): Model $\alpha$ uses a parametrisation of the MT data and was used in the analysis of the Test 3′ data, Model $\beta$ uses the thinnest of the PCs together with the smallest complex refractive index and Model $\gamma$ the thickest PC together with the largest complex refractive index (see text).*

representative of the corresponding spread at 374.5 nm and that the range of values for the PC thickness of various PMTs found in [75] was representative of the uncertainty in the PC thickness. With these two assumptions, the largest change in the shape of the efficiency curve was obtained by taking once the smallest of the complex refractive index ($n_3 + ik_3 = 1.10 + i\ 1.70$) together with the smallest PC thickness (16.4 nm) and once the largest of the range of values for the complex refractive index ($n_3 + ik_3 = 2.75 + i\ 2.50$) together with the largest thickness of the PC (30.0 nm), where the values for the complex refractive indices were calculated from the mean value of the parametrisation and the spread at 390 nm from MT. Both of these configurations are shown in Figure 6.10 as Model $\beta$ and Model $\gamma$ respectively. GDs were generated for each of these models and analysed with the original MC simulations (which use Model $\alpha$).

From Figure 6.10, it can be seen that the change in shape essentially produces a change in the ratio of photons detected at angles smaller than 45° and photons detected at larger angles (the forward-backward ratio). Using Model $\beta$, this ratio decreases, causing more photons to be detected at large angles. These are mostly photons that have scattered upon an SC. An increase in the detection efficiency of these photons requires more scat-

| | 24 m | 44 m | "24 m + 44 m combined" |
|---|---|---|---|
| $\lambda_A$ | $\pm^{0.5}_{0.5}$ | $\pm^{0.5}_{0.5}$ | $\pm^{0.5}_{0.5}$ |
| $\lambda_{SC}$ | $\pm^{10}_{13}$ | $\pm^{9}_{12}$ | $\pm^{10}_{12}$ |
| $\lambda_{LC}$ | $\pm^{8}_{8}$ | $\pm^{6}_{6}$ | $\pm^{7}_{7}$ |
| $\langle cos\theta \rangle_{LC}$ | $\pm^{0.06}_{0.04}$ | $\pm^{0.02}_{0.02}$ | $\pm^{0.02}_{0.02}$ |

**Table 6.7:** *Best estimate of the systematic errors due to the uncertainty in the shape of the detector angular efficiency.*

tering with Model $\alpha$ to obtain the same number of photons in the tail and therefore causes an underestimation of the $\lambda_{SC}$. For Model $\gamma$ where the "bump" in the angular efficiency has been removed (and the curve resembles very closely to a cosine function), less photons must scatter when using Model $\alpha$ to compensate for the reduced efficiency, and the opposite trend for $\lambda_{SC}$ can be seen. The forward-backward ratio also affects the other parameters to various extents. The variation of the $\langle \cos\theta \rangle_{LC}$ shows a similar behaviour to the $\lambda_{SC}$, with a smaller $\langle \cos\theta \rangle_{LC}$ producing more photons in the tail. The change in shape in the peak also causes the $\lambda_{LC}$ to vary. The larger number of unscattered photons (arriving at an angle perpendicular to the PMT surface) at 24 m than at 44 m causes the ratio of the total number of photons detected at each distance to change when the detector angular efficiency changes, resulting in a small uncertainty in the absorption length. All of these effects are summarized in Table 6.7.

### 6. Wavelength Dependence of SC Scattering

As discussed in Section 2.3.1, SC scattering follows approximately a $\lambda^{-4}$ dependence. This had to be modified because of the dependence of the refractive index upon wavelength. The final results were therefore shown to yield an exponent $-4.32 \pm 0.31$, which was used in the determination of the SC scattering length at the central wavelength of the source, as discussed in Section 5.2.2. To estimate the importance of using a different exponent in the determination of the SC scattering length, the shift in the SC scattering length in the convolution with the wavelength spectrum of the source (Figure 3.5, p. 43) was analysed by assuming once an exponent of -4.01 and once of -4.63. The difference in SC scattering lengths was found to be less than 0.5 m (at the best parameter values for the September 1999 data) and thus negligible in comparison to all the other systematic errors.

### Total Experimental Systematic Errors

Table 6.8 shows a summary of all the experimental systematic errors (not including the ones due to the background-noise subtraction and the choice of the range for the fit to the minimum). All errors were added in quadrature. These results, together with those in Table 6.2 (p. 92), show that the systematic errors dominate the overall results obtained from the measurements with Test 3′.

Amongst the experimental uncertainties, the largest unknowns in the computation of the absorption length are the source-detector distance and the stability of the LED

| | 24 m | 44 m | "24 m + 44 m combined" |
|---|---|---|---|
| $\lambda_A$ | $\pm^{1.1}_{1.0}$ | $\pm^{1.2}_{1.0}$ | $\pm^{1.1}_{1.0}$ |
| $\lambda_{SC}$ | $\pm^{15}_{16}$ | $\pm^{17}_{15}$ | $\pm^{16}_{16}$ |
| $\lambda_{LC}$ | $\pm^{22}_{23}$ | $\pm^{13}_{11}$ | $\pm^{17}_{16}$ |
| $\langle cos\theta \rangle_{LC}$ | $\pm^{0.12}_{0.12}$ | $\pm^{0.05}_{0.07}$ | $\pm^{0.07}_{0.07}$ |

**Table 6.8:** *Best estimate of the total experimental systematic uncertainties, where all systematic errors were added in quadrature.*

intensity. For the SC scattering length, the largest errors arise from the uncertainty in the detector angular efficiency whilst for the LC scattering length and its angular distribution the major uncertainty results from the shape of the calibration spectrum.

### 6.3.5 Model Limitations

The model for the optical properties at the ANTARES site (see Section 2.7), used in the analysis described in the previous sections, approximates the LC scattering angular distribution with a single Henyey-Greenstein function (Eq. 2.8, p. 20). With this model, a $\langle \cos\theta \rangle_{LC} = 0.54$ was found. Given that turbulence-induced fluctuations in the refractive index are expected to cause photons to scatter at very small angles, it is necessary to investigate to what extent the presence of an additional class of scatterers with a very forward-peaked scattering angular distribution is compatible with these results (i.e. cannot be ruled out with the measurements of Test 3′).

MC simulations were generated with the parameters from the best water model (given in the last column of Table 6.2, p. 92) together with an additional type of scatterers ($LC'$). Because the relevant scattering parameter for very forward-peaked scattering is the effective scattering length (see Section 5.4), the average cosine for these $LC'$ was arbitrarily chosen as $\langle \cos\theta \rangle_{LC'} = 0.996$ (corresponding to an average scattering angle $\langle \theta \rangle_{LC'} = 5°$). The $\lambda_{LC'}$ was varied to find the minimum value above which no significant change in the shape of the photon arrival time distribution could be detected. This was very conservatively taken as the $\lambda_{LC'}$ giving a $\chi^2$ larger than the minimum without this additional scattering component at the $5\sigma$ level (>99.999% confidence level!). This analysis gives $\lambda_{LC'} \approx 70$ m, which corresponds to an effective scattering length $\lambda^E_{LC'} \approx 17500$ m, about fifty times larger than the effective scattering length found from the best water model for which $\lambda^E_{LC} \sim 376$ m. Figure 6.11 shows the 44 m data of the September 1999 immersions and two MTDs with varying amounts of very forward-peaked scattering: with a scattering length of 1 m for this additional component, the change in shape is clearly evident. As the scattering length is increased, the change in shape disappears, at which point this component cannot be distinguished with Test 3′. Given the best water model obtained previously, Test 3′ thus cannot rule out the presence of an additional class of very forward-peaked scattering centres with $\lambda^E_{LC'} \gtrsim 17.5$ km.

The presence of small-angle scattering from turbulence-induced fluctuations in the refractive index is thus not incompatible with the results presented in Table 6.2. However,

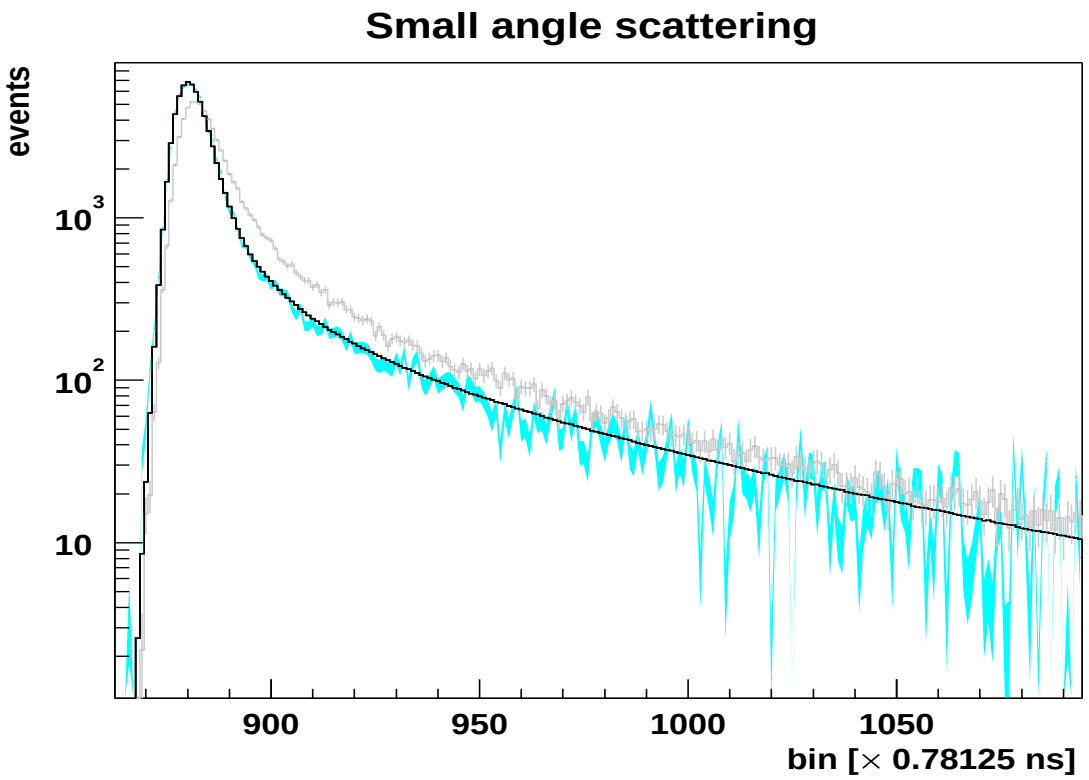


**Figure 6.11:** *The solid dark grey band shows the September 1999 data (44 m) where the width of the band corresponds to the statistical error at each bin. The light grey curve corresponds to the water model with $\lambda_{LC'} = 1$ m and the black histogram with $\lambda_{LC'} = 70$ m, both with $\langle \cos\theta \rangle_{LC'} = 0.996$.*

having a much larger effective scattering length, this additional class of scatterers is not expected to cause any significant change in the arrival time distributions of photons for the ANTARES detector.

### 6.3.6 Correlations

In the analysis described in the previous sections, all variables were assumed to be uncorrelated, resulting in the statistical errors being larger than if the correlations were taken into account. In this section, the correlations between each of the optical parameters are calculated for the combined data of the two distances using the following method:

1. A two-dimensional grid of high-statistics MCs, keeping all but two of the parameters constant (at the values of the overall minimum $\chi^2$) at a time, was scanned using refined step sizes:

| | $\lambda_A$ | $\lambda_{SC}$ | $\lambda_{LC}$ | $\langle \cos\theta \rangle_{LC}$ |
|---|---|---|---|---|
| Original step size | 1.0 m | 10 m | 5 m | 0.03/0.04 |
| Refined step size | 0.1 m | 1 m | 2 m | 0.01 |

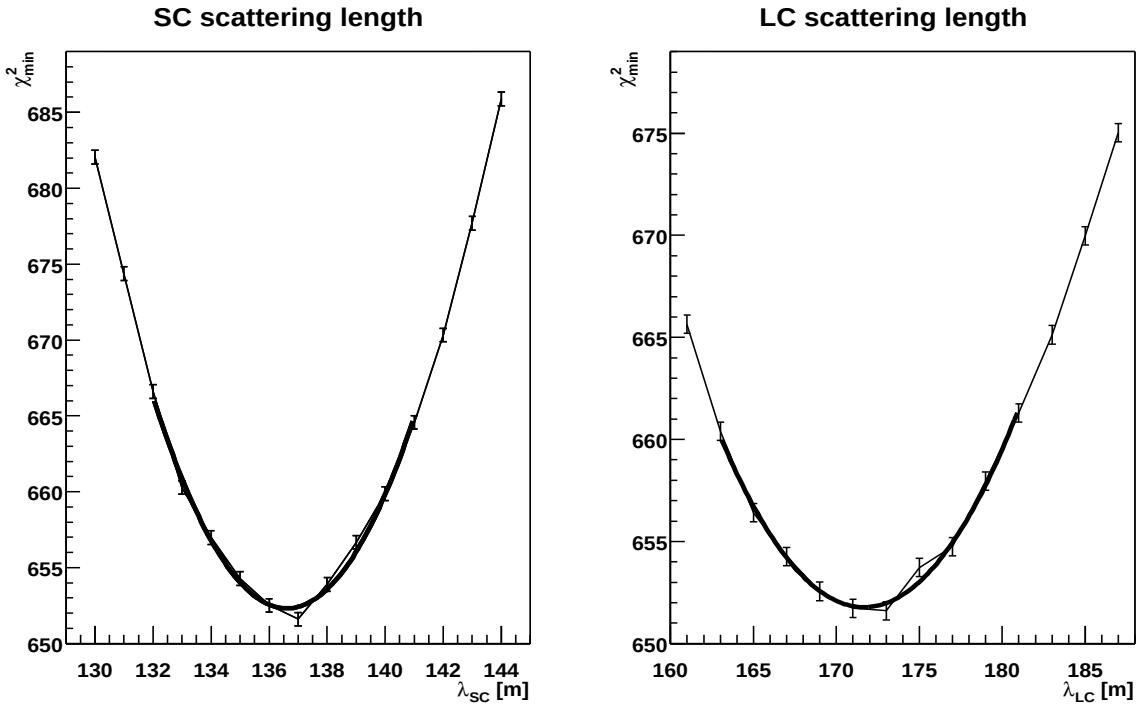


**Figure 6.12:** *Second order polynomial fit to the $\chi^2$ versus $\lambda_{SC}$ for a given $\lambda_{LC}$, to extract the two $\lambda_{SC}$ where $\chi^2 = \chi^2_{min} + 1$ (left). Similar fit to the $\chi^2$ versus $\lambda_{LC}$ for each value of $\lambda_{SC}$ (right).*

2. For each point on the grid, the $\chi^2$ was calculated from Eq. 6.1 (as described previously).

3. Given the fluctuations in the $\chi^2$ due to the limited MC statistics, the values of the parameter combinations with $\chi^2_{min} + 1$ (the error ellipse) were obtained by fitting a second order polynomial for each slice of a given parameter, keeping the other parameter value constant (see Figure 6.12). This yields a series of data points which have a $\chi^2 = \chi^2_{min} + 1$.

4. An ellipse was fitted to these data points (Figure 6.13), using a standard procedure to calculate the correlation coefficients [68], which are summarized in the following matrix:

$$\begin{bmatrix} & \lambda_A & \lambda_{SC} & \lambda_{LC} & \langle\cos\theta\rangle_{LC} \\ \lambda_A & 1 & -0.19^{(*)} & -0.12^{(*)} & -0.08^{(*)} \\ \lambda_{SC} & & 1 & -0.87 & -0.96 \\ \lambda_{LC} & & & 1 & -0.84 \\ \langle\cos\theta\rangle_{LC} & & & & 1 \end{bmatrix}.$$

The entries marked with $^{(*)}$ in this matrix are compatible with zero to within the step size of the parameters and the errors on the ellipse parameters.

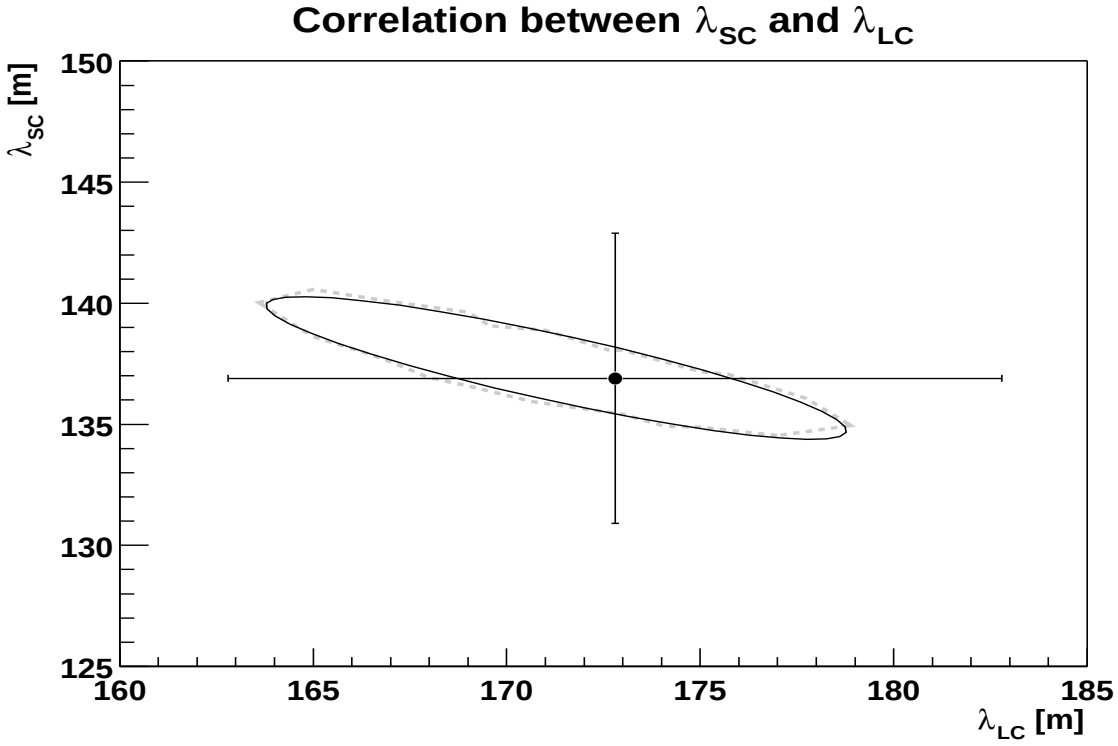


**Figure 6.13:** *Example of an error ellipse (solid line) for $\lambda_{SC}$ versus $\lambda_{LC}$, fitted to the data points with $\chi^2 = \chi^2_{min} + 1$ (dashed line). The point with error bars shows the uncorrelated errors.*

The correlation coefficients of the absorption length with the other parameters is relatively small (and consistent with zero). This is consistent with the fact that the absorption length is mainly determined by the relative number of counts at the two distances and neither of the other variables considerably affects this number.

The strong anti-correlation between the remaining parameters should come as no surprise. The strongest of all correlations is between $\lambda_{SC}$ and $\langle\cos\theta\rangle_{LC}$. This is explained by the fact that a change in $\langle\cos\theta\rangle_{LC}$ directly simulates a change in the amount of backscattering and therefore of SC scattering. The correlation between $\lambda_{SC}$ and $\lambda_{LC}$ can be understood from Eq. 5.3 (p. 67), with a certain degeneracy for parameter combinations with the same average scattering length. Whilst not complete, the degeneracy between $\lambda_{LC}$ and $\langle\cos\theta\rangle_{LC}$ can be understood in terms of the effective scattering length (for reasons described in Section 5.4).

From Figure 6.13, it is clear that for the variables which are strongly correlated, the correlated statistical errors are significantly smaller than the uncorrelated ones. The impact of these correlations upon the final results is however small, because the experiment is limited overall by the systematic errors. The final results are therefore presented with their uncorrelated errors.

| | 24 m | 44 m | "24 m + 44 m combined" |
|---|---|---|---|
| $\lambda_A$ | $26.1 \pm 0.5 \pm^{1.2}_{1.1}$ | $25.9 \pm 0.5 \pm^{1.3}_{1.1}$ | $25.9 \pm 0.5 \pm^{1.2}_{1.1}$ |
| $\lambda_{SC}$ | $137 \pm 8 \pm^{16}_{17}$ | $148 \pm 15 \pm^{25}_{20}$ | $137 \pm 6 \pm^{17}_{17}$ |
| $\lambda_{LC}$ | $160 \pm 15 \pm^{23}_{23}$ | $165 \pm 16 \pm^{14}_{13}$ | $173 \pm 10 \pm^{17}_{17}$ |
| $\langle cos\theta \rangle_{LC}$ | $0.56 \pm 0.07 \pm^{0.13}_{0.12}$ | $0.51 \pm 0.06 \pm^{0.08}_{0.08}$ | $0.54 \pm 0.05 \pm^{0.08}_{0.08}$ |

**Table 6.9:** *ANTARES optical properties in the UV (374.5 nm): final results for the September 1999 immersions. The first and second errors correspond to the uncorrelated statistical and total systematic errors respectively.*

### 6.3.7 Final Results

The final results for the September 1999 data are shown in Table 6.9. The first and second errors correspond to the uncorrelated statistical and total systematic errors respectively (where the systematic errors from the background noise and the fit range were added in quadrature with the total experimental systematic errors, summarized in Table 6.8, p. 102). Whilst the systematic errors are large compared to the statistical errors, the parameters are overall well constrained. The good agreement between the 24 m, the 44 m and the combined data shows that the experiment and its systematic errors are well understood and that the analysis method developed in this chapter is very reliable.

## 6.4 UV (374.5 nm) July 1999 Immersions: Results

The data taken during the July 1999 immersions were taken at 15 m and 24 m. The lower statistics (compared to the September 1999 data) caused the statistical errors for each of the parameters to be larger for these data, and the shorter distance combination resulted in a larger sensitivity to various of the experimental uncertainties. Amongst others, the accurate knowledge of the shape of the air spectrum was found to be much more crucial at the shorter distance, where the shape of the arrival time distribution of the photons resembles much more that of the air spectrum than at larger distances, where the shape has effectively been smeared out through scattering. This effect is shown in Table 6.4 (p. 97), where the impact of the air calibration spectrum upon both $\lambda_{LC}$ and $\langle \cos\theta \rangle_{LC}$ is larger at 24 m than at 44 m. Additionally, because of the larger ratio of direct to scattered photons at the shorter distances, the number of photons in the tail of the distribution is relatively small and makes the distinction between the parameters extremely difficult. The 15 m data, in particular, were found to have such large statistical and systematic errors that no information could be extracted. The 24 m data could however still be analysed

| *parameter* | July 1999 |
|---|---|
| $\lambda_A$ | $23.4 \pm 0.5 \pm^{2.0}_{1.3}$ |
| $\lambda_{SC}$ | $130 \pm 23 \pm^{27}_{18}$ |
| $\lambda_{LC}$ | $250 \pm 38 \pm^{69}_{86}$ |
| $\langle cos\theta \rangle_{LC}$ | $0.45 \pm 0.11 \pm^{0.17}_{0.27}$ |

**Table 6.10:** *ANTARES optical properties in the UV (374.5 nm): results for the July 1999 immersions.*

making use of the normalisation of the 15 m data, using the same analysis method as for the September 1999 data. The systematic error calculations were performed for the best model as before. The results from this analysis are summarized in Table 6.10 and the MC of the best water model is plotted together with the data in Figure 6.14.

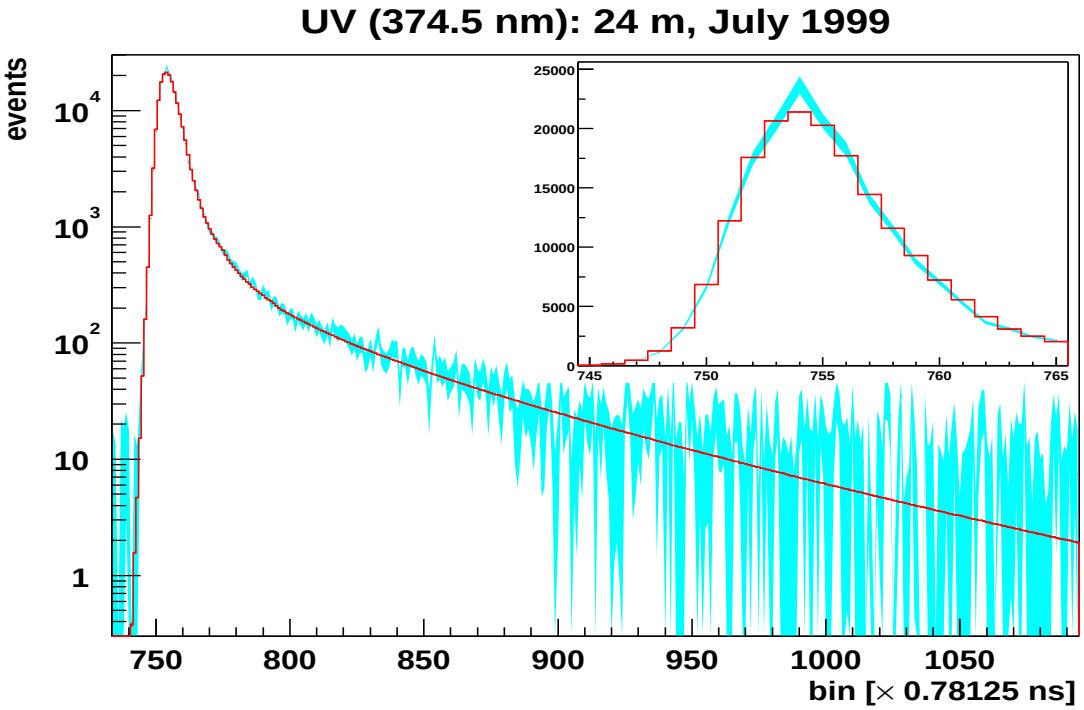


**Figure 6.14:** *July 1999 immersions (5.15 V): shown are the data (grey band) and the best fit MC simulation (histogram) normalised as described in Section 6.1. The statistical errors for the data are shown by the width of the band. The statistical errors of the MC simulation are too small to be visible.*

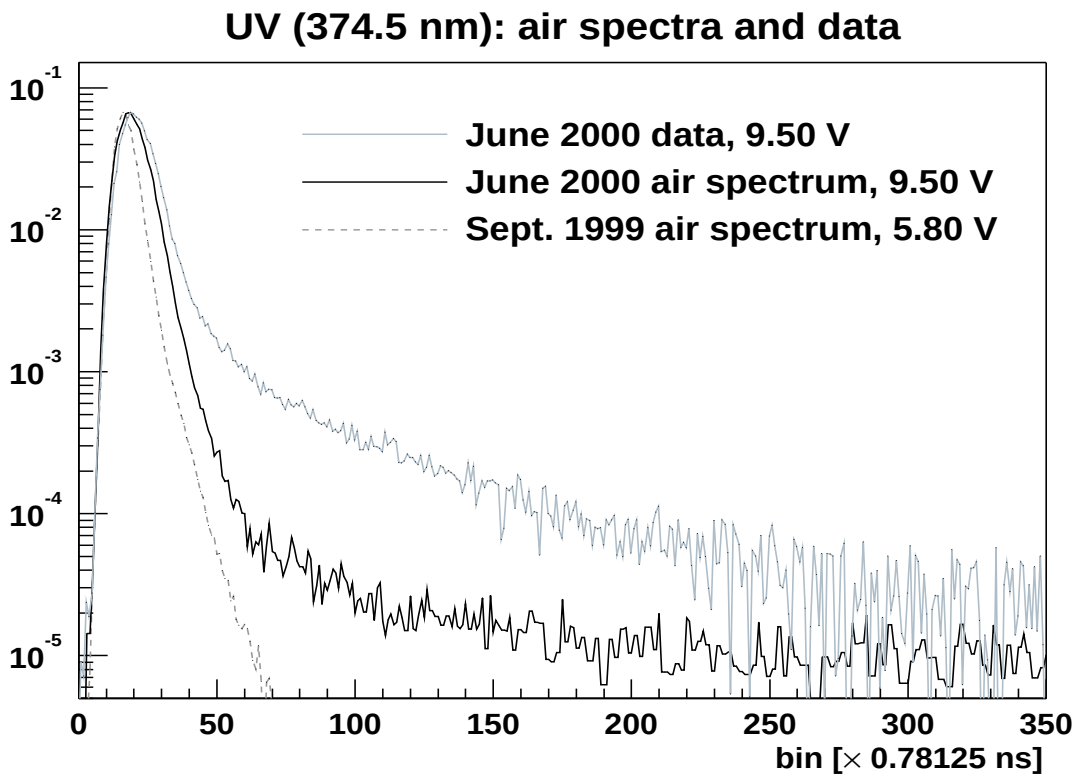


**Figure 6.15:** *Year 1999 air spectrum in the UV (taken by the author under very controlled conditions) versus Year 2000 air spectrum in the UV (not taken by the author and under much less controlled conditions).*

## 6.5 Year 2000 Immersions

### 6.5.1 UV Data: 374.5 nm

In Section 5.2.3, the importance of using an accurate air spectrum was discussed. For the Year 1999 data, these air spectra were very carefully measured by the author in Oxford, using the setup described in Section 3.5.2. The air spectra for the Year 2000 immersions were measured in Saclay by different people and under different conditions from those at Oxford. A comparison of these air spectra with those measured by the author (Figure 6.15) shows that the Year 2000 air spectra have a long tail, with a similar number of events towards the end of the tail of the spectrum as the data taken during the immersions. This tail is however non-existent for any of the air spectra measured by the author and raised therefore concerns about the accuracy of these spectra.

The long tail could be explained by assuming that either there was a problem with the LEDs (or the LED drivers) or scattered light was detected during the measurements of these air spectra (in which case the scattering is not only limited to the tail, but would also affect the shape of the peak). The second of these reasons is the most plausible because the measurements were taken under much less controlled conditions than the Year 1999 air spectra, in a different place and by different people (not including the author). Because

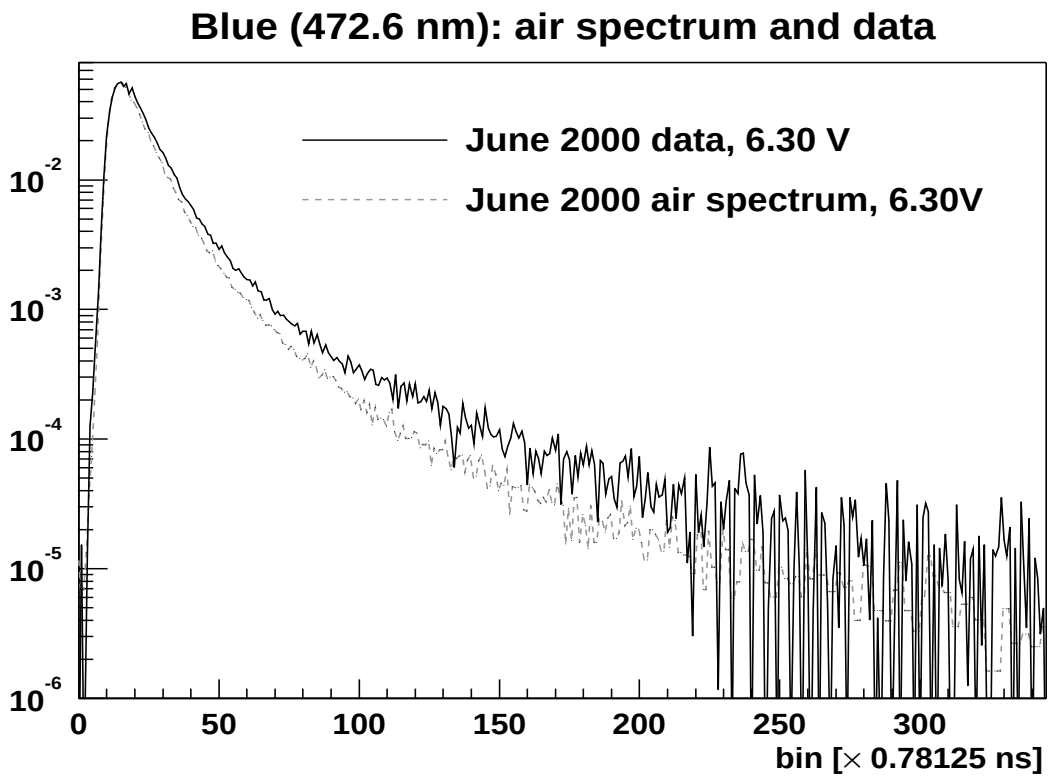


**Figure 6.16:** *Year 2000 air spectrum (measured under much less controlled conditions than described in Section 3.5.2) and data spectrum in the blue.*

the effects that distinguish the optical parameters are relatively small, the unreliability of these UV calibration spectra prevented the analysis of the UV 2000 data.

### 6.5.2 Blue Data: 472.6 nm

A very similar (although much worse) problem was detected for the blue data of the same immersions. Figure 6.16 shows a plot of the air spectrum together with a data spectrum acquired during one of the immersions.

The large fraction of hits in the tail of the air spectrum are due to late photons from the light source. With much larger values expected for the absorption and scattering lengths and hence a much smaller capability of distinction between the individual parameters than in the UV, whether the cause was a bad choice of the LEDs, scattering in the air spectrum, or a combination of both factors, there was no hope to be able to extract any of the scattering parameters. Because the air spectra were however taken at the same time as the UV 2000 air spectra described in the previous section, there is a strong suspicion that the much less controlled conditions surrounding the experiment during the measurement of these calibration air spectra contributed to their contamination. No other air spectra were taken for these measurements and various changes to the configurations in the meantime precluded the re-measurement of these spectra, leaving no accurate air spectra for the analysis of any of the Year 2000 data.

## 6.6 Variation of Optical Properties with Depth

To measure the variation of the optical properties over the range of depths of the future ANTARES detector, the Test 3′ experiment was immersed at a depth 400 m above the sea bed (corresponding to the top of the ANTARES lines) in addition to the measurements performed at 100 m above the sea bed (see Section 3.4).

Due to bad weather conditions, however, measurements could only be made at one distance. Because the analysis of the data uses measurements at two different distances, the optical properties could not be determined directly. Indirectly, it was however possible to check the consistency between the measurements at the two depths by performing the $\chi^2$ test between the two data (instead of the usual data-MC comparison). The result gave a satisfactory $\chi^2/df = 340.51/355$, showing that, within its limitations, Test 3′ could not detect any variations in the optical properties between the different depths.

## 6.7 Summary

In this chapter, the analysis method for the Test 3′ data was presented (Section 6.1). The model-independent effective absorption lengths and background-noise rates were calculated (Section 6.2). The optical properties of the best available data in the UV (September 1999) were analysed, showing first that they were incompatible with a water model without LCs (Section 6.3.1). The individual data were then compared to check for potential variations in the optical properties between different acquisitions (Section 6.3.2) and a detailed description of the analysis of the combined data was given (Section 6.3.3). Various systematic errors were identified and quantified with appropriate MC simulations (Section 6.3.4). The analysis results for the July 1999 data were then presented (Section 6.4). Various problems with the air spectra of the Year 2000 immersions were identified (Section 6.5). Potential variations in the optical properties over the range of depths of the ANTARES detector were investigated by comparing the measurements at the two extremes of this range (Section 6.6).

# Chapter 7

# ANTARES Results: Discussion

This chapter discusses the results from the measurements with Test 3′ at the ANTARES site and compares them to those from other experiments (described in Section 2.5). The results are then briefly discussed in the context of the ANTARES detector performance. Ideas for future measurements, to improve the knowledge about the optical properties gained up to the present, are given.

*Experimental confirmation of a prediction is merely a measurement. An experiment disproving a prediction is a discovery.*

*E. Fermi (1901-1954)*

## 7.1 Introduction

The results of the measurements with the Test 3′ experiment at the ANTARES site are summarized in Table 6.1 (p. 84), Table 6.9 (p. 106) and Table 6.10 (p. 107). In Sections 7.2-7.4, these results are discussed and compared to other measurements of the optical properties of various waters. In Section 7.5, a discussion of the stability of these results is given. In Section 7.6, the knowledge of the optical properties from the measurements with Test 3′ is used to estimate the ANTARES detector performance and, in Section 7.7, ideas to improve this knowledge are discussed.

## 7.2 Absorption

The absorption length was deduced very accurately from the measurements with Test 3′ for the immersions in the Year 1999. For the Year 2000 data, due to the problems mentioned in Section 6.5, only the effective absorption length could be deduced. This yields a lower limit to the absorption length which, in the UV, is $\sim$4 m larger than the effective absorption length.

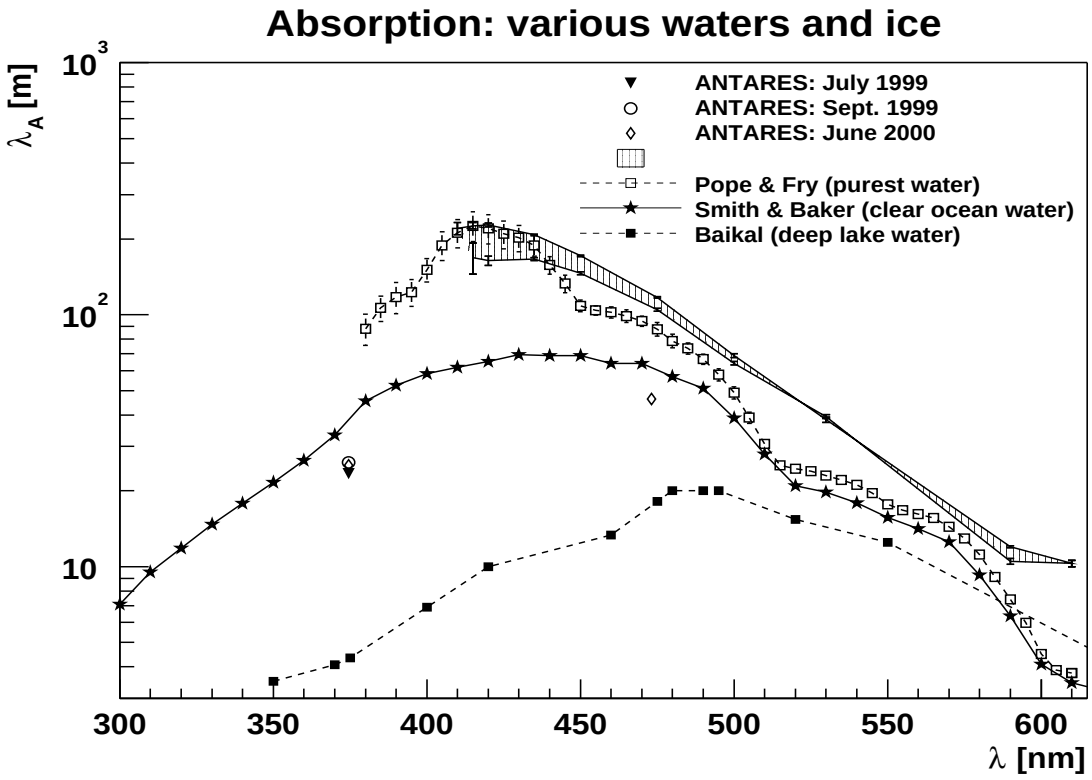
Absorption: various waters and ice
$\lambda_A$ [m]
$10^3$
$10^2$
10
300
350
400
450
500
550
600
λ [nm]
ANTARES: July 1999
ANTARES: Sept. 1999
ANTARES: June 2000
Pope & Fry (purest water)
Smith & Baker (clear ocean water)
Baikal (deep lake water)

In comparison, the water of lake Baikal [42] shows a decrease in the absorption length below 490 nm by more than 60% with respect to the clear ocean waters. From more recent measurements [44], the absorption length at 475 nm was found to be more than 50% shorter than the one at the ANTARES site. In contrast, the measurements of the optical properties of the deep ice, at the South Pole by the AMANDA Collaboration, show a much longer absorption length, similar to (and larger above 450 nm than) the purest water of PF. The specific feature which relates to all the measurements is the wavelength dependence, which is very similar for all waters (and ice), although the Baikal values are shifted somewhat towards longer wavelengths.

## 7.3 SC Scattering

As discussed in Section 2.3.1, SC scattering can be attributed to scattering from ICs smaller than approximately $\lambda/20$. This type of scattering is often referred to as "pure water scattering" in the literature. However, it was shown in Section 2.3 that this terminology can be misleading because very small impurities can exhibit the same scattering angular distribution as the small density fluctuations in the pure water (and that therefore the distinction between various scattering centres is better made on grounds of size). Therefore, measurements of the angular distribution at 90° to the incident beam direction in the determination of the "pure water" scattering coefficient (using Eq. 2.18, p. 22) will be affected by the presence of very small impurities. Similarly, the measurements of the SC scattering length with Test 3′ are also affected by these impurities (since Test 3′ only distinguishes between the scatterers on the basis of their angular distribution). The results from what the literature refers to as the "pure water" measurements (and what is referred to in this thesis as SC scattering measurements) of different waters are thus not expected to be the same (but should be so in the limit of infinitely pure water).

Morel [17] compared the measurements of the "pure water" scattering coefficient from various experiments. Except for one experiment, which used the method of distillation, all used filters with a pore size of 0.1 or 0.22 $\mu$m to purify the water. The range of values for the "pure" fresh water scattering coefficient from the various experiments is large, yielding values of approximately 100-150 m in the UV at 374.5 nm[1]. Whilst Morel explained the discrepancies between these results in terms of the accuracy of the calibration of the individual experiments, differences due to the contamination of the waters with impurities cannot be excluded either because the size of the filters (100 nm at best) allowed impurities of size $\lambda/20 \approx 20$ nm (at ~400 nm wavelengths) to pass into the "pure water". The results are nonetheless very useful as a comparison to the measurement results from Test 3′.

In addition to the purity of the water, to be able to compare the results from Morel to the results obtained from the measurements with Test 3′, various factors need to be taken into account: in particular the conditions of salinity, temperature and pressure as well as the factor $\delta$ in Eq. 2.18 (p. 22) will affect the values of the SC scattering coefficient. The impact of each of these is estimated below.

[1] These values were calculated from measurement results at other wavelengths using a $\lambda^{-4.32}$ dependence.

The presence of salt in the water was found [17] to increase the SC scattering coefficient by 18-34% for salinities of ∼38‰. From these results, the approximate range of expected values of the SC scattering length of "pure" sea water is calculated as 75-127 m.

The measurement results described by Morel were obtained at atmospheric pressure, compared to the pressure of 240 atm at the ANTARES site, and at temperatures of 18-25°C, on average 8.4°C larger than those obtained with Test 3′ (at 13.1°C). The dependence of the SC scattering coefficient upon the pressure and temperature was analysed in detail by Kokorin & Shifrin [56]. A fairly linear dependence upon the pressure was observed, leading to a decrease in the scattering coefficient by approximately 3.5%[2] between 1 and 240 atm. The SC scattering coefficient was found to decrease approximately by ∼3% (which can also be calculated from Eq. 2.2) for the decrease in temperature between the measurements from Morel and those with Test 3′. Both the pressure and temperature dependence can be understood by noting that an increase in pressure and a decrease in temperature both reduce the density fluctuations, which are expected to be the largest contribution to SC scattering in clear waters. The overall effect is thus to increase the SC scattering length by ∼6.8%, yielding the expected range of values for the "pure" water SC scattering length at the salinity, pressure and temperature conditions at the ANTARES site as 80-136 m.

A final uncertainty needs to be taken into account: the factor $\delta$. Taking the extremes of the observed values from Table 1 of [17] ($\delta_{min} = 0.05$ and $\delta_{max} = 0.15$) and using Eq. 2.18 (p. 22), the maximum uncertainty was calculated as $-11.5\%$ and $+7\%$ in $\lambda_{SC}$, yielding the final range of $\lambda_{SC}$ as 71 m$\leq \lambda_{SC} \leq$ 146 m.

Figure 7.2 shows the results obtained at the ANTARES site in the UV for both the July 1999 and September 1999 data. The agreement between the July and September data is very good. This was to be expected since the SC scattering length is not expected to vary significantly in clear natural waters where the concentration of impurities is small. These results are also consistent with those of other measurements, although the ANTARES measurements favour the upper end of that range. This result is no surprise given that these experiments rely upon the purification of the water, which is crucial in the accurate determination of the SC scattering length. The relatively large pore size of the filters used in the purification of the water leaves room not only for the very small impurities but also for scattering centres larger than $\lambda/20$ (the approximate upper limit for SC scattering) to remain in the so called "pure" water, and these latter could introduce an unknown but to smaller $\lambda_{SC}$ systematic shift. This effect is not present in the measurements made at the ANTARES site since they do not rely upon the purification of the water (and they only include the content of the very small impurities in the results of $\lambda_{SC}$).

Figure 7.3 shows the range of $\lambda_{SC}$ obtained when the upper limit of the range of values for $\lambda_{SC}$ from the UV (September 1999 data) is extrapolated to other wavelengths using $\lambda_{SC} \propto \lambda^{-4.63}$ and the lower limit of that range using $\lambda_{SC} \propto \lambda^{-4.01}$, representing the extremes of the wavelength dependence derived in Section 2.3.1.

[2] A similar result can be obtained from the measurements of the isothermal compressibility in [76] and Eq. 2.2 (p. 17).

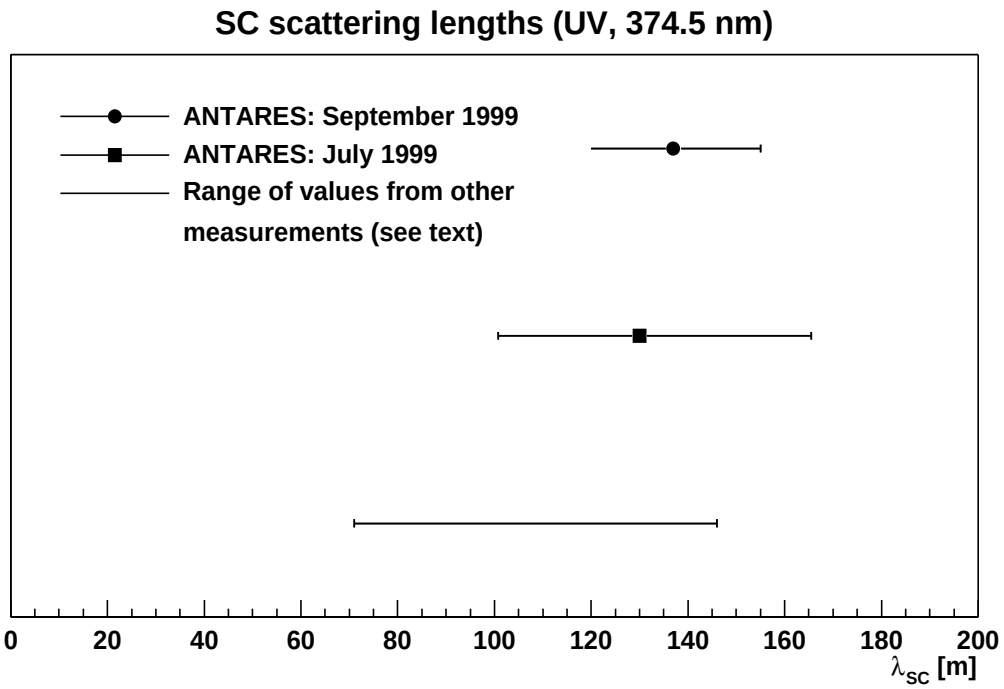


**Figure 7.2:** *SC scattering lengths at the ANTARES site, at a depth of 2400 m and a temperature of 13.1° C. The range computed from the results of various other experiments summarized in [17] is also shown (see text for an explanation).*

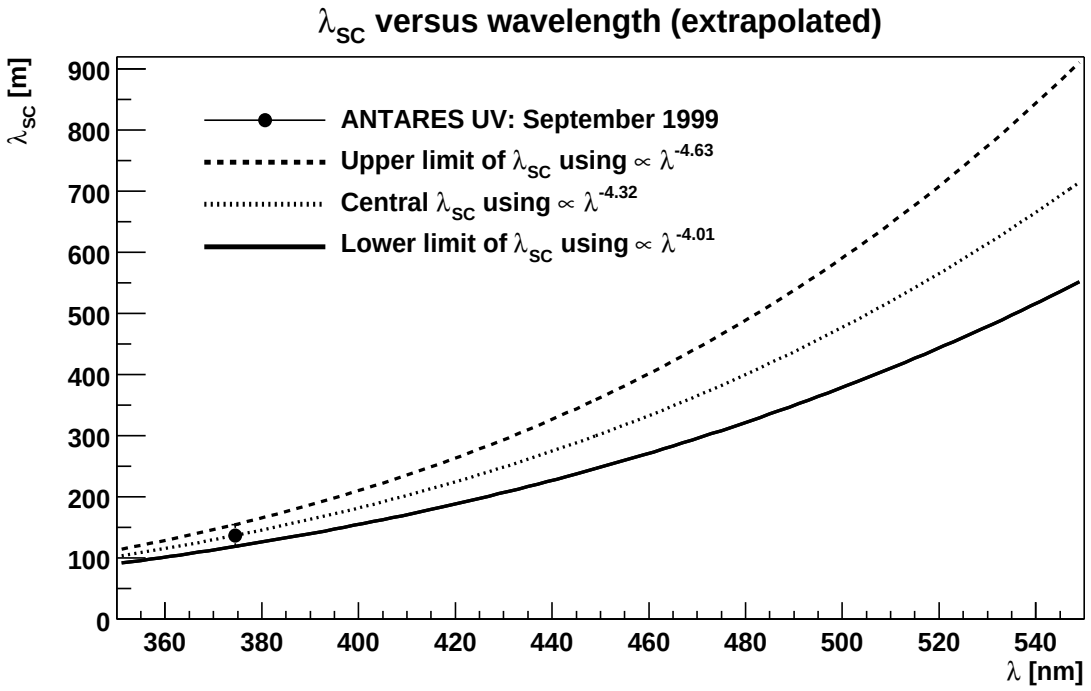


**Figure 7.3:** *Extrapolation of the SC scattering length from the measurements at the ANTARES site in the UV, using the two extreme models for the wavelength dependence of $\lambda_{SC}$ (as described in Section 2.3.1). The central value is also shown.*

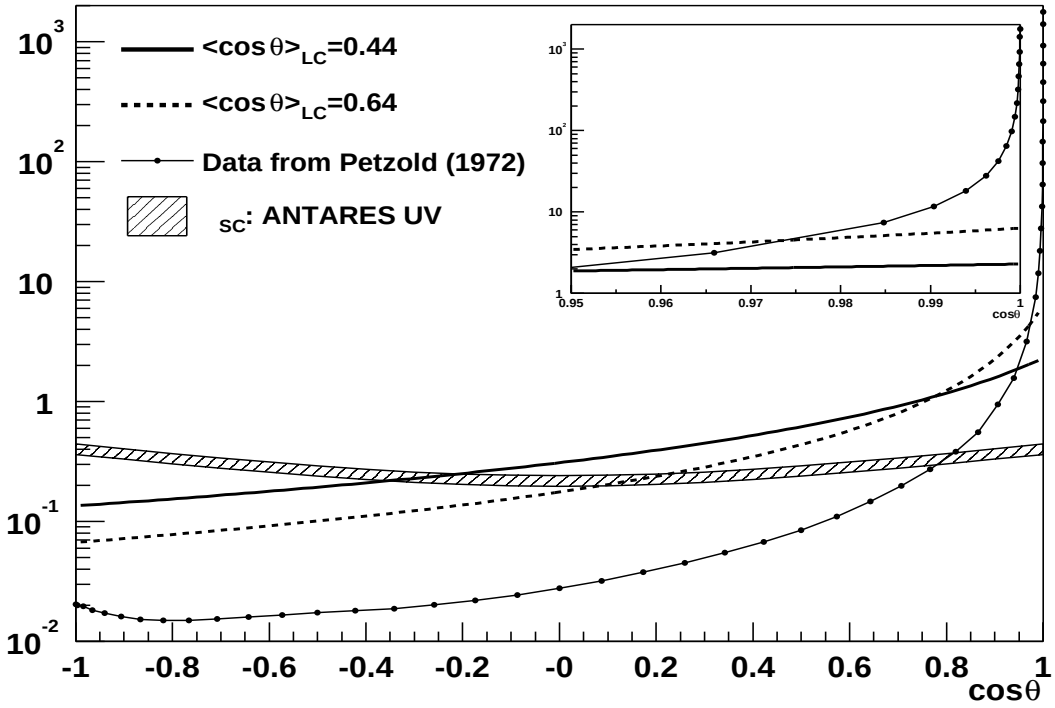


**Figure 7.4:** *Lower limit (solid line) and upper limit (dashed line) of the* $\langle \cos\theta \rangle$ *of the LC angular distribution at the ANTARES site, extracted from the September 1999 measurements at 374.5 nm. Also shown are the SC angular distributions with the correct probabilities relative to the LC angular distributions.*

## 7.4 LC Scattering

The density and size distribution of LCs, also commonly referred to as particulate impurities or "Mie" scatterers, is fairly unpredictable and strongly variable between different sites. Figure 7.4 shows a summary of the results for the range of LC scattering angular distributions obtained in the UV at the ANTARES site during the immersions in September 1999, using the model described in Section 2.7. The results at the ANTARES site yield a much less forward-peaked scattering angular distribution than the data obtained by Petzold [18] on "average" ocean waters. This can be attributed to various factors:

1. Test 3′ is unable to rule out the presence of an additional type of scatterers with a very forward-peaked scattering angular distribution.

2. The measurements by Petzold for three different waters show a significant variability in the shapes between different waters, suggesting that the use of an "average" scattering angular distribution function (computed from these three) is not appropriate.

3. The measurements by Petzold were performed at a different wavelength (514 nm) and pressure (∼160 atm) from those used in the measurements at the ANTARES

site (374.5 nm and ∼240 atm respectively), which could both have an impact upon the angular distribution.

As shown in Section 6.3.5, Test 3′ cannot make the distinction between the best water model found using a single Henyey-Greenstein function to represent the angular distribution of LC scatterers and a model in which additional scattering centres with a very forward-peaked angular distribution are present. The effective scattering length of this additional component was found to be larger than ∼17500 m. Depending upon the value of $\langle \cos\theta \rangle_{LC'}$ for these scatterers, the overall $\langle \cos\theta \rangle_{LC}^{T}$ of all LC scatterers could vary significantly. As an example, if $\langle \cos\theta \rangle_{LC'} = 0.90$ then $\langle \cos\theta \rangle_{LC}^{T} \simeq 0.57$, whilst if $\langle \cos\theta \rangle_{LC'} = 0.99$ then $\langle \cos\theta \rangle_{LC}^{T} \simeq 0.76$. The possibility that $\langle \cos\theta \rangle_{LC}^{T}$ is closer to the values found by Petzold than the results, obtained using a single Henyey-Greenstein function for the LC scattering angular distribution, suggest can thus not be ruled out with Test 3′.

The results of the scattering angular distribution measurements by Petzold show a non-negligible variation in the measured volume scattering functions (see Figure 3.13 of [32]) between turbid harbours, which exhibit more forward-peaked scattering, and clear ocean waters, with less forward scattering, yielding a range of $0.88 < \langle \cos\theta \rangle_{LC} < 0.95$. Similarly, Morel's measurements [53], shown in Figure 7.5, display a much less forward-peaked angular distribution for the clear Tyrrhenian water compared to the turbid English Channel. The range of shapes for the LC scattering angular distribution (and hence of $\langle \cos\theta \rangle_{LC}$) is thus expected to be large – a result confirmed by the ANTARES measurements with Test 3′. The results are very well in agreement with the general trend, since the ANTARES water is expected to be in the regime of very clear ocean waters, where the angular distribution is less forward peaked.

The measurements by Petzold were performed at a wavelength of 514 nm. There is however no reason to believe that the scattering angular distribution function should be independent of wavelength. Indeed, it would be expected that photons of different wavelengths probe particles of different kinds and of different sizes. The importance of this wavelength dependence is apparent from the results of Morel, shown in Figure 7.5. Although the measurement range of angles is limited to 30°-150°, the variation of the shape of the scattering angular distribution function with wavelength is clearly evident for the clear Tyrrhenian Sea, and the general trend is to cause less forward-peaked scattering for smaller wavelengths. By subtracting the SC contribution from the total angular distribution, it was shown that the shape of the LC angular distribution is indeed wavelength dependent.

In addition to the wavelength dependence, there is also evidence ([77], Figure 11) that the scattering angular distribution is less forward peaked for larger depths. One could imagine this to be due to the fact that the "same" particle under a larger pressure will be reduced in size, hence exhibiting less forward-peaked scattering properties.

In view of the impacts of the water quality, the wavelength of the light and the depth, upon the shape of the scattering angular distribution function, the results obtained from

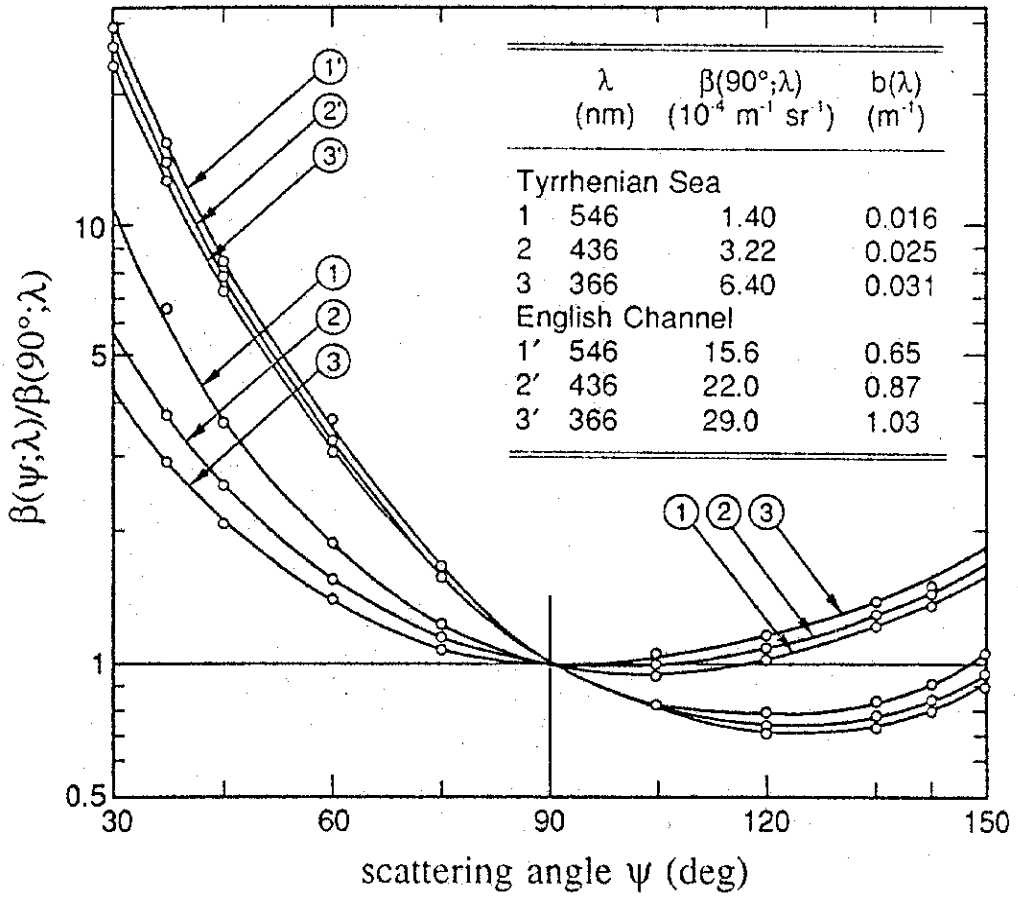


**Figure 7.5:** *Wavelength dependence of total scattering angular distribution functions measured in various waters (redrawn from [53]).*

the measurements with Test 3′ at the ANTARES site are not unreasonable and well in agreement with the general trends observed.

## 7.5 Stability of Optical Properties with Season and Depth

The optical properties deduced from the July 1999 data do not show any significant variation with respect to those from the September 1999 data: all the parameters are consistent with each other to within the statistical and systematic errors. Indeed, because the absorption length is mainly determined by the effective absorption in the water, it was not expected to vary between the July 1999 and September 1999 data, given that the effective absorption lengths (shown in Table 6.1, p. 84) were consistent with each other to within the errors. In the limit of a low content of very small impurities in the water, the SC scattering length is expected to be relatively stable since in this limit it is mainly dependent upon the compressibility and the temperature of the water. The compressibility is not expected to show any significant variations and the temperature

was measured to be very stable (see discussion in Section 2.7.3). The good agreement of the July 1999 and the September 1999 data suggests that, if such impurities are present in the water at the ANTARES site, their concentration is relatively stable. To within the large ranges of values for both the LC scattering length and the $\langle \cos\theta \rangle_{LC}$ (due to about 3 times less statistics than for the September 1999 data at the same distance) and the large systematic errors from the background-noise subtraction as well as the increased sensitivity to the LED intensity fluctuations compared to the September 1999 data, no distinction between the $\lambda_{LC}$ and $\langle \cos\theta \rangle_{LC}$ of these data and those of the September 1999 data could be made.

However, an increase in the effective absorption length from ∼22 m to ∼25 m at 374.5 nm between the Year 1999 data and the Year 2000 data was found (Section 6.2.1). These results suggest that variations in the optical properties can occur at least on the time scale of the order of one month and that regular calibration measurements with the ANTARES detector are important. Further measurements are needed to quantify the time scale of these variations.

The indications are that the optical properties are relatively stable as a function of depth (Section 6.6) over the range of the instrumented ANTARES detector (2100 m to 2400 m). From the theory, the impacts of the variation in pressure upon the SC scattering length and the refractive index over the range of the two depths are small. The pressure difference between the immersions at the two depths is of the order of 30 bar and leads to a change in the $\lambda_{SC}$ of ∼0.4% (using the results on the pressure dependence of the pure water scattering lengths from [56]). The variation of the refractive index with pressure was calculated to be less than 0.2% using Eq. 2.23 (p. 35). The apparent stability of the remaining parameters seems to suggest that the water layers at those depths are fairly homogeneous. Additional measurements are however needed to verify these results.

## 7.6 ANTARES Detector Performance

From the current measurement results at UV wavelengths, the absorption length is known within ∼5%, yielding uncertainties in the detection efficiency of photons at 60 m distance from their point of emission of the order of 12% (UV) and 7% (blue). At high energies, where sufficient photons are emitted by the muons, this effect is expected to be negligible. At lower energies, detailed detector simulations are required to quantify this effect.

The average scattering length from the measurements in the UV is $76.5 \pm 6.8$ m and the average cosine of the total angular distribution is $0.24 \pm 0.05$. The water optical properties in the blue (where the ANTARES detector is most efficient) are not expected to be less favourable than in the UV from which, using the results from Figures 1.6 (p. 10) and 1.7 (p. 11), the accuracy on the detector efficiency is estimated at 20% and on the neutrino angular resolution at 0.1°, with an overall resolution better than 0.65° for 1 TeV neutrinos and 0.25° for 100 TeV neutrinos. The optical properties are thus not expected to be a significant limitation to the ANTARES detector performance.

## 7.7 Future Measurements

For further measurements with Test 3′, as well as future calibration measurements of the optical properties with the ANTARES detector, various factors should be considered:

1. **Calibration:** Accurate measurements of several air spectra under very carefully controlled conditions are needed for each configuration to avoid the loss of data like the June 2000 data. In this respect, measurements at longer source-detector distances would be beneficial, since they are less susceptible to the accurate measurement of these air calibration spectra. This is because the larger the distance, the larger the fraction of scattered photons compared to direct photons, causing the shape of the air spectra to be smeared out and thus to be less crucial in the accurate determination of the optical parameters.

2. **Wavelengths:** For a complete understanding of the ANTARES detector performance, it is essential to measure the optical properties at various wavelengths over the wavelength range of sensitivity of the ANTARES detector (350-550 nm), since the variation of the optical properties with wavelength is not yet fully understood. For the measurements with Test 3′, it is essential to choose the appropriate source-detector distance for each wavelength for optimal results[3]: at blue wavelengths for example, measurements at larger distances than 44 m are important, since the scattering parameters are expected to be larger than those in the UV, making the distinction between the optical parameters at the distances used in the UV measurements more difficult. The problem with the current blue LEDs of Test 3′ and their driver should be investigated. A narrower pulse width from these LEDs is essential for an accurate discrimination between the optical parameters.

3. **Depth and seasonal variations:** Although no variations in the optical properties were found between the currently available measurements at two different seasons and at two different depths, more data with much better statistics are needed for a better understanding of these factors.

In addition to the above considerations for further measurements with Test 3′ and measurements with the future ANTARES detector, by far the most useful measurements to improve the understanding of the optical properties at the ANTARES site would be in situ measurements of the scattering angular distributions at the correct wavelengths. These would eliminate any uncertainties about the actual shape of the scattering angular distribution, which could only be assumed in the measurements with Test 3′ (e.g. small-angle scattering, which Test 3′ cannot distinguish, would be resolved). With one less variable parameter, the required computing times would be reduced by a factor of $\sim$15, making it possible to obtain better statistics with less CPU time. The measurements of the scattering angular distribution could possibly be done with an adapted version of the experiment described in [18], although the technical implications for such a design would clearly be huge.

[3] For the calibration with the future ANTARES detector, many different distances will be available automatically.

## 7.8 Summary

In this chapter, the results of the measurements of the optical properties at the ANTARES site were discussed and compared to those of other experiments. Based on the expectations from other experiments, a good agreement was found for the absorption length (Section 7.2) and the SC scattering length (Section 7.3). The results obtained for the $\langle \cos\theta \rangle_{LC}$ at the ANTARES site were shown to be in good agreement with the general trends of various measurements of angular distributions under different purity conditions, at different depths and at different wavelengths (Section 7.4). From the measurements at different seasons and different depths at the ANTARES site, no significant variations in the optical properties could be detected (Section 7.5). The optical properties measured at the ANTARES site were briefly related to the ANTARES detector performance (Section 7.6). Ideas to improve the current knowledge of the optical properties at the ANTARES site were discussed (Section 7.7).

# Conclusions

*Given so much time, the "impossible" becomes possible, the possible probable, and the probable virtually certain. One has only to wait: time itself performs miracles.*

*G. Wald (1906-1997)*

In the present study, a stand-alone experiment was described to measure the optical properties in situ, at a depth of 2400 m, at the ANTARES site. The measurements were performed at two different wavelengths: 374.5 nm, close to the cut-off of light transmission through the OM, and 472.6 nm, close to the expected wavelength of maximum OM detection efficiency of Cherenkov light in water. However, only the former could be fully analysed. A robust analysis method was developed for these data, separating the optical properties into four components: an absorption length, a scattering length for SCs and a scattering length for LCs as well as its angular distribution (the angular distribution of SCs was fixed).

The quality of the water, summarized in Table 8.1 through the parameters describing the optical properties at the ANTARES site, was found to be very close to that of the purest natural waters: the absorption lengths (at 374.5 nm and 472.6 nm) and the SC scattering length (at 374.5 nm) were shown to be close to the upper range of values found for typical natural waters and for purified samples of water respectively. The absorption length at 374.5 nm was found to be about 50% of the horizontal distance between the

| *Parameter* | *UV (374.5 nm)* | *Immersion* | $\lambda_A^E$ [m] |
|---|---|---|---|
| $\lambda_A$ [m] | $25.9 \pm 0.5 \pm {}^{1.2}_{1.1}$ | July 1999 (UV) | $20.9 \pm 0.2$ (stat.) $\pm^{1.1}_{1.0}$ (syst.) |
| $\lambda_{SC}$ [m] | $137 \pm 6 \pm {}^{17}_{17}$ | Sept. 1999 (UV) | $21.8 \pm 0.1$ (stat.) $\pm^{0.7}_{0.5}$ (syst.) |
| $\lambda_{LC}$ [m] | $173 \pm 10 \pm {}^{17}_{17}$ | June 2000 (UV) | $25.2 \pm 0.1$ (stat.) $\pm^{0.8}_{0.6}$ (syst.) |
| $\langle\cos\theta\rangle_{LC}$ | $0.54 \pm 0.05 \pm {}^{0.08}_{0.08}$ | June 2000 (blue) | $46.0 \pm 0.4$ (stat.) $\pm^{2.4}_{2.0}$ (syst.) |

**Table 8.1:** *Left two columns: optical parameters at the ANTARES site at 374.5 nm (UV), September 1999. Right two columns: effective absorption lengths for the immersions at 374.5 nm and 472.6 nm (blue).*

strings of the ANTARES detector and at 472.6 nm approximately equal to the spacing between them. At 374.5 nm, the scattering length between LCs was found to be large compared to the distance between the individual strings of the detector and of the same order of magnitude as the maximum horizontal extension of the instrumented volume of the 10-string detector. The SC scattering length was found to be about 20% smaller than this. The average scattering length (at 374.5 nm) was found to be of the same order of magnitude as the distance between the individual strings. The angular distribution of LCs at a wavelength of 374.5 nm was shown to be in good agreement with the general trend for the experimental conditions at the ANTARES site, yielding average scattering angles of $\sim 57^\circ$ (excluding very forward-peaked scattering) compared to average scattering angles of $\sim 23^\circ$ at a wavelength of 514 nm.

Once the ANTARES detector is operational, the optical properties are planned to be monitored on a continuous basis using laser beacons at the bottom of each string, together with a dedicated instrumentation line which will host a LED ball as well as a laser beacon. This will yield the opportunity to make detailed measurements of the arrival time distributions of the photons emitted by each of these light sources at many distances simultaneously. The MC code and the analysis method developed in this thesis will provide essential tools for the analysis of these arrival time distributions.

**In conclusion, with the experiment described in this thesis, it was possible to extract the absorption length, the scattering length and (under general assumptions about the shape) a scattering angular distribution separately. These results are essential for a complete understanding of the performance of the ANTARES detector, given the different impact of each of the optical parameters upon it. Given that the optical properties in the blue are not expected be less favourable than in the UV, the accuracy on the detector efficiency is expected to be better than 20%, and the overall angular resolution is expected to be better than 0.65° at 1 TeV and 0.25° at 100 TeV, with an uncertainty of less than 0.1°, hence keeping the ANTARES detector angular resolution below its projected aim of sub degree.**

**The analysis method developed in this thesis, for the measurements of the in situ water optical properties at the ANTARES site, was found to be powerful and, in addition to being an essential tool for the analysis of future measurements with Test 3′ (and improved versions thereof), is expected to be very useful for the continuous monitoring of the optical properties with future calibration measurements using the ANTARES detector.**

# Appendix A

# Details of the TDC

This appendix describes the details of the TDC of the Test 3′ experiment, supplementing the description in Section 3.5.1.

During the data acquisition, for each trigger of the LEDs, the FPGA sends a signal to the TDC to start the ATW. A few clock cycles later, the FPGA sends out another signal which is split into a TTL signal, sent to one of the inputs of the TDC, and a low voltage differential signal, sent via a 50 m long twisted pair electrical cable to the driver in the LED sphere (to pulse the LEDs). During the ATW of the TDC, it can register the front edge of several TTL signals and latch each of them into a register.

The TDC has two input channels. One was used for the trigger of the LEDs and the other for the PMT signal. Each signal is time-stamped and latched into the internal FIFO register of the TDC. The TDC registers the time of arrival of each signal that triggers the TDC in the order in which they arrived, irrespective of whether this signal came from the first or the second input to the TDC: it is unable to distinguish between these two inputs. Whilst several TTL signals can be registered by the TDC during each ATW, there is a dead time of about 50 ns between any two signals. The cause for this dead time is that it takes the TDC approximately 2 clock cycles to latch any time-stamped event into its FIFO. During this time, no other signal can be time stamped. In the Test 3′ experiment, most of the photons arrive within 20 ns and therefore the 50 ns dead time effectively limits the use of the TDC to single-hit measurements.

A certain time interval before the end of the ATW (predefined in the software of the FPGA), the FPGA reads the FIFO of the TDC and addresses the results via a data bus to the MBX, where the results are stored on a RAM chip. The time of this process varies with the number of hits registered by the FIFO of the TDC and can even extend the ATW. The FIFO must be emptied whilst the ATW is open. To ensure that the FPGA was given sufficient time to retrieve the data from the TDC FIFO and to put them into its own FIFO before the FPGA was read by the MBX, a software controlled delay was introduced into the readout of the FPGA FIFO by the MBX.

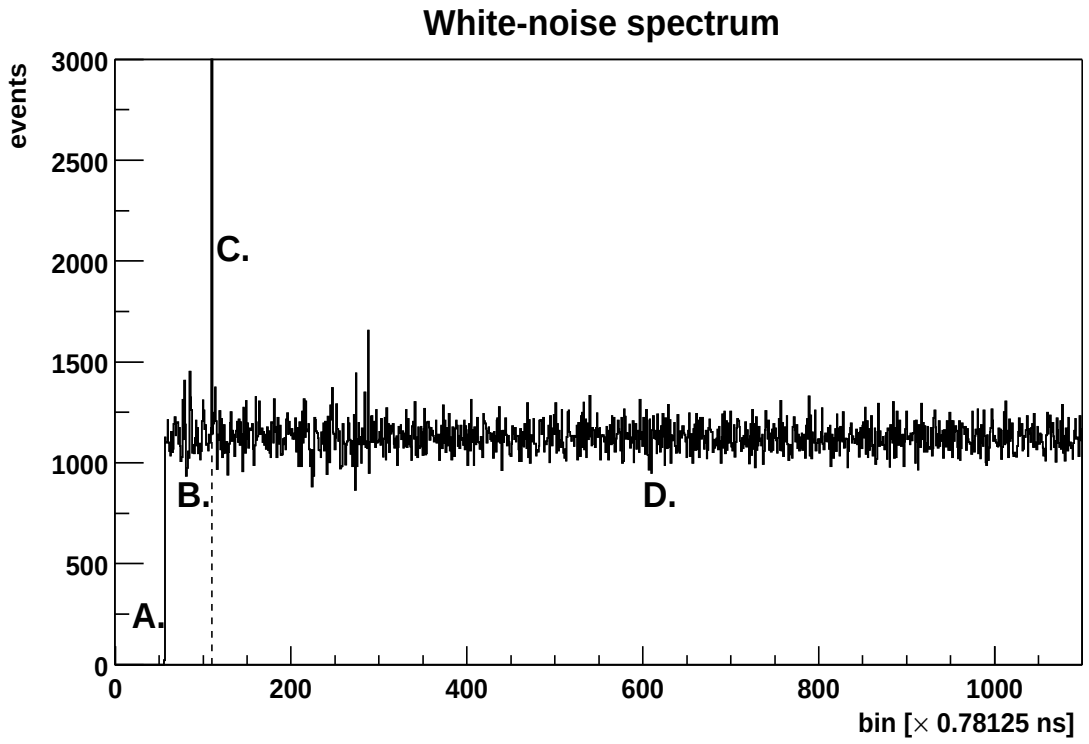


**Figure A.1:** *White-noise spectrum taken in a dark room in the laboratory. Three regions (A., B. and D.) and a peak (C.) can be distinguished (see text).*

To study the acquisition electronics, a series of white-noise spectra were taken under controlled random diffuse background light conditions in a darkened laboratory with the LEDs switched off, causing photons to be randomly detected across the spectrum. Figure A.1 shows a typical spectrum acquired with setup A (described in Section 3.2), where the events registered in the histogram are "second" hits. In general, this hit corresponds to the PMT trigger of the TDC, because it usually arrives after the LED trigger[1]. However, due to a specific delay between the time at which the ATW of the TDC is started and that at which the LED trigger is sent to the TDC, there is time for a random background hit to produce the first input to the TDC, in which case the LED trigger becomes the second input. This can be seen in Figure A.1 as a large spike in bin 110 (C.): the LED trigger consistently produces a trigger in one bin only, showing the stability of its time stamp[2]. The hits in region B. correspond to events where two background hits were registered by the TDC before the LED trigger.

The absence of hits in region A. of the spectrum (bins 0 to 56) is explained by the fact that, due to the dead time (a little less than 2 clock cycles) of the TDC between two consecutive hits, the first hit to be registered in the second register comes after

[1]Note that the time of the LED trigger registered by the TDC is different from the time at which the LEDs are pulsed, since the signal triggering the LEDs must travel through 50 m of electrical cable before pulsing the LEDs.

[2]This feature was eliminated for setups B and C (Table 3.1, p. 47) by removing the LED trigger cable from the input to the TDC and registering the first event instead.

approximately 44 ns (corresponding to bin 56), because it must necessarily be preceded by a signal filling the first register of the TDC FIFO.

The slight slope which appears in the the white-noise spectrum is attributable to the single-hit nature of the TDC (as discussed in Section 4.2), which favours earlier hits over later hits. The amount by which the detection rate of earlier photons is larger than that of later photons depends upon the overall trigger rate of the TDC (i.e. upon the event rate).

For the data shown on the right-hand plot of Figure 4.1 (p. 57), a different configuration was used (corresponding to that of setups B and C). Only the PMT trigger cable was connected to the TDC (the cable for the trigger signal from the LEDs was disconnected) and the first hit was registered. From the previous discussions, this explains why hits are observed in bins 0 to 56 with this configuration. The slight excess of events in those bins was attributed to a small electronic defect, causing the TDC to register a most significant bit as zero when it should have been non-zero for approximately 0.3% of all events, uniformly across the spectrum.

# Appendix B

# Angular Efficiency of the Detector Sphere

This appendix describes the MC code that was developed to simulate the angular efficiency of the detector sphere of the Test 3′ experiment. Photons are tracked individually from the outside medium and refracted at the various interfaces. The photon detection efficiency of the PMT is taken into account, using the results from various measurements of the thickness and the complex refractive index of several photocathodes by other experiments.

The detector used in the measurements of the light transmission properties at the ANTARES site (Figure B.1) is a 17″ diameter pressure-resistant glass sphere (PRGS), with a thickness of ∼15 mm. It houses a 30 mm diameter PMT with a biakali photocathode (ETL-9125SA). This tube is glued to the PRGS by means of optically matching silicone rubber gel from Wacker[1]. The angular efficiency of this PRGS is not known because of the practical difficulties associated with measuring it in water and was therefore computed with MC simulations. The tabulated results from these simulations were used in the analysis of the Test 3′ data.

The average photon detection efficiency at each angle was simulated in 1° steps between 0 and 90° with respect to the normal to the PMT plane. For each angle, a parallel beam of photons of the same diameter as the PRGS (Figure B.2) was simulated and the average number of photon hits was recorded. Because the beam covers the entire sphere, any refractions and reflections that could lead to the detection of photons (which would otherwise not have reached the PMT) were taken into account.

For each angle, $5 \times 10^7$ photons were randomly chosen from within the beam cross section of radius $r$, by drawing from a $\sqrt{r}$ distribution to sample uniformly over the surface area. Each of these photons was propagated to the outer surface of the sphere. The coordinates of the point of impact as well as the angle of incidence with respect to the normal to the sphere surface at the point of impact were calculated.

[1]Reference SilGel 612 A/B, Wacker-Chemie GmbH, Hans-Seidel-Platz 4, 81737 Munich, Germany.

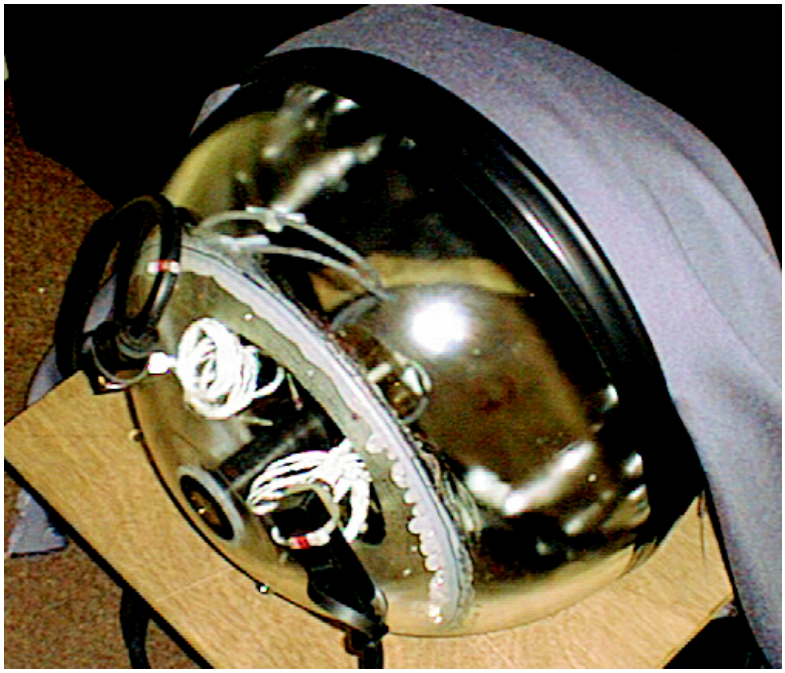

**Figure B.1:** *The detector OM incorporating a ETL-9125SA 30 mm PMT for Test 3′.*

To take into account the unpolarized nature of the light source of Test 3′, the photon's state of polarization was randomly chosen, with a 50% probability of being either in the parallel or perpendicular state. This was important because of the different reflection and transmission probabilities at the various interfaces, as well as the different PMT detection efficiencies, between the photons with different polarization states.

The photon's wavelength was randomly chosen from the source's wavelength spectrum (Figure 3.5, p. 43) and the refractive index of the water, corresponding to its wavelength, was determined from Eq. 2.23 (p. 35). Using the refractive index of the glass sphere (1.47 for the wavelength range $300 < \lambda < 600$ nm [20]) and the refractive index of the water, the transmission probability at the water-glass interface was calculated from [78]

$$T_{\parallel} = \left(\frac{n_t cos\theta_t}{n_i cos\theta_i}\right) \times \left(\frac{2n_i cos\theta_i}{n_i cos\theta_t + n_t cos\theta_i}\right)^2 \quad \text{and} \tag{B.1}$$

$$T_{\perp} = \left(\frac{n_t cos\theta_t}{n_i cos\theta_i}\right) \times \left(\frac{2n_i cos\theta_i}{n_i cos\theta_i + n_t cos\theta_t}\right)^2, \tag{B.2}$$

for the parallel and perpendicular polarization states of the photons respectively, where $n_i$ and $n_t$ are the refractive indices of the medium of the incident and of the transmitted photon respectively, and the angles are with respect to the normal to the surface at the interface.

The photon was then refracted and propagated until it reached the glass-gel interface. Once again, the angle of incidence with respect to the local normal was calculated. The

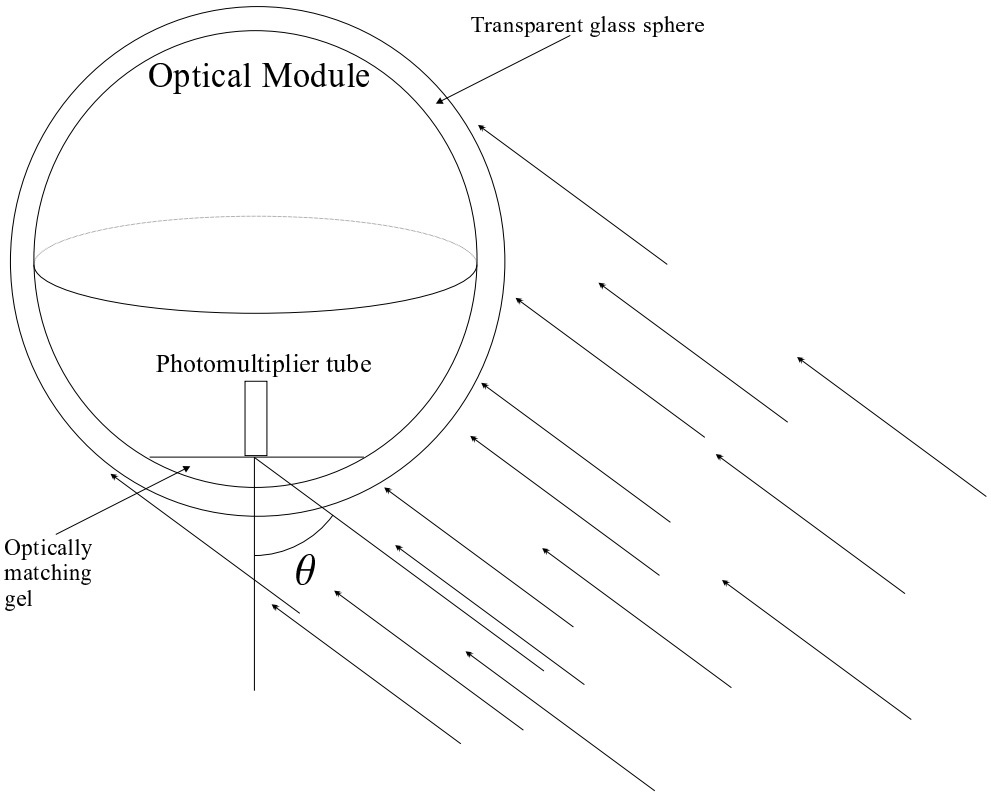


**Figure B.2:** *Sketch of the detector OM used in the measurements with Test 3′. In the simulations, the incident photon flux is uniform over the entire surface area of the OM. Each of a large number of photons is tracked individually until it is either lost or registered by the PMT with its appropriate weight, yielding an average detection efficiency for each angle (see text).*

transmission probability was calculated and the direction of propagation of the photon was adjusted for the refraction at the interface, using the nominal refractive index of 1.404 for the gel [20]. If the photon's direction was such that it reached the PMT, the probability of not being absorbed in the glass or the gel was calculated using

$$p_{trans} = e^{-\frac{d_G}{\lambda_G}} \times e^{-\frac{d_g}{\lambda_g}}, \tag{B.3}$$

where $\lambda_G \approx 0.35$ m (resp. 0.45 m) and $\lambda_g \approx 0.46$ m (resp. 0.74 m) are the absorption lengths in the glass and gel respectively at the UV (resp. blue) wavelengths (see Figure 2.1, p. 15), and $d_G$ and $d_g$ are the distances traveled by the photon in the glass and the gel respectively.

The detection efficiency of the photon by the PMT was then taken into account. This detection efficiency varies with the angle of incidence upon the photocathode (PC) due to the different photon absorption probabilities in the PC layer. The efficiency is dependent upon the refractive index of the PMT glass and the complex refractive index of the PC layer as well as its thickness. The complex refractive index $n_{real} + i\, n_{imag}$ of the PC layer

| *Parameter* | *Value* |
|---|---|
| $\alpha_{real}$ | 8.493 |
| $\beta_{real}$ | $-1.1957 \times 10^4$ |
| $\gamma_{real}$ | $8.0152 \times 10^6$ |
| $\delta_{real}$ | $-1.6849 \times 10^9$ |
| $\alpha_{imag}$ | 5.6859 |
| $\beta_{imag}$ | $-1.0532 \times 10^4$ |
| $\gamma_{imag}$ | $6.0645 \times 10^6$ |
| $\delta_{imag}$ | $-9.8148 \times 10^8$ |

**Table B.1:** *Table of coefficients from the fits of Eqs. B.4 and B.5 to the PC complex refractive index data from Moorhead and Tanner.*

was calculated by using the results from the fit of the following function to the Moorhead and Tanner data [75]:

$$n_{real}(\lambda) = \alpha_{real} + \frac{\beta_{real}}{\lambda} + \frac{\gamma_{real}}{\lambda^2} + \frac{\delta_{real}}{\lambda^3} \quad \text{(B.4)}$$

$$n_{imag}(\lambda) = \alpha_{imag} + \frac{\beta_{imag}}{\lambda} + \frac{\gamma_{imag}}{\lambda^2} + \frac{\delta_{imag}}{\lambda^3}, \quad \text{(B.5)}$$

where the various parameters are given in Table B.1[2] and $\lambda$ is the wavelength in [nm]. This complex refractive index was used in the calculation of the PC efficiency, using the results described in [79] and taking the PC thickness as 23 nm.

It should be noted that in the above simulations, only direct photons, i.e. those which were not reflected at any of the interfaces, were tracked to the PMT. Photons which were reflected at the water-glass interface were considered to be lost, because the probability of being scattered back into the sphere is very small due to the large ratio of absorption to backscattering in the water. Photons that are reflected at the glass-gel interface technically could still reach the detector. However, at worst 1.9% of the photons are reflected before reaching the plane of the PMT cathode, of which at most 16% are reflected back into a direction such that they could reach the PMT. The maximum percentage of neglected photons is therefore 0.3%, of which most will not even reach the PMT, because only photons that have an angle of incidence close to the normal to the PMT plane are reflected at both interfaces such that they hit the PMT. Moreover, photons which are reflected twice before reaching the detector are more likely to be absorbed due to the increased path length. The detection efficiency of these indirect photons was thus found to be very small and was therefore neglected in the high-statistics simulations of the OM angular efficiency spectrum.

Figure B.3 shows the overall average photon detection efficiency of the OM (solid line) as a function of the angle of incidence with respect to the normal to the PC plane. The

[2] This is the same parametrisation as the one used by the SNO Collaboration in their MC.

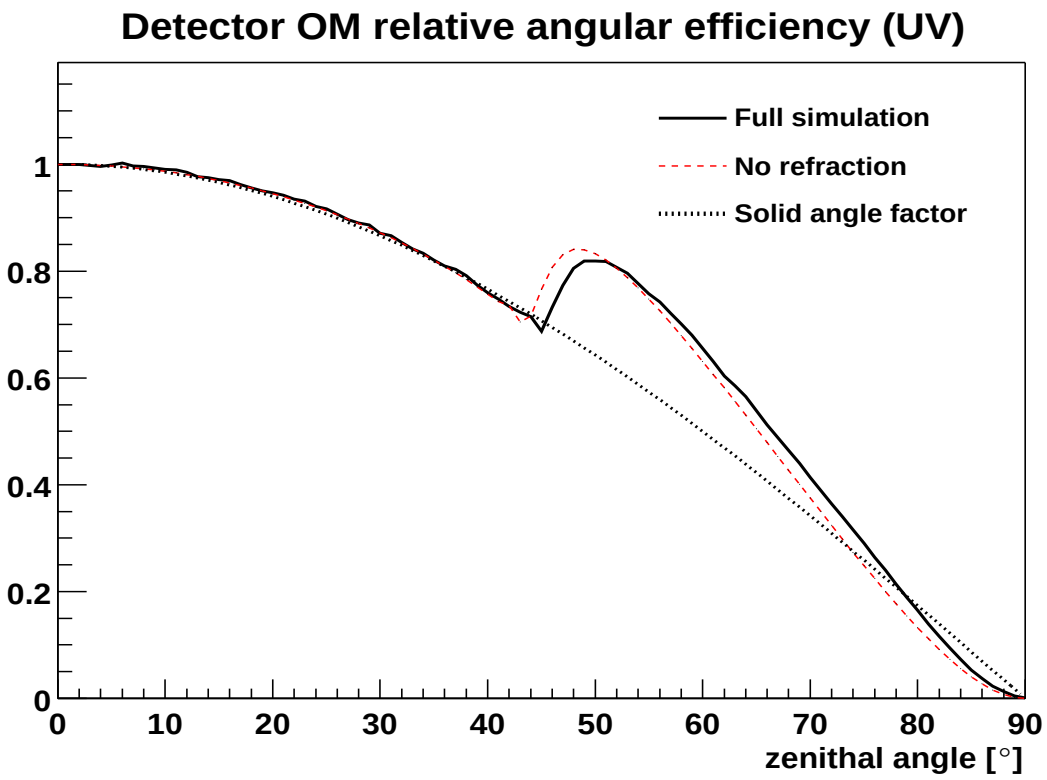


**Figure B.3:** *Simulated relative average detector efficiencies as a function of the angle of incidence with respect to the normal to the PMT plane at a central wavelength of the source of 374.5 nm.*

efficiency when the refraction at the interfaces is neglected is also shown (dashed line). The dotted line is a cosine curve, corresponding to the relative surface area of the PMT as a function of the angle of incidence. The difference between neglecting refractions (and reflections) at the various interfaces and a full MC simulation including these factors is relatively small, and the main difference between the cosine curve and the full simulation comes from the PC detection efficiency. An estimate of the potential systematic errors associated with the choice of model described in this appendix is given in Section 6.3.4.

# Appendix C

# Sampling from Discrete Distributions

This appendix describes two different methods for sampling randomly from discrete distributions. One of the methods is shown to reproduce the input distribution with much better accuracy.

To randomly sample from a given function $f(x)$, a random number $r$ between 0 and 1 is drawn and compared to the value $x$ of the cumulative function normalised to unit area. The value of the cumulative function $c(x)$ at $x$ is determined by

$$c(x) = \frac{\int_0^x f(x')dx'}{\int_0^\infty f(x')dx'}. \tag{C.1}$$

If the continuous function is replaced by a discrete distribution $f(x_i)$, a similar procedure can be applied. It is however important not to create the cumulative distribution $c(x_i)$ by simply summing over the individual bins:

$$c(x) = c(x_{i-1}) + f(x_i), \tag{C.2}$$

(where $x_{i-1} < x < x_i$)[1] as this creates a flat rate between the discrete points $x_{i-1}$ and $x_i$ of the sampled distribution (as shown in Figure C.1). A better approximation of the original distribution can be obtained by replacing the discrete sum by an integral, such that for any value $c(x)$ between $x_{i-1}$ and $x_i$

$$c(x) = c(x_{i-1}) + \int_{x_{i-1}}^{x} f(x')dx', \tag{C.3}$$

[1]It was implicitly assumed in the above expression that the distribution was previously normalised to unit area.

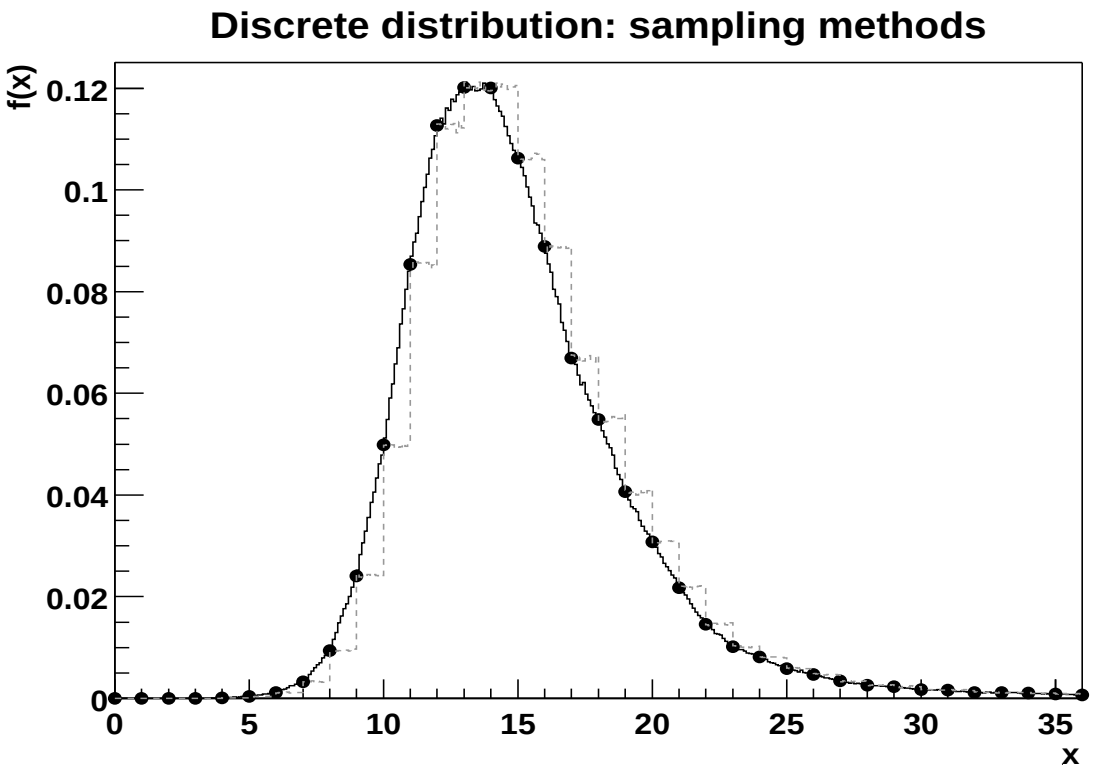


**Figure C.1:** *Distributions obtained when sampling randomly from a discrete distribution (dots), using the sum over the discrete bins in the original distribution to create the cumulative distribution (dashed line) and calculating the appropriate area under the original distribution to create the cumulative distribution (solid line).*

where $f(x')$ is obtained by interpolating linearly between the adjacent points of the original distribution:

$$f(x) = f(x_{i-1}) + \frac{f(x_i) - f(x_{i-1})}{x_i - x_{i-1}} \times (x - x_{i-1}). \tag{C.4}$$

Combining Eq. C.3 and Eq. C.4, $c(x)$ can be written as

$$\begin{aligned} c(x) &= c(x_{i-1}) + f(x_{i-1}) \times (x - x_{i-1}) + \frac{f(x_i) - f(x_{i-1})}{x_i - x_{i-1}} \times \frac{(x - x_{i-1})^2}{2} \qquad \text{(C.5)} \\ &= \left[ c(x_{i-1}) + x_{i-1} \left( \frac{x_{i-1}}{2} \times \frac{f(x_i) - f(x_{i-1})}{x_i - x_{i-1}} - f(x_{i-1}) \right) \right] \\ &\quad + x \times \left[ f(x_{i-1}) - x_{i-1} \frac{f(x_i) - f(x_{i-1})}{x_i - x_{i-1}} \right] \\ &\quad + \frac{x^2}{2} \times \left[ \frac{f(x_i) - f(x_{i-1})}{x_i - x_{i-1}} \right]. \qquad \text{(C.6)} \end{aligned}$$

If $r$ is the sampled random number between bins $x_{i-1}$ and $x_i$, the corresponding value $x$ is computed by solving for $r = c(x)$ in Eq. C.6, which can be rewritten as

$$r = \gamma + \beta x + \alpha x^2. \tag{C.7}$$

The value $x$ for the sampled value $r$ is thus:

$$x = \frac{-\beta \pm \sqrt{\beta^2 - 4\alpha(\gamma - r)}}{2\alpha}. \tag{C.8}$$

Only one of the two solutions will yield a solution consistent with $x_{i-1} < x < x_i$ (which is the correct value!).

Using the sampling technique described above, the original distribution could be very accurately reproduced without the steps (as shown on Figure C.1).

# Appendix D

# Spread in $\chi^2$ versus Monte Carlo Statistics

This appendix describes some of the limitations of the $\chi^2$ test in the comparison of a distribution of events (the data) with another distribution with much larger statistics (the MC). A large number of MCs differing only by their starting seed for the random number generator are compared to the data. The resulting spread in the $\chi^2$ distribution is investigated for different MC statistics. The impact of this spread upon the analysis of the Test 3′ data are explained, showing that very large statistics are needed to obtain a $\chi^2$ value that is not limited by these fluctuations.

Let $x_1, x_2, ..., x_n$ be the data points of an experimental distribution which is to be analysed with MC simulations having $n$ different variables, using the $\chi^2$ test to find the parameter combination which yields the best fit to the data. If the MC simulations are replaced by a function $f_i(p_1, p_2, ..., p_n)$, the best value for each of the parameters $p_1, p_2, ..., p_n$ is found by minimizing the $\chi^2$ defined by

$$\chi^2(p_1, p_2, ..., p_n) = \sum_i \frac{[x_i - f_i(p_1, p_2, ..., p_n)]^2}{\sigma_i^2} \tag{D.1}$$

with respect to each of the parameters, where the sum is over all bins $i$ and the $\sigma_i$ are the errors on the theoretical prediction of the number of entries in each bin[1]. The error on each of the parameters is found from the required change in the parameter to give a $\chi^2$ larger than the minimum by 1 (yielding a 68% confidence interval that the true value of the parameter is included in the chosen results).

When the number of entries in each bin are obtained from some statistical distribution (e.g. a MC simulation), in general, they will not correspond to the true mean (unless the

[1]For reasons explained in [68] (pp. 103-104), they are however usually estimated from the observed number of events instead.

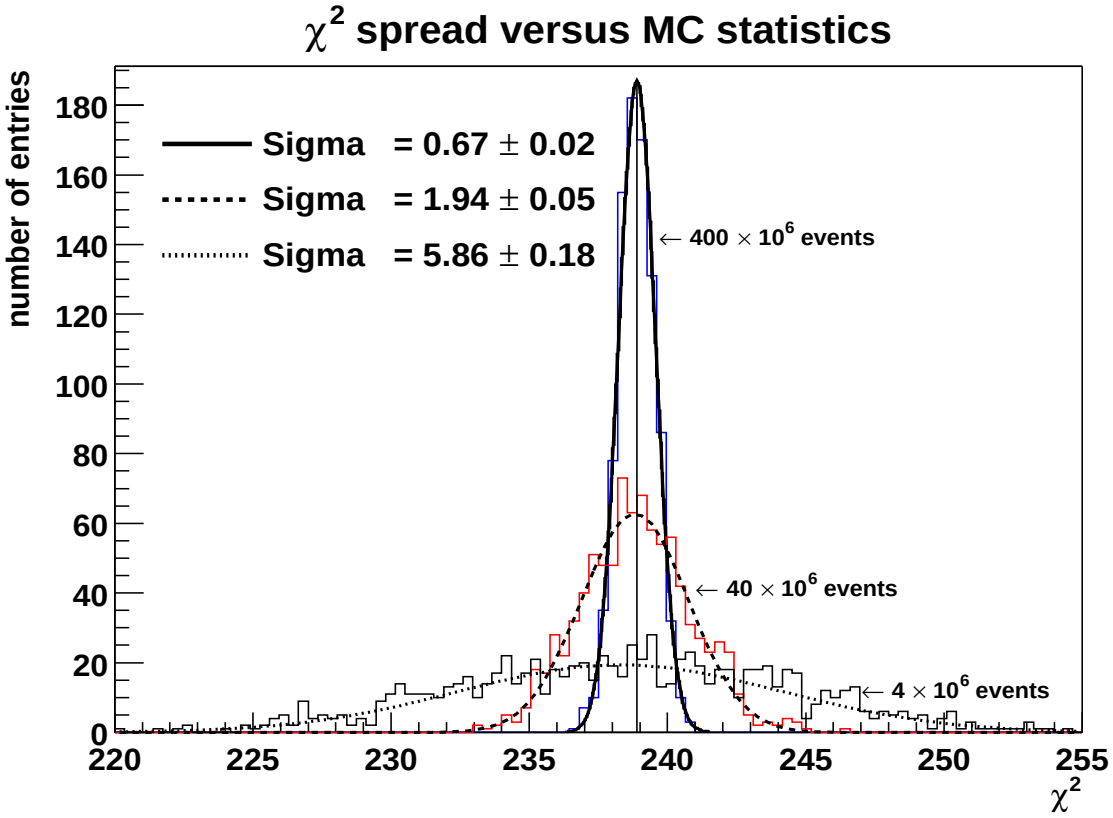


**Figure D.1:** *Spreads in $\chi^2$ values from the analysis of a distribution of $1.8 \times 10^5$ events, sampled from a straight line (the simulated experimental data), with three different sets of "MC" distributions, sampled from the same line, with 4M, 40M and 400M events respectively. For each set, 900 distributions with identical input parameters (i.e. offset and slope) but different starting seeds for the random number generator were produced.*

statistics is infinite). Instead, when the MC simulations are repeated many times with the same set of parameters but different starting seeds for the random number generator, a spread in the number of entries for each bin is obtained. In the limit of an infinite number of repetitions, the mean of this spread of values corresponds to the true mean. However, unless the MC statistics is infinite, the value of the true mean is not known and the $\chi^2$ will depend upon the best estimate of the mean (which can vary) rather than the actual mean, causing the $\chi^2$ to fluctuate.

To analyse the effect of the MC statistics upon the $\chi^2$ in the analysis of a data distribution, $1.8 \times 10^5$ events ("the data" distribution) were sampled from a line segment with a given slope. This distribution was analysed with a distribution obtained from the same segment but sampling much larger statistics (the "MC" distribution). Nine hundred "MC" distributions from the same segment but with different seeds for the random number generator were produced and each was compared to "the data", using Eq. D.1 to calculate the $\chi^2$. Figure D.1 shows the spread in $\chi^2$ values for several levels of statistics of the "MC" distributions, where the $\sigma_i^2$ in Eq. D.1 were taken as $\sigma_{data}^2(i) + \sigma_{MC}^2(i)$, the

statistical errors on the number of entries of the "data" and the "MC" added in quadrature. The errors on the "MC" distributions reflect the uncertainty in the theoretical estimate of the number of entries in each bin. The means of all three $\chi^2$ distributions are identical, but the spread varies from $\sigma^N(\chi^2) = 5.86 \pm 0.18$ for $N = 4M$ samples to $\sigma^N(\chi^2) = 0.67 \pm 0.02$ for $N = 400M$ samples, scaling very approximately as

$$\frac{\sigma^{N_1}(\chi^2)}{\sigma^{N_2}(\chi^2)} \approx \sqrt{\frac{N_2}{N_1}}. \tag{D.2}$$

In addition to the MC statistics, the $\chi^2$ spread also depends upon the number of bins in the distributions, because the spread is effectively added in quadrature for each bin. In general, the required MC statistics thus depends upon the number of bins in the data and the larger this number, the larger the statistics required to keep the spread at a sufficiently low value.

When MC distributions are used to find the best set of parameters (which in the case of the line segment are its offset and slope), call it the "model", for the data distribution, and only one MC distribution is produced for each model, the $\chi^2$ corresponds to a random choice from the distribution of Figure D.1. If the parameters are varied to find the best model (determined by the minimum $\chi^2$) for the "data" distribution, the danger is that the parameters yielding the minimum $\chi^2$ merely correspond to the model which gave the largest fluctuation downwards in the $\chi^2$ and that these parameters are not necessarily close to the actual best fit (see [80] for more details).

The required statistics to overcome this problem are extremely large. As an example, to reduce the $\chi^2$ spread in the case of the linear distribution to $\sim$0.1, it is necessary to draw of the order of $10^{10}$ events for "data" with $1.8 \times 10^5$ events, i.e. about $10^5$ times the "data" statistics!

# Appendix E

# Photon Propagation – Analytical Model

This appendix describes an analytical model for the analysis of the Test 3′ data for the specific case where multiple scattering can be neglected. It then discusses the validity of this model by comparing it with some MC simulations.

Given the very large computing resources required for the simulation of the various water models, it would be preferable if these simulations could be approximated by an analytical expression. The complexity of the trajectory of photons in water is however such that no exact analytical solution is possible. This problem can be simplified very much for the specific case where the photons scatter at most once between the source and the detector, i.e. where the scattering length is sufficiently large that multiple scattering can be neglected. In this limit, the three-dimensional scattering problem can be reduced to two dimensions. This is done as follows: consider the geometric setup shown in Figure E.1, where the isotropic light source and the detector are located at the focal points of an ellipse.

All photons from the light source that scatter on any point of the ellipse into the direction of the detector travel identical distances to reach it. A photon emitted by the source has a probability $dP(R)$ of reaching the detector after scattering once given by

$$dP(R) = \int \frac{d\Omega}{4\pi} \times e^{-\frac{r}{\lambda_S}} \times \frac{dr}{\lambda_S} \times \gamma \times \tilde{\beta}(\theta_\Sigma) \times e^{-\frac{r'}{\lambda_S}} \times e^{-\frac{r+r'}{\lambda_A}} \times \frac{A_D}{4\pi r'^2} \epsilon^D(\theta'), \qquad \text{(E.1)}$$

where $R = r + r'$ is the total distance traveled by the photon. The terms on the right-hand side of Eq. E.1, in the order in which they appear, correspond to the probability of emitting the photon into a particular direction from the source, the probability of not scattering for a distance $r$, then scattering in a distance $dr$ given a scattering length $\lambda_S$, the probability of either encountering a LC or SC scatterer $\gamma$, the probability of scattering at an angle $\theta_\Sigma$ to reach the detector, the probability of not scattering for a distance $r'$

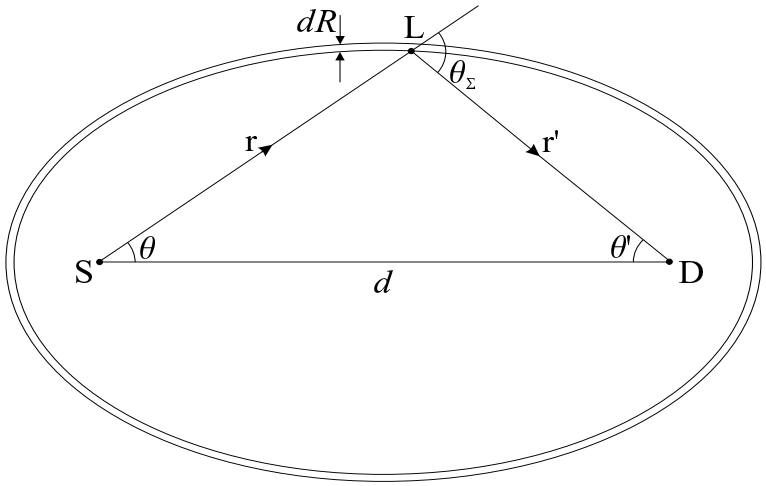


**Figure E.1:** *The isotropic light source $S$ is located at one of the focal points of the ellipse and the detector $D$ at the other focal point. All photons from the source that scatter on any part of the ellipse travel identical distances to the detector.*

before reaching the detector, the probability of not having been absorbed during the entire path and last but not least the probability of detecting the photon as a function of the angle of incidence upon the PMT, as derived in Appendix B. The integral is taken over all distances $r$, such that $R$ is constant. Eq. E.1 can be rewritten as

$$\frac{dP}{dR} = \frac{1}{4\pi} \frac{e^{-R(\frac{1}{\lambda_S}+\frac{1}{\lambda_A})}}{\lambda_S} A_D \int d\Omega \frac{dr}{dR} \frac{\epsilon'^D(\theta')}{4\pi r'^2} \left( p_{LC} \, \widetilde{\beta}_{LC}(\theta_\Sigma) + p_{SC} \, \widetilde{\beta}_{SC}(\theta_\Sigma) \right), \tag{E.2}$$

where $d\Omega = -2\pi \; d\cos\theta$ is the solid angle subtended by the light source at location $L$, $p_{LC}$ and $p_{SC}$ are the probabilities of LC and SC scattering given by Eq. 5.5 (p. 69) and the $\widetilde{\beta}$ with the respective subscripts are the corresponding angular distribution functions, normalised to unit area. $\epsilon'^D(\theta')$ is the angular efficiency of the OM, where $\theta'$ is given by Eq. E.3, and $dr/dR$ and $r'$ are given by Eqs. E.4 and E.5 respectively:

$$\theta' = \arccos\left( \frac{2Rd - R^2\cos\theta - d^2\cos\theta}{R^2 + d^2 - 2Rd\cos\theta} \right), \tag{E.3}$$

$$\frac{dr}{dR} = \frac{(R^2 - 2Rd\cos\theta + d^2)}{2(d\cos\theta - R)^2} \quad \text{and} \tag{E.4}$$

$$r' = \frac{2Rd\cos\theta - d^2 - R^2}{2(d\cos\theta - R)}. \tag{E.5}$$

The photon scattering angle $\theta_\Sigma$ is given by

$$\cos\theta_\Sigma = \frac{2d^2\cos^2\theta - 2dR\cos\theta - d^2 + R^2}{2dR\cos\theta - R^2 - d^2} \tag{E.6}$$

and the limits on the integral are

$$-1 \leq \cos\theta \leq \frac{2Rd}{d^2+R^2}, \tag{E.7}$$

where the upper limit on the cosine is determined by the angular acceptance of the detector OM. To take into account the $4\pi$ detection efficiency in the MC simulations, it is necessary to multiply Eq. E.2 by $4\pi d^2$. The number of photons $dN$ (from the simulations) as a function of the time $dt$ can be written as

$$\begin{aligned}\frac{dN}{dt} &= d^2 \times N_{trig} v_{gr} \times \frac{A_D}{\lambda_S} e^{-R(\frac{1}{\lambda_S}+\frac{1}{\lambda_A})} \\ &\times \int_{-1}^{\frac{2Rd}{d^2+R^2}} \frac{\epsilon'^D(\theta')}{2dR\cos\theta - d^2 - R^2} \left( \frac{\lambda_S}{\lambda_{LC}} \,\widetilde{\beta}_{LC}(\theta_\Sigma) + \frac{\lambda_S}{\lambda_{SC}} \,\widetilde{\beta}_{SC}(\theta_\Sigma) \right) d\cos\theta,\end{aligned} \tag{E.8}$$

where $N_{trig}$ is the total number of triggers and $v_{gr}$ is the group velocity of the photons in the medium, calculated from Eqs. 2.22 and 2.23 (p. 35). To the time distribution obtained from Eq. E.8, it is necessary to add the contribution of unscattered photons (also rescaled by the $4\pi d^2$ factor):

$$\frac{dN}{dt} = 4\pi d^2 \times N_{trig} v_{gr} \times \frac{A_D}{4\pi d^2}\, e^{-R(\frac{1}{\lambda_S}+\frac{1}{\lambda_A})} = N_{trig} v_{gr} \times A_D\, e^{-R(\frac{1}{\lambda_S}+\frac{1}{\lambda_A})} \tag{E.9}$$

Figure E.2 compares MC simulations and the analytical model for two cases: for the best water model at the ANTARES site in the UV (from the measurements with Test 3′) and for (hypothetical) measurements in the blue in the absence of LC scatterers, where $\lambda_{SC}$ was extrapolated from the UV using the $\lambda^{-4.32}$ dependence, both with a source-detector distance of 23.94 m.

The agreement between the analytical model and the MC simulation with $\lambda_{SC} = 374$ m is very good. This was to be expected since the probability of scattering more than once is very small ($\lesssim 0.2\%$). In the other case, the average scattering length $\lambda_S \approx 76$ m yields a probability of scattering more than once $> 4\%$, more than one order of magnitude larger, which evidently is not negligible. This shows as an overestimation of the number of photons that scattered at small angles by the analytical model, given that in the MCs these have actually scattered more than once, causing them to be detected later. At larger time delays, the analytical model underestimates the number of hits because those photons that would have been registered at longer time delays were registered earlier.

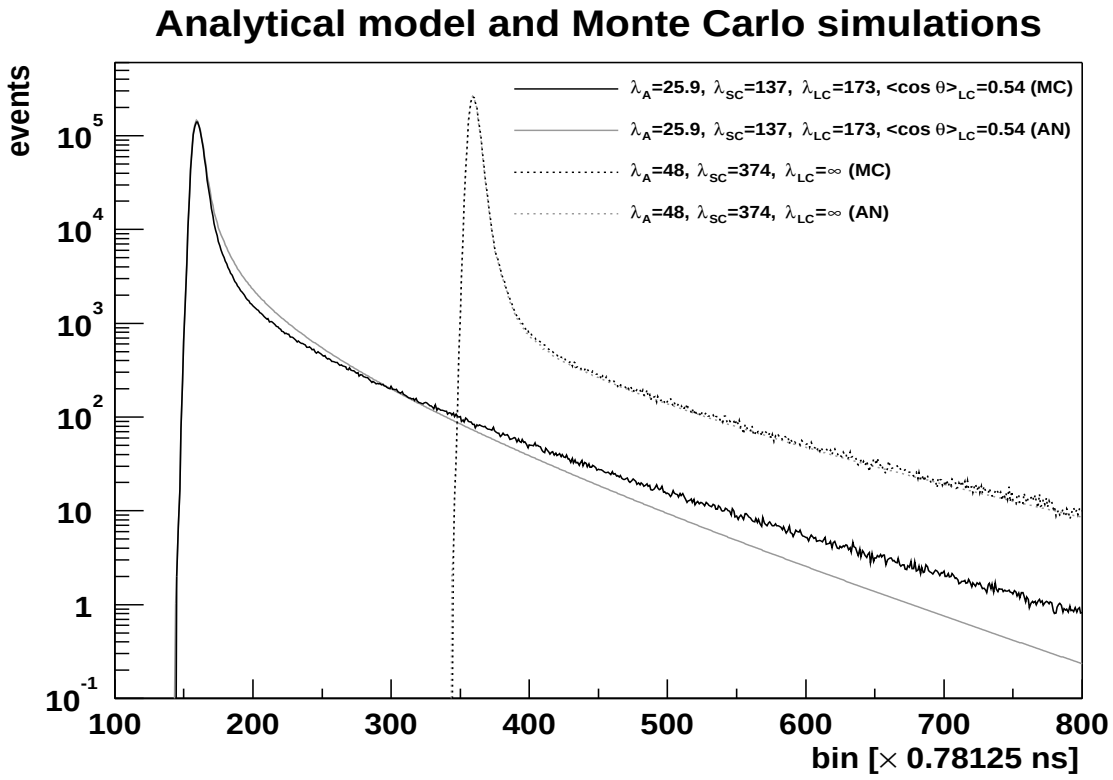


**Figure E.2:** *Comparison of the analytical model (AN) with MC simulations (MC) for the best water model in the UV at the ANTARES site and for SC scattering at blue wavelengths (472.6 nm).*

Whilst the analytical model is therefore not directly useful in the final analysis of the data from the current measurements with Test 3′, it could however be used to yield an estimate of the optical parameters in the limit where the scattering lengths are much larger (e.g. at other wavelengths and with different purity conditions), hence providing a valuable starting point for MC simulations.

# Bibliography


[1] D.J. Bird et al. (The FLYSEYE Collaboration). *Astrophys. J.*, **441**, 1 (1994) 144–150. astro-ph/9410067.

[2] N. Hayashida et al. (The AGASA Collaboration). *Astrophys. J.*, **522**, 1 (1999) 225–237. astro-ph/0008102.

[3] J. Cronin, T. Gaisser, & S. Swordy. *Sci. Amer.*, **276** (1997) 44–49. http://astroparticle.uchicago.edu/archives.htm.

[4] M. Punch et al. (The WHIPPLE Collaboration). *Nature*, **358**, 160 (1992) 477–478.

[5] D. Petry et al. (The HEGRA Collaboration). *ICHEP'96*, **2** (1996) 1577–1580.

[6] E. Waxman. *Nucl. Phys. Proc. Suppl.*, **87** (2000) 345–354. astro-ph/0002243.

[7] R. Enomoto et al. (The CANGOROO Collaboration). *Nature*, **416** (2002) 823–826. http://www.nature.com/nature/links/020425/020425-4.html.

[8] A. Kouchner. "Possibilité d'observation, par le téléscope ANTARES, de neutrinos de haute énergie associés aux sursauts gamma et validation des techniques de détection à l'aide d'un prototype". Ph.D. thesis, Université Paris 7 - Denis Diderot UFR de Physique (2001).

[9] K. Greisen. *Phys. Rev. Lett.*, **16**, 17 (1966) 748–750.

[10] G.T. Zatsepin & V.A. Kuz'min. *JETP Lett.*, **4** (1966) 78.

[11] F. Aharonian et al. (The HEGRA Collaboration). "Variations of the TeV energy spectrum at different flux levels of Mkn 421 observed with the HEGRA system of Cherenkov telescopes" (2002). Submitted to Astron. Astrophys.

[12] J. Jelley. *Phys. Rev. Lett.*, **16**, 11 (1966) 479–481.

[13] The ANTARES Collaboration. "A Deep Sea Telescope for High Energy Neutrinos". astro-ph/9907432 (1999). http://antares.in2p3.fr.

[14] E. Waxman & J. Bahcall. *Phys. Rev.*, **D59** (1999) 023002. hep-ph/9807282.

[15] T.K. Gaisser, F. Halzen & T. Stanev. *Phys. Rept.*, **258** (1995) 173–236.

[16] David J.L. Bailey. "Monte Carlo tools and analysis methods for understanding the ANTARES experiment and predicting its sensitivity to Dark Matter". D.Phil. thesis, Wolfson College, Oxford University (2002). In preparation.

[17] A. Morel. "Optical Aspects of Oceanography", chapter 1, pages 1–24. Academic Press New York (1974).

[18] T.J. Petzold. "Volume scattering functions for selected ocean waters." Scripps Institution of Oceanography, University of California, San Diego (1972). SIO Ref. 72-78.

[19] The ANTARES Collaboration. "Technical Design Report". Technical report, ANTARES, http://antares.in2p3.fr (2001).

[20] P. Amram et al. (The ANTARES Collaboration). *Nucl. Instrum. Meth. A*, **484** (2002) 369–383. astro-ph/0112172.

[21] P. Amram et al. (The ANTARES Collaboration). "Sedimentation and Fouling of Optical Surfaces in the ANTARES Site" (2002). Preprint submitted to Astroparticle Physics.

[22] M. Karolak, T. Chaleil, F. Desages, H. Lafoux. "Recette of the pilot-production of Hamamatsu 10 inch PMT". ANTARES Internal note, ANTARES-Opmo/2001-003 (2001).

[23] NAUTILUS MARINE SERVICE GmbH (Private Communication), Haferwende 3, D-28357 Bremen (Germany). http://www.nautilus gmbh.de (2002).

[24] C.F. Bohren, D.R. Huffman. "Absorption and Scattering of Light by Small Particles". Wiley (1983).

[25] M. Kerker. "The Scattering of Light". Academic Press (1969).

[26] M.v. Smulochowski. *Annalen der Physik*, **25** (1908) 205–226.

[27] A. Einstein. *Annalen der Physik*, **33** (1910) 1275–1298.

[28] Lord Rayleigh (J. W. Strutt). *Philos. Mag.*, **41** (1871) 107–120, 274–279, 447–454.

[29] Lord Rayleigh. *Philos. Mag.*, **12**, 73 (1881) 81–101. Fifth Series.

[30] Lord Rayleigh. *Proc. Roy. Soc.*, **97** (1920) 435–450. **98** (1920) 57-64.

[31] G. Mie. *Annalen der Physik*, **25**, Vierte Folge (1908) 377–445.

[32] Curtis D. Mobley. "Light and Water, Radiative Transfer in Natural Waters". Academic Press (1994).

[33] P. Askebjer et al. (The AMANDA Collaboration). *Appl. Opt.*, **36**, 18 (1997) 4168–4180.

[34] W.S. Pegau, D. Gray, J.R.V. Zaneveld. *Appl. Opt.*, **36**, 24 (1997) 6035–6046.

[35] R.M. Pope, E.S. Fry. *Appl. Opt.*, **36**, 33 (1997) 8710–8723.

[36] F.M. Sogandares, E.S. Fry. *Appl. Opt.*, **36** (1997) 8699–8709.

[37] J. Cabannes. *J. Phys.*, **6** (1920) 129–142.

[38] D. Stramski, D.A. Kiefer. *Prog. Oceanog.*, **28** (1991) 343–383.

[39] J.T.O. Kirk. "Light and photosynthesis in aquatic ecosystems". Cambridge University Press, second edition (1994).

[40] P.B. Price, L. Bergström (The AMANDA Collaboration). *Appl. Opt.*, **36**, 18 (1997) 4181–4194.

[41] E. Andres et al. (The AMANDA Collaboration). *Astropart. Phys.*, **13** (2000) 1–20. astro-ph/9906203.

[42] I. Belolaptikov et al. (The Baikal Collaboration). *Nucl. Phys. Proc. Suppl. B*, **19** (1991) 388–395.

[43] I. Belolaptikov et al. (The Baikal Collaboration). *Astropart. Phys.*, **7** (1997) 263–282.

[44] V.A. Balkanov et al. (The Baikal Collaboration). *Appl. Opt.*, **38**, 33 (1999) 6818–6825.

[45] R.C. Smith, R.L. Ensminger, R.W. Austin, J.D. Bailey, G.D. Edwards. *Proc. Soc. Photo-Opt. Instrum. Eng.*, **208** (1979) 27.

[46] R.C. Smith, K.S. Baker. *Appl. Opt.*, **20**, 2 (1981) 177–184.

[47] E.S. Fry, G.W. Kattawar, R.M. Pope. *Appl. Opt.*, **31**, 12 (1992) 2055–2065.

[48] C.F. Bohren. *Appl. Opt.*, **23**, 17 (1984) 2868.

[49] A. Bricaud, C. Roesler, J.R.V. Zaneveld. *Limnol. Oceanogr.*, **40**, 2 (1995) 393–410.

[50] G. Riccobene et al. (The NEMO Collaboration). *Nucl. Instrum. Meth. A*, **487**, 3 (2002) 423–434. astro-ph/0109005.

[51] C.D. Mobley, B. Gentili, H.R. Gordon, Z. Jin, G.W. Kattawar, A. Morel, P. Reinersman, K. Stammes, R.H. Stavn. *Appl. Opt.*, **32**, 36 (1993) 7484–7505.

[52] M. Ravisankar, A.T. Reghunath, K. Sathiandanan & V.P.N. Nampoori. *Appl. Opt.*, **27** (1988) 3387–3394.

[53] A. Morel. "Optics of the sea", chapter 3.1, pages 1–76. NATO Agard Lect. Ser., 61 (1973).

[54] J.S. Bartlett, K.J. Voss, S. Sathyendranath, A. Vodacek. *Appl. Opt.*, **37**, 15 (1998) 3324–3332.

[55] B.R. Marshall, R.C. Smith. *Appl. Opt.*, **29** (1990) 71–84.

[56] A.M. Kokorin, K.S. Shifrin. *IZV AN SSSR FIZ ATM*, **25**, 2 (1989) 193–201.

[57] L.A. Kuzmichev. *Nucl. Instr. Meth. A*, **482** (2002) 304–306. hep-ex/0005036.

[58] R.C. Millard, G. Seaver. *Deep-Sea Res.*, **37**, 12 (1990) 1909–1926.

[59] J. Brunner. "The refraction index at the Antares site". ANTARES-Site/2000-001 (2000). ANTARES Internal Note.

[60] A. Ivanoff. *Introduction à l'Océanographie, Paris*, **1** (1972) 83. Table 5.2.

[61] X. Quan, E.S. Fry. *Appl. Opt.*, **34**, 18 (1995) 3477–3480.

[62] R. Austin, G. Halikas. "The index of refraction of seawater." (1976). Visibility Laboratory SIO (Univ. Calif.), SIO No. 76-1.

[63] S. Tilav (Private Communication), Oxford University (UK) (2000).

[64] W.H. Schuster. "The data-acquisition software for the ANTARES Test 3′ experiment" (1999). http://antares.in2p3.fr/users/wolf/code/DAQ.html.

[65] MINOS electronics. Technical Report (Oxford).

[66] PARAFIL Ltd. "Propriétés à Long Terme". Technical report, Linear Composites Ltd. (2001).

[67] F. James. *Comput. Phys. Commun.*, **10** (1975) 343–367.

[68] L. Lyons. "Statistics for nuclear and particle physicists". Cambridge University Press (1986).

[69] Lars Bergström. "Routine from FastCal program". Physics Department, Stockholm University, SCFAB, S-106 91 Stockholm, Sweden.

[70] J.T.O Kirk. *Appl. Opt.*, **38**, 15 (1999) 3134–3140.

[71] J. McMillan (Private Communication), Sheffield University (UK) (2001).

[72] P. Amram et al. (The ANTARES Collaboration). *Astropart. Phys.*, **13** (2000) 127–136. astro-ph/9910170.

[73] N. Palanque-Delabrouille. "Optical background measurements, Tests 1.6 and 1.8 in the ANTARES site". ANTARES-site/1998-002 (1998). ANTARES Internal Note.

[74] F. Devillez, C. Racca. "Optical background measurements by Test 1.12 in the ANTARES site". ANTARES-site/2001-001 (2001). ANTARES Internal Note.

[75] M.E. Moorhead, N.W. Tanner. *Nucl. Instrum. Meth. A*, **378** (1996) 162–170.

[76] D.R. Lide, editor. "Handbook of Chemistry", chapter 6, pages 6-139. CRC Press (1995-1996).

[77] A. Morel. *J. Chim. Phys.*, **10** (1966) 1359-1366.

[78] E. Hecht. "OPTICS". Addison-Wesley Publishing Company Inc., second edition (1997).

[79] T.H. Chyba, L. Mandel. *J. Opt. Soc. Am. B*, **5**, 6 (1988) 1305–1311.

[80] W.H. Schuster. "Monte-Carlo simulations: limitations for the analysis of data". ANTARES-Site/2001-005 (2001). ANTARES Internal Note.